Systematic and Statistical Uncertainties in the Characterization of Gravitational-Wave Sources

by

Yiwen Huang

B.S., University of California, Los Angeles (2017)

Submitted to the Department of Physics
in partial fulfillment of the requirements for the degree of

Doctor of Philosophy in Physics, Statistics, and Data Science

at the

MASSACHUSETTS INSTITUTE OF TECHNOLOGY

February 2023

Author .....
Department of Physics
Jan 27, 2023

Certified by .....
Salvatore Vitale
Associate Professor of Physics
Thesis Supervisor

Accepted by .....
Lindley Winslow
Associate Department Head of Physics

Systematic and Statistical Uncertainties in the Characterization of Gravitational-Wave Sources

by

Yiwen Huang

Submitted to the Department of Physics
on Jan 27, 2023, in partial fulfillment of the
requirements for the degree of
Doctor of Philosophy in Physics, Statistics, and Data Science

Abstract

With the increasing number of gravitational-wave (GW) detections made by LIGO-Virgo-Kagra during the first three observing runs, the field of GW astrophysics has a growing need for prompt and precise parameter estimation (PE) of GW sources. To better understand the limitations of the current PE practices and to develop a more robust approach to analyze future GW sources, this thesis explores the impact of various aspects of data analysis, including priors, waveform models, noise characterization, and instrumental calibration errors, on the final PE results. This thesis demonstrates that in the case of marginal signals, the choice of priors can greatly impact the PE results and the subsequent astrophysical interpretation, especially when population-informed priors are not yet available. As the detector sensitivity improves, two other sources of systematic errors become increasingly relevant: waveform approximants and instrumental calibration errors. In the second half of the thesis, we conclude that the current waveform approximants for neutron star-black hole mergers are unlikely to introduce systematic errors comparable to the statistical uncertainties for sources that can be detected with current and near-future detector sensitivity. In terms of the calibration errors, we show that they will not impede the standard siren measurement of the Hubble constant in the coming decades. This thesis examines the impact of various data analysis choices on the final results with extensive PE runs unparalleled in the previous literature and can continue to provide valuable guidance for PE analysis for future generations of GW detectors.

Thesis Supervisor: Salvatore Vitale
Title: Associate Professor of Physics

Acknowledgments

First and foremost, I would like to thank my family: Hong Huang and Chen Ping, without whom I would not have ever been able to begin my physics journey ten years ago.

I would like to express my profound gratitude to my thesis advisor, Salvatore Vitale, for his instrumental role in guiding me throughout my career in gravitational-wave astrophysics. His expertise was invaluable in shaping my research. Salvo held a very high standard towards my work and challenged me to push my limits. This work would not have been possible without Salvo's guidance.

I am grateful for all the suggestions from my thesis committee, Professor Nergis Mavalvala, Professor Christopher Paus, and Professor Jesse Thaler, throughout my thesis work. I would also like to extend my heartfelt appreciation to my peers and collaborators for their academic and professional guidance: Prof. Hsin-Yu Chen, Prof. Carl-Johan Haster, Prof. Ling Sun, Prof. Francois Foucart, Dr. Ken K.Y. Ng, Dr. Maximiliano Isi, Dr. Vijay Varma, Prof. Aaron Zimmerman, Dr. Jeff Kissel, Prof. John Veitch, Dr. Hannah Middleton, Dr. Halston Lim, Sylvia Biscoveanu, Lisa Drummond, Geoffrey Mo, Calvin Leung, Nicholas Demos, Christopher Whittle, Jeff Krupa, Dr. Taweewat "Champ" Somboonpanyakul, Michael Calzadilla, Dr. Ani Chiti, Dr. Honggeun Kim, Dr. Xueying Guo, Stephanie O'Neil, Mason Ng, Joe Smolsky, Dr. Field Rogers, Nicholas Mehrle, David Berardo, Dr. Richard Mittleman, Dr. Lisa Barsotti, and many others.

I would like to thank all my friends who went out of their way to support me: Boya Song, Mantian Xue, Xiaoting Qin, Yizhi Zhu, Linqing Wei, Ziyan (Zoe) Zhu, Hanyu Gong, Xinyi Huang, Xingyi Shi, Zhenghao Fu, Qianfan Zhang, Yong Chen, Shaoying Tan, Liuyi Fang, Tongtong Liu, Preksha Naik, and Siyi Hu. I would also like to acknowledge Kexin Wu, Ziyan (Daisy) Zhang, Sijia Wu, Yixian (Lexi) Li, Bridget Derksen, Yueqiao Wu, Zhichen Shi, Ting Lu, Tong Tong, Tianmi Fang, Paxton Turner, Siyi Chen, Chaoying Zhu, Binqing Lyu, Yuan Feng, and many others, whose presence in my life brought me joy and ease during my study.

I would like to express my gratitude to Professor Matthew Evans, Prof. Deepto Chakrabarty, Dr. Erik Katsavounidis, Prof. Scott Hughes, Catherine Modica, Sydney Miller, Marie Woods, Debbie Meinbresse, and many others in the MIT Physics community for their support in the development of my academic and professional career.

Last but not least, I would like to thank all my cat friends: my cat Erwen, my roommate's cat Coco, and my parents' cat Huanghuang who has kept my parents in good company while I am not home.

While I cannot mention every individual by name, I would like to extend my sincerest gratitude to all who have supported and assisted me throughout my degree and in completing this thesis. I would not have been able to achieve this accomplishment without them.

Contents

List of Figures

List of Tables

Chapter 1

Introduction

In classical physics, time is considered to proceed constantly and independently for all objects, and gravity is viewed as a force acting on massive objects. This understanding of physics was widely accepted until Albert Einstein published the general theory of relativity (GR) in 1916. According to GR, gravity is no longer a force, but rather the curvature of space-time caused by the presence of massive objects. This curvature of space-time in turn influences the motion of other massive objects.

One of the predictions of GR is the existence of gravitational waves (GWs), which are "ripples" in the fabric of space-time caused by massive, accelerating objects [1]. It was not until 2015 that the Advanced Laser Interferometer Gravitational-Wave Observatory (LIGO) [2] successfully detected GWs from a binary black hole merger (BBH), providing the first direct evidence of GWs. This discovery opened up a new field of GW astrophysics, which provides a complementary way of observing the universe through GWs, complementary to the traditional astronomy that uses electromagnetic radiation (EM).

Any acceleration of a massive object can produce GWs, but detecting a GW signal on Earth is an extremely challenging task. GWs can be so weak when they reach Earth that they are easily drowned out by noise sources such as earthquakes or passing trains. To overcome this challenge and detect GWs on Earth, we utilize Michelson interferometers, which record the laser interference patterns to measure the differential changes, referred to as strain, in the arms of the interferometers. If we have multiple

detectors in an appropriate configuration, we can pinpoint the sources of the GWs in the sky. A more detailed description of this technique will follow in Section 1.2.

1.1 GW Sources

The first indirect evidence of GWs came from the observation of the Hulse-Taylor binary pulsars [3], where the decay of the orbital energy of the pulsars matched the prediction of energy loss due to the emission of GWs. The most violent and powerful events in the Universe, compact binary coalescences (CBCs): mergers of compact objects like black holes (BHs), neutron stars (NSs), or white dwarfs, can produce GWs directly observable on Earth. The source of the first directly detected GWs, GW150914, indeed falls in this category.

Some of the expected sources of GWs are also luminous in the EM band, which allows for the possibility of multi-messenger observations. The detection of the binary neutron star merger (BNS) GW170817 and the associated counterparts across all of the EM spectrum from radio to γ-rays (AT2017gfo/GRB170817A) [4–15] marked the beginning of the era of multi-messenger astrophysics based on photons and GWs. GW170817 allowed us to set constraints on the equation of state (EoS) of NSs [16], confirm the heavy metal production in BNSs [7, 10, 17–20], search for evidence of p-g modes [21] and put bounds on the component NS masses and spins [5]. The host of GW170817 was identified, and the EM data confirmed the connection between short gamma-ray bursts and BNSs, lead to the observation of the kilonova, and yielded insights on the details of the EM emission accompanying the merger [22–25]. Information from both the GW and the EM sides was used to measure the Hubble constant in a standard siren approach that is independent of the cosmic distance ladder [26].

Though LIGO-Virgo has joined research forces since 2010, GW170814 was the first BBH event detected by the LIGO-Virgo network. In 2021, Kagra collaboration joined the team since the third observing run, making the collaboration LIGO-Virgo-Kagra (LVK). To date, LVK has reported the detection of ninety-three GWs from CBCs in

the data collected during their first three observing runs [27–30]. The trend of the increasing number of GW detections is illustrated in Fig. 1-1. As more detections are made, they will make it possible to constrain the role of stellar wind, rotation, and metallicity in the progenitor stars [31], measure the merger rate [32], the spin and mass distribution [33–40] and perform stringent tests of GR in its strong-field regime [41–46].

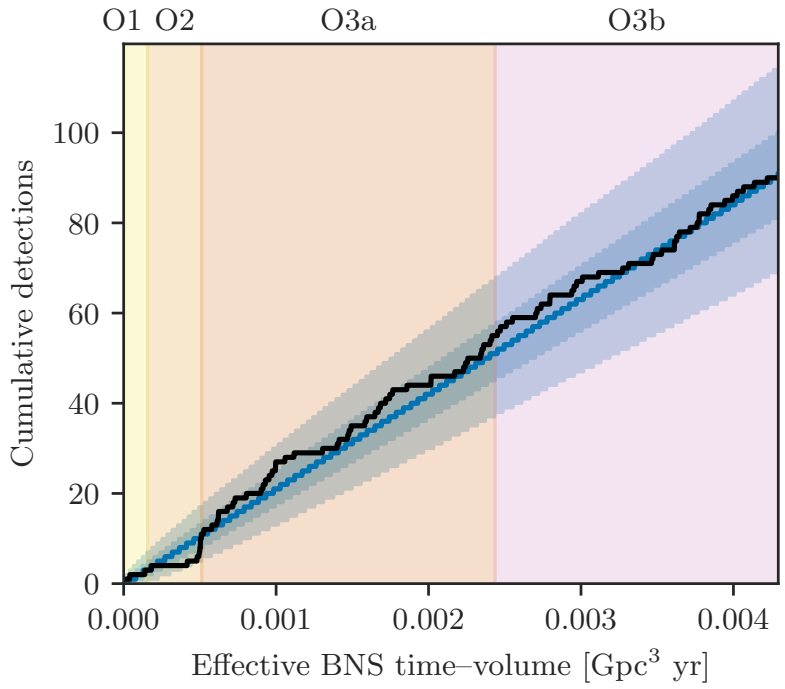

Figure 1-1: Total number of CBC detections versus the effective surveyed time–volume of the detector network for BNSs [29], reproduced from the third Gravitational-wave Transient Catalog (GWTC-3) [27].

Besides those three mentioned above, several other events have fascinating scientific implications. For example, GW190425, the second BNS detected using GWs, has a total mass that exceeds that of any other known galactic neutron star binaries[47]. Additionally, GW190521 is to date the most massive BBH detected, with its component masses being 85 and 66 solar masses ($M_\odot$) [48]. The resulting BH remnant has a mass of 142 $M_\odot$ and is the first unambiguous detection of an "intermediate-mass" black hole (IMBH).

GW190412 is the first BBH event with clear evidence of an unequal mass ratio [49],

and thus provides important new information on the properties of BBHs and their formation mechanisms. GW190814 is another BBH event with an extreme mass ratio, with the heavier BH being almost ten times as heavy as the lighter component [50]. This event also raises new questions about the nature of the lighter object, which is heavier than any other previously identified NS detected through EM [51] or GW. The lighter component in this event has a mass that falls within the hypothesized $2.5 - 5\ M_{\odot}$ lower mass gap [52–55], which is a region where no NSs or BHs have been previously observed. This discovery helps to refine current models and theories of the properties of compact objects and their possible formation mechanisms.

So far, no other EM counterparts have been identified and associated with a CBC event detected using GWs. This includes GW190425, the second BNS event, and the first-ever detected neutron star-black hole (NSBH) events, GW200105 and GW200115 [56]. Several limitations make identifying EM counterparts difficult, such as the large uncertainties in the sky localization of the event during parameter estimation (PE), which are much larger than the field-of-view of typical telescopes. Moreover, there is usually a trade-off between the field of view and the sensitivity of a telescope. Improving the rapidity and reliability of PE, especially in terms of sky localization, will be one of the critical challenges for multi-messenger astronomy. To increase the chances of identifying EM counterparts in the future, there have been proposals to build telescopes specific for GW follow-ups like the High Energy Stereoscopic System (H.E.S.S.) [57], the WINTER telescope [58] and many more, besides instruments that have dedicated telescope time for GW follow-ups like the Dark Energy Camera (DECam), Zwicky Transient Facility (ZTF) [59], Fermi Gamma-ray Space Telescope, to name a few.

In addition to the upcoming observing runs of LVK, there are the proposed third-generation ground-based GWs detectors, Cosmic Explorer [60] and Einstein Telescope [61]. These proposed detectors are expected to have much higher sensitivity and thus larger detection volume, allowing us to observe a much greater number of GW sources in the coming decades. Furthermore, the Laser Interferometer Space Antenna (LISA) [62] is a planned array of satellites that can detect GWs at much lower

frequencies, allowing us to study a wider variety of sources such as supermassive BBHs and binary white dwarfs. These new developments present countless opportunities in the future of GW astronomy and a growing demand for fast and accurate source characterization of GW detections.

In the following sections, I will briefly describe some common practices and concepts used in the GW data analysis pipeline, as illustrated in Fig. 1-2: GW data in Sec. 1.2, and Bayesian statistics in Sec. 1.3.

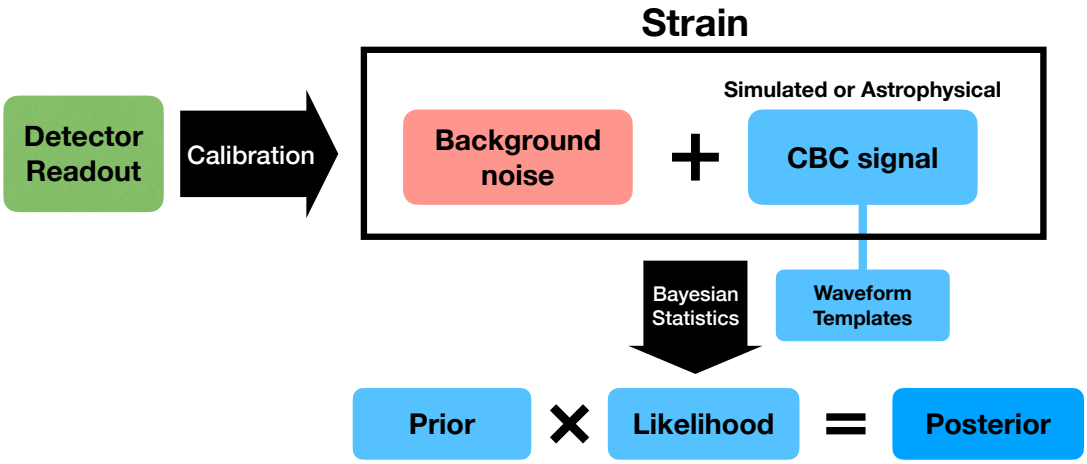

Figure 1-2: The GW data analysis pipeline.

1.2 GW Data

Each of the current aLIGO-Virgo detectors is a dual-recycled Fabry-Pérot Michelson laser interferometer (IFO) [64, 65], as illustrated in Fig. 1-3. Its data stream $\boldsymbol{d}_{\mathrm{IFO}}$ is obtained from a voltage signal, $\boldsymbol{e}_{\mathrm{IFO}}$, measured from the output power of the laser incident on a photodetector. The process of converting $\boldsymbol{e}_{\mathrm{IFO}}$ into $\boldsymbol{d}_{\mathrm{IFO}}$ is referred to as calibration [66], further discussed in Sec. 5.1.

The data in each IFO in the presence of a GW signal can be written as $\boldsymbol{d}$:

$$\boldsymbol{d} = \boldsymbol{h} + \boldsymbol{n} \tag{1.1}$$

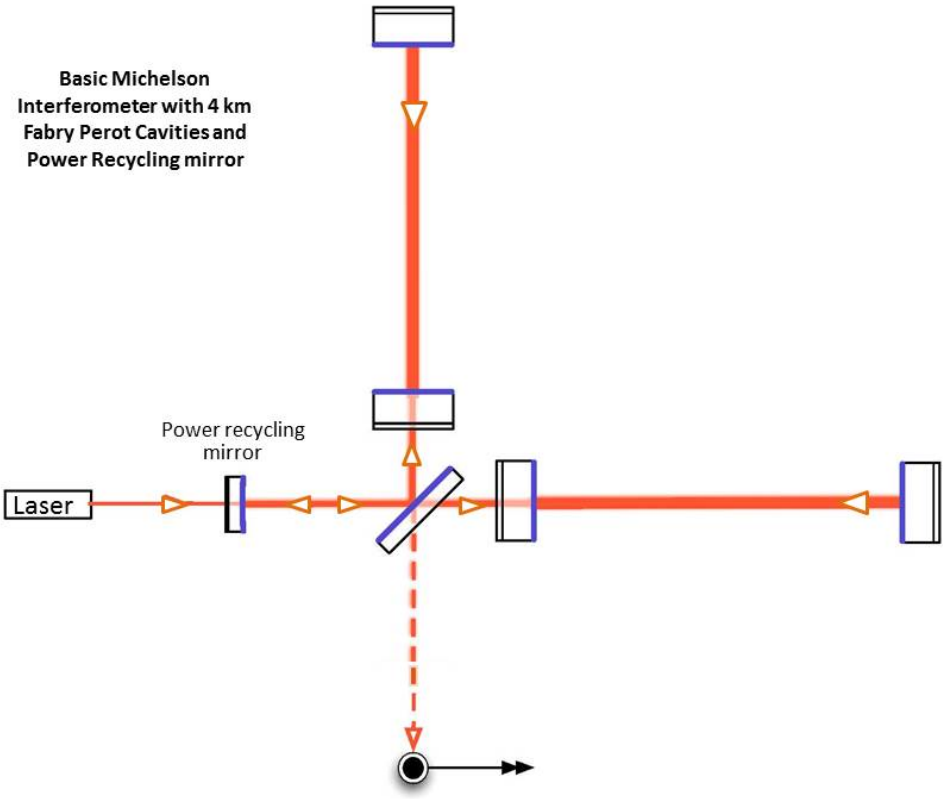

Figure 1-3: Michelson Interferometer, reproduced from Ref. [63].

where $\boldsymbol{h}$ is the GW signal and $\boldsymbol{n}$ is the background noise. With the data stream $\boldsymbol{d}$ from all detectors in hand, we want to measure the unknown source parameters, $\boldsymbol{\theta}$.

We can describe the GWs emitted by a binary of two point masses in a quasi-circular orbit by a set of 15 parameters, $\boldsymbol{\theta}$, including masses, spins, coalescence phase, polarization, as well as extrinsic parameters such as luminosity distance, inclination angle, arrival time on Earth, and sky position. Different parameterizations are possible for the mass parameters, including the asymmetric mass ratio $q = m_2/m_1$ (m_1, m_2 are the component masses, with $m_1 \geqslant m_2$ by convention), and the chirp mass $\mathcal{M}$:

$$\mathcal{M} = (m_1 m_2)^{3/5}(m_1 + m_2)^{-1/5}.$$

In general, six parameters are needed to describe the spins of the binary: two dimensionless spin magnitudes a_1, a_2 defined as $a_i = |\mathbf{S_i}|/m_i^2$ where $\mathbf{S_i}$ is the spin

vector; the tilt angles t_1, t_2 between the spin vectors and the orbital angular momentum at some reference frequency (usually equal to the lower frequency used in the analysis,) and two azimuth angles. While individual black hole spins ($\boldsymbol{S_i}$) are difficult to measure, a combination of the two spins called the effective spin $\chi_{\rm eff}$ [67–70] is usually much better measured [30, 39, 71–74]. The effective spin is the mass-weighted projection of the component spins, along the orbital angular momentum $\boldsymbol{L}$:

$$\chi_{\rm eff} = \left(\frac{m_1 \boldsymbol{\chi}_1 + m_2 \boldsymbol{\chi}_2}{m_1 + m_2} \right) \cdot \frac{\boldsymbol{L}}{|\boldsymbol{L}|} \,. \tag{1.2}$$

Note that we will be using natural units, $G = c = 1$, throughout this thesis.

Each NS in the binary adds additional complexity caused by the tidal deformation of the NS and its potential disruption before the merger. BNSs would thus require two additional parameters to model their linear tidal deformability [75–79].

The loudness of a given GW signal can be assessed with its optimal signal-to-noise ratio (SNR), $\rho_{\rm opt}$, defined in each IFO as [80]:

$$\rho_{\rm opt} = [\langle h(\boldsymbol{\theta}, f) | h(\boldsymbol{\theta}, f) \rangle]^{1/2} \tag{1.3}$$

where $h(\boldsymbol{\theta}, f)$ is the frequency-domain waveform projected in the detector, $S_n(f)$ is the power spectral density (PSD) of the detector noise, and the noise weighted scalar product is defined as:

$$\langle a(\boldsymbol{\theta}, f) | b(\boldsymbol{\theta}, f) \rangle \equiv 4 \int_{f_{\rm low}}^{f_{\rm high}} \frac{a(\boldsymbol{\theta}, f) b(\boldsymbol{\theta}, f)^*}{S_n(f)} df \tag{1.4}$$

where $f_{\rm low}$ and $f_{\rm high}$ are the frequency bounds, usually 20 Hz and 1024 Hz. When we have a network with multiple IFOs, we report the values of the network SNR, which we obtain by adding in quadrature the values from each detector. LVK's search algorithms calculate and report a matched-filter SNR [30, 81], defined as:

$$\rho_{\rm MF} = \frac{\sum_{IFO} \langle d | h(\boldsymbol{\theta}, f) \rangle}{\sqrt{\sum_{IFO} \langle h(\boldsymbol{\theta}, f) | h(\boldsymbol{\theta}, f) \rangle}}. \tag{1.5}$$

The optimal SNR is the expectation of the matched-filter SNR in the limit where the noise can be considered perfectly Gaussian.

1.3 Bayesian Statistics

We use Bayesian inference [82, 83], the standard practice in the field, to measure the unknown parameters of the detected signals [84, 85], and calculate their posterior probability density function (PDF):

$$p(\boldsymbol{\theta}|\boldsymbol{d}, H) = \frac{p(\boldsymbol{\theta}|H)p(\boldsymbol{d}|\boldsymbol{\theta}, H)}{p(\boldsymbol{d}|H)} \tag{1.6}$$

where $p(\boldsymbol{\theta}|H)$ is the prior probability density of $\boldsymbol{\theta}$, under the hypothesis H, and the second term in the numerator is the likelihood:

$$p(\boldsymbol{d}|\boldsymbol{\theta}, H) \propto \exp\left(-\frac{1}{2}\langle \boldsymbol{d} - h(\boldsymbol{\theta})|\boldsymbol{d} - h(\boldsymbol{\theta})\rangle\right). \tag{1.7}$$

The likelihood is defined so that it is maximized when the $\boldsymbol{d} - h(\boldsymbol{\theta})$ is closest to Gaussian noise with the detector PSD. The normalization constant $p(\boldsymbol{d}|H)$ is the evidence for the model H:

$$Z = p(\boldsymbol{d}|H) = \int \mathrm{d}\boldsymbol{\theta} p(\boldsymbol{d}|\boldsymbol{\theta}, H)p(\boldsymbol{\theta}|H). \tag{1.8}$$

Under the assumptions that the noise streams are statistically uncorrelated, the total likelihood can be written as a product of individual likelihoods from each IFO as: [86]

$$p(\boldsymbol{d}|\boldsymbol{\theta}, H) = \prod_{\mathrm{IFO}} p(\boldsymbol{d}_{\mathrm{IFO}}|\boldsymbol{\theta}, H) \tag{1.9}$$

where the product spans all the instruments in the network.

Given the multidimensional posteriors, Eq. (1.6), the posterior PDFs of any specific parameter can be found by marginalizing all the other parameters:

$$p(\theta_1|\boldsymbol{d}, H) = \int d\theta_2 ... d\theta_N p(\boldsymbol{\theta}|\boldsymbol{d}, H) \tag{1.10}$$

This thesis aims to investigate the impact of potential systematic errors on the PE of GW signals. The study can be divided into two main sections, each focusing on a distinct scenario for PE. The first part of the thesis examines the PE of marginal events with low SNRs. Chap. 2 discusses marginal events of various morphologies with SNRs around the detection threshold, mainly how precisely and accurately the sources can be characterized. Chap. 3 examines the choices made during the PE process of seven marginal astrophysical BBHs reported by an independent data analysis pipeline outside LVK: the choices of priors, the waveform models, the characterization of background noise, and the sampler.

The second part of the thesis explores the opposite limit, where the signals are strong enough that statistical uncertainties are small and systematic errors from inaccurate models become more prominent. Chap. 4 performs extensive PE runs to investigate NSBH waveform approximants, and Chap. 5 studies errors arising as the detector read-out is converted to the strain data.

The main objective of this thesis is to investigate the limitations of PE and to provide a comprehensive guide for future PE analysis and its astrophysical interpretation, by thoroughly examining the various components of the PE pipeline. The following four chapters will describe in detail how each analysis was conducted, to make the methodology easily reproducible and applicable to other GW analyses. The research described in each chapter corresponds to the publications [87], [88], [89] and [90], respectively.

Chapter 2

Marginal Simulated Events

The noise from GW detectors is not perfectly Gaussian. Non-Gaussian noise artifacts (often referred to as *glitches*) limit the sensitivity of GW searches [91]. To assess the significance of a candidate event, its SNR (or another detection statistics) is compared with the distribution of SNRs from the background, which is usually estimated either by time-sliding the data of different instruments [92] or by constructing the network SNR distribution assuming noise is independent in each detector [93]. Unfortunately, the distribution of SNRs from glitches increases much faster than those from CBCs as the SNR decreases [94, 95]. This can limit the benefits of lowering the threshold while searching for CBC signals and following them up in the EM band. For example, Ref. [96] has shown that lowering the threshold false alarm rate to one per month (week) would result in only 39% (13%) of the BNS candidate being of astrophysical origin. Observers who decide to follow up on marginal events would thus have to deal with a large number of false positives.

In this chapter, we look at a complementary aspect of marginal events: namely, the fact that their characterization can be challenging or inconclusive. Virtually all of the GW literature focusing on the characterization of GWs from compact binaries has considered clear detections, generating simulated GW signals with optimal SNRs above some thresholds (often ~ 12). In this study, we reverse that approach and only consider sources *weaker* than what could be considered as a clear detection.

We simulate BNS, BBH, and NSBH sources and add them to real interferometric

noise of LIGO and Virgo, re-colored to have the spectral behavior expected in the third observing run (O3), started in 2019 [92]. We analyze the sources at different optimal network SNRs, as defined in Eq. (1.3), from 6 to 12, and show exactly how the quality of the PE process degrades as the optimal network SNR decreases. We find even at optimal network SNRs of 12, BNS sources cannot be localized to areas smaller than ~ 400 deg^2 (90% credible interval). Meanwhile, the luminosity distance is always measured with relative uncertainties larger than 40%. It is not uncommon that the sky position and luminosity distance cannot be measured. This reveals the challenges of finding an EM counterpart to a weak GW source and making a compelling case that the association is real. The chirp mass, usually the best-measured parameter, shows signs of multimodality, especially for heavy systems. At optimal network SNRs of 7 or below, we obtain chirp mass posterior distributions that are multimodal, or with very large tails for most of the sources we consider. The uncertainty in the mass ratio is large for heavy systems, whereas it can be as small as 0.07 for NSBHs at optimal network SNRs of 12. Finally, we show that, especially for NSBH, the effective spin [97–100] can be measured at very low optimal network SNRs.

We use nested sampling implementation of LALInference [84] to stochastically explore the parameter space and produce posterior distributions for $\boldsymbol{\theta}$. To reduce the computational cost of the likelihood evaluations, we use the reduced order quadrature (ROQ) approximation [101]. Sampling the parameter space to measure the properties of weak signals in the presence of strong priors can be challenging. In App. A.1 we report on some sanity checks we have performed to verify the code had properly converged.

For BNSs, we start the analysis at 24 Hz, following the LIGO and Virgo collaborations [77], while for all other sources, we start at 20 Hz.

2.1 Noise and Signal Generation

The necessary ingredients to simulate an end-to-end analysis of a GW signal are thus the generation of a synthetic GW signal and a stretch of data to which the signal can

be added. This section describes our approach to generating these quantities, starting from the noise.

We work with a network of two Advanced LIGO instruments (Hanford and Livingston) and the Advanced Virgo detector. To make this study immediately relevant to O3, we work with noise streams with the projected O3 sensitivity for each instrument. The PSD, $S_n(f)$, of a stretch of data is defined as the average of the noise autocorrelation over the duration of the data segment [81]. It is trivial to produce Gaussian noise colored to have any specific PSD, and this is the approach followed in a significant fraction of the GW literature. However, when dealing with marginal events, using real noise seems important, as small noise artifacts or fluctuations might significantly impact the characterization of weak signals.

We use public real data from the first observing run (O1) [102] and re-color it to have the projected O3 spectral behavior[1]. More specifically, we select five GPS times in O1 such that the data around them do not contain any (known) astrophysical events nor significant instrumental artifact that would have resulted in vetoing that of data (Ref. [102] provides a list of data segments which are considered clean by the LIGO and Virgo collaboration). The O1 times we used for our analysis are listed in Table 2.1. We download the corresponding five data files for each of the LIGO instruments from Ref. [102] and use a routine of the GstLAL algorithm [93, 103–106] to apply the expected O3 power spectrum (specifically the lower bounds of the "Late" curve (2018-19) for Advanced LIGO and of the "Mid" curve (2018-19) for Advanced Virgo in [107].).

Since Virgo was not running with the Advanced LIGO in O1, no Virgo O1 data is available for those five GPS times. We simulate Virgo data as follows. For each GPS time, we pick a Hanford frame corresponding to one of the *other* four GPS times, shift the time stamp to coincide with the desired GPS time, and re-color it to the projected O3 Virgo PSD.

We stress that while recoloring O1 data to a target sensitivity (O3, in this case) gives a way to make predictions about the performances of future observing runs,

[1]This study was conducted before O3.

it also has limitations. In particular, it will not capture new types of instrumental artifacts that might arise as the instruments get more sensitive. On the other hand, recoloring archival data maintains old instrumental artifacts that might very well be solved in the future. However, as our signals do not overlap with major instrumental artifacts, and given the lack of alternatives, we proceed with recolored data and use Hanford data as time-shifted mock Virgo data.

The PSDs *estimated* with the BayesWave algorithm [108] for one of the data streams produced with this method are shown for each interferometer in Figure 2-1 (colored curves), together with the projected O3 curves (black lines) that we use to recolor the O1 data.

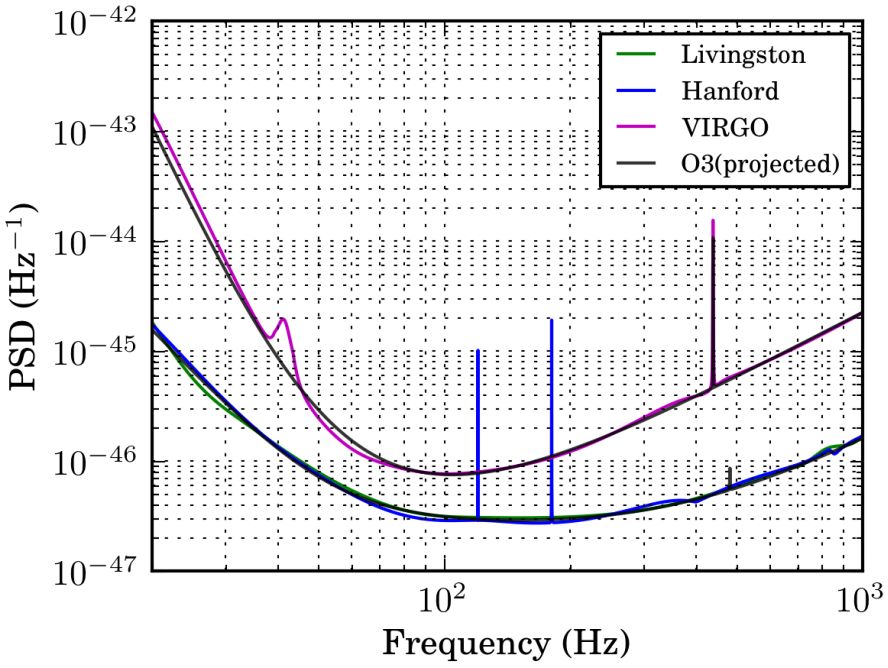

Figure 2-1: PSD of the recolored data for Advanced LIGO (green for Livingston, blue for Hanford) and Advanced Virgo (purple). The black lines are PSD for each instrument at the projected O3 sensitivities [107].

To generate the waveform signals, we use the IMRPhenomPv2 waveform approximant. This is an inspiral-merger-ringdown (IMR) waveform with an effective precessing spin [109–111]. We keep all the phase and amplitude corrections supported by the waveform.

GPS time	Date	Time
1135924088	2016 Jan 04	06:27:51
1135989351	2016 Jan 05	00:35:34
1136267078	2016 Jan 08	05:44:21
1136506663	2016 Jan 11	00:17:26
1136594611	2016 Jan 12	00:43:14

Table 2.1: Original O1 times in GPS and GMT. These are the times at which signals are "injected".

We prefer to work with the optimal SNR, instead of the matched-filter SNR, since the optimal SNR can be calculated from the waveform before it is added to the noise, without any knowledge of the exact realization of the noise. In the rest of the chapter, we will refer to optimal SNR as SNR, unless otherwise specified.

Clear detections typically have matched-filter network SNRs well above 12 for heavy objects [112–117], whereas BNS can be detected with high confidence at lower matched-filter network SNR [77, 118]. Since we wish to focus on marginal events, we generate signals with lower network SNRs: $[6, 7, 8, 9, 10, 12]$. We consider 4 representative CBC systems, BNSs, NSBHs, stellar-mass BBHs, and heavy stellar-mass BBHs (hBBHs). These representative morphologies capture some of the key features that can be present in CBC signals: long inspirals with little or no spin (BNSs); high mass ratio and visible spin precession (NSBHs) and heavier objects with little inspiral (BBHs and hBBHs). The masses and spins of each system are given in Table 2.2. In this study, we neglect tidal effects for BNS and NSBH to keep the computational cost reasonable. Given that tidal deformability is hard to measure even for loud events such as GW170817, they would not have been measurable with the marginal sources we consider in this chapter.

When the inclination angle is larger than ~ 70 degrees, the cross-polarization becomes negligible, affecting the estimation of the extrinsic parameters [119–121]. Thus, we consider two different inclination angles for each source: 30 degrees and 80 degrees, to take into account the effect of polarization. We assign the same geographical

coordinate to all of our simulated sources. Specifically, they are overhead of the two LIGO detectors, the positions where most events should be detected. This results in roughly equal SNRs in the two LIGO detectors. We can quantify the sensitivity of each detector to a particular direction and polarization with the square root of the sum of the antenna pattern, F, squared [81]:

$$F^{\mathrm{IFO}} = \sqrt{F_{+}^{\mathrm{IFO}}(\alpha, \delta, \psi)^2 + F_{\times}^{\mathrm{IFO}}(\alpha, \delta, \psi)^2}$$

where α is the right ascension, δ is the declination, and ψ is the polarization of the GW signal. We have the same values for all of our sources: $F^H = F^L = 0.7$, $F^V = 0.3$. Each system has its distance scaled to give the desired SNR and added to the recolored data at the five GPS times of Table 2.1. In total, we analyze 4 (mass bins) $\times$ 2 (inclinations) $\times$ 6 (SNRs) $\times$ 5 (GPS times) = 240 simulated events.

Type	$m_1(M_\odot)$	a_1	$t_1(^\circ)$	$m_2(M_\odot)$	a_2	$t_2(^\circ)$
BNS	1.4	0	0	1.4	0	0
NSBH	8	0.8	46	1.4	0	0
BBH	12	0.6	60	6	0.1	60
hBBH	30	0.6	60	30	0.6	60

Table 2.2: The intrinsic parameters for the four morphologies considered in this study.

2.1.1 Choice of Priors

Bayesian inference requires explicit priors, in our case $p(\boldsymbol{\theta}|H)$ under the hypothesis that a CBC signal is present in the data. For all parameters except the luminosity distance (see below), we use the same priors used by the LIGO and Virgo collaboration for the CBCs detected as of the time of writing this chapter [5, 77, 85, 113–117]. We use isotropic priors for sky position, orbital orientation, and spin orientation. For the dimensionless spin magnitude, we used uniform priors in the range $[0, 0.89]$ for BHs [85, 113–117] and $[0, 0.05]$ for NSs [5, 77]. The priors on the component masses

are also uniform, in the range in which the corresponding ROQ basis is valid [101].

The most natural prior for the luminosity distance would be a prior uniform in volume, $p(d_L) \sim d_L^2$, since the detection horizon for CBC is tens or hundreds of megaparsecs, depending on the total mass. This is indeed the prior used in LIGO-Virgo papers.

In this study, we prefer to use a *uniform* prior on the luminosity distance, and then re-weight the samples to enforce a uniform-in-volume prior. The reason is as follows. The nested sampling algorithm samples the prior [122] to calculate the evidence Z, obtaining the posterior distribution as a by-product. When using a uniform-in-volume distance prior, the nested sampling algorithm will spend a significant fraction of time exploring the region of parameter space where the distance is large. If we could run the algorithm for an arbitrarily large number of steps, it would eventually converge to the correct parameters. But when using a finite number of steps for low-significance events like the ones we are considering, the algorithm might in practice not explore properly the part of the parameter space where the distance is small, since it would have to overcome a significant prior penalty. By sampling with a uniform-in-distance prior we avoid this issue. The sampler can easily explore the whole distance range, and the correct prior is applied in post-processing with a standard rejection sampling approach.

2.2 Results

In this section, we report the uncertainty in measuring some of the key parameters of the simulated events. Unless otherwise specified, we used 90% credible intervals (CI). Those are either absolute intervals (in the appropriate units) or relative to the true value (in percentages).

2.2.1 Extrinsic Parameters

Extrinsic parameters such as sky location and luminosity distance are of fundamental importance for EM follow-ups. Although the details of the follow-up to GW triggers

vary with the facility and geographical factors (e.g. altitude of the source) [12], one usually tries to cover all or part of the sky uncertainty area (or sky-distance uncertainty volume). In fact, three-dimensional uncertainty volumes have been routinely released in low latency by the LIGO and Virgo collaboration for significant events in the first and second observing runs. Lowering the threshold for making triggers public would in general imply a significant increase of the false positive fraction [96]. In this section, we show that an EM follow-up campaign might be prohibitive even for events of astrophysical origin.

In Figure 2-2, we show the 90% credible regions (deg^2) for all the sources we analyzed. Each color represents a different morphology (red for BNS, purple for NSBH, blue for BBH, green for hBBH), whereas the shape of the bullet indicates the inclination angle (circles for 30°, stars for 80°). The optimal network SNR (for the remaining of this section we will drop the "network") is reported in the horizontal axis. Notice that we have artificially introduced a small horizontal offset while plotting to avoid significant superposition between data from different morphologies. The five markers for each (SNR, morphology, inclination) set correspond to the results from the five GPS times.

We see the expected overall trend of decreasing uncertainties with increasing SNRs. At SNRs below 10, we find that some sources are localized to uncertainties of $10,000$ deg^2 or more. However, even at these SNRs, there are sources that can be localized within areas of $[400 - 1,000]$ deg^2. We have verified that these variations are due to the specific data stream into which events were added. In particular, we find that one of the five GPS times produces systematically lower uncertainties. At these low SNRs, the actual noise realization can significantly impact the outcomes of the PE process. As the SNRs increase, the signals can be more easily distinguished from the noise, and the latter plays less of a role.

The loudest events we consider have SNRs of 12. For most of those, the 90% credible regions of sky localization are of [200-1,000] deg^2. These large error areas would make it extremely challenging to pursue a systematic EM follow-up in any band other than radio [123–125], where wide-field instruments can be deployed. For

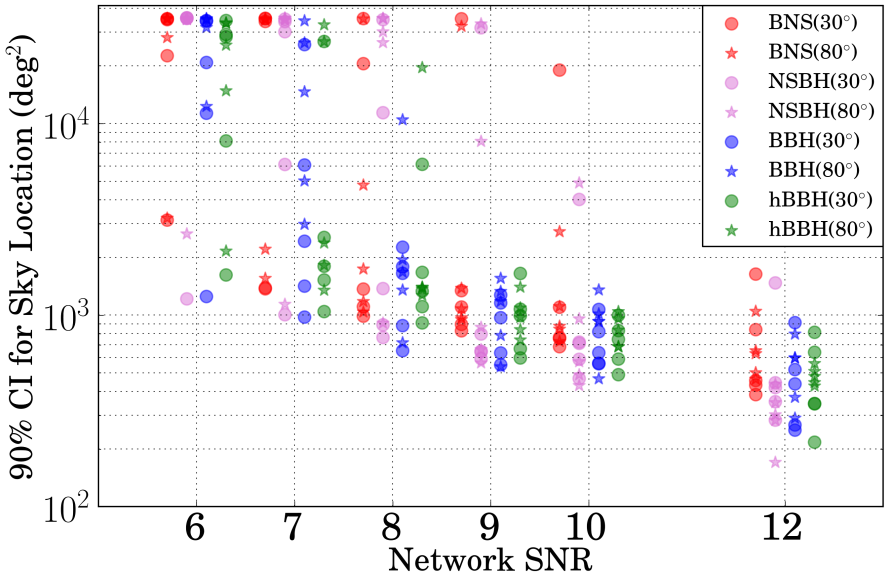

Figure 2-2: Size of 90% credible regions of the marginalized posteriors for sky location vs. network SNR.

comparison, Ref. [126] simulated a large number of BNS with astrophysically motivated parameters and found that 50% of the BNS detectable by a LIGO-Virgo network (at their sensitivity of the second observing run) would have a 90% CI of 235 deg^2 or smaller if a detection threshold of matched-filter network SNR above 12 is used.

Similar wild variations in precision can be seen for the luminosity distance d_L, Figure 2-3. Relative uncertainties are above 40% at all SNRs, and very often above 100%. We observe that NSBHs typically yield the smallest uncertainties. This is expected since we allowed spin precession for NSBHs, as given in Table. 2.2. Spin precession, together with the high mass ratios of NSBHs, helps break the degeneracy between distance and inclination angle, leading to smaller uncertainties [38, 120, 127].

2.2.2 Intrinsic Parameters

We now discuss the estimation of intrinsic parameters: masses and spins.

For clear detections, the (detector-frame) chirp mass (defined in Eq. (1.2)) is typically measured very well, with relative uncertainties of $\sim 0.01\%$ for BNSs [5, 128, 129] and around 15% for heavier objects [85, 112–117]. The chirp mass is measured

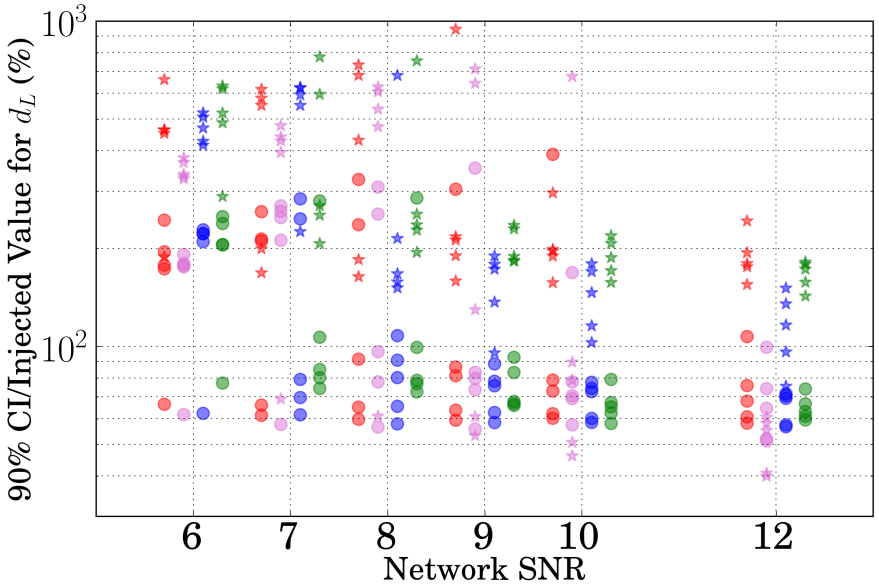

Figure 2-3: 90% CI of the marginalized posteriors / injected value for d_L vs. network SNR.

better for low-mass systems because it affects the phase evolution at the lowest Post Newtonian order [130], and thus can be measured better for signals with long inspirals. Since the merger frequency decreases as the total mass increases, BNSs are the sources for which the chirp mass can be best measured.

In Figure 2-4, we report the relative 90% uncertainty for the chirp mass against the network SNR. Overall, we see that BNSs have the smallest relative uncertainties followed by NSBHs, BBHs, and hBBHs. The different morphologies are thus naturally sorted by their total masses, as expected.

We will first discuss the high-SNR end of the simulations, as the weakest events deserve a separate discussion. At SNRs 10 and 12, the BNSs have relative uncertainties between 0.03% and 0.1%. This is in the ballpark of what one could have guessed using a $1/\mathrm{SNR}^2$ scaling argument [80], with GW170817 as a reference point. This simple analysis is not totally accurate, since the variance scales like $1/\mathrm{SNR}^2$ only at large SNRs. For smaller SNRs, higher-order corrections must be taken into account [131, 132], and the uncertainties in the plot are indeed well above what a simple scaling argument would suggest. At the high end of our SNR distribution, we find that the

results from different GPS times and orientations are grouped together with very few exceptions. The uncertainty mostly depends on the morphology. Due to their

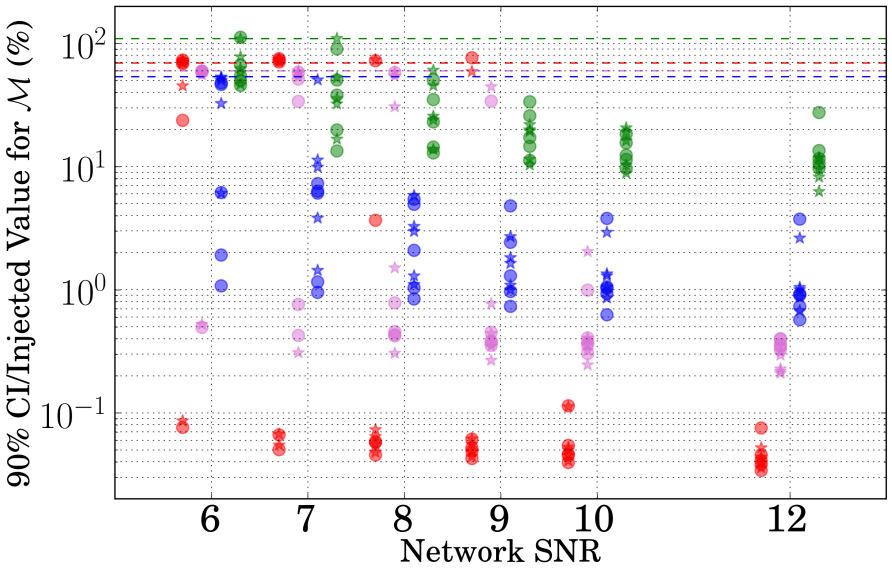

Figure 2-4: Relative 90% credible interval for the chirp mass vs. network SNR. The dashed lines represent the relative 90% width of the prior.

relatively long inspirals, NSBHs are the second-best source type, with uncertainties between 0.2% and $\sim$ 2% at SNRs 10 and 12, including all data realizations and orientations. Stellar-mass BBHs have uncertainties between 0.5% and $\sim$ 4%, a factor of 2 worse than NSBHs, while heavy BBHs are considerably worse, with uncertainties between 5% and 30% (again, at SNR 10 and 12).

As the SNRs decrease, we observe two distinct populations: one that roughly continues the trend we see at SNR 10 and 12 with some degradation; and another with much larger uncertainties, comparable to the prior width, especially for BNSs. The latter are events for which the posteriors are not unimodal. One could expect that at low SNRs, noise fluctuations can seriously impact the measurement of the chirp mass since it is obtained by "following" the phase evolution of the waveform signal through thousands of cycles [133]. We get a (rough) classification of the chirp mass posteriors by using the *find_peaks* routine of Scipy [134] using a prominence threshold of 9% of the main peak to trigger the recognition of additional modes. While more sophisticated statistical tests could be used, this gives us at least an idea of what fraction of the

posteriors is clearly unimodal. A distinct type of chirp mass posteriors appears often enough to deserve some discussion: those with clearly uni-modal posteriors but with tails large enough to span most if not all of the prior range. These are sources for which the likelihood profile is shallow and does not dominate the underlying prior distribution.

We thus introduce three categories: unimodal; "unimodal-wide", which we define as posteriors with one clear peak but a 90% uncertainty larger than 50% of the prior range; and multimodal posteriors. Examples of each are shown in Figure 2-5.

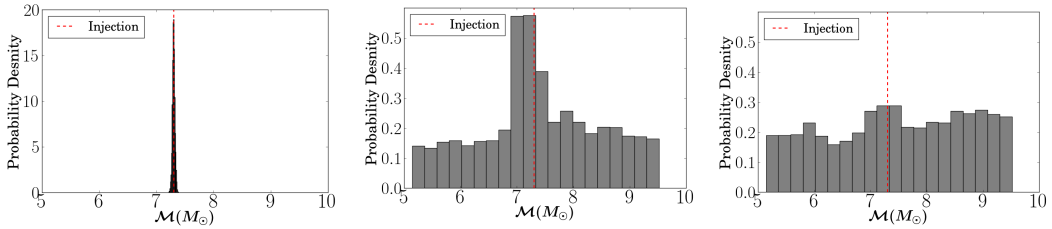

(a) Unimodal. The network SNR is 12.

(b) "Unimodal-Wide". The network SNR is 7.

(c) Multimodal. The network SNR is 6.

Figure 2-5: Representative posterior distribution for the chirp mass. All systems are BBHs with true inclination angle of 80°. The range is the same in all panels on the x-axis.

We apply this classification scheme to all events and show the fraction of events that belong to each category in Figure 2-6. At SNRs 10 and 12, all morphologies but BBHs show unimodal posteriors. Some of the BBHs at these SNRs have hints of secondary modes that do not significantly broaden the 90% CIs, as clear from Figure 2-4. On the opposite end, at SNRs 6 and 7, most events have multimodal posteriors, or a broad posterior filling up most of the prior range with just a hint of a peak at the true chirp mass value.

Next, we consider the asymmetric mass ratio q, Figure 2-7. We expect NSBHs to yield the best measurements, since spin-induced precession breaks the degeneracy between mass ratio and spins [38, 120, 127, 135], improving the measurability of both. For NSBHs, we find uncertainties as small as 0.07 for SNRs of 12 and orientations close to edge-on. For the NSBHs with orientation close to face-on, the uncertainty is systematically worse, at all SNRs. The reason is again the correlation. When orbital

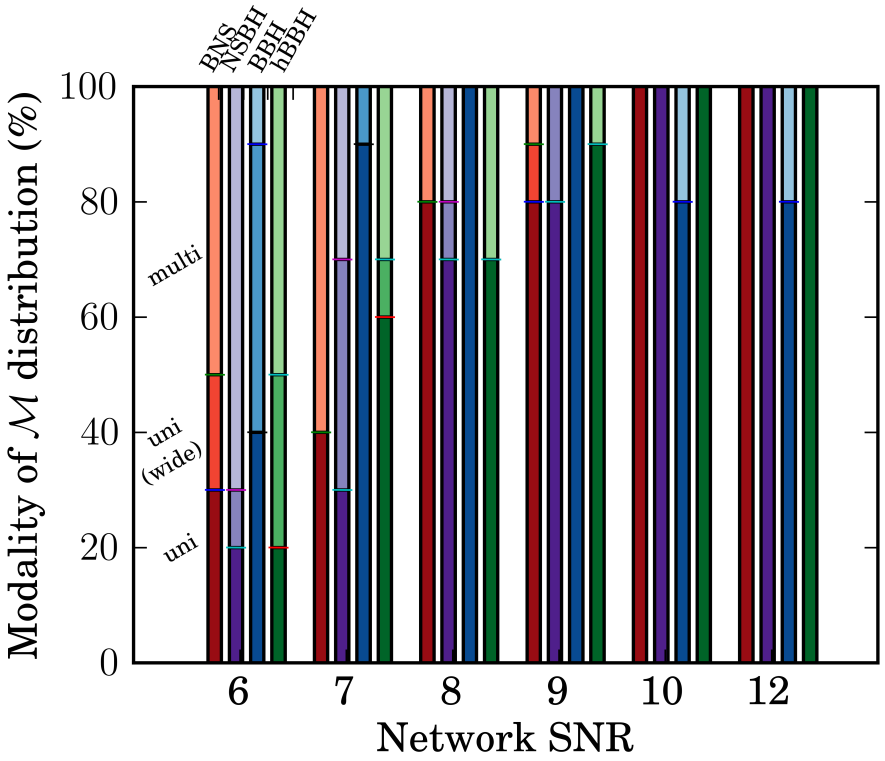

Figure 2-6: Proportions for uni-modal, uni-modal (wide) and multimodal posterior distributions for chirp mass (%) vs. network SNR.

precession is present, inclinations closer to 90° yield better spin measurement [38, 39]. The smaller spin uncertainties result in smaller mass ratio uncertainties. The same trend is visible for the BBHs. However, the hBBHs have comparable uncertainties regardless of the orientation, because the hBBHs in our simulations are equal-mass, which suppresses spin precession. Owing to their longer inspiral phase, the uncertainties are of $[0.3 - 0.5]$ for most BNSs in the SNR range of $7 - 12$, better than those for BBHs and hBBHs. These results suggest that if the real source is a marginal NSBH with visible spin precession, one might be able to distinguish between an NSBH and a low-mass BBH, but not so easily between a BNS and a low-mass NSBH.

We now look at the estimation of the spins. Since individual spins are hard to measure even for loud sources [5, 38, 39, 85, 112–117, 135] we focus on the the effective inspiral spin, $\chi_{\rm eff}$, as defined in Eq. (1.2). Importantly, the effective spin can be used to distinguish between different astrophysical formation channels [128, 136], instead

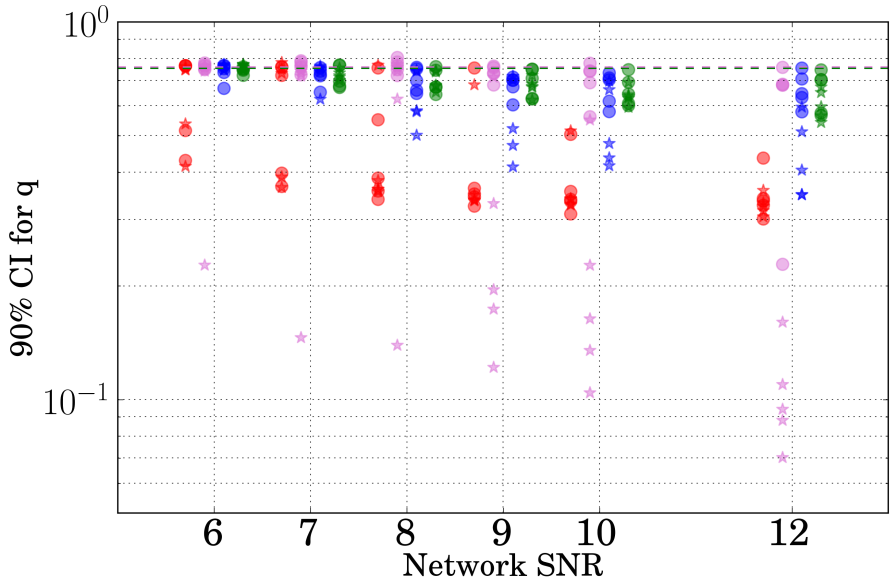

Figure 2-7: 90% CI of the marginalized posteriors for mass ratio q vs. network SNR. The dashed line represents the 90% CI for the q prior.

of relying on the measurement of the individual spins [33, 137]. We report the 90% CI for $\chi_{\rm eff}$ in Figure 2-8, where the horizontal dashed lines represent the 90% of the prior width. For all sources that include at least one BH, the uncertainties at SNRs of 12 are between ~ 0.08 and ~ 0.3, a factor of $2-10$ narrower than the prior. At SNRs of 10, the uncertainties for these systems are between ~ 0.1 and ~ 0.4. For the same reasons we described while discussing the mass ratio results, the effective spin estimation is best for NSBH with edge-on orientations. Heavy BBHs are the worst since they have short inspirals and mass ratios of unity. As the SNRs decrease, the $\chi_{\rm eff}$ posterior is still informative for some sources. Conversely, for the BNSs, even at SNRs of 12, the posteriors are only marginally narrower than the prior.

To quantify the amount of information gained about $\chi_{\rm eff}$ after analyzing the data, we calculate the Kullback-Leibler (K-L) divergence [138] of the posterior Q over the prior P:

$$D_{KL}(P||Q) = \sum_i P(i) \ln \frac{Q(i)}{P(i)} \tag{2.1}$$

where the index i spans the samples. This is shown in Figure 2-9. For most sources with at least one BH at SNRs of 12, the data yield more than 1 nat of information.

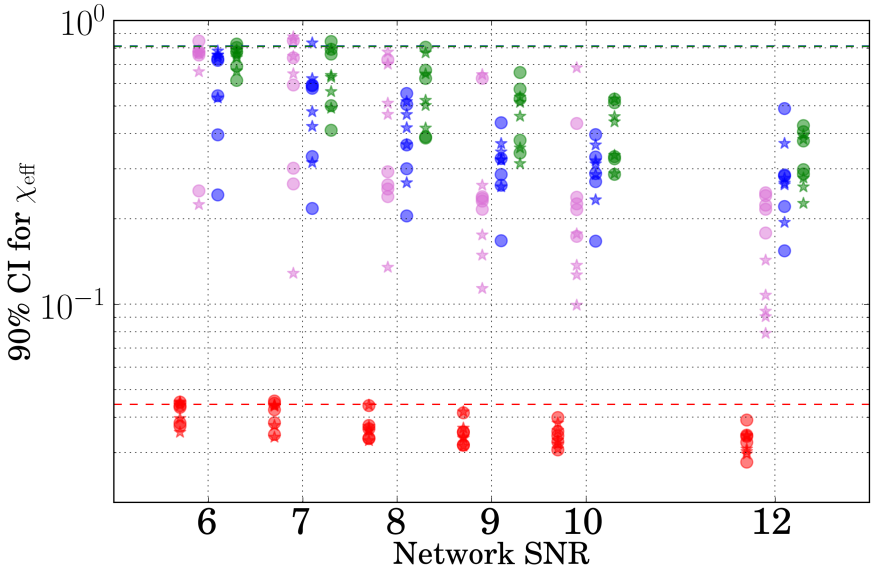

Figure 2-8: 90% CI of the marginalized posteriors for $\chi_{\rm eff}$ vs. network SNR. The dashed line represents the 90% CI for $\chi_{\rm eff}$ prior.

The most information is gained for NSBHs, while the data is usually less informative for BNSs. At SNRs of 12, the typical information gained for BNSs is ~ 0.1 nats, while at low SNRs, no information is gained, which implies that the posterior is basically the prior. This is consistent with Figure 2-8. As the SNR decreases, the data cannot significantly update the prior, and the K-L divergence can get values below 0.1 nats. In App. A.2, we report the median K-L divergence over the five GPS times for all parameters and all signal morphologies.

2.3 Conclusion

CBCs, the most common source of GWs detectable by ground-based detectors, are expected to be distributed uniformly in volume. This implies that their SNRs ρ should be distributed as ρ^{-4}: for each loud detection, there should be many more marginal signals in the data. In practice, lowering the threshold matched-filter network SNR (or other detection statistics) will not increase the number of detections with the fourth power since the background from instrumental and environmental sources increases more steeply. As the detection threshold is lowered, candidate events will compete

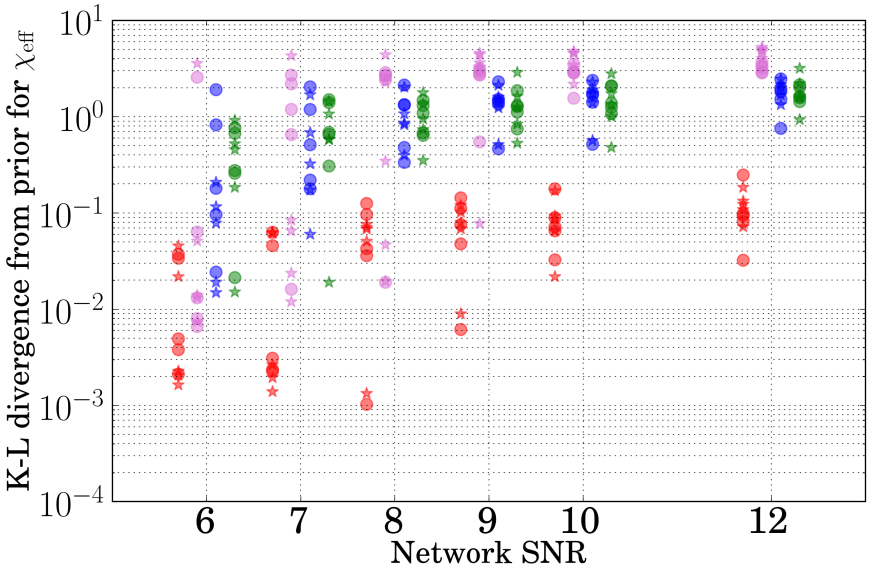

Figure 2-9: K-L divergence for $\chi_{\rm eff}$ vs. network SNR.

with background events of non-astrophysical origins [96, 118, 139, 140].

However, it is still the case that a significant fraction of detections made in the next few years will be marginal. In this chapter, we have explored what kind of astrophysical information can be extracted from these weak signals. This topic was not extensively studied in the literature since most existing work focuses on clear detections (see Ref. [140]).

We have simulated GWs from various CBC sources with different network SNRs, from 6 to 12, and added them into real interferometric data. We have considered a network made by the two Advanced LIGOs and the Advanced Virgo detector at their expected sensitivity for O3, which began in April 2019.

We have shown that the 90% credible regions in the sky localization of the sources are of $[200 - 1,000]$ deg^2 for network SNRs of 12 for all signal morphologies. As the network SNR decreases, the uncertainty increases and a larger spread between different noise realizations is present, which confirms that the specific noise realization can seriously affect the outcome of the analysis at very low SNRs. Most sources are not localized at all at the lowest SNRs we consider. However, it is essential to notice that for those events, it is not systematically the case that other parameters are not

measured (e.g., the chirp mass). The reason is that a single detector is enough to measure an intrinsic parameter like the chirp mass, while at least two are needed to constrain the sky position through time triangulation as well as amplitude and phase consistency [141–143].

The measurement of the luminosity distance, which could be used to infer the Hubble constant if a counterpart is found [26, 120, 144–146] (or statistically, in the absence of counterparts [147, 148]), is also challenging for similar reasons. We have found relative uncertainties for the luminosity distance to be above 40% even for the loudest event we considered and above 100% for a significant fraction of events. These numbers suggest that wide-field radio is the only viable option for following up on marginal CBC events. There is also the possibility that an EM counterpart, e.g., a gamma-ray burst, is found independently, which could be used to confirm the astrophysical nature of the GW candidate. However, given the large uncertainties in sky position and distance, one might have to deal with a significant background of EM signals, making it difficult to claim a solid association.

We have verified that intrinsic parameters, such as the detector-frame masses and the effective spin, can usually be constrained and do not simply yield the prior. We have found that the chirp mass can be estimated to be better than 0.1% for BNSs, 2% for NSBHs, and 4% for stellar-mass BBHs, at SNRs of 10 and 12. As the SNR decreases, the uncertainties increase gradually for the bulk of the source. Still, for some noise realizations, the posteriors start to be multimodal or develop fat tails, dramatically increasing the uncertainty. Most of the BBHs in the simulation yield uncertainties in the range $\sim [0.5 - 10]$ %. Owing to their shorter inspirals, hBBHs have larger uncertainties, above 5% at SNRs of 12 and above 8% at SNRs of 10 or lower.

The mass ratio can only be significantly constrained for sources with visible spin precession (NSBHs) or long inspirals (BNSs). At SNRs of 12, the 90% can be as small as ~ 0.07 for our NSBHs, and $[0.3 - 0.5]$ for BNSs.

Finally, the effective spins can be constrained, obtaining posterior distributions a factor of many narrower than the prior for systems with large mass ratios and

spin precession. For those at SNRs of 10, the uncertainty can be as small as ~ 0.1, although ~ 0.4 is more common (the prior width is 0.89). Using the K-L divergence, we quantified the amount of information provided by the data. For systems with at least one BH, that number is usually above one nat. For BNSs, we have used a more restrictive prior (the prior width is 0.05) and obtained that the data usually yield only a limited amount of information. At SNRs of 12, the typical K-L divergence we have found for BNSs is 0.1 nats. However, as the SNR decreases, the data does not allow for significant updates on the prior, and the K-L divergence can get values below 0.1 nats.

Based on the uncertainties mentioned above, it might occasionally be possible to associate a marginal source with a specific astrophysical class (e.g., BBH rather than BNS). It is important to remember that even if each event individually is not particularly informative, the whole population of marginal events can be used and contribute to the astrophysical inference of the underlying population. Moreover, this can be done even if one is not sure about their astrophysical origin since the probability that the event is astrophysical can be folded in the analysis [140].

Chapter 3

Marginal Astrophysical Signals

The parameters of observed BBHs [71, 74] encode information about the underlying BBH population and about the evolutionary history of the BHs and their progenitors. The masses and spins of the BHs in particular can be used to infer the formation mechanism of the observed binaries. Usually, two families of formation scenarios are considered: classical binary evolution in the galactic field [149–163], or dynamical formation either in the galactic field [164], or in dense environments such as clusters [165, 166] or AGN disks [167–170][1]. This latter scenario could also result in repeated mergers, which would produce heavier BHs [171–173].

The spins of the BHs, specifically the relative orientation of the BH spins in a binary, can be used to discriminate between these formation channels: formation in the field is expected to result in spins that are nearly aligned with the orbital angular momentum (if tides are efficient in spinning up the progenitors), while dynamical formation should not set any such preferential direction [174]. Unfortunately, it is often hard to measure the *individual* spins of BHs in binaries very precisely [39, 175, 176]. While it is still possible to measure the relative occurrence of BBHs in the different formation channels using the component spins and their orientation, hundreds of detections would be required before a firm measurement can be achieved [33, 177, 178].

Formation channels that preferentially align the spins with the orbital angular

[1] Other possibilities exist: e.g. primordial black holes [165, 166].

momentum should thus have positive values of $\chi_{\rm eff}$, as defined in Sec. 1.2. This is not necessarily true for dynamically formed BBHs: since all BH spin orientations are equally likely for those, the expected distribution for $\chi_{\rm eff}$ is centered around zero. The effective spin can thus be used to infer the astrophysical origin of individual sources, and to reconstruct the overall population of BHs in binaries and of their progenitors [71, 179, 180].

Remarkably, all of the BBHs reported by the LIGO-Virgo collaboration in the first two observing runs are consistent with having small or zero $\chi_{\rm eff}$ [30] at 90% confidence. The two sources for which the largest $\chi_{\rm eff}$ was measured are GW151226 ($0.2^{+0.2}_{-0.1}$, median and 90% CI) and GW170729 ($0.4^{+0.2}_{-0.3}$).

In Zackay *et al.* [73] and Venumadhav *et al.* [74], an independent analysis of the public data released by the LIGO-Virgo collaboration [181–184] has revealed nine additional potential GW signals, among which three signals have appreciable $\chi_{\rm eff}$: GW151216, GW170403, and GW170121. Especially remarkable are the spins reported for GW151216 and GW170403, where GW151216 was reported as having a large and positive effective spin of $\chi_{\rm eff} = 0.8^{+0.1}_{-0.2}$ [73], while $\chi_{\rm eff} = -0.7^{+0.5}_{-0.3}$ [74] was inferred for GW170403, making it the largest negative effective spin BBH so far.

The algorithms used by this independent pipeline [74, 185] were optimized to detect the faintest individually observable events in the population of BBHs, and hence several of the detected signals had relatively modest values of the SNR. As the information content of observed signals scales with their SNR[2], the data will have the least constraining power on the intrinsic parameters for faint events such as GW151216 and GW170403.

In light of this fact, it is worth carefully considering the impact on the inferred parameters of the various analysis choices adopted in parameter estimation: the Bayesian priors, GW waveform model, and the treatment of the instrumental noise, particularly its PSD [186]. For example, Ref [187] has shown how the $\chi_{\rm eff}$ measurement of the LIGO detection GW151012 [30] is sensitive to the prior choice; while Ref. [188]

[2]Squared information, as defined in the sense of Shannon's information theory, is proportional to the squared SNR.

has shown how the treatment of the noise PSD can impact the source characterization analysis.

In this chapter, we continue our discussion of marginal CBC signals in Chap. 2, but with the seven BBHs reported in Zackay *et al.* [73] and Venumadhav *et al.* [74]. We perform PE with the procedures discussed in [73, 74, 189], as well as the ones used by LIGO-Virgo in the analysis of the first GW Transient Catalog (GWTC-1) [30].

Our results underline that the specific configuration of the analysis can have a significant impact on the astrophysical inference of some of the BBHs detected to date, especially if they have low SNRs. In particular, we show that the high $\chi_{\rm eff}$ of GW151216 and GW170403 can be significantly reduced depending on the spin priors used in the analysis. The tails of the distribution need to be interpreted with care and in the context of the analysis choices, such as the method used to estimate the PSD and the length of data analyzed. For studies that build on the estimated parameter distributions for such sources, it is important to be aware of these analysis choices before interpreting the results.

3.1 Method

We perform PE using three distinctive sets of analysis choices, as detailed in Table 3.1, with different choices of the sampler, prior, PSD estimation method, and waveform models. Configs. A and B follow standard procedures of analysis adopted by the LVK in its publications so far. In these configurations, we perform the matched-filter analysis using the LALSuite software package [190] and explore the parameter space stochastically using the nested sampling algorithm implemented in LALInference [82, 191]. The PSDs are estimated using the BayesWave algorithm [188, 192, 193], over four-second segments centered around the merger time of each candidate event. We use data from the same segments to evaluate the likelihood, Eq. 1.7, restricting the domain of the integrals in Eq. 1.4 to the frequency range $[20, 512]$ Hz.

Configuration	PSD	Sampler	Prior	Waveform
A	BayesWave	LALInferenceNest [82, 191]	3D Isotropic spin	`IMRPhenomPv2` [111, 194, 195]
B	[188, 192, 193]		Aligned-spin, χ_z same as Config. A	SEOBNRv4_ROM [196]
C	Welch's method w/ drift factor [185]	pyMultiNest [197–200]	Aligned-spin, flat in $\chi_{\rm eff}$ [73]	`IMRPhenomD` [194, 195]

Table 3.1: Main differences between the configurations used in this chapter. More details are provided in the text.

The configurations also use different waveform models, all of which describe the complete inspiral-merger-ringdown (IMR) of a CBC and are calibrated against numerical relativity simulations of BBHs. Config. C uses the phenomenological waveform model `IMRPhenomD` [194, 195] which assumes BH spins to be (anti-)aligned to the orbital angular momentum. The model used by Config. A, `IMRPhenomPv2`, is constructed from the same aligned-spin model but is extended to include an effective description of the effects from spin-precession through a rotation of the underlying `IMRPhenomD` model [111, 194, 195]. Config. B uses a separately developed aligned-spin-only model, SEOBNRv4_ROM, based on the effective-one-body framework [196].

Because the inner product, Eq. (1.4), depends on the noise PSD and the waveform model, both of these factors can impact the measured SNR. Keeping everything else the same, we would expect a precessing waveform approximant to be able to recover more SNR than a spin-aligned one, due to the extra degrees of freedom. This is indeed what we observe comparing Configs. A and B, Sec. 3.2. Configs. B and C instead use spin-aligned waveforms, but with different PSDs and analysis software. In particular, the algorithms we use to estimate the PSD adopt different strategies to limit the effect of noise non-stationary and non-Gaussianity [185, 188, 192, 193, 201]. We find that the matched-filter SNRs for Configs. B and C calculated at the maximum likelihood point usually differ by a few percent in either direction.

Configs. A and B use priors routinely employed in LVK publications [4, 5, 83, 202–206]. Config. A (precessing analysis) uses a uniform prior in the dimensionless spin magnitude for each BH, in the range $[0, 0.99]$, and an isotropic prior for the spin orientation. Config. B uses a waveform model that assumes aligned spins, and we use the prior from Config. A for the spin component along the orbital angular momentum, χ_{iz}. Finally, Config. C, a spin-aligned analysis with `IMRPhenomD`, uses a spin prior that is uniform in the effective inspiral spin, $\chi_{\rm eff}$. These prior choices are shown in Fig. 3-1, where we plot the prior distributions for $\chi_{\rm eff}$, the magnitude of the component spins $|\chi|$, and the projection of the primary's spin along the angular momentum (χ_z). Note that for the two spin-aligned analyses, $|\chi| = |\chi_z|$ by definition.

We stress that the prior on $\chi_{\rm eff}$ for Config. C is quite different from that for Config.

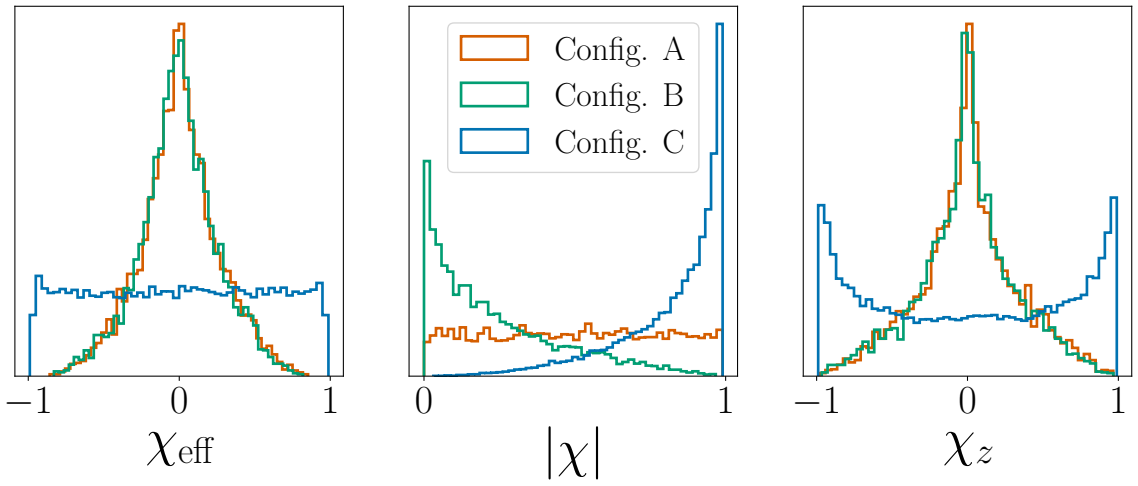

Figure 3-1: Spin priors on the effective spin $\chi_{\rm eff}$, the individual spin magnitude $|\chi|$, and the z-component of spin χ_z, used in the three configurations. Note that for aligned-spin waveforms (Configs. B and C), $|\chi_i| = |\chi_{i,z}|$ where $i = 1, 2$ corresponds to individual components of the binary.

A or B, especially toward the edges. Configs. A and B penalize *a priori* large $\chi_{\rm eff}$, and thus systems for which the spins are large in magnitude and nearly aligned with the orbital momentum. Conversely, Config. C achieves a prior that is flat in $\chi_{\rm eff}$, by *a priori* preferring large individual spin magnitudes.

The three analyses all use similar priors in the other parameters: in particular, they all use priors that are uniform over the detector-frame component masses, in a range large enough that the posteriors are not truncated; uniform over the sphere for the sky position and the orientation of the orbit with respect to the line of sight; proportional to the square of the luminosity distance; and uniform in the geocenter arrival time and phase.

3.2 Results

In this section, we report the results of our analyses on all of the GW events identified in Zackay *et al.* [73] and Venumadhav *et al.* [74]. For all events, we report the medians and 90% CIs on detector-frame chirp mass $\mathcal{M}$, mass ratio $q = m_2/m_1 \in [0, 1]$, effective spin $\chi_{\rm eff}$, and luminosity distance D_L. For all configurations, we follow the definition

of the SNRs in Refs. [73, 74] for the sake of consistency[3]:

$$\rho = \sqrt{\sum_{IFO}(2\langle d|h\rangle - \langle h|h\rangle)}. \tag{3.1}$$

and report the values corresponding to the maximum likelihood.

For Configs. A and B, we also report the *natural log* Bayes factor for the GW signal model over the Gaussian noise model ($\ln\mathcal{B}_{S/N}$) [83, 191, 207]. The Bayes factor can be obtained as the ratio of the evidence of two alternative models H_1 and H_2:

$$\mathcal{B}_{H_1/H_2} \equiv \frac{Z(H_1)}{Z(H_2)} \tag{3.2}$$

$\mathcal{B}^{H_1}_{H_2} > 0$ if H_1 is preferred. By comparing the ratio of evidences for competing models, one can quantify the relative belief that a given model represents the true signal in the data [191] in a way that also automatically penalizes models with more degrees of freedom or larger priors. Here, we can compare $\ln\mathcal{B}_{S/N}$ of Configs. A and B to quantify the relative confidence.

We first present an overview of the results in Fig. 3-2, which shows contours in the $\mathcal{M}$–$\chi_{\rm eff}$ plane that encloses 90% of the probability for the seven events discussed in this chapter. We show Configs. A and C, and omit Config. B to avoid overcrowding. Solid (dotted) lines and a dot (cross) mark the contours and the maximum likelihood point for Config. A (C). The posteriors on the parameters are formally consistent with each other within their CIs, but there are points of difference between the different configurations. The differences are relatively minor for most of the events, but notable in the case of GW151216 and GW170403. We will therefore first discuss these two cases, and then briefly review the properties of the other events, for which results are consistent across the analyses. To better quantify the discrepancies between the different configurations, especially for these two events with large spins, we additionally report the posterior percentile of $\chi_{\rm eff}$ values on both tails of the distribution.

[3]Note that SNRs reported by LVK [30] is the matched-filter SNR, defined in Eq. (1.5).

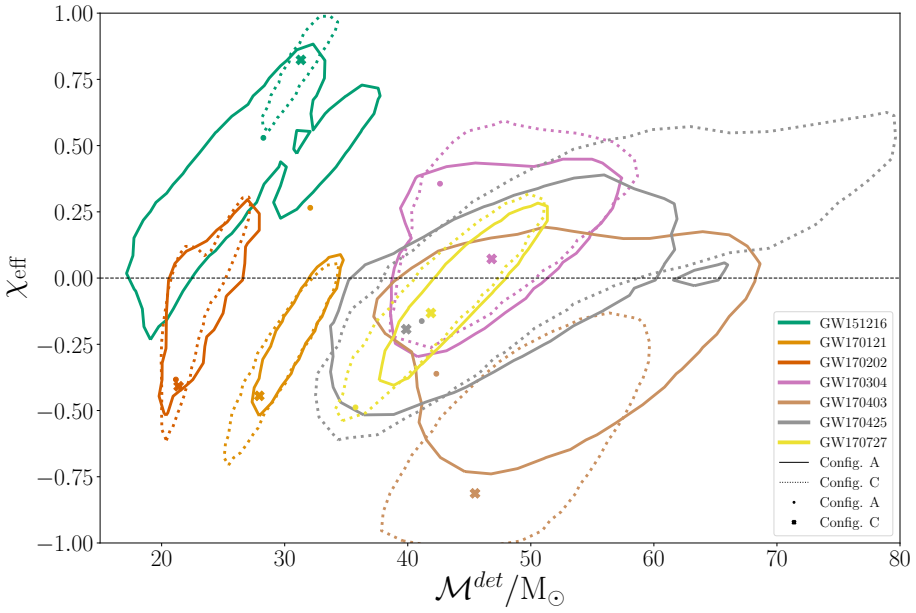

Figure 3-2: Joint 2D posterior for $\chi_{\rm eff}$ vs. detector-frame $\mathcal{M}$ for all the events analyzed in this chapter, for Config. A and C. We do not show Config. B to avoid overcrowding the plot. For Config. A (C) the maximum likelihood estimate is indicated with a dot (cross) and the edge of the 90% contour by a solid (dotted) line.

3.2.1 GW151216

GW151216 was reported by Zackay *et al.* [73] as having a high and positive effective spin, $\chi_{\rm eff} = 0.8^{+0.1}_{-0.2}$. Our results are shown in Fig. 3-3 and summarized in Table 3.2.

Of all the events analyzed in this chapter, the differences in the inferred parameters across the configurations are the clearest for GW151216. The chirp mass posteriors from Configs. A and B show fat tails, which are often associated with faint signals such as the ones analyzed here [87]. Conversely in Config. C, the distribution of the chirp mass is narrower and centered at $\sim 31\ M_\odot$. All of the estimates are compatible with their CIs. Similarly, the mass ratio measurements, while having large posterior overlaps, peak at rather different values. Configs. A and B have median values of $q = 0.4$ and $q = 0.5$ respectively, whereas Config. C has a median value of $q = 0.7$. Configs. A and B give marginal, but still non-zero, support for equal mass binaries ($q = 1$). The median for the luminosity distance is above 1.5 Gpc for all configurations, with Config. C placing the source at the largest distance among three analyses, $D_L = 2.4^{+1.2}_{-1.1}$ Gpc.

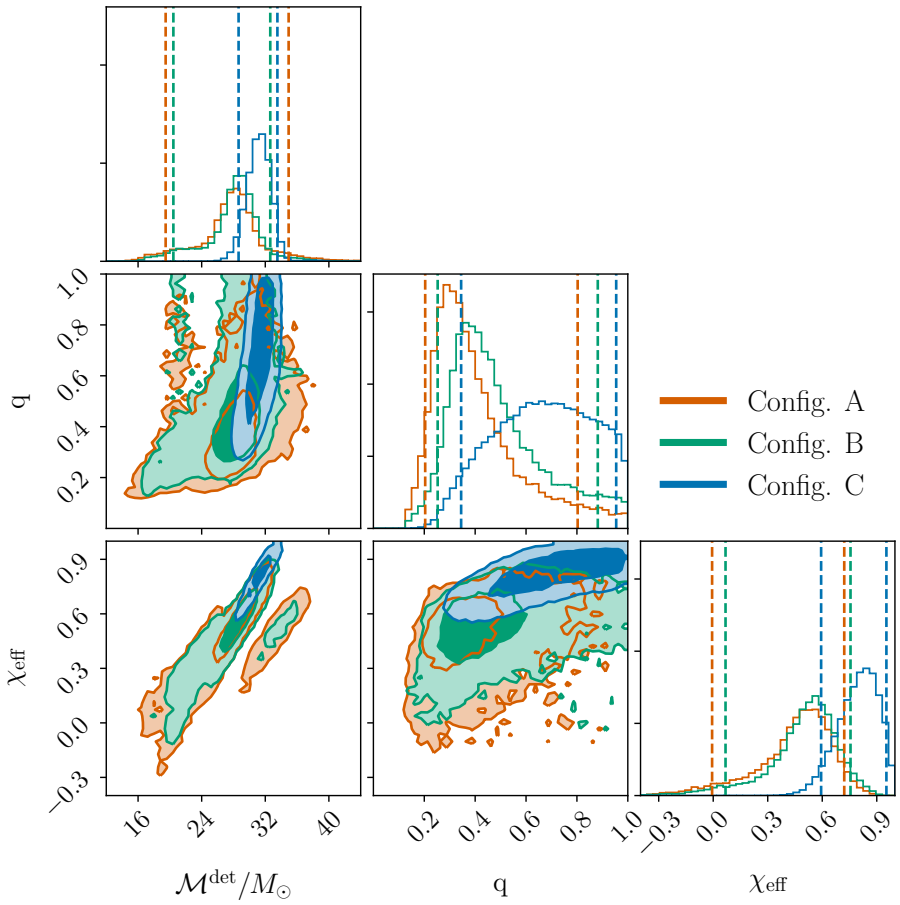

Figure 3-3: Corner plot for posterior distributions for GW151216, red for Config. A, green for Config. B and blue for Config. C. The dashed lines mark the 90% CI, and the dark (light) shaded area marks the 50%(90%) contour, the same for all corner plots to follow.

Finally and more importantly, we observe differences in the estimation of $\chi_{\rm eff}$. Config. C finds that $\chi_{\rm eff}$ is large and positive, while Configs. A and B have low levels of support for $\chi_{\rm eff} = 0$. More specifically, Config. A finds $\chi_{\rm eff} = 0.5^{+0.2}_{-0.5}$ and Config. B finds $\chi_{\rm eff} = 0.7^{+0.2}_{-0.9}$. Both of these posteriors peak at positive values for $\chi_{\rm eff}$, but have long tails extending towards small values. The fact that different analyses yield $\chi_{\rm eff}$ posteriors that peak at different values can be at least partially explained by the very different priors that are used, see Fig. 3-1. Configs. A and B penalize *a priori* large values of $\chi_{\rm eff}$, thus reducing the prior support at large values.

The $\ln\mathcal{B}_{S/N}$ values of Configs. A and B are similar, with a natural log Bayes factor of 0.2 in favor of Config. A. This suggests that there is not enough information

Configuration	A	B	C
$\mathcal{M}/M_\odot$	28^{+7}_{-8}	29^{+3}_{-12}	31^{+2}_{-3}
q	$0.4^{+0.5}_{-0.2}$	$0.5^{+0.4}_{-0.3}$	$0.7^{+0.3}_{-0.3}$
$\chi_{\rm eff}$	$0.5^{+0.2}_{-0.5}$	$0.7^{+0.2}_{-0.9}$	$0.8^{+0.1}_{-0.2}$
D_L/Gpc	$1.6^{+1.3}_{-0.8}$	$1.5^{+0.4}_{-0.8}$	$2.5^{+1.2}_{-1.1}$
SNR	8.6	8.4	8.5
$\ln\mathcal{B}_{S/N}$	10.8	10.6	15.5
$p(\chi_{\rm eff} \leq 0 \mid \mathbf{d})$	5.2%	3.4%	0.0%
$p(\chi_{\rm eff} \geq 0.8 \mid \mathbf{d})$	1.3%	2.6%	52.5%

Table 3.2: Properties for GW151216 estimated using three different configurations. In the upper half, the median values are reported for the source parameters, with error bars marking the span of the 90% CIs. The SNRs are calculated using Eq. (3.1), and the values here correspond to the maximum likelihood. $\ln\mathcal{B}_{S/N}$ is the natural log Bayes factor (Note that its value depends on the noise realization, so since Configs. A and B use a *different* approach to estimate the noise of a different data segment from that in Config. C, the $\ln\mathcal{B}_{S/N}$ values are *expected* to differ). Tables for other events follow the same reporting setup. $p(\chi_{\rm eff} \leq 0 \mid \mathbf{d})$ and $p(\chi_{\rm eff} \geq 0.8 \mid \mathbf{d})$ marks the probability for $\chi_{\rm eff}$ to take values less than or equal to 0 and greater or equal to 0.8, respectively.

available to either support or rule out the presence of spin-precession in GW151216, as found in [73]. As an additional test, we repeat the analysis of Config. A while fixing the spins to be zero. We observe a natural log Bayes factor of 2.4 (2.2) in favor of precessing (aligned) spins over zero spins.

It is worth pointing out that any differences in the inferred values of $\mathcal{M}$, q, $\chi_{\rm eff}$, and D_L across various analyses are expected to be correlated, as there are significant degeneracies between these parameters [72, 208, 209]. In the region of parameter space relevant for GW151216, the tightest correlation involves $\mathcal{M}$, $\chi_{\rm eff}$, q. Hence changing the prior on $\chi_{\rm eff}$ can affect the inference of the other parameters as well.

We have verified that the choice of waveform models does not play a significant role in the differences by performing a supplementary analysis where all the other analysis choices including the priors and PSDs are the same as Config. B, and only the waveform is varied from SEOBNRv4_ROM to `IMRPhenomD`. We find no appreciable

difference in the posteriors.

As mentioned in Section 3.1, the other points of difference between the configurations are (a) the length of data used, (b) the choice of the sampler, (c) the method used to infer the PSD, and consequently, to compute the likelihood, and (d) the choice of prior. We performed a number of tests to narrow down the reasons for the discrepancy in the inferred parameters; we present associated details in App. B.

In line with our intuition, we find that the most important cause of the differences in the choice of prior: using a '3D isotropic' spin prior causes the mode of the posterior for $\chi_{\rm eff}$ to shift to lower values. This is consistent with the analysis in Zackay *et al.* [73], in which the inference performed using the same prior as in Config. B gives $\chi_{\rm eff} = 0.6^{+0.2}_{-0.2}$. None of the other factors (method of PSD estimation, sampler, waveform, segment length, etc.) have as significant an impact on the results.

Apart from the shift in the posteriors for $\chi_{\rm eff}$, there is an additional effect: the tails of the posteriors are systematically broader in Configs. A and B, respectively with 5.2% and 3.4% of the $\chi_{\rm eff}$ posterior distributions extending below 0 (a similar effect was also reported in Ref. [210], with even more dramatic tails in the posteriors,) as compared to 0.0% of Config. C. Configs. A and B also show significantly less support at high $\chi_{\rm eff}$ values, 1.3% and 2.6% above $\chi_{\rm eff} = 0.8$ compared to 52.5% for Config. C. Deeper investigation shows that this additional phenomenon is related to a combination of the sampler used, and the treatment of spectral lines in the data when calculating the likelihood. Further details can be found in App. B. In light of these investigations, we conclude whether the $\chi_{\rm eff}$ posterior of GW151216 is an outlier compared to the other systems we discuss in this chapter, Fig. 3-2, depends strongly on the details of the analysis.

Config. A recovers SNR of 8.6, and Config. B (C) recover a similar SNR of $\sim 8.4(8.5)$. The $\ln\mathcal{B}_{S/N}$ values are also comparable, 10.8 and 10.6 from Configs. A and B.

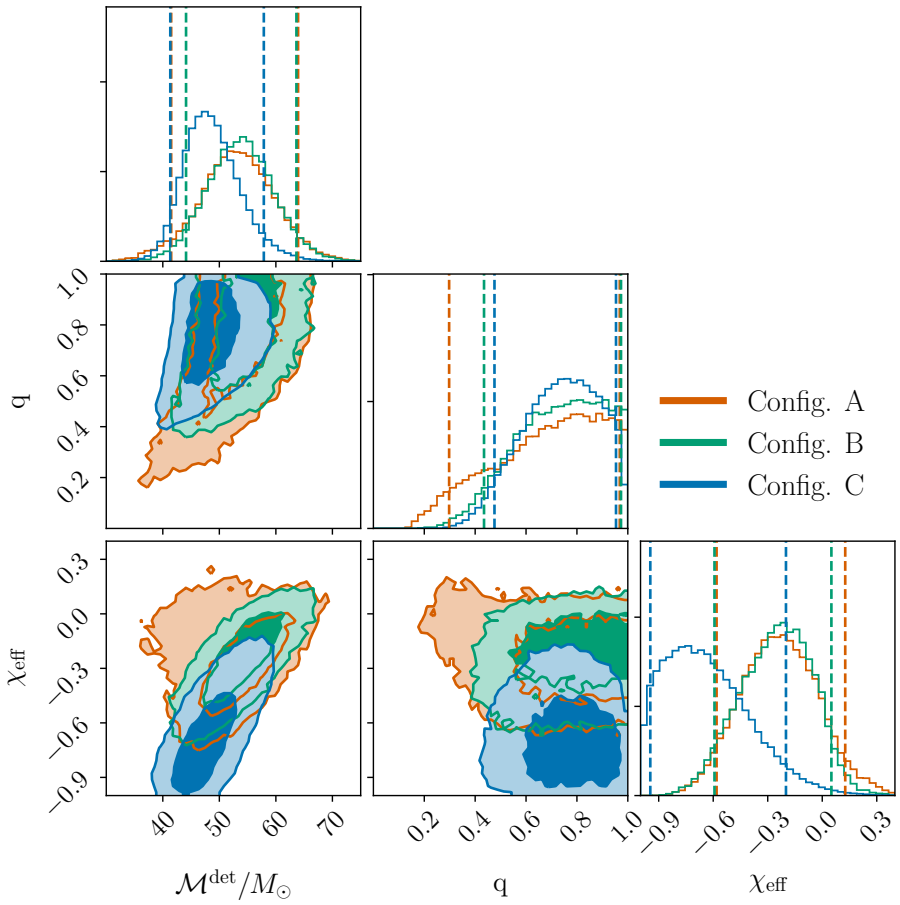

Figure 3-4: Corner plot for posterior distributions for GW170403, red for Config. A, green for Config. B and blue for Config. C.

3.2.2 GW170403

In Venumadhav *et al.* [74], GW170403 was found to have large and negative $\chi_{\rm eff}$. With Config. C we find $\chi_{\rm eff} = -0.7^{+0.5}_{-0.3}$, which excludes $\chi_{\rm eff} = 0$ from the 90% CI, with 1.2% of the $\chi_{\rm eff}$ posterior distributions extending above 0, and 42.7% below -0.7. On the contrary, we find that Configs. A and B yield posteriors with larger support at $\chi_{\rm eff} = 0$, Tab. 3.3. Config. A ($\chi_{\rm eff} = -0.2^{+0.4}_{-0.3}$) and Config. B ($-0.2^{+0.3}_{-0.4}$) have 14.0%(1.2%) and 9.6%(1.4%) of the $\chi_{\rm eff}$ posterior distributions extending above 0 (below -0.7), respectively.

Fig. 3-4 shows a difference between aligned and precessing waveform models, most clearly seen in the joint q–$\chi_{\rm eff}$ posterior. The precessing degrees of freedom allowed in Config. A to alter the well-known correlation between $\chi_{\rm eff}$ and mass ratio [72, 208],

Configuration	A	B	C
$\mathcal{M}/M_\odot$	53^{+11}_{-12}	54^{+10}_{-10}	48^{+10}_{-7}
q	$0.7^{+0.3}_{-0.4}$	$0.7^{+0.2}_{-0.3}$	$0.7^{+0.2}_{-0.3}$
$\chi_{\rm eff}$	$-0.2^{+0.4}_{-0.3}$	$-0.2^{+0.3}_{-0.4}$	$-0.7^{+0.5}_{-0.3}$
D_L/Gpc	$2.8^{+2.3}_{-1.5}$	$3.2^{+2.2}_{-1.6}$	$2.7^{+1.5}_{-1.2}$
SNR	8.4	8.1	8.2
$\ln\mathcal{B}_{S/N}$	11.8	11.2	14.6
$p(\chi_{\rm eff} \leq -0.7\|\mathbf{d})$	1.2%	1.4%	42.7%
$p(\chi_{\rm eff} \geq 0\|\mathbf{d})$	14.0%	9.6%	1.2%

Table 3.3: Properties for GW170403 estimated using three different configurations. $p(\chi_{\rm eff} \leq -0.7|\mathbf{d})$ and $p(\chi_{\rm eff} \geq 0|\mathbf{d})$ marks the probability for $\chi_{\rm eff}$ to take values less than or equal to -0.7 and greater or equal to 0, respectively.

yielding a broader posterior distribution for the mass ratio, whose lower end of the 90% CI now reaches ~ 0.3. Again, we do not find enough information to confirm or rule out the presence of effects due to spin-induced orbital precession.

However, the posteriors for q, $\mathcal{M}$, and D_L are more consistent across our analysis configurations for GW170403 than they are for GW151216. This suggests that the small differences we observe for GW170403 can be entirely or nearly entirely explained by the different priors used for $\chi_{\rm eff}$, which "push" the posteriors in Configs. A and B closer to 0. Similar to the findings in [187], varying the prior choices has a more substantial effect on low-SNR observations like the events analyzed in this chapter, so general caution should be exercised when drawing astrophysical inferences using quantities that are as strongly dependent on the priors as the $\chi_{\rm eff}$ measurements presented here. On the other hand, the comparison with GW151216 suggests that for low-SNR events the specific realization of the noise and the detector behavior around the trigger time may amplify the differences introduced by the PSD estimation, which is quite different in Configs. A and B compared to Config. C.

We notice that Config. C has a more pronounced tail at negative $\chi_{\rm eff}$, resulting in stronger support at lower values of the chirp mass. Systems with more negative $\chi_{\rm eff}$

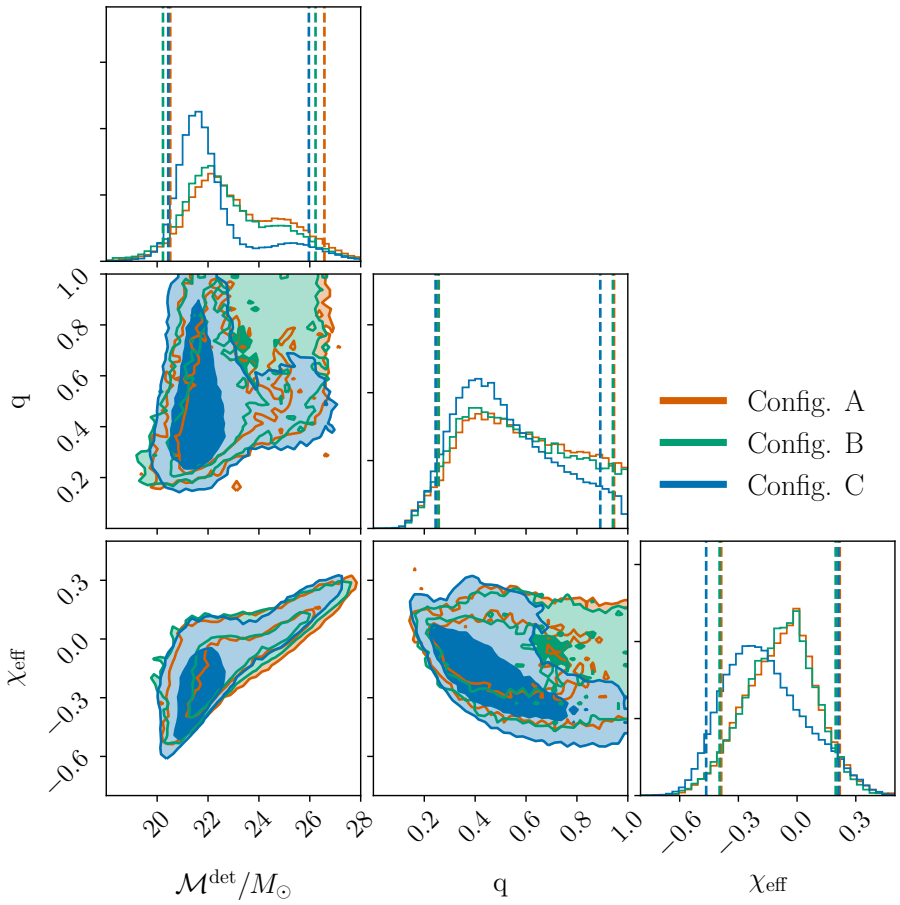

Figure 3-5: Corner plot for posterior distributions for GW170202, red for Config. A, green for Config. B and blue for Config. C.

produce shorter GW signals [72]. This can be roughly compensated for by decreasing the chirp mass [209].

3.2.3 GW170202

All the analyses yield consistent results for GW170202, as seen in Tab. 3.4 and Fig. 3-5. The detector-frame chirp mass for GW170202 is estimated to be $22^{+4}_{-1}\ M_\odot$ ($23^{+4}_{-2}\ M_\odot$) with flat-in-$\chi_{\rm eff}$ prior (or otherwise). Of all the sources we discuss in this work, GW170202 is the one for which we measure the lowest mass ratio, consistently across the configurations: Config. A yields $q = 0.6^{+0.4}_{-0.3}$, while Configs. B and C have an even lower median, $q = 0.5^{+0.4}_{-0.3}$ and $q = 0.5^{+0.4}_{-0.2}$, respectively. The $\chi_{\rm eff}$ posterior is broadly consistent across the three analyses, with Configs. A and B peaking closer to zero, as

Configuration	A	B	C
$\mathcal{M}/M_\odot$	23^{+4}_{-2}	23^{+4}_{-2}	22^{+4}_{-1}
q	$0.6^{+0.4}_{-0.3}$	$0.5^{+0.4}_{-0.3}$	$0.5^{+0.4}_{-0.2}$
$\chi_{\rm eff}$	$-0.1^{+0.3}_{-0.3}$	$-0.1^{+0.3}_{-0.3}$	$-0.2^{+0.4}_{-0.3}$
D_L/Gpc	$1.5^{+1.1}_{-0.8}$	$1.5^{+1.0}_{-0.8}$	$1.5^{+0.8}_{-0.6}$
SNR	8.5	8.3	8.5
$\ln\mathcal{B}_{S/N}$	10.5	10.9	13.9

Table 3.4: Properties for GW170202 estimated using three different configurations.

expected, given that their priors prefer values closer to zero.

3.2.4 GW170121, GW170304, GW170425, GW170727

Set-up	A	B	C
$\mathcal{M}/M_\odot$	31^{+3}_{-3}	31^{+3}_{-3}	29^{+4}_{-3}
q	$0.8^{+0.2}_{-0.3}$	$0.8^{+0.2}_{-0.3}$	$0.8^{+0.2}_{-0.3}$
$\chi_{\rm eff}$	$-0.2^{+0.2}_{-0.2}$	$-0.2^{+0.2}_{-0.3}$	$-0.3^{+0.3}_{-0.3}$
D_L/Gpc	$1.3^{+0.9}_{-0.7}$	$1.3^{+0.9}_{-0.8}$	$1.3^{+0.9}_{-0.7}$
SNR	10.8	10.7	10.9
$\ln\mathcal{B}_{S/N}$	30.9	31.1	34.6

Table 3.5: Properties for GW170121 estimated using three different configurations.

GW170121 has the highest SNR among the events discussed in the chapter. The PE results are consistent with a heavy, near-equal-mass BBH with a preference for negative values of $\chi_{\rm eff}$, at a luminosity distance of ~ 1.3 Gpc. Our results are shown in Fig. 3-6 and summarized in Table 3.5.

GW170304 and GW170425 are similar systems, with detector-frame chirp masses of $\sim 47\ M_\odot$, $\chi_{\rm eff}$ posteriors centered near zero, luminosity distance of ~ 3 Gpc and a preference for nearly equal masses, as shown in Figs. 3-7 and 3-8, and Tables 3.6 and 3.7.

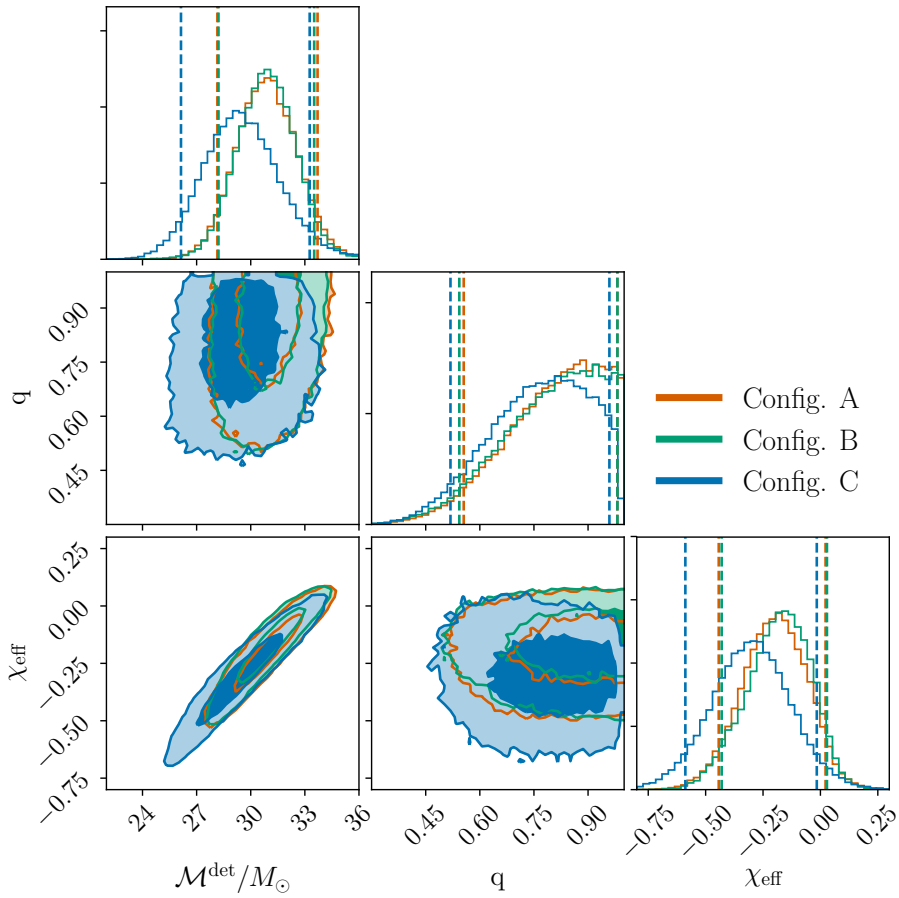

Figure 3-6: Corner plot for posterior distributions for GW170121, red for Config. A, green for Config. B and blue for Config. C.

While small differences are seen across the configurations, the posteriors obtained from the three analyses are all broadly consistent, and depict very similar results: GW170304 and GW170425 are broadly similar to the majority of the BBHs discovered in LIGO-Virgo data: massive systems with nearly equal component masses and (apparent) $\chi_{\rm eff}$ values consistent with zero. These heavy BBHs may arise from a common formation scenario [30, 71].

The same is true for GW170727, as seen in Tab. 3.8 and Fig. 3-9, which appears only slightly less massive and closer, at a recovered median distance of ~ 2.5 Gpc. For all configurations, the $\chi_{\rm eff}$ posterior is centered around zero. It is worth stressing that even though the SNR reported for Config. A in Table 3.8 is 10% higher than that for Config. B, we do not find significant evidence supporting the precessing model, with

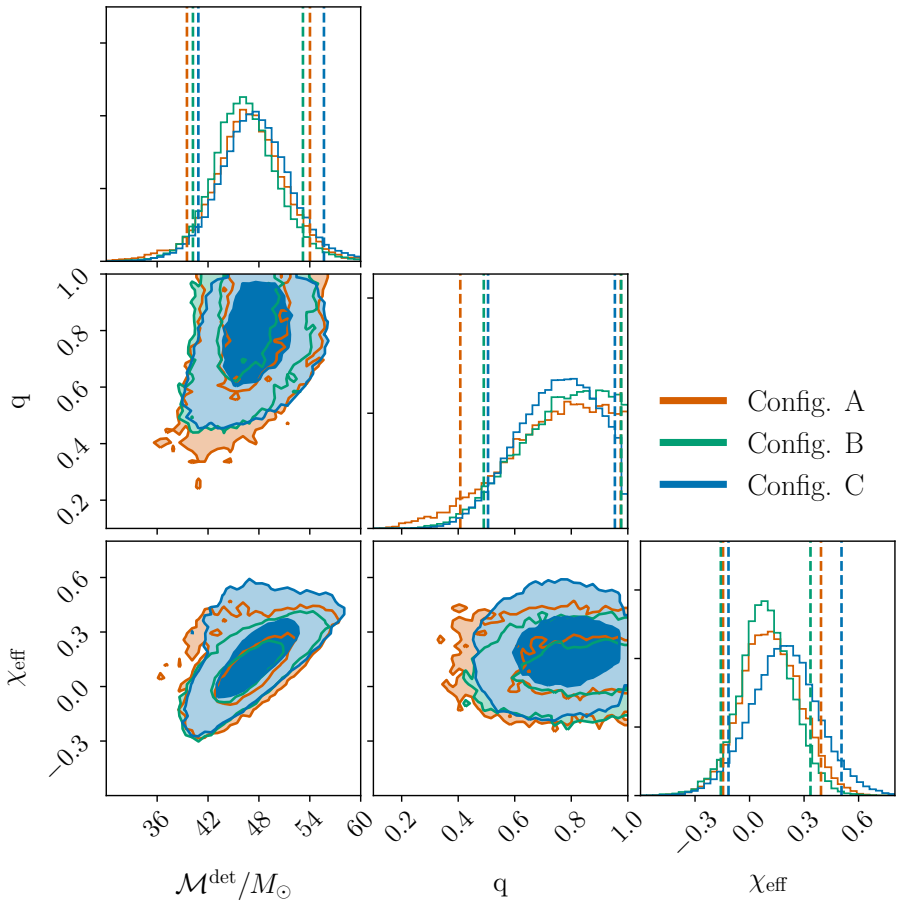

Figure 3-7: Corner plot for posterior distributions for GW170304, red for Config. A, green for Config. B and blue for Config. C.

the two configurations yielding similar Bayes factors. The reason is that the SNRs we report are calculated at the point in parameter space that yields the maximum likelihood, whereas the Bayesian evidence, and hence the Bayes factors, are integrated over the whole parameter space, Eq. 1.8. The median SNR is thus a better tracer for the evidence. We indeed find that the median SNRs of Configs. A and B only differ by a fraction of a percent.

3.3 Conclusion

In this chapter, we compare the source property measurements of the seven BBHs first presented in Zackay *et al.* [73] and Venumadhav *et al.* [74]. The analysis therein

Configuration	A	B	C
$\mathcal{M}/M_\odot$	47^{+7}_{-7}	46^{+7}_{-6}	48^{+8}_{-7}
q	$0.8^{+0.2}_{-0.4}$	$0.8^{+0.2}_{-0.3}$	$0.8^{+0.2}_{-0.3}$
$\chi_{\rm eff}$	$0.1^{+0.3}_{-0.3}$	$0.1^{+0.2}_{-0.2}$	$0.2^{+0.3}_{-0.3}$
D_L/Gpc	$2.7^{+1.6}_{-1.4}$	$2.6^{+1.6}_{-1.4}$	$3.0^{+1.6}_{-1.3}$
SNR	9.0	8.7	8.7
$\ln\mathcal{B}_{S/N}$	16.0	15.7	18.1

Table 3.6: Properties for GW170304 estimated using three different configurations.

Configuration	A	B	C
$\mathcal{M}/M_\odot$	46^{+16}_{-8}	45^{+13}_{-8}	48^{+26}_{-10}
q	$0.7^{+0.3}_{-0.3}$	$0.7^{+0.3}_{-0.3}$	$0.7^{+0.3}_{-0.3}$
$\chi_{\rm eff}$	$0.0^{+0.3}_{-0.3}$	$0.0^{+0.3}_{-0.3}$	$0.1^{+0.4}_{-0.4}$
D_L/Gpc	$2.8^{+2.0}_{-1.4}$	$2.7^{+1.9}_{-1.4}$	$3.3^{+2.9}_{-1.6}$
SNR	8.4	8.4	8.0
$\ln\mathcal{B}_{S/N}$	14.2	14.3	13.2

Table 3.7: Properties for GW170425 estimated using three different configurations.

(corresponding to Config. C in this chapter) includes two BBHs with $\chi_{\rm eff}$ significantly deviating from zero. We also perform PE analyses using the standard algorithms of LVK [30, 83, 211] where we use both waveform models allowing for spin-precession (Config. A) and assuming spins (anti-)aligned to the orbital angular momentum (Config. B). In the analysis for Configs. A and B, the data from the GW detectors is assumed to be described by a stationary and Gaussian noise process modeled on a four-second-long data segment under analysis using the spectral model in BayesWave, whereas Config. C assumes the noise to be well described by a PSD estimated through Welch's method from a significantly longer data segment surrounding the GW signal, multiplied by a time-dependent normalization measured on a ~ 15 second scale. The three configurations also differ significantly in their respective prior assumptions on

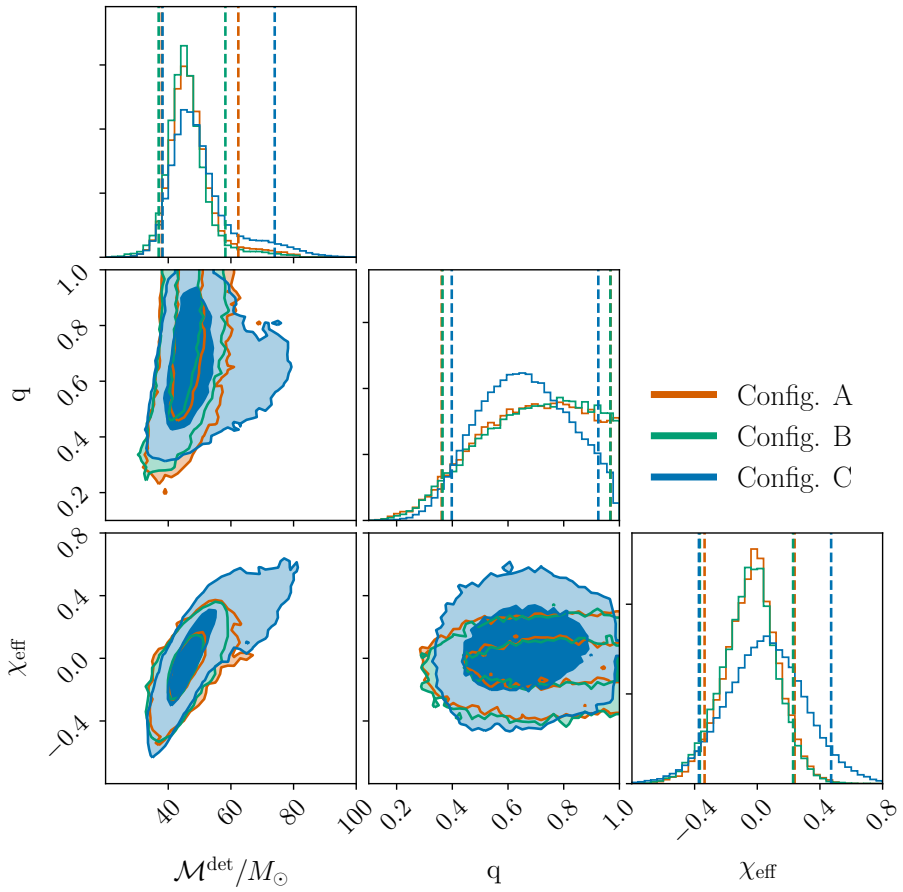

Figure 3-8: Corner plot for posterior distributions for GW170425, red for Config. A, green for Config. B and blue for Config. C.

the BH spin parameters, which as shown by [187], could have a significant effect on the inferred posterior distributions, especially for high-mass BBH systems with low SNRs, such as the ones presented in this study.

Compared to Zackay *et al.* [73] and Venumadhav *et al.* [74], Configs. A and B recover lower values for $\chi_{\rm eff}$, consistent with zero or low component spins for all reported BBHs, Fig. 3-2. In particular, for GW151216, Ref. [73] reported a positive $\chi_{\rm eff}$ of $0.8^{+0.1}_{-0.2}$, while we report $\chi_{\rm eff} = 0.5^{+0.2}_{-0.5}$ and $\chi_{\rm eff} = 0.7^{+0.2}_{-0.9}$ (corresponding to Config. C, A and B, respectively). Similarly for GW170403, Ref. [73] reported a negative $\chi_{\rm eff}$ of $-0.7^{+0.5}_{-0.3}$, while we report $\chi_{\rm eff} = -0.2^{+0.4}_{-0.3}$ and $\chi_{\rm eff} = -0.2^{+0.3}_{-0.4}$ (again corresponding to Config. C, A, B).

Ultimately, one should choose priors that reflect the underlying population of

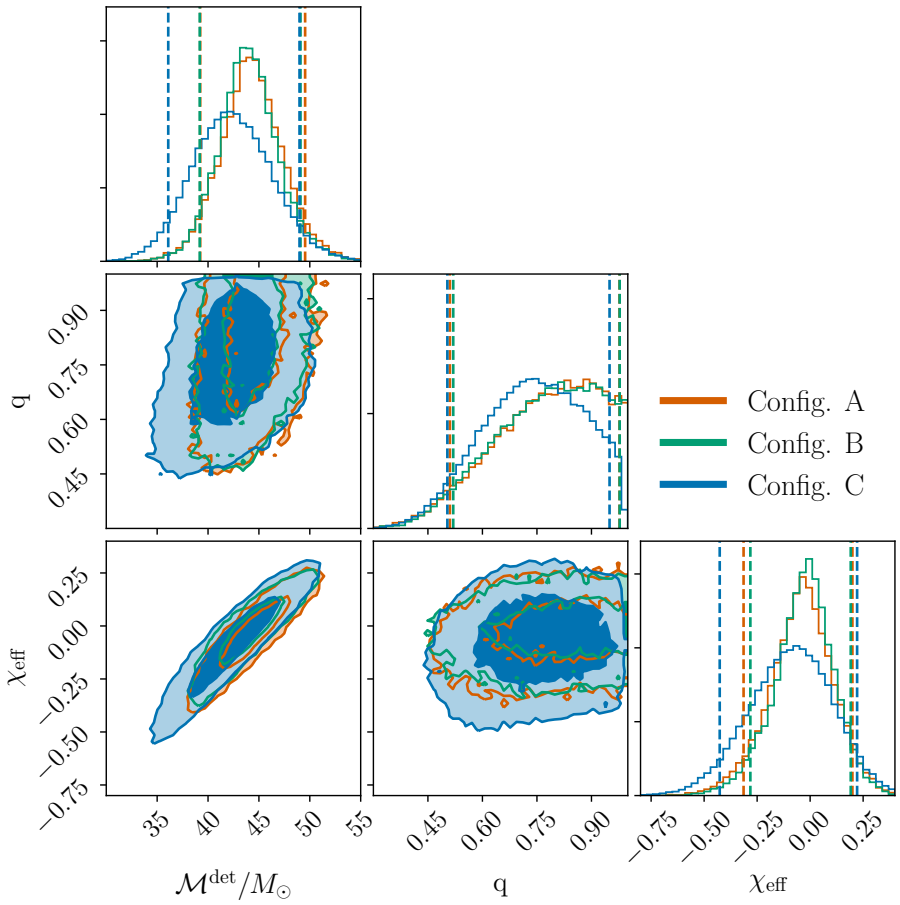

Figure 3-9: Corner plot for posterior distributions for GW170727, red for Config. A, green for Config. B and blue for Config. C.

BHs. To measure this population's mass and spin distributions, the prior choices applied for any individual event must be removed so as not to double count the prior probability impact, and the "raw" likelihood distributions need to be used to infer the properties of the population [30, 71]. Such an analysis was carried out in [212], whose population-informed posteriors broadly agree with those derived in this work. Future PE analysis will benefit from using population-informed priors, especially as the number of detected GW events grows.

Configuration	A	B	C
$\mathcal{M}/M_\odot$	44^{+5}_{-5}	44^{+5}_{-5}	42^{+7}_{-6}
q	$0.8^{+0.2}_{-0.3}$	$0.8^{+0.2}_{-0.3}$	$0.7^{+0.2}_{-0.2}$
$\chi_{\rm eff}$	$-0.0^{+0.2}_{-0.3}$	$-0.0^{+0.2}_{-0.3}$	$-0.1^{+0.3}_{-0.3}$
D_L/Gpc	$2.4^{+1.3}_{-1.2}$	$2.4^{+1.3}_{-1.2}$	$2.5^{+1.3}_{-1.1}$
SNR	10.2	9.4	9.0
$\ln\mathcal{B}_{S/N}$	22.6	22.5	20.9

Table 3.8: Properties for GW170727 estimated using three different configurations.

Chapter 4

Waveform Systematics

Key to the interpretation of GW detections and signal analysis is the development of accurate and computationally efficient GW waveforms, which are used to measure the parameters of the signal by matching the model waveforms[1] against the GW data.

GW models are usually calibrated against waveforms obtained directly with numerical relativity (NR) codes, which solve Einstein's equations computationally [213–216]. The presence of matter in combination with a singularity makes NSBHs exciting systems to study, but also very challenging to simulate compared to BBH systems. Due to the high computational cost and significant technical difficulties of NR NSBH simulations, there are only a handful of high-resolution NSBH waveforms [217–221] publicly available in the Simulating eXtreme Spacetimes (SXS) GW database , and just over one hundred lower-resolution NSBH waveforms generated using the SACRA code, which has been used to calibrate various waveform approximants but is not publicly available [222, 223].

Furthermore, one usually does not directly use NR waveforms to measure the parameters of detected CBCs (but see Refs. [224, 225]), due to their high individual computational cost and sparsity across the parameter space. Instead, surrogate, phenomenological, or effective-one-body (EOB) GW models are produced, which are calibrated against NR simulations. To make these waveform models fast enough to be

[1] In what follows we will use "waveform model" and "waveform approximant" as synonyms, as they are both commonly used in GW literature.

calculated millions of times, as required by stochastic samplers, and in some cases due to limitations in the very NR simulations that the models are calibrated against, only some of the relevant physical features are included (for example, spin precession but not tidal deformability). Due to the lack of a large NR database, and the fact that all of the physics that is relevant to describe a CBC can induce *measurable* effects in NSBHs[2], these systems are potentially prone to systematic errors due to waveform modeling.

In this chapter, we create hybrids from recent NSBH NR simulations to produce full inspiral-merger-ringdown waveforms that are then added to the data stream of a three-detector GW network made of the two Advanced LIGO [226] and the Advanced Virgo [227] detectors. We simulate signals at various mass ratios, SNRs, and orbital orientations, and measure their parameters with stochastic samplers, using a suite of phenomenological and EOB models. Our work significantly extends what was done by Ref. [220], which explored NSBH waveform systematics by only looking at waveform overlaps, instead of performing a full Markov Chain Monte Carlo (MCMC) measurement of all of the binary parameters. Ref. [228] looked at parameter estimation for NSBH sources, but only used a single waveform model, `Lackey_Tidal_2013_SEOBNRv2_ROM` [222, 229, 230], and did not measure extrinsic parameters or source-frame masses.

Since the BH in NSBHs contributes most of the total spin, these systems can yield precise measurements of BH spins [50, 231]. Furthermore, the potentially large mass ratio[3] will enhance the effect of eventual spin precession [232], also making it easier to measure the BH spin with good precision [39, 175, 233, 234]. Similarly, the impact of higher multipoles is larger for systems with large mass ratios, paving the way to tests of the multipolar structure of GR [49, 235].

If the BH is light enough, or with significant spin [236–245] (otherwise the NS

[2]For example, higher order modes are formally present in all CBC signals, but are suppressed for systems close to equal mass. This is the reason why waveform models that do not model them perform well with most of the BBHs detected to date. The same will not necessarily be true for NSBHs.

[3]Note that two conventions exist for the mass ratio. LVK usually defines the mass ratio in the range $[0, 1]$. We will follow the opposite convention (primarily used in the NR community) and define $q = m_1/m_2$, with $m_1 \geq m_2$.

will cross the event horizon before it can be significantly disrupted) tidal effects might also be present. Furthermore, the potential presence of significant spin-induced orbital precession would break the degeneracy between luminosity distance and orbital inclination, which could make NSBHs significant contributors to the measurement of the Hubble constants with standard sirens [119].

As mentioned above, our goal is to verify if current waveform approximants can be used to accurately constrain the unknown parameters of NSBH systems. If not, we wish to check which parameters are more susceptible to biases, and at which SNR these biases become significant compared to the statistical uncertainties. The following sections provide more details on the generation and construction of inspiral-merger-ringdown NSBH waveforms used in this work and the data analysis approaches to measuring their parameters.

4.1 Simulated Signals

One can decompose the GW strain into a sum of spin-weighted spherical harmonics [235] as:

$$h(t, \theta_{JN}, \psi_0) = \sum_{l=2}^{\infty} \sum_{m=-l}^{l} h_{lm}(t) {}^{-2}Y_{lm}(\theta_{JN}, \psi_0) \tag{4.1}$$

where θ_{JN} is the angle between the line of sight and the orbital angular momentum [4], ${}^{-2}Y_{lm}$ are spin -2 weighted spherical harmonics, and ψ_0 is the initial binary phase [1]. In general, the $(l = 2, |m| = 2)$ mode is dominant [235, 246–250] and higher order modes (HOMs) are suppressed. This is particularly true for low-mass systems with a mass ratio close to unity [249, 251–257]. The impact of HOMs is also reduced in systems that are observed close to "face-on", i.e. with the orbital angular momentum aligned with the line-of-sight since in this case, the angular structure of the spin-weighted spherical harmonics suppresses the magnitude of the higher order terms relative to the dominant $(l = 2, |m| = 2)$ mode. This is consistent with the fact that GW190412 [49] and GW190814 [50], the first two CBC detections with visible imprints of HOMs, are

[4] For a binary with observable spin-precession, the inclination angle θ_{JN} can vary significantly over time. In this work, we, therefore, define θ_{JN} always at a reference GW frequency of 100 Hz.

NR Waveforms	$M_{BH}/M_\odot$	$M_{NS}/M_\odot$	NS equation of state	Λ_{NS}	r_{NS}/km	Modes $(l, \lvert m\rvert)$
q6 [217]	8.4	1.4	$\Gamma 2(\kappa = 92.12)$[5]	526	13.3	(2,2) (3,3) (2,1) (4,4) (5,5)
q3 [221]	4.05	1.35	H1[6]	624	12.3	(2,2) (3,3) (2,1) (4,4)
q2 [221]	2.8	1.4	$\Gamma 2(\kappa = 101.45)$	791	14.4	(2,2) (3,3)

Table 4.1: NR waveforms used for the post-inspiral part of the simulated signals. Full waveforms are obtained by hybridizing with `NRHybSur3dq8Tidal` waveforms. See the body for more details. Note all the NSs and BHs are non-spinning.

also the GW events with the most asymmetric mass ratio reported to date, at around 4 and 9, respectively.

To generate realistic GWs emitted from NSBHs, we use NR simulations carried out by the SXS collaboration. We consider three different NR simulations [217, 221] produced by the SXS collaboration using the SpEC code [240, 259] at the highest available resolution. In Tab. 4.1, we report their corresponding masses, spins, HOMs, as well as the tidal deformability of the NS, defined as:

$$\Lambda_{\rm NS} = \frac{2}{3} k_2 \left(\frac{R_{\rm NS}}{M_{\rm NS}} \right)^5 \tag{4.2}$$

where $R_{\rm NS}$ and $M_{\rm NS}$ are the radius and mass of the NS, k_2 is its tidal Love number describing the susceptibility of its shape to change in response to a tidal potential [260], and we use natural unites, $G = c = 1$. Waveforms that include tidal features often parameterize the finite size effects through the tidal deformability of each individual NS, or a single additional parameter proportional to the lowest-order correction to the phase evolution of the waveform in a post-Newtonian expansion, the effective tidal deformability of the binary. Other finite size effects, including for example the impact of the disruption of an NS by a BH, are then modeled as a function of the

tidal deformability of the NS. While there is no obvious reason for tidal deformability to be the most relevant parameter for finite-size effects beyond the lowest-order post-Newtonian correction to the waveform, tidal deformability has worked well enough as a proxy for other finite-size effects within the accuracy of existing waveform models[7].

The NR waveforms used in this chapter are for non-spinning NSs and BHs. This limitation does not make our analysis less relevant or urgent since most of the BHs and all of the NSs discovered with GWs to date are consistent with having small or no spin [30, 209]. In the rest of this chapter, we will often use the mass ratios of the systems, as reported in the first column of Tab. 4.1, to refer to the individual NSBH simulations.

The EoS for cold, supranuclear matter in these simulations is such that the resulting tidal deformability is toward the high end of the region still allowed by previous GW observations [5, 47]. Specifically, the q6 and q2 NR waveforms use a simple Γ-law EoS, where the pressure P, density ρ, temperature T, and specific internal energy ϵ are related by $P = \kappa\rho^{\Gamma} + \rho T$, $\epsilon = P/\rho/(\Gamma - 1)$. Both simulations use $\Gamma = 2$, while $\kappa = 92.12$ for q6 and $\kappa = 101.45$ for q2[8]. This results in the NS having a tidal deformability of $\Lambda = 526$ for q6, and $\Lambda = 791$ for q2. Finally, q3 uses a piece-wise polytropic EoS (H1, defined in [258]). For the $1.35M_{\odot}$ NS considered in the simulation, this EoS leads to a tidal deformability of $\Lambda = 624$.

We note that while q2 and q6 are relatively long waveforms by the standard of hydrodynamic simulations (> 20 cycles), q3 is comparatively short (13.3 cycles). In all cases, these simulations contain only the last few cycles before the two compact objects merge, while we need to simulate the full GW signals starting at the low-frequency cut-off of GW detectors (i.e. 20 Hz) for the purpose of this study.

We use the hybridization scheme described in Ref. [261] to combine the NR simulations with models for the early-inspiral section of the waveform. The late and post-inspiral phases from NR are smoothly attached to the early-inspiral section

[7]In this work, we will assume that the BH is not tidally deformed and that all finite-size effects can be accurately modeled as functions of the NS tidal deformability.

[8]Simulations using a Γ-law EoS can in theory be rescaled to any mass, at constant mass ratio and NS compactness. However, we do have to choose a mass scale when injecting the waveform into detector data. In this work, we set the mass of the NS to $1.4M_{\odot}$.

predicted by the `NRHybSur3dq8Tidal`[9] model [262].

We use the infrastructure described in Ref. [263] to project the hybrid signals into the data streams of a network of the two Advanced LIGO detectors (Hanford and Livingston) and the Virgo detector. To better isolate biases due to waveform systematics from offsets due to Gaussian noise fluctuations, we work with a zero-noise realization of the data [264], i.e. a data stream where the noise is zero at each time or frequency bin (whereas the noise PSD itself is non-zero).

We probe the effect of the orbital orientation on the results by simulating every source at two different inclinations θ_{JN}, representative of a "typical" [265] detection (30°, "face-on") and of a high-inclination system (70 degrees, close to "edge-on"). As mentioned above, larger inclinations should make the effects of HOMs more visible and, conversely, increase the bias when these effects are not taken into account but would significantly contribute to the overall signal [254, 255]. Finally, all of these systems are put at two distances to give a network SNR of 30 (comparable to the loudest CBC discovered to date) and 70. The masses in Tab. 4.1 are to be interpreted as detector-frame masses, with the astrophysically relevant source-frame masses being smaller by a factor of $(1+z)$, with z being the redshift of the source. Strictly speaking, the masses reported by NR simulations should be treated as defined in the source frame. However, given the proximity of our sources (App. C.1), the masses differ by at most a few percentages, affecting the mapping between the NS mass and radius by an amount much smaller than either statistical or systematic uncertainties. In the rest of the chapter, we will only report the measurements of the source-frame masses. Finally, the sky location of all sources is fixed to the (arbitrary) value of 60° for both the right ascension and the declination.

[9] `NRHybSur3dq8Tidal` is constructed by adding post-Newtonian tidal effects to the underlying BBH model `NRHybSur3dq8` [261]. Therefore it only includes the inspiral part of the waveform.

4.2 Waveform Models

The choice of the waveform approximants, i.e. the waveform models we use to characterize the hybrid waveforms described in the previous section, enters the analysis through the term $h(\boldsymbol{\theta})$ in the likelihood as discussed in Sec. 1.3.

When we conducted this study, no waveform that accounts for all of the relevant features, including tidal effects, spin precession, and HOMs, was available in the LIGO Algorithm library [190]. We, therefore, use a range of approximants that have some but not all of these features. These are reported in Tab. 4.2, together with a list of the physical features that are included and, when relevant, their range of validity (which usually restricts the mass ratio and/or the BH spin). Details on the priors assumed in the analyses are given in App. C.3.

Waveform Approximant	Tides	PrecessionHOMs $(l, \lvert m \rvert)$	NSBH-amplitude correction	Validity Range
SCINRv4_ROM (`SEOB`) [196, 266]				
SEOBNRv4_NRTidal_ROM (`SEOBT`) [196, 266–268]	✓			
SEOBNRv4_ROM_NRTidalv2_NSBH (`SEOBNSBH`) [196, 266, 269]	✓		✓	BH spin=[-0.5,0.8]
`Lackey_Tidal_2013_SEOBNRv2_ROM` (`LEA+`) [222, 228–230]	✓		✓	q=[2,5], BH spin=[-0.5,0.5]
IMRPhenomNSBH (`IMRNSBH`) [270]	✓		✓	BH spin=[-0.5,0.5]
IMRPhenomPv2 (`IMRp`) [111, 194, 195]		✓		
IMRPhenomPv2_NRTidal (`IMRpT`) [111, 194, 195, 267, 268]	✓	✓		
IMRPhenomXHM (`IMRXHM`) [271, 272]		(2,1),(3,2), (3,3),(4,4)		

Table 4.2: Waveform approximants used to characterize the source parameters of the simulated NSBH signals. We report their full name and a short label (in typewriter fonts) used in the body of the chapter, whether they support tides, spin precession, HOMs (if yes, which modes), correction to their amplitude tuned for NSBH sources, and eventual restrictions in their parameter space.

The waveform approximants used in this study are constructed following either the EOB formalism [196, 230, 251, 273–276], or based on the phenomenological extension to analytical post-Newtonian waveforms (IMRPhenom) [69, 194, 195, 271, 272, 277]. Both approaches smoothly extend the inspiral waveforms with models of binary merger-ringdown, calibrated against a set of spin-aligned BBH NR waveforms.

SEOBNRv4_ROM (henceforth: `SEOB`) [196, 266] describes BBH inspiral-merger-ringdown signals with general spins aligned to the orbital angular momentum. For computational efficiency, we evaluate the likelihood (cf. Eq. (1.7)) using a ROQ [101] version of SEOBNRv4 expressed in the frequency-domain. SEOBNRv4_ROM_NRTidal (`SEOBT`) [196, 266–268] builds on the baseline BBH model `SEOB` by adding a correction of the waveform phase through a prescription of tidal effects found in BNS systems, calibrated against a set of BNS NR simulations [267, 268]. `Lackey_Tidal_2013_SEOBNRv2_ROM` (`LEA+`) [222, 228–230] adds both phase and amplitude corrections specific to NSBH systems, but is constructed from a reduced order model (ROM) of the older SEOBNRv2 BBH baseline waveform model [230]. We also use a ROQ implementation for `LEA+`. SEOBNRv4_ROM_NRTidalv2_NSBH (`SEOBNSBH`) [269] is also based on `SEOB` and dedicated to describing NSBH systems, but adds both a phase correction (through an updated formalism to the one included in `SEOBT` [278]) as well as corrections to the waveform amplitude based on the model of Ref. [244].

From the IMRPhenom waveform family, we use IMRPhenomNSBH (`IMRNSBH`) [270] constructed from the aligned-spin BBH baseline IMRPhenomC [69] with updated phase [278] and NSBH-specific amplitude [244] corrections similar to `SEOBNSBH`. As a comparison to other GW analyses, we also include a ROQ implementation of IMRPhenomPv2 (`IMRp`) [111, 194, 195], which has been used for the majority of CBC analyses in recent years. This waveform is based on the newer aligned-spin IMRPhenomD [194, 195] BBH baseline, extended to also capture spin-induced orbital precession through an effective precession formalism [111]. We also use IMRPhenomPv2_NRTidal (`IMRpT`) [111, 194, 195, 267, 268], which further augments `IMRp` by adding a phase correction based on the same BNS tidal description as used in `SEOBT`[10].

[10]Note that the two BNS NRTidal models, `SEOBT` and `IMRpT`, do not include a description for the

Finally, we use IMRPhenomXHM (`IMRXHM`) [271, 272], which is based on the recent IMRPhenomXAS model [277] and describes aligned-spin BBH waveforms including HOMs. Note that `IMRXHM` does not include any phase or amplitude corrections from the presence of an NS in the binary.

Overall, the choice of waveform models used for this study is determined by a compromise between covering a large variety of families and physics, while keeping the computational cost reasonable. This second factor is the reason why we do not include other waveform approximants with HOMs, for example, the time-domain `SEOBNRv4HM` [279, 280][11].

We analyze all of the hybrid signals we generated with all of these waveform models (with some exceptions for the `LEA+` model, used for $q = 3$ only due to its limited range of validity on the mass ratio). As mentioned above, none of the waveform families account for all of the relevant physical effects. However, given that none of the hybrid waveforms we use to simulate the detected sources has precessing spins, we do not expect large biases in the recovered parameters for waveforms that do not model spin precession, while the lack of tides and HOMs might have a visible impact, depending on the mass ratio, inclination angle, and SNR of the source systems.

4.3 Results

In this section, we summarize the main findings of our study, with sections dedicated to the most significant astrophysical parameters that can be inferred from GW observations. As mentioned above, each signal is simulated at two different inclination angles (30° and 70°) and two network SNRs (30 and 70). Unless otherwise stated, we quote the 90% CI, either absolute or relative to the true value. The full results of uncertainties can be found in App. C.

post-merger section (either a BH ringdown or an NS remnant oscillation) of the waveform.

[11] We note that a frequency-domain ROM of the aligned-spin `SEOBNRv4HM` [279] model was made available as this study reached completion [281].

4.3.1 Masses

Chirp Mass

For low-mass CBCs, the best-constrained parameter is the chirp mass $\mathcal{M}$, as defined in Eq. (1.2). $\mathcal{M}$ also appears in the waveform amplitude, together with the luminosity distance D_L and the redshift z:

$$\mathcal{A} \sim ((1+z)\mathcal{M})^{5/3}/D_L \, . \tag{4.3}$$

While this would suggest that these two parameters are positively correlated [209], in practice for CBCs with NSs and/or stellar mass BHs, the phase evolution determines the chirp mass so precisely that it can be treated as known in the amplitude of the signal (which is usually measured much less precisely). Indeed, for NSBH systems like those reported here, there are $\mathcal{O}(1000)$ observable inspiral cycles, leading to a precise $\mathcal{M}$ measurement from the waveform phase alone. For example, for the sources we analyze, the typical fractional uncertainty for $\mathcal{M}$ is $\lesssim 1\%$, whereas the luminosity distance has fractional uncertainties of $\sim 50\%$, due to its correlation with the orbital orientation, see Sec. 4.4.

However, we do find a clear anti-correlation between $\mathcal{M}^{\rm source}$ and D_L, as seen in Figs. 4-1 to 4-6, where $\mathcal{M}^{\rm source}$ is the rest-frame (or source-frame) chirp mass of the NSBH: when one increases the other decreases. This behavior can be explained by the fact that what is measured from the GW data is the detector-frame chirp mass, which is larger than the source-frame mass by a factor $(1+z)$. Thus, to convert detector-frame chirp mass to the astrophysically interesting source-frame chirp mass, one must use the measured luminosity distance (and assume a cosmology; we use the Planck 2015 cosmological parameters[12] [282]). For a given measured detector-frame mass, if the source were a bit farther away (higher z), the source-frame mass would have to be slightly smaller in order to yield the same detector-frame value. This is indeed what we find, and is worth stressing, as the uncertainty on the luminosity

[12]We use the cosmology defined in the `TT+lowP+lensing+ext` column of Tab. 4 from [282]. This corresponds to $\Omega_M = 0.3065$, $\Omega_\Lambda = 0.6935$, $w_0 = -1$ and $H_0 = 67.90$ kms^{-1}Mpc^{-1}.

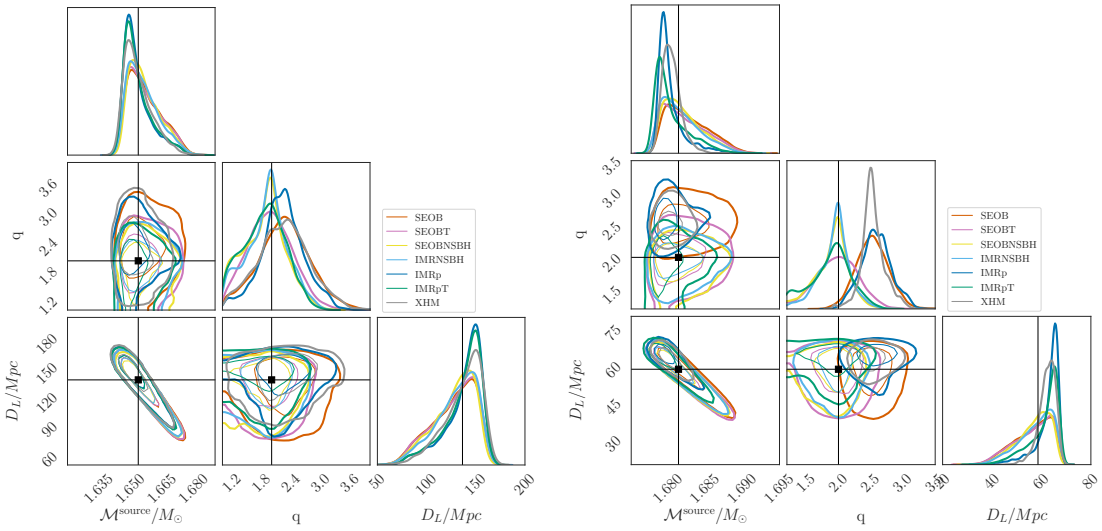

(a) SNR 30. (b) SNR 70.

Figure 4-1: Corner plot of posterior distributions for chirp mass $\mathcal{M}^{\rm source}$, mass ratio q, and luminosity distance D_L, recovered by different approximants for $q = 2$, inclination 30°. The thin (thick) lines mark the 50% (90%) contour, the same for all corner plots to follow.

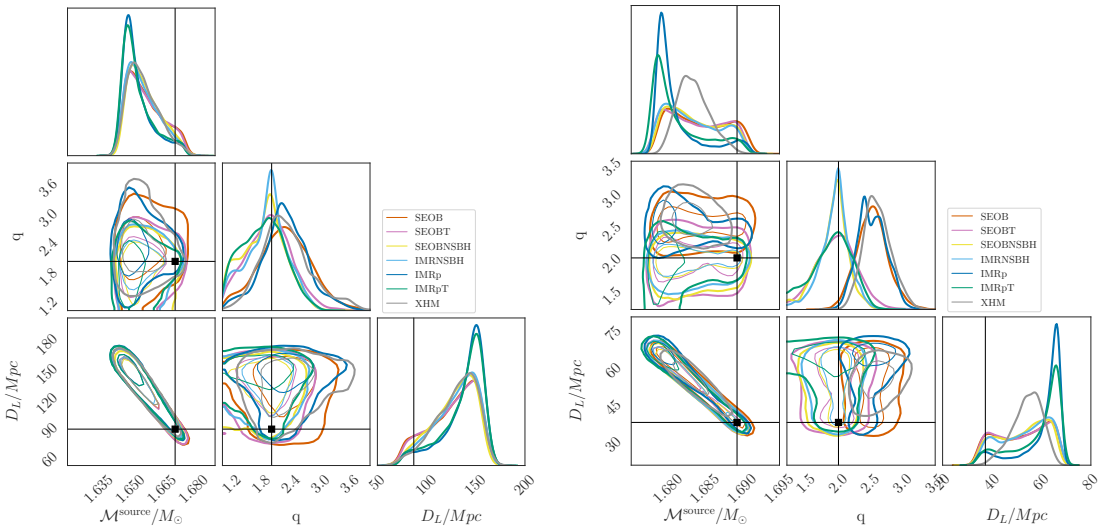

(a) SNR 30. (b) SNR 70.

Figure 4-2: Corner plot of posterior distributions for chirp mass $\mathcal{M}^{\rm source}$, mass ratio q, and luminosity distance D_L, recovered by different approximants for $q = 2$, inclination 70°.

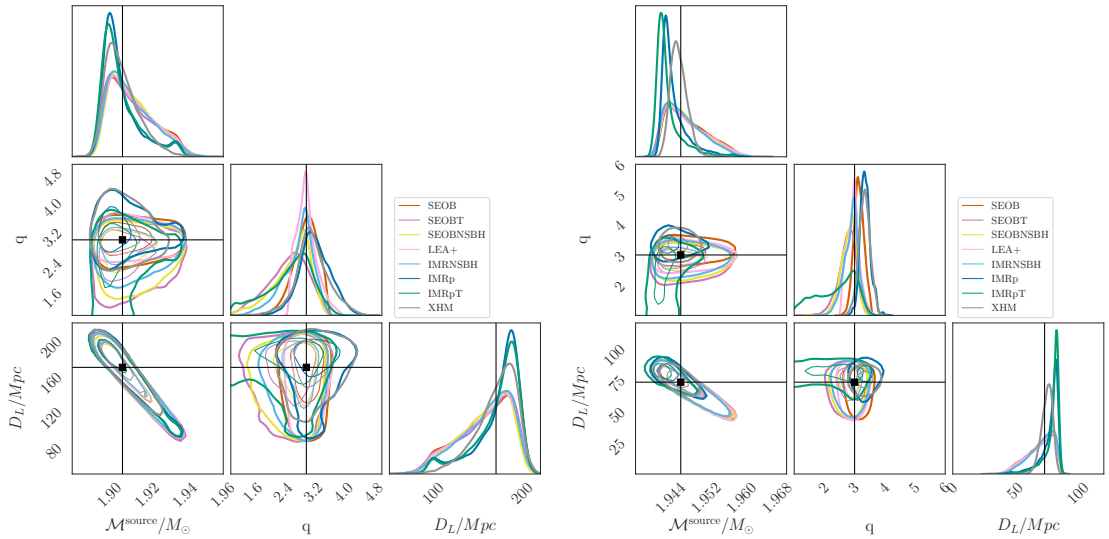

(a) SNR 30. (b) SNR 70.

Figure 4-3: Corner plot of posterior distributions for chirp mass $\mathcal{M}^{\rm source}$, mass ratio q, and luminosity distance D_L, recovered by different approximants for $q = 3$, inclination 30°.

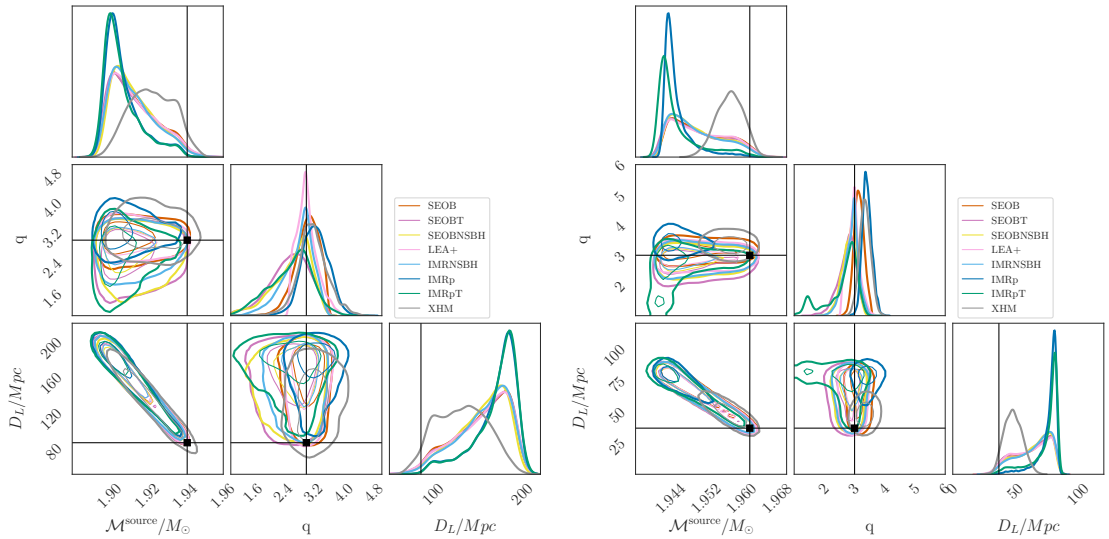

(a) SNR 30. (b) SNR 70.

Figure 4-4: Corner plot of posterior distributions for chirp mass $\mathcal{M}^{\rm source}$, mass ratio q, and luminosity distance D_L, recovered by different approximants for $q = 3$, inclination 70°.

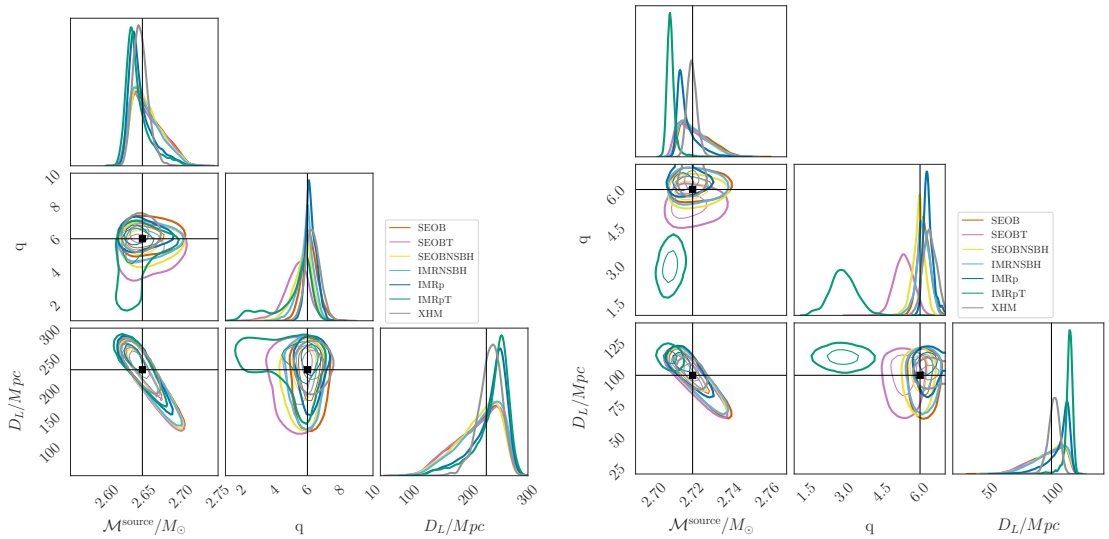

(a) SNR 30. (b) SNR 70.

Figure 4-5: Corner plot of posterior distributions for chirp mass $\mathcal{M}^{\rm source}$, mass ratio q, and luminosity distance D_L, recovered by different approximants for $q = 6$, inclination 30°.

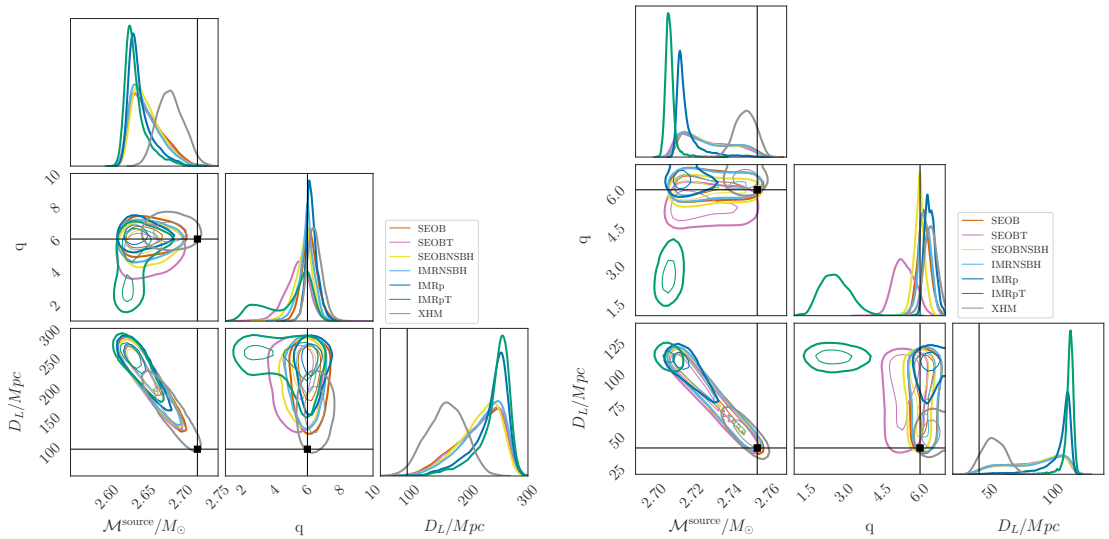

(a) SNR 30. (b) SNR 70.

Figure 4-6: Corner plot of posterior distributions for chirp mass $\mathcal{M}^{\rm source}$, mass ratio q, and luminosity distance D_L, recovered by different approximants for $q = 6$, inclination 70°.

distance is often a significant factor in the statistical and systematic uncertainty for the source-frame chirp mass.

For most of the systems we analyze, especially for the inclination 30° binaries, the true $\mathcal{M}^{\text{source}}$ value is recovered within the 90% CI and little difference is seen between approximants. The situation is quite different for the systems with an inclination equal to 70°: for those, the source-frame chirp mass is usually underestimated. In turn, this happens because the distance is overestimated (as explained in Sec. 4.4). This bias is reduced or even absent when using `IMRXHM` for systems with large mass ratios, large inclinations, and SNRs, since in that case, HOMs become observable enough to help break the distance-inclination degeneracy, thus yielding unbiased chirp mass estimates (e.g. Figs. 4-6 and Sec. 4.4).

On the other hand, there is only a marginal difference in the recovery of $\mathcal{M}^{\text{source}}$ between waveform models that do or do not include NS tidal effects. However, the same is not necessarily true for other parameters, as discussed below.

Mass Ratio

As we will discuss further in Sec. 4.3.2, it is largely the binary mass ratio, together with the BH spin and NS EoS, that determines if and to which extent the finite-size effects of the NS will leave an observable imprint in the detected GW signal [239, 243, 244]. For the $q = 2$ binaries, for which tidal effects are largest, the waveforms that do not model the NS tidal disruption recover a strongly biased posterior of q, with the true value of $q = 2$ only barely included in the tail of the posterior for the SNR 70 sources, Figs. 4-1b and 4-2b.

For the $q = 3$ binaries of Figs. 4-3 and 4-4, the tidal effects present are less prominent and hence all waveform models show similar performance in recovering the true mass ratio, with the exception of the non-tidal IMRPhenom-based waveforms, `IMRp` and `IMRXHM`, which produce results only marginally consistent with the true value.

When $q = 6$, Figs. 4-5 and 4-6, the NS is not expected to disrupt before plunging into the BH, and hence tidal effects are unmeasurable (as shown in Figs. 4-11 and 4-12).

For these sources, it is the two waveform models that are explicitly calibrated against (near-equal-mass) BNS simulations, `SEOBT` and `IMRpT`, that produce biased mass-ratio posteriors, with `IMRpT` being farther away from the true value. While at SNR 30, Figs. 4-5a and 4-6a, a second peak is already visible closer to an equal mass ratio, the main peak is still present around the true value of $q = 6$. It is only for the loud signals that the peak at the true value disappears, resulting in a significant bias, especially for `IMRpT`. For the $q = 6$ sources, the two specialized NSBH waveforms, `IMRNSBH` and `SEOBNSBH`, and the BBH waveforms measure the mass ratio comparably well, whereas `IMRXHM` remains overall better suited as it can deliver more precise distance and inclination measurements, Sec. 4.4, and hence a better measurement of the source-frame masses.

Overall, we find the absolute statistical uncertainties for q on the order of ~ 0.8 at SNR 70 for the NSBH-tuned models without much dependence on the true value of q. While the absolute value of the 90% CI stays roughly constant with q, the relative uncertainty is three times smaller for $q = 6$ than for $q = 2$. For the SNR 30 signals, the absolute uncertainties are naturally higher and fall into the range of 1.2-1.6 for all three systems.

NS and BH Masses

One of the most attractive features of NSBHs is the potential of a precise measurement of the NS mass, including putting constraints on its maximum value, which is still under debate [283–287]. Unfortunately, this is hard to achieve even at high SNRs with BNSs, due to their mass ratios being close to unity [288].

This is particularly true if one follows an agnostic approach, without assuming *a priori* that a compact object lighter than 2 $M_\odot$ is necessarily an NS, and allows for the object to assume spins larger than what an NS could nominally support [289, 290]. In that case, a known spin-mass ratio degeneracy will significantly increase the uncertainty in both parameters [72]. This was clearly shown with the first BNS source [4], for which the upper value of the 90% CI for the primary mass increases by $\sim 40\%$ ($\sim 18\%$) when the spin magnitude limit is increased from 0.05 to 0.89 for

spin-aligned (spin-precessing) waveforms. Similar differences have been reported for GW190425 [47]. For BNSs, the spin prior will usually determine whether it is possible to set a significant upper bound on the NS masses.

We want to verify if NS mass measurements obtained from NSBHs are more precise, as one would expect from their larger mass ratios, and more accurate. We find that for the SNR 30 binaries, Figs. 4-13a to 4-18a, all waveform models perform comparatively well in recovering the true binary masses. The exception is the $q = 3$ binaries, Figs. 4-15a and 4-16a: two of the models which allow for NS tidal effects and are dedicated to BNS systems (`SEOBT` and `IMRpT`) have wider tails towards more equal-mass binaries, and hence heavier NSs (Figs. 4-3a and 4-4a). This behavior is also seen for the $q = 6$ binaries, Figs. 4-17a and 4-18a, with `IMRpT` having especially large tails. On the other hand, note that the `IMRNSBH` and `SEOBNSBH` analyses are more constraining on the NS and BH masses compared to these "BNS-tuned" waveform models, similar to the discussion in Sec. 4.3.1.

For the SNR 70 binaries, severe biases are visible, due to two different factors. The true values are outside of the 90% CIs for the $q = 2$ binaries, Figs. 4-13b and 4-14b when using approximants that do not support NS matter effects. This is to be expected since tidal effects are most visible at small mass ratios, and in light of the fact that tides and mass ratios enter the GW phase in combination [291]. This bias of $\sim 0.1 M_\odot$ for the recovered NS mass, though only a small fractional error, could be detrimental when propagated to the inference on the NS EoS, which is very sensitive to changes in the NS mass. It is also interesting to note that the HOMs included in the `IMRXHM` model do not affect the inferred masses for these binaries, and indeed recover the same biased masses as the other waveform models without NS matter effects. A similar behavior is also seen for the $q = 3$ binaries, Figs. 4-15b and 4-16b, where again the models without NS matter effects show larger biases in the NS and BH masses, more so for `IMRp` and `IMRXHM` than for `SEOB`, though the effects are smaller than the those for the $q = 2$ binaries.

For the $q = 6$ binaries, Figs. 4-17b and 4-18b, we see even stronger biases, but the reason is now different. As the more asymmetric mass ratio reduces the observational

impact of the tidal effects, the "BBH-like" models can describe the system quite well, and the models tuned to BNS-like (thus light and nearly equal-mass) tidal effects (`SEOBT` and `IMRpT`) greatly misestimate the NS and BH masses. This might be due to the conditioning applied to the end of `SEOBT` and `IMRpT` waveforms, which would be outside of the most sensitive part of the detector bandwidth for BNS-like systems, but might leave a detectable imprint for NSBHs with increased mass ratios and total masses as the binary merger now occurs at frequencies where the detectors are more sensitive.

Analyses of CBCs containing an object whose mass is reasonably consistent with being an NS can intuitively be expected to exhibit some form of tidal effects. Waveform models that allow for such effects could therefore be believed to measure the source parameters better, as they nominally contain a more accurate description of all relevant physical effects. Naively following these assumptions for the $q = 6$ binaries would, as shown here, potentially lead to significant errors in the inferred astrophysics. As an example, the `IMRpT` analysis in Fig. 4-18b would, if taken in isolation, have a strong impact on the inferred maximum NS mass, a parameter which in turn affects the constraints on the NS EoS [283–287, 292]. It is worth noticing that one can quantitatively assess the relative goodness of fit to the data of two models by computing Bayes factors, as previously described in Sec. 3.2. We find that the BNS-tuned tidal waveforms are strongly disfavored even when compared to non-tidal waveforms for $q = 6$ and SNR 70, which could be used as a figure of merit to exclude them from parameter estimation for specific candidate events. Further details about Bayes factors are also given below, in Sec. 4.3.2.

4.3.2 Matter Effects

Together with the mass, the radius is probably the most interesting astrophysical quantity one can infer from the GW observations of NSs. As seen above, in Eq. (4.2), this information is encoded in the tidal deformability of NSs, which directly enters the phase evolution of GW signals, though at high post-Newtonian orders [268, 293–296]. In this section, we will discuss the measurement of both radius and tidal deformability.

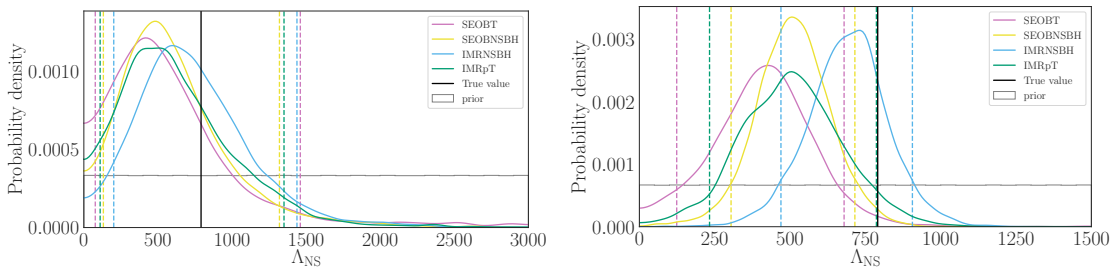

(a) $\Lambda_{\rm NS}$, SNR 30. (b) $\Lambda_{\rm NS}$, SNR 70.

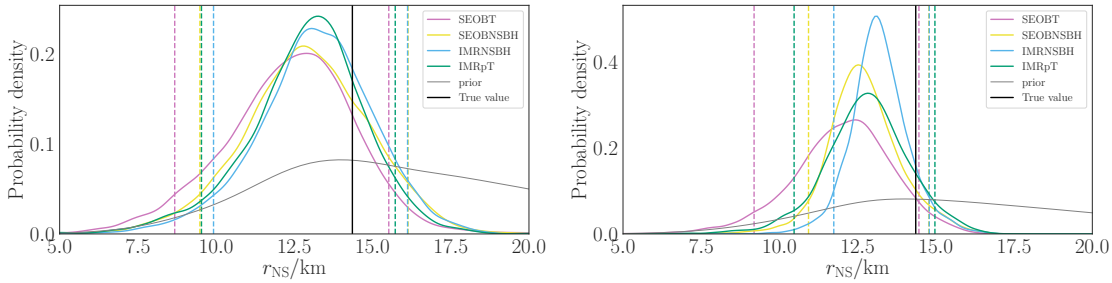

(c) $r_{\rm NS}$, SNR 30. (d) $r_{\rm NS}$, SNR 70.

Figure 4-7: Posterior distributions for $\Lambda_{\rm NS}$ and $r_{\rm NS}$ recovered by different approximants for $q = 2$, inclination 30°. The dashed lines mark the 90% CIs, the same for all 1D plots to follow.

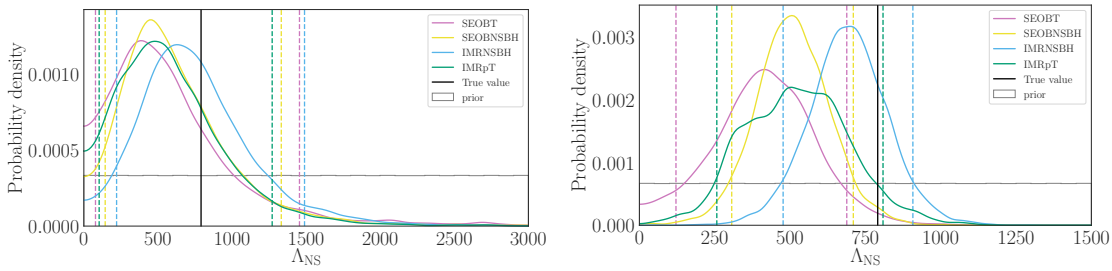

(a) $\Lambda_{\rm NS}$, SNR 30. (b) $\Lambda_{\rm NS}$, SNR 70.

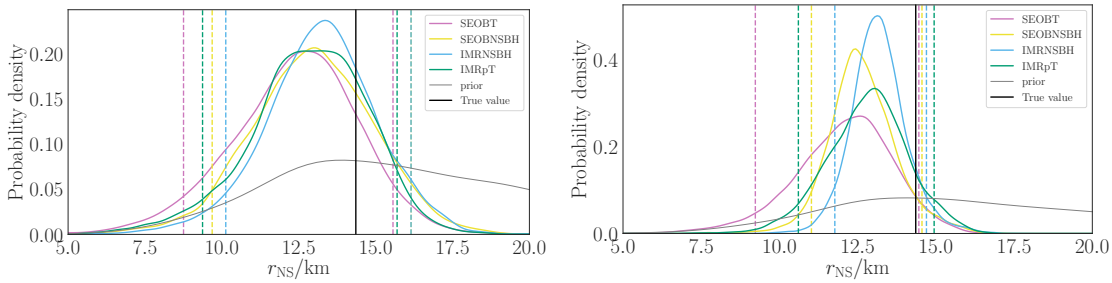

(c) $r_{\rm NS}$, SNR 30. (d) $r_{\rm NS}$, SNR 70.

Figure 4-8: Posterior distributions for $\Lambda_{\rm NS}$ and $r_{\rm NS}$ recovered by different approximants for $q = 2$, inclination 70°.

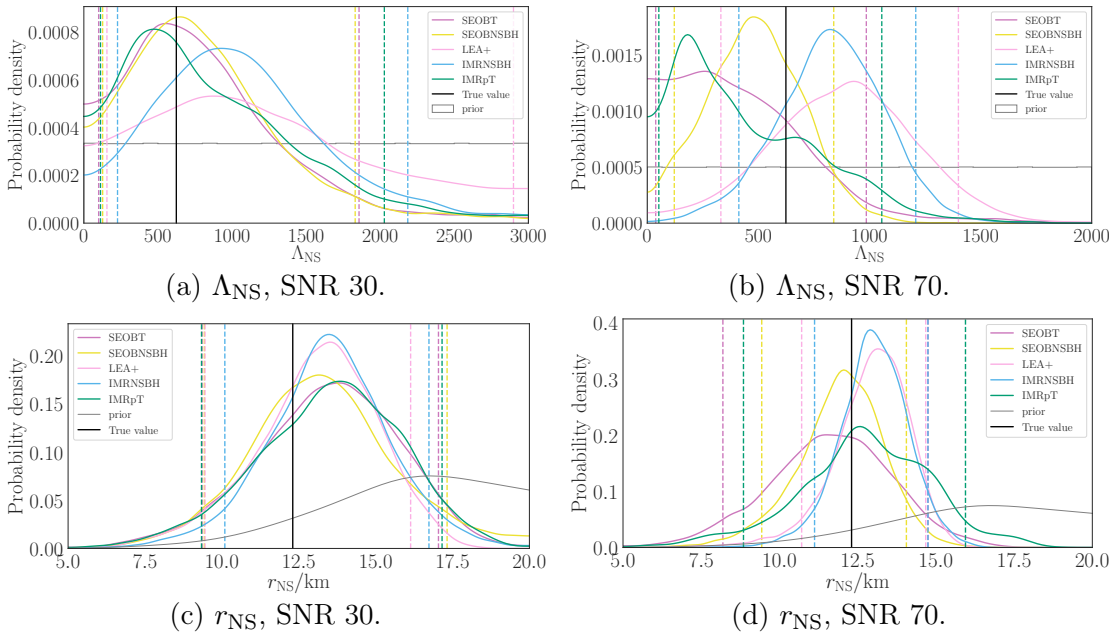

(a) $\Lambda_{\rm NS}$, SNR 30. (b) $\Lambda_{\rm NS}$, SNR 70.

(c) $r_{\rm NS}$, SNR 30. (d) $r_{\rm NS}$, SNR 70.

Figure 4-9: Posterior distributions for $\Lambda_{\rm NS}$ and $r_{\rm NS}$ recovered by different approximants for $q = 3$, inclination 30°.

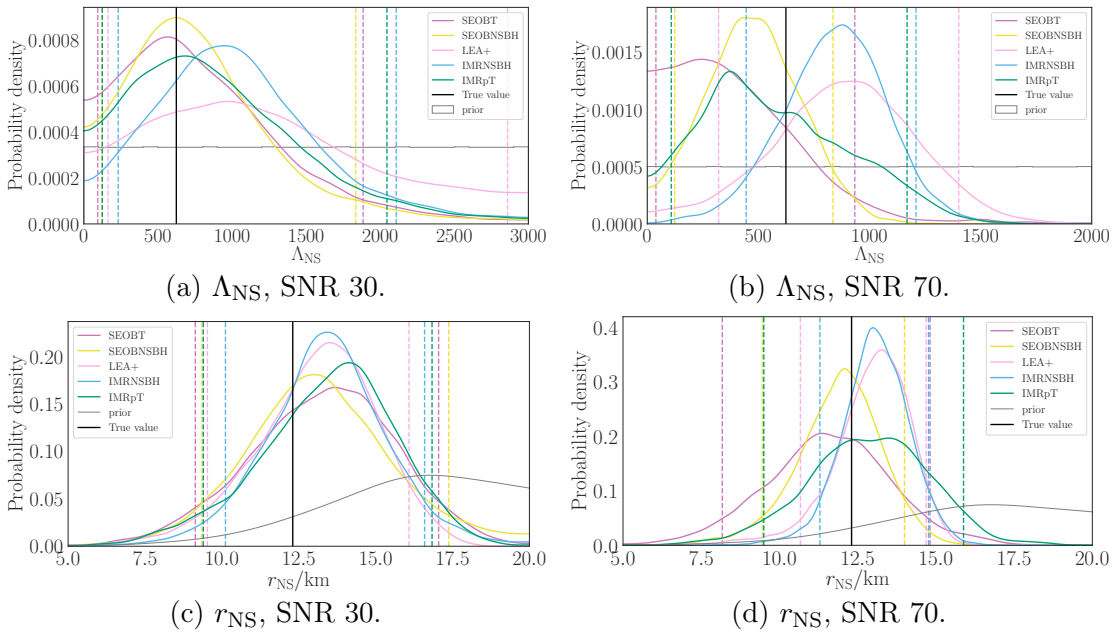

(a) $\Lambda_{\rm NS}$, SNR 30. (b) $\Lambda_{\rm NS}$, SNR 70.

(c) $r_{\rm NS}$, SNR 30. (d) $r_{\rm NS}$, SNR 70.

Figure 4-10: Posterior distributions for $\Lambda_{\rm NS}$ and $r_{\rm NS}$ recovered by different approximants for $q = 3$, inclination 70°.

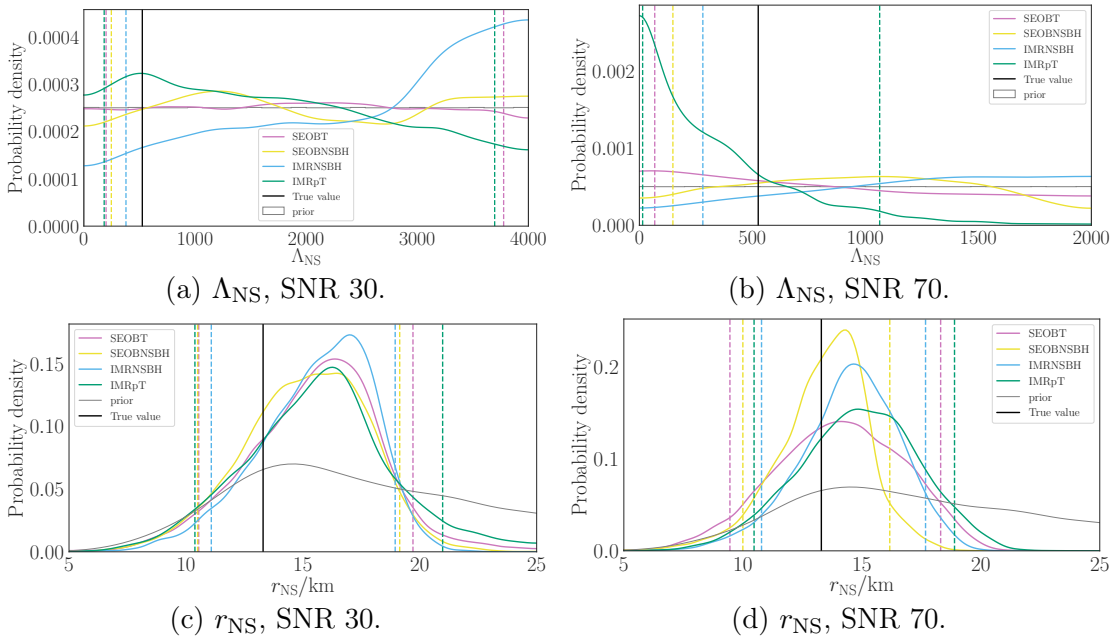

(a) Λ_{NS}, SNR 30. (b) Λ_{NS}, SNR 70.

(c) r_{NS}, SNR 30. (d) r_{NS}, SNR 70.

Figure 4-11: Posterior distributions for Λ_{NS} and r_{NS} recovered by different approximants for $q = 6$, inclination 30°.

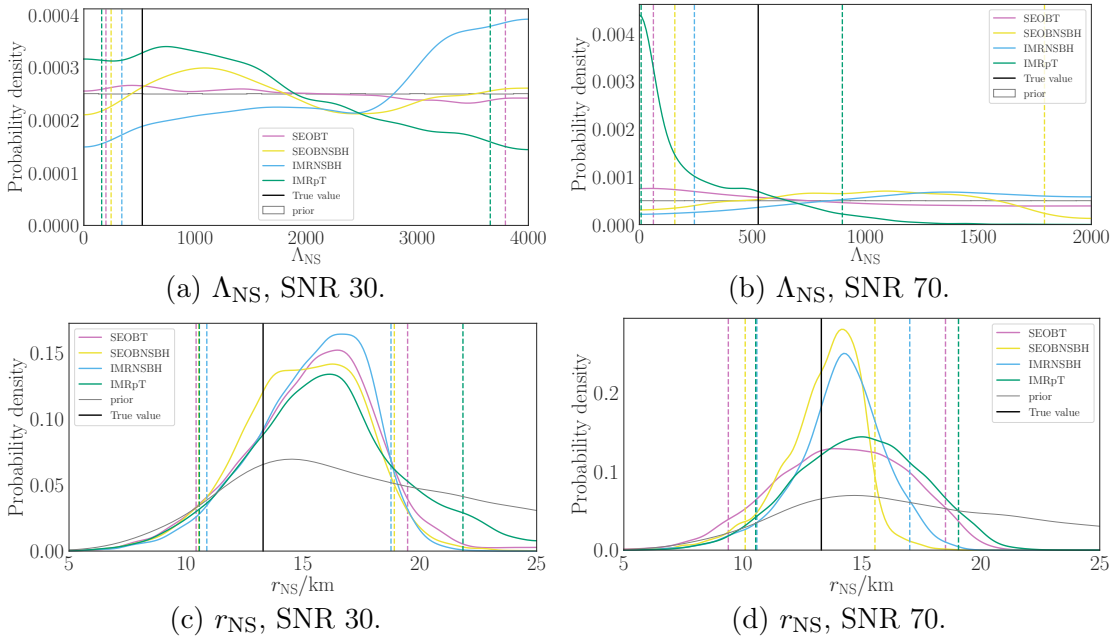

(a) Λ_{NS}, SNR 30. (b) Λ_{NS}, SNR 70.

(c) r_{NS}, SNR 30. (d) r_{NS}, SNR 70.

Figure 4-12: Posterior distributions for Λ_{NS} and r_{NS} recovered by different approximants for $q = 6$, inclination 70°.

NS Tidal Deformability

While GWs carry information about the NS tidal deformability, whether these effects are in practice observable depends heavily on the binary parameters, for a fixed SNR. Specifically, if the mass ratio is too large, the NS will cross the event horizon of the BH before any significant tidal disruption can occur. The exact value of the mass ratio above which tidal effects are shut off also depends on the BH spin (as it affects the position of the outer event horizon) and the NS compactness or, equivalently, its radius $r_{\rm NS}$, see App. C.2 [236–245]. Therefore, we do not expect to gain significant information about tides from the $q = 6$ signals. We stress that, if one is agnostic and does not a priori exclude the existence of BHs with masses comparable to NSs, measuring the deformability of the secondary object as being non-zero would be the main way to *prove* that it was not a BH (unless EM emission is detected, which would be an even stronger indication that an NS was involved in the merger).

Indeed, at a mass ratio of $q = 6$, NR simulations that nominally include the effects of a tidally disrupted NS are indistinguishable from "pure BBH" simulations, with the tidal signature on the generated waveform being comparable to, or smaller than, the numerical precision of current NR simulations. Thus, we do not expect to be able to constrain the tidal deformability for these types of high mass-ratio NSBHs.

On the other hand, as discussed in Sec. 4.1, we should be able to constrain the tidal deformability better for binaries with less asymmetric mass ratio. In light of the above discussion, we expect the $q = 2, 3$ binaries to be the more favorable configurations in this analysis to measure $\Lambda_{\rm NS}$: a low-mass BH (within the putative mass gap between NSs and BHs [54, 297, 298]) with a relatively massive NS. We stress that BHs with masses in the gap have likely already been discovered: the lighter component of GW190814 was a $\sim 2.6\ M_\odot$ compact object, making it either the heaviest NS or the lightest BH ever found [50]. Moreover, the total mass of GW190425 was $\sim 3.3 M_\odot$ [47, 299, 300]: if the final product of the merger were a BH, which is likely, it would have masses in between the BHs of our $q = 2$ and $q = 3$ signals[13]. The tidal deformability

[13]Whether such a BH would have a high probability of merging again, with an NS, is highly dependent on the environment where it formed.

is indeed best constrained for the most equal-mass system in our study, the $q = 2$ binaries, Figs. 4-7a and 4-8a. We note, however, that for these signals, $\Lambda_{\rm NS}$ is generally underestimated for all waveform models, while still containing the true value within the 90% CIs at SNR 30. For the SNR 70 sources, the statistical uncertainty shrinks, while the offsets remain comparable. We find that the true value of $\Lambda_{\rm NS}$ is outside of the 90% CIs for all waveforms but `IMRNSBH` and `IMRpT`, including `SEOBNSBH` that is nominally tuned for this kind of source. It is worth mentioning that `SEOBNSBH`, `IMRpT`, and `SEOBT` all roughly agree with each other and underestimate $\Lambda_{\rm NS}$ by a similar amount, where `SEOBNSBH` provides the most constrained posterior among the three.

The situation is not too different for the $q = 3$ binaries, for which we can additionally use the `LEA+` model, whose range of validity is limited to $q \in [2, 5]$. At SNR 30, Figs. 4-9a and 4-10a, the peak of the $\Lambda_{\rm NS}$ posterior is close to the true value for all approximants, which also agree well with each other, with the exception of `LEA+` and `IMRNSBH` whose posteriors slightly overestimate the $\Lambda_{\rm NS}$ (while still containing the true value within their very large 90% CIs). A more complex picture emerges when SNR is 70, Figs. 4-9b and 4-10b. In this case, we observe that posteriors cluster around two values, one larger and one smaller than the true $\Lambda_{\rm NS}$, with the true value roughly in between the two sets. `IMRpT` yields the longest tail in the posteriors among the approximants with its 90% CI only slightly wider than the others. It is worth stressing that the differences we see do not simply align with the underlying base model (IMRPhenom or EOB), as instead happening for, e.g., the luminosity distance, Sec. 4.4 below. We do not have a simple (or complicated) explanation for these features, which could arise from the detailed way each approximant implements and calibrates tidal corrections. We also observe this difference in the results from NSBH-tuned models: while based on the results from `IMRNSBH` (or `LEA+`, for $q3 =$) we would be able to place $\Lambda_{\rm NS} = 0$ at a very low confidence level, `SEOBNSBH` finds a non-negligible amount of posterior support there and would not allow to rule out that the secondary is in fact a BH for which $\Lambda_{\rm NS} = 0$. However, even at an SNR of 70, the systematic uncertainties caused by waveform models on $\Lambda_{\rm NS}$ are still within the statistical uncertainties. Thus, we can still use any waveforms that include tidal

effects, both the ones dedicated to BNSs and the ones to NSBHs, without producing significant bias in the results. We will require specialized NSBH waveforms only when we have detections with significantly higher SNRs.

For the $q = 6$ sources at SNR of 30, (Figs. 4-11a and 4-12a), the recovered posteriors on $\Lambda_{\rm NS}$ are not much different from the prior, explicitly showing that for non-spinning systems at such a large mass ratio, there is no information about the NS composition, since the NS plunges into the BH horizon before it is significantly deformed. At SNR 70, this general behavior still persists but with a slightly more discernible fall off at high $\Lambda_{\rm NS}$ (not visible in the plots, due to the range we show in the horizontal axis, but conveyed by the 90% CIs quoted in App. C.1). The clear exception is `IMRpT` whose posterior has a visible peak at $\Lambda_{\rm NS} = 0$ and is significantly different from the prior (only the upper bound of the 90% for `IMRpT` is visible in this case, Figs. 4-11b and 4-12b). To a smaller extent, `SEOBT` shows the same trend. However, as discussed in Sec. 4.3.1, these approximants also recover significantly biased mass parameters, and have unfavorable Bayes factors compared to other approximants at $q = 6$, further discussed in Sec. 4.3.2.

NS radius

Another astrophysically important quantity, capable of constraining the NS EoS through GW and EM observations [16, 47, 301–305], is the radius of the NS, $r_{\rm NS}$. Unlike $\Lambda_{\rm NS}$, $r_{\rm NS}$ is not directly encoded in the GW signal but rather inferred from the measurements of the NS mass and $\Lambda_{\rm NS}$ using fitting formulae (see App. C.2).

We report these posteriors in panels (c) and (d) of Figs. 4-7 to 4-12. Overall, the radius is not constrained with high precision at SNR 30, with typical 90% CI widths of ~ 7 km (compare with $\lesssim 4$ km for the BNS GW170817 [16], which had a comparable SNR). The fact that the NSBHs we study do not provide radius measurements as precise as GW170817 is due to the dependency of the tidal terms on the mass ratio, and the fact that fewer waveform cycles are in the band for CBCs with larger chirp masses.

For the $q = 2$ binaries, the inferred $r_{\rm NS}$ distributions show a smaller spread than

the respective $\Lambda_{\rm NS}$ posteriors. For SNR 70 especially (Figs. 4-7d and 4-8d), the inferred $r_{\rm NS}$ is underestimated, though the true value is still contained within the 90% CI.

A similar behavior is seen in the $q = 3$ binaries, again with a reduced spread compared to $\Lambda_{\rm NS}$. In the SNR 70 analyses (Figs. 4-9d and 4-10d), `SEOBNSBH` and `SEOBT` return distributions for $r_{\rm NS}$ centered around the true value, whereas `IMRNSBH` and `LEA+` slightly overestimate $r_{\rm NS}$, while still including the true value at a high confidence level.

For the SNR 70 sources, typical 90% CIs are of $\sim 3-4$ km $(4-5$ km) for $q = 2$ $(q = 3)$.

As with $\Lambda_{\rm NS}$, the $q = 6$ analyses recover very broad posteriors for $r_{\rm NS}$ and only exclude extremely large values of the radius (≥ 20 km), Figs. 4-11 and 4-12, with the SNR 70 posteriors more constraining than those of the SNR 30 sources. It is worth stressing that most of this information does not come from $\Lambda_{\rm NS}$, but rather from the NS mass measurements (see Sec. 4.3.1). Finally, while `IMRpT` finds very biased posteriors for $\Lambda_{\rm NS}$ and NS mass at $q = 6$, the two biases cancel out, giving a derived posterior on $r_{\rm NS}$ not too different from what is obtained with other approximants.

Model Selection

As mentioned above, the relative goodness of fit of waveform models to the data in hand can be quantified by calculating the Bayes factors between them, as defined in Eq. (3.2). If one calls H_1 the model where the approximant A_1 is used to analyze the data, and H_2 the model where the approximant A_2 is used, $\mathcal{B}^{A_1}_{A_2} = \frac{Z(H_1)}{Z(H_2)} > 0$ if the model H_1, i.e. if the waveform model A_1, is preferred. In Tab. 4.3 to 4.6 we present the *natural log* Bayes factor between some of the models used in this study.

As one would expect, for the $q = 2$ binaries, there is more support for models that include tidal effects. `SEOBNSBH` and `IMRNSBH` match the data equally well and have large odds ratios relative to all other models, likely due to the fact that they have been tuned specifically for NSBH signals, and that they do not allow for a spin in the NS and only allow a smaller range for the BH spin, see the priors in Tab. C.8. Because the true NS spin is *actually* zero, `SEOBNSBH` and `IMRNSBH` are not penalized by that limitation, and their odds ratios are boosted by the smaller prior volume. The

SEOBNSBH/Sim.	SEOB	SEOBT	LEA+	IMRNSBH	IMRp	IMRpT	IMRXHM
BHNSq2s0	51.96	41.15	-	-0.35	42.54	42.64	-
BHNSq3s0	2.30	2.99	-0.06	-0.27	3.95	3.46	-
BHNSq6s0	2.62	4.81	-	0.24	4.29	6.35	-2.92

Table 4.3: ln$\mathcal{B}$ for different approximants, SNR 30, inclination 30°, reported as the odds ratio to the ln$\mathcal{B}$ of SEOBNSBH.

SEOBNSBH/Sim.	SEOB	SEOBT	LEA+	IMRNSBH	IMRp	IMRpT	IMRXHM
BHNSq2s0	51.62	40.71	-	-0.29	42.25	42.11	-
BHNSq3s0	2.43	2.96	0.06	-0.10	3.58	3.70	-
BHNSq6s0	2.42	5.11	-	0.01	3.90	6.13	-15.67

Table 4.4: ln$\mathcal{B}$ for different approximants, SNR 30, inclination 70°, reported as the odds ratio to the ln$\mathcal{B}$ of SEOBNSBH.

SEOBNSBH/Sim.	SEOB	SEOBT	LEA+	IMRNSBH	IMRp	IMRpT	IMRXHM
BHNSq2s0	279.38	214.03	-	-0.27	220.98	218.13	-
BHNSq3s0	3.42	4.97	0.29	-0.27	6.15	6.61	-
BHNSq6s0	2.64	21.20	-	1.55	6.45	17.39	-

Table 4.5: ln$\mathcal{B}$ for different approximants, SNR 70, inclination 30°, reported as the odds ratio to the ln$\mathcal{B}$ of SEOBNSBH.

SEOBNSBH/Sim.	SEOB	SEOBT	LEA+	IMRNSBH	IMRp	IMRpT	IMRXHM
BHNSq2s0	277.24	212.81	-	-0.18	219.73	216.79	-
BHNSq3s0	3.46	5.41	0.40	-0.30	6.89	7.42	-
BHNSq6s0	2.67	23.47	-	1.53	6.21	17.87	-

Table 4.6: ln$\mathcal{B}$ for different approximants, SNR 70, inclination 70°, reported as the odds ratio to the ln$\mathcal{B}$ of SEOBNSBH.

same would not necessarily be true if the source contained a spinning NS. SEOBT is significantly favored over SEOB, while there is only mild support for IMRpT over IMRp even at an SNR of 70.

The results for the $q = 3$ binaries are qualitatively different. Here we observe that IMRXHM is mildly preferred over the NSBH approximants. This suggests that at this mass ratio, not modeling HOMs is penalized more than not modeling tides. The LEA+ model (with further constraints on the mass ratio prior) performs as well as the other two newer NSBH approximants. The comparisons between SEOBT and SEOB, as well as between IMRpT and IMRp, are rather inconclusive compared to the results for the $q = 2$ binaries.

For the $q = 6$ binaries, IMRXHM has the highest Bayes factor among all the approximants, since it is the only approximant included here that accounts for HOMs, which are more significant at higher mass ratios. Moreover, the preference is stronger for higher inclinations where HOMs have a more significant amplitude. The NSBH approximants perform slightly better than non-tidal waveforms and much better than the two tidal models that are tuned for BNS systems. It is interesting to observe that $q = 6$ SEOB (IMRp) does better than SEOBT (IMRpT). This is not because tides are not measurable, and hence "unnecessary" in the model: as we have seen before, no significant constraints can be placed on $\Lambda_{\rm NS}$ (see Sec. 4.3.2) for these sources, and not much information is gained relative to the prior distribution. In this case, no significant Occam penalty [306] is assigned to the models with tides. Hence, the fact that the BNS-tuned tidal waveform models are disfavored over their related non-tidal models for the $q = 6$ binaries must be attributed to their failure to adequately describe the NSBH waveforms in that mass range.

4.3.3 Spins

There are multiple reasons why an accurate measurement of the BH spins of NSBH systems is essential. First, the BH spin should be measured more precisely in NSBHs than in BBHs, since the potentially large mass ratio of NSBHs enhances the effect of spin precession and spin-orbit coupling, yielding a more significant amount of

phase and amplitude modulation than what would be present in an equal mass system with similar spins. NSBHs might very well be the systems that yield the most precise measurement of BH spins in the next few years. It is thus essential that accuracy follows. Second, spins are a good tracer of the formation channel of compact binaries [33, 178–180, 307, 308]. A precise and accurate measurement of spins could be critical to determine whether the formation pathways of BBH and NSBH systems are different. When the masses of the compact objects in a binary are comparable, GWs provide a good measurement of the effective spin, $\chi_{\rm eff}$, the mass-weighted projection of the total spin along the orbital angular momentum [67–70] as defined in Eq. (1.2).

As the mass ratio increases, the spin of the primary becomes the leading contribution to $\chi_{\rm eff}$ (this is even more true for an NSBH, as NSs are expected to have small spins), and one indeed finds that the spin of the primary becomes measurable [175, 309, 310].

Because our simulations have non-spinning BHs and NSs, we will not be able to probe the quality of spin measurement for large spins. However, it is still very interesting to show if waveform systematics affect the measurement of small spins in NSBH because (a) most of the BH found to date are consistent with having small or no spin [71, 179, 180, 308] and (b) there is a correlation between effective spin and mass ratio [72], as well as between mass ratio and tidal parameters [291], hence different waveforms might produce visibly different posteriors. We expect the biases to be more visible when the mass ratio is small enough that the NS can acquire significant tidal deformation and disruption before merging with the BH.

Indeed, this is what our simulations show, in Figs. 4-13 and 4-14 for $q = 2$. While some differences in behavior between tidal and non-tidal approximants are already visible at SNR 30, it is only when the signals are very loud, at SNR 70, that the tension becomes significant compared to the statistical uncertainties. For these loud simulations, Figs. 4-13b and 4-14b, the models that include tides recover the true value of $\chi_{\rm eff}$ and q, with the 90% CI of ~ 0.1 (with some minor differences depending on the inclination angle and the tidal waveform model). As discussed in Sec. 4.3.1, biases in the results from models without tides are also visible for the mass ratio and

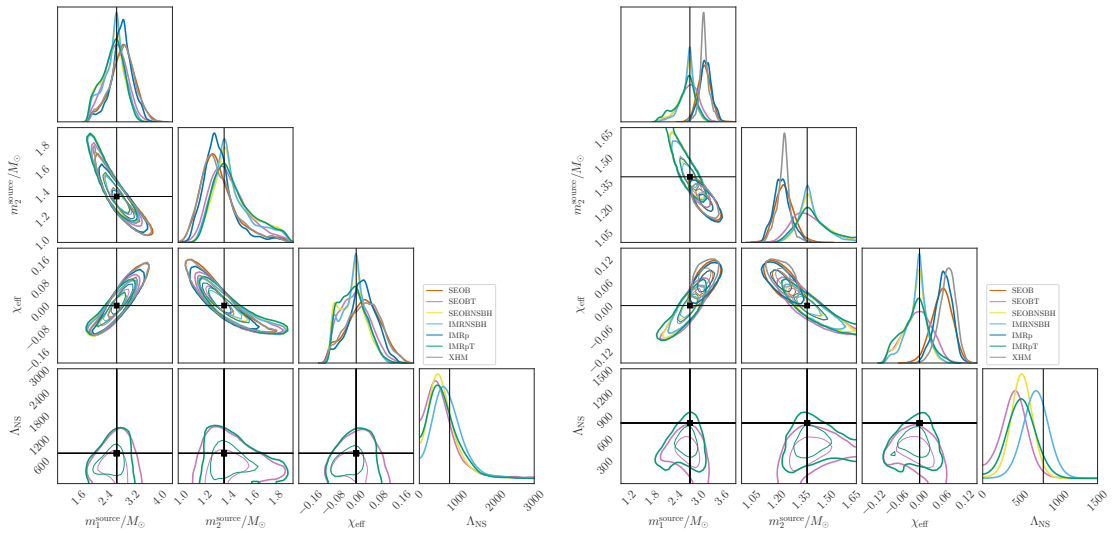

(a) SNR 30. (b) SNR 70.

Figure 4-13: Corner plot of posterior distributions for component masses $m_1^{\rm source}$ and $m_2^{\rm source}$, the effective spin $\chi_{\rm eff}$ and the tidal deformability $\Lambda_{\rm NS}$ recovered by different approximants for $q = 2$, inclination 30°.

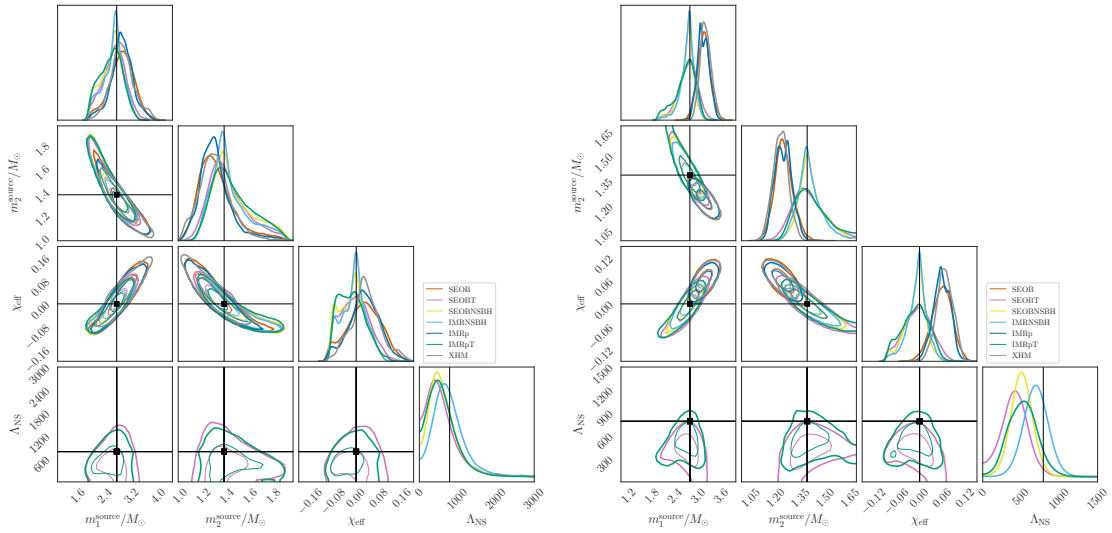

(a) SNR 30. (b) SNR 70.

Figure 4-14: Corner plot of posterior distributions for component masses $m_1^{\rm source}$ and $m_2^{\rm source}$, the effective spin $\chi_{\rm eff}$ and the tidal deformability $\Lambda_{\rm NS}$ recovered by different approximants for $q = 2$, inclination 70°.

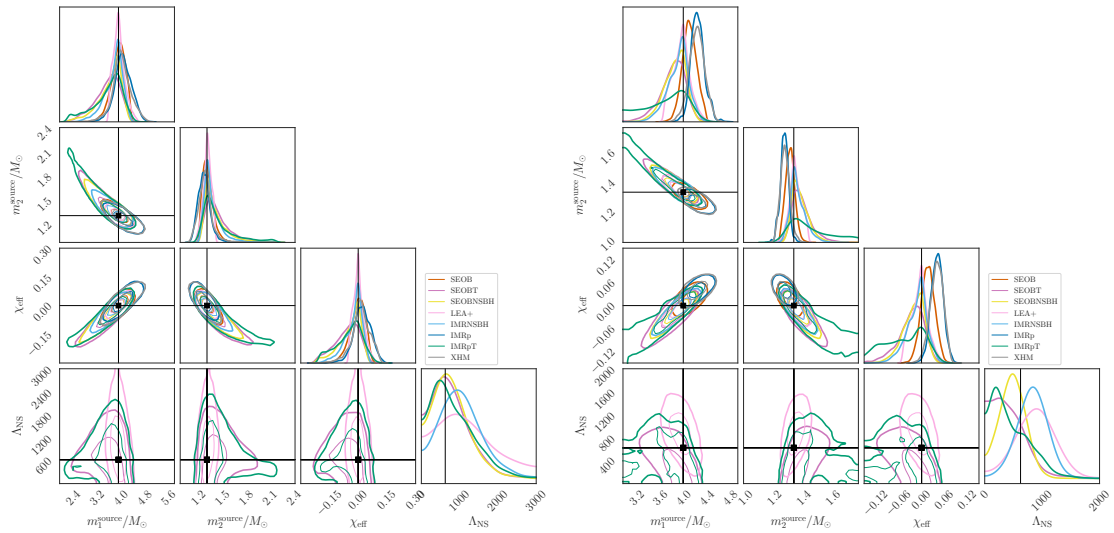

(a) SNR 30. (b) SNR 70.

Figure 4-15: Corner plot of posterior distributions for component masses m_1^{source} and m_2^{source}, the effective spin χ_{eff} and the tidal deformability Λ_{NS} recovered by different approximants for $q = 3$, inclination 30°.

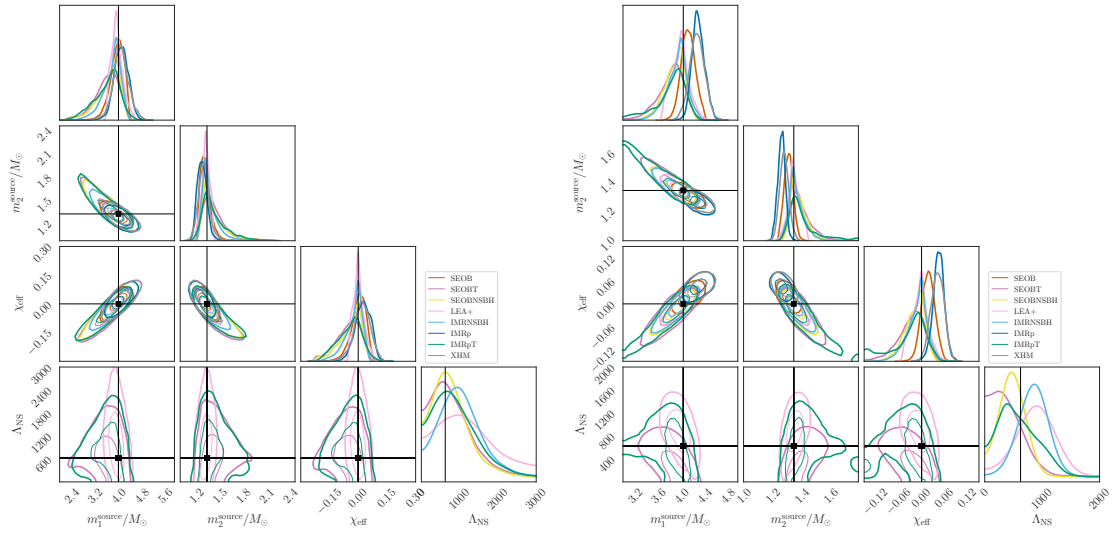

(a) SNR 30. (b) SNR 70.

Figure 4-16: Corner plot of posterior distributions for component masses m_1^{source} and m_2^{source}, the effective spin χ_{eff} and the tidal deformability Λ_{NS} recovered by different approximants for $q = 3$, inclination 70°.

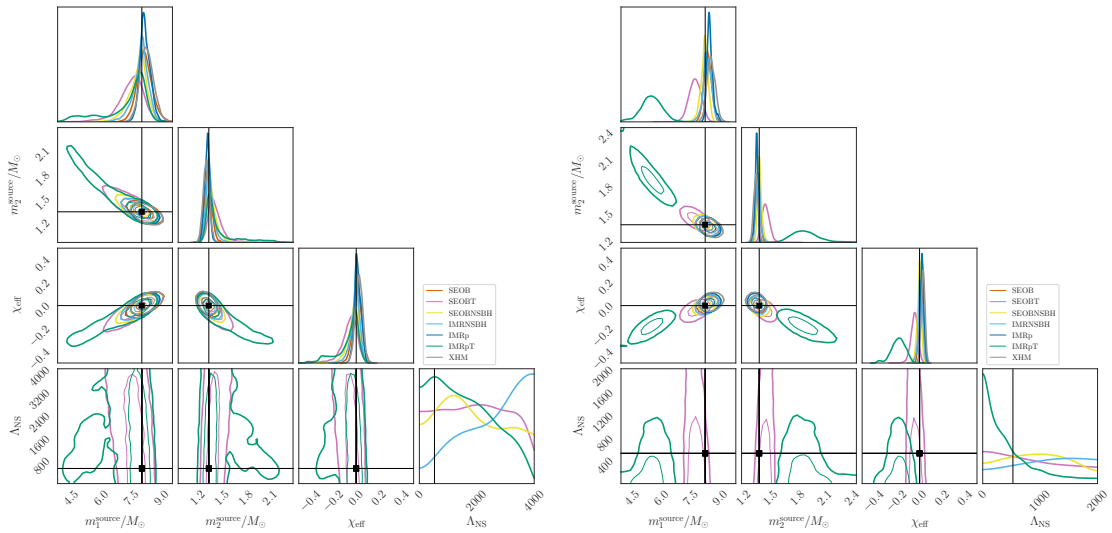

(a) SNR 30. (b) SNR 70.

Figure 4-17: Corner plot of posterior distributions for component masses m_1^{source} and m_2^{source}, the effective spin χ_{eff} and the tidal deformability Λ_{NS} recovered by different approximants for $q = 6$, inclination 30°.

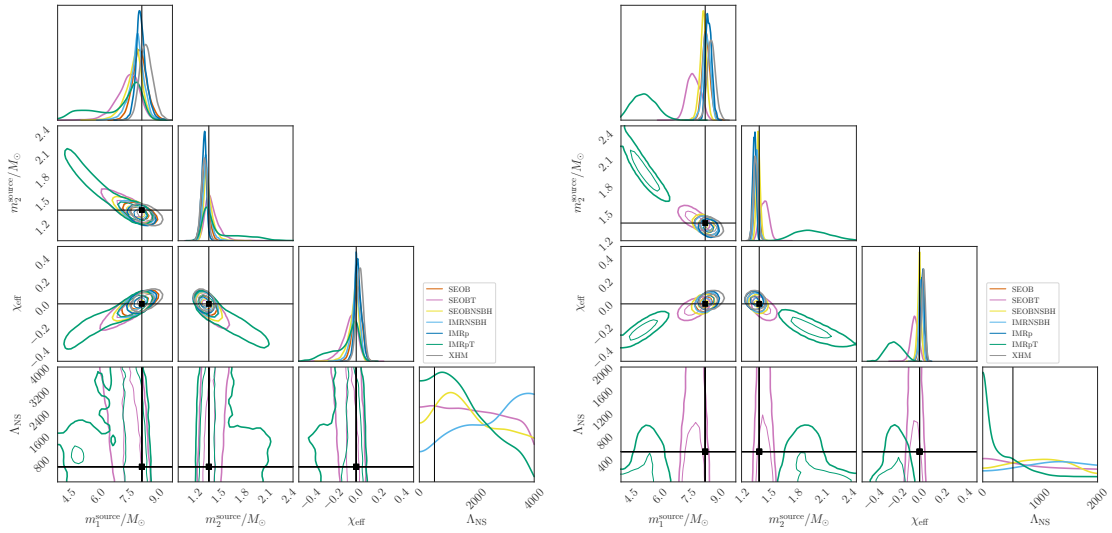

(a) SNR 30. (b) SNR 70.

Figure 4-18: Corner plot of posterior distributions for component masses m_1^{source} and m_2^{source}, the effective spin χ_{eff} and the tidal deformability Λ_{NS} recovered by different approximants for $q = 6$, inclination 70°.

hence for the component masses. For all of these parameters, the true values are marginally included in or excluded from the 90% CIs. We do not observe significant differences between the NSBH-tuned waveforms and the other tidal waveforms. It is also worth stressing that the `IMRXHM` waveform does not perform better, or even differently, than the other non-tidal waveforms, showing explicitly that even at SNRs of 70, the missing tidal terms have a dominant effect on the waveform systematics over the missing HOMs for small mass ratios.

As the mass ratio increases, the biases in the spin posteriors become less and less apparent, as one would expect given that the effect of tides decreases with more unequal masses. However, for $q = 3$ at SNR 70, Figs. 4-15b and 4-16b, we still see a bias for the non-tidal IMR models, whereas the EOB models are consistent with the true values of $\chi_{\rm eff}$ and masses. In general, we find that non-tidal IMR models tend to overestimate $\chi_{\rm eff}$ and, due to its correlation with q [72], to overestimate the mass ratio. Finally, for $q = 6$, Fig. 4-17 and 4-18, the true value of $\chi_{\rm eff}$ and masses are within the 90% CIs even at SNR 70 for all non-tidal approximants. This suggests that for such a high mass ratio, even higher SNRs would be needed for the measurement of $\chi_{\rm eff}$ and masses to be limited by waveform systematics. On the other hand, we observe that `IMRpT`, which has tidal effects, gives significantly biased results at this high mass ratio. While the statistical uncertainties are large enough at SNR 30 that the posterior is consistent with the true values, the same is no longer true at SNR 70, and for both masses and $\chi_{\rm eff}$, the `IMRpT` posteriors are in significant tension with the true values (even the component spin magnitude is heavily biased, as presented in Tab. C.6). In fact, while less pronounced than for `IMRpT`, one can see that even `SEOBT` starts diverging from the other approximants at $q = 6$. This can be explained by the fact that `SEOBT` and `IMRpT` are constructed with the goal of matching the late inspiral of BNSs, for which the mass ratios are close to unity. Thus, for mass ratios high enough, waveforms without tidal terms actually do better than waveforms with tidal terms tuned to only BNS mergers. As the true mass ratio increases, we are using these two models further and further from their range of validity.

This explanation for the biases is corroborated by the total lack of biases in `LEA+`

(only used for the $q = 3$ analysis), `IMRNSBH`, and `SEOBNSBH`, all of which have tidal terms that have phase and amplitude corrections tuned against NSBH systems. For all of the simulations, we find that `LEA+`, `IMRNSBH`, and `SEOBNSBH` yield the most precise estimates of $\chi_{\rm eff}$. However, more than representing a true feature of these models, this is merely a consequence of their prior support as they do not allow spin in the NS and thus enable a narrower range of spin for the BH. This reduces correlations in the GW phase, and hence yields a better measurement of the only spin parameter.

To summarize, we find that the 90% CIs for $\chi_{\rm eff}$ are typically around ~ 0.16 for the SNR 30 sources (with small variations depending on the mass ratio) and ~ 0.08 for the SNR 70 sources. In fact, the ratio of statistical uncertainties for any given source when measured at SNR 70 and at 30 is close to the ratio of SNRs, as one would expect for loud enough sources for which the Fisher matrix limit is valid [264, 311–313].

Given that the NS spin is expected to be very low, and the mass ratio of these events is far from unity, one might also hope to measure the BH spin instead of only $\chi_{\rm eff}$. In general, we find that `IMRp` and `IMRpT` yield consistently larger uncertainties, followed by spin-aligned waveforms (`SEOBT`,`IMRXHM`,`SEOB`) and by single-spin waveforms (`LEA+`, `IMRNSBH`, and `SEOBNSBH`). As in the case of $\chi_{\rm eff}$, these differences can be explained with the reduced parameter space covered by different models. `IMRp` and `IMRpT` include a prescription for effective spin-orbit precession and cover a higher dimensionality than any other waveforms in our set. Conversely, `LEA+`, `IMRNSBH`, and `SEOBNSBH` only allow the BH to be spinning (with a smaller maximum amplitude), and only along the orbital angular momentum (see Tab. 4.2) while setting the NS spin to be exactly 0.

It is worth stressing that for none of our configurations can we constrain the magnitude of the NS spin (for the waveform models that allow it to vary from 0) to below ~ 0.4 at the 90% CIs. This suggests that even for NSBHs, constraining the NS spin to values consistent with the range of spins of known pulsars will be challenging and require extremely loud sources. We do not expect this conclusion to depend significantly on the fact that our BHs did not have any spin, as Ref. [175] reported similarly poor constraints on the NS spin in $10 - 1.4\ M_\odot$ NSBH with precessing spins, although they worked with inspiral-only waveforms that do not include tides or HOMs.

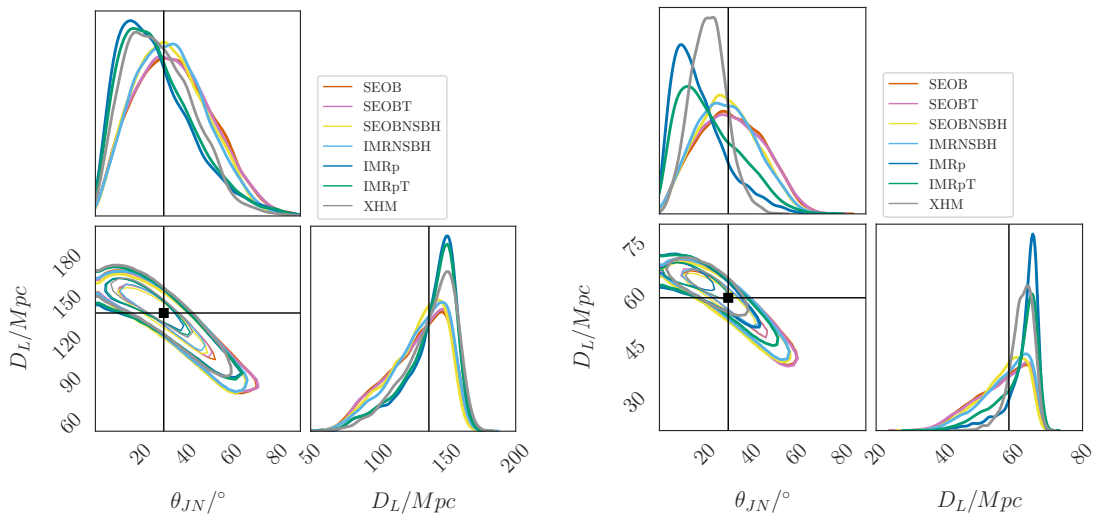

(a) SNR 30. (b) SNR 70.

Figure 4-19: 2D contour plot of posterior distributions for luminosity distance D_L and the inclination angle θ_{JN}, recovered by different approximants for $q = 2$, inclination 30°.

4.4 Extrinsic Parameters

In this section, we focus on the measurements of the inclination angle and the luminosity distance, both of great importance for fully exploiting the scientific potential of NSBHs. At least some of the NSBHs are expected to produce EM radiation as they merge [236–245, 314–317], making an accurate measurement of their luminosity distance crucial for a successful EM follow-up campaign. Furthermore, the potentially small statistical uncertainty in their luminosity distance results allows NSBHs to be valuable standard sirens in measuring the Hubble constant [119]. Measurements of the orbital orientation could be used to distinguish between competing kilonova models [318] and, more generally, to study their detailed emission angular pattern at all wavelengths.

We report the inclination/luminosity distance corner plots for the face-on (i.e., true inclination 30°) systems in Figs. 4-19, 4-21, and 4-23. It is worth underlining a few common features (see the complete set of results in App. C.1). First, the only waveform model with HOMs among those we use, `IMRXHM`, yields smaller statistical errors and offsets relative to the true value. Smaller statistical errors are not unexpected since the true signals *do* have HOMs, which are known to help break the distance-inclination

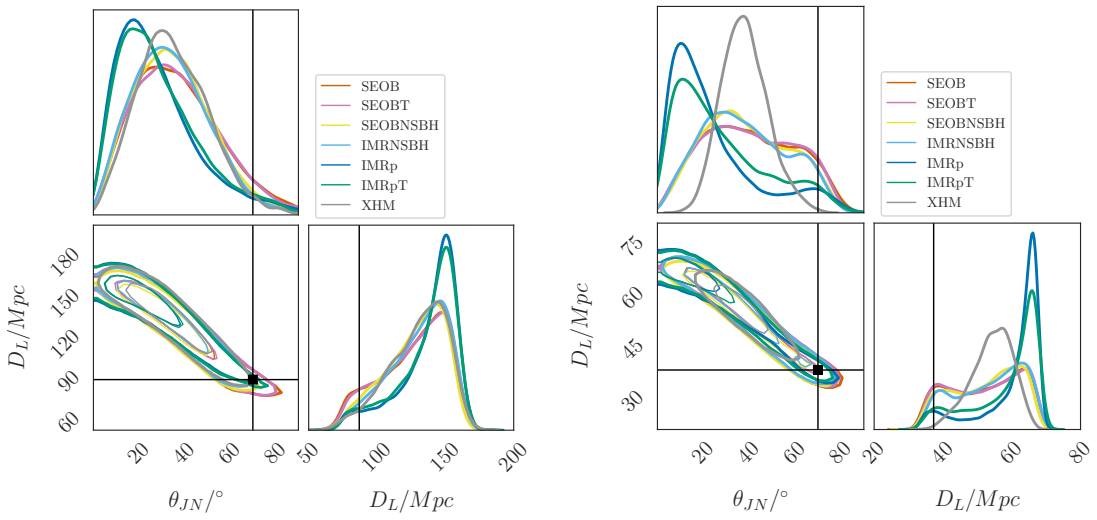

(a) SNR 30. (b) SNR 70.

Figure 4-20: 2D contour plot of posterior distributions for luminosity distance D_L and the inclination angle θ_{JN}, recovered by different approximants for $q = 2$, inclination 70°.

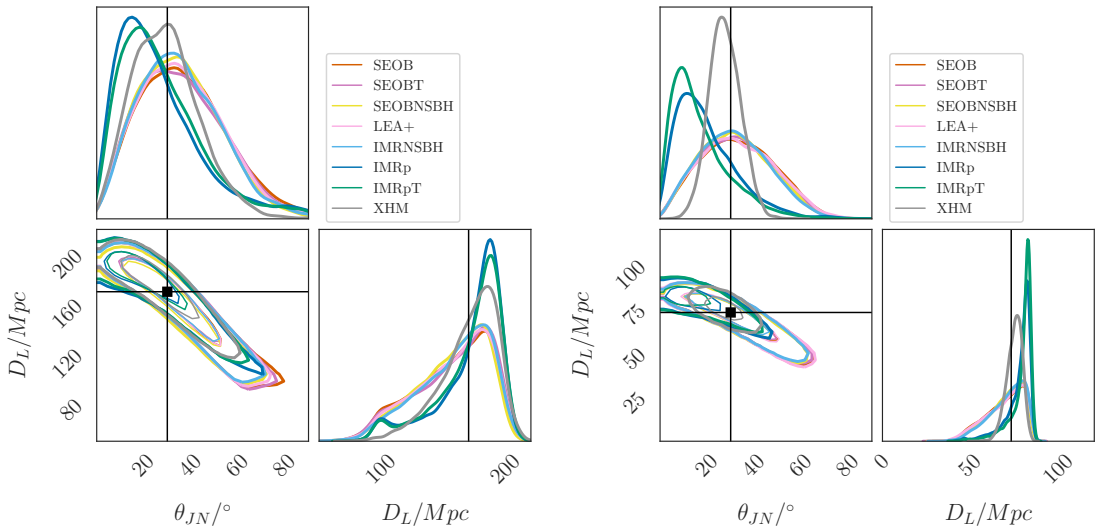

(a) SNR 30. (b) SNR 70.

Figure 4-21: 2D contour plot of posterior distributions for luminosity distance D_L and the inclination angle θ_{JN}, recovered by different approximants for $q = 3$, inclination 30°.

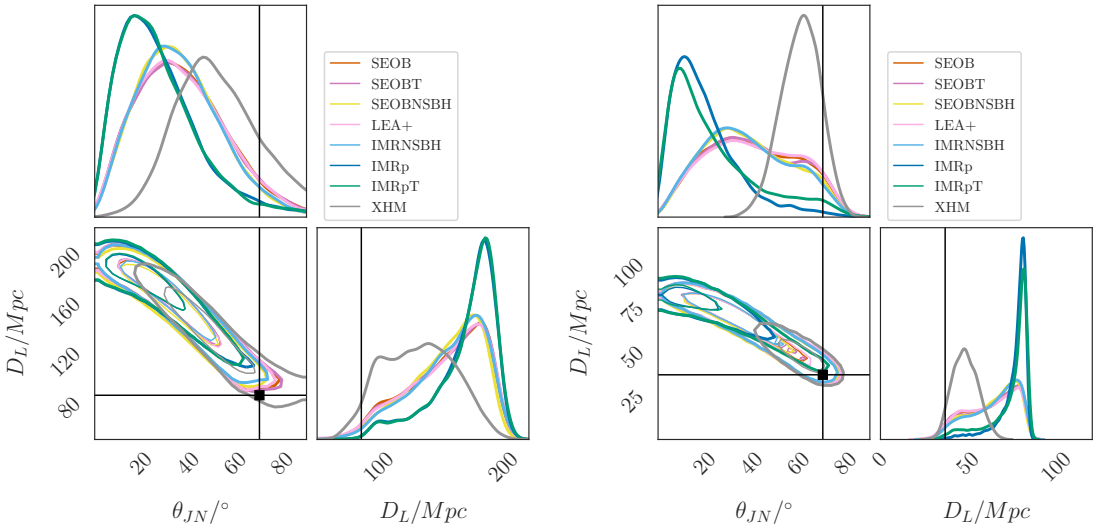

(a) SNR 30. (b) SNR 70.

Figure 4-22: 2D contour plot of posterior distributions for luminosity distance D_L and the inclination angle θ_{JN}, recovered by different approximants for $q = 3$, inclination 70°.

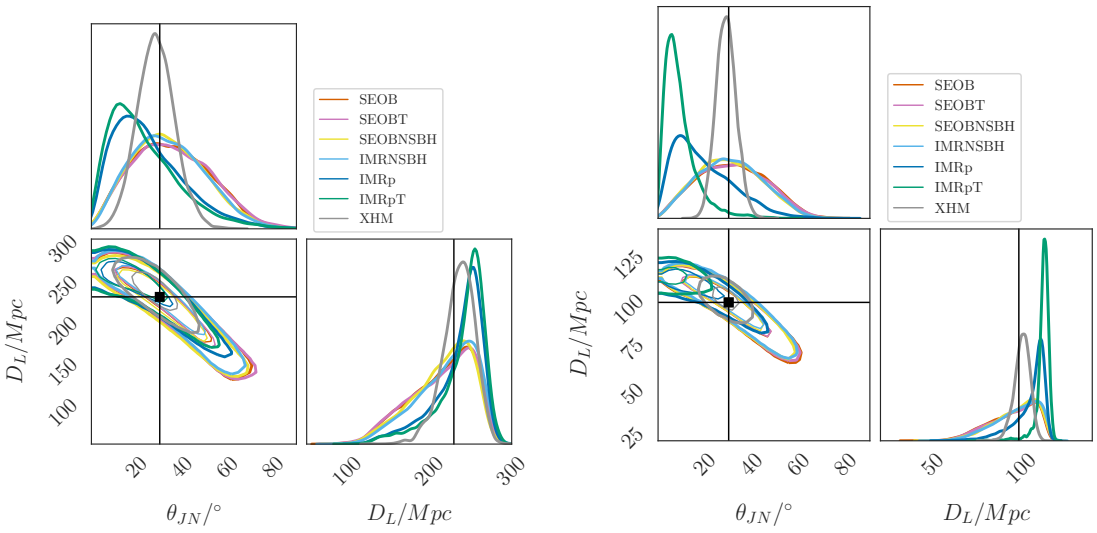

(a) SNR 30. (b) SNR 70.

Figure 4-23: 2D contour plot of posterior distributions for luminosity distance D_L and the inclination angle θ_{JN}, recovered by different approximants for $q = 6$, inclination 30°.

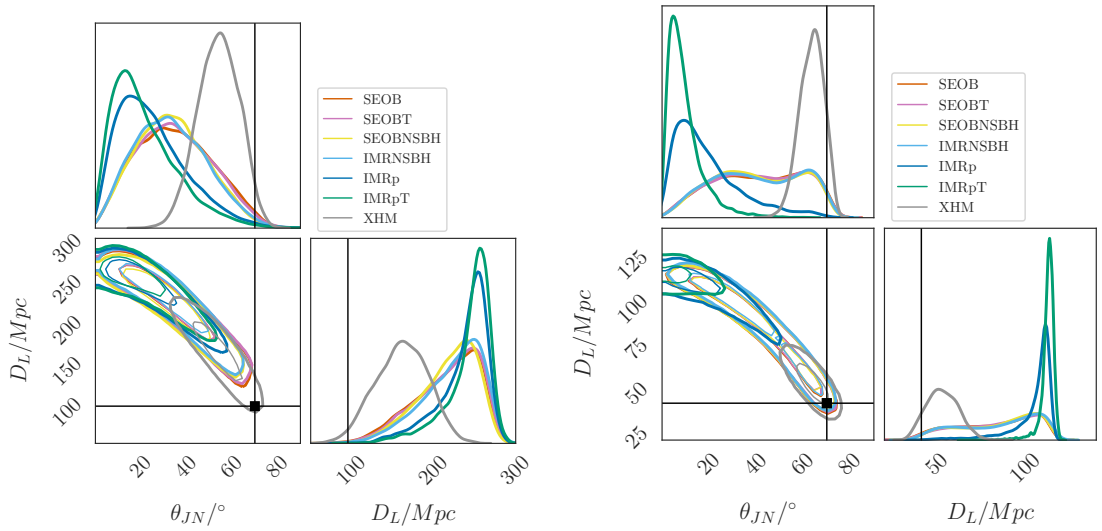

(a) SNR 30. (b) SNR 70.

Figure 4-24: 2D contour plot of posterior distributions for luminosity distance D_L and the inclination angle θ_{JN}, recovered by different approximants for $q = 6$, inclination 70°.

degeneracy [319], hence reducing the statistical uncertainty. One might be surprised that systematic errors are the smallest for `IMRXHM` even when the mass ratios are small, even though it does not allow for tides. This can be explained by the fact that HOMs affect the overall amplitude since they change the angular dependence on the orbital orientation, while tides only affect the late inspiral and mostly the phase of the waveform, thus not as directly related to distance and inclination. This also explains why, while `IMRXHM` performs similarly to other IMR waveforms at small mass ratios for which HOMs are less important, it does significantly better at $q = 6$. For example, at SNR 30 and inclination 30°, the 90% relative uncertainty for the luminosity distance is 45% for all IMR models when $q = 2$, but decreases to 32% only for `IMRXHM` when $q = 6$, while staying above 40% for the other IMR approximants. Biases for the luminosity distance usually lie within the 90% CIs for the recovered posteriors, with typical offsets on the order of $\sim 5 - 15\%$ of the statistical uncertainty for SNR 30. As the SNR increases, the statistical uncertainties shrink, making systematic offsets perceptually more important, though usually still smaller than the corresponding statistical uncertainty. The only exception is the `IMRpT` posterior for $q = 6$, Fig. 4-23b,

which is very narrow and only marginally consistent with the true value. As already discussed above, this approximant yields biases for most parameters at $q = 6$, which is quite far from its intended region of validity.

The situation is quite different when the sources are simulated at an inclination angle of 70°. We find that most waveform families severely overestimate the distance, with the true value barely included in the posterior, Figs. 4-20, 4-22, and 4-24. This results in an orbital orientation measurement closer to face-on/off and, in turn, affects the estimation of the source-frame chirp mass, as seen above. This behavior is not unexpected and can be explained with the strong Bayesian prior in the distance (proportional to D_L^2, and roughly uniform in comoving volume at the relatively small distances in our simulations), as well as the fact that the waveform approximants without HOMs do not strongly depend on the inclination angle. In a Bayesian framework, it is thus often more advantageous to overestimate the distance (which comes with a prior boost) and compensate by measuring an orientation closer to face-on/off. This was explicitly shown for models without HOMs in Ref. [119] (see also Ref. [121]). It is also consistent with the fact that the only model with HOMs in our set, `IMRXHM`, usually recovers a posterior closer to the true value, and more and more so as the mass ratio increases, which enhances the effect of HOMs, as discussed above. For the $q = 3$ and $q = 6$ sources, the `IMRXHM` posterior is clearly separated from all approximants at both SNRs.

Overall, the medians of the results for the high inclination sources are offset from the true value by significant fractions of the statistical uncertainty. The smallest offset we observe is $\sim 40\%$ of the statistical uncertainty for `IMRXHM` when $q = 6$. Typical values are 50% or larger. The relative statistical uncertainties on the distance for the high inclination sources are not significantly smaller than those for the systems closer to face-on. In fact, they can be larger. This is partially an artifact of quoting the 90% CIs relative to the true value: as the inclination increases, the true distance of the source must be decreased to keep the same SNR. Since the absolute uncertainty can increase with the true distance faster than decreasing with the inclination, the relative uncertainties on the inclination can get larger (see Fig. 1 of Ref. [119]).

Furthermore, it is interesting to compare non-HOM models based on the EOB vs. the IMRPhenom formalisms. We see that the results from all models generally peak at similar values, but the EOB-based models usually yield luminosity distance posteriors with a tail toward small distances, more pronounced than those for the IMRPhenom-based models. While we do not have a complete explanation, we note the EOB-based models we are using do not allow for spin-precession, unlike `IMRp` and `IMRpT`. Because spin precession causes amplitude (and phase) modulation that also breaks the distance-inclination degeneracy [232], the precessing models may yield better constraint posteriors because some distance-spin configurations would be excluded when precession is not observed. This interpretation seems to be supported by the behavior of `IMRNSBH`, which is IMRPhenom-based but does not allow for precession. We see, for example in Fig. 4-23a, how its posterior follow closely those of the EOB models rather than those of the other IMRPhenom models.

Overall, our results show that all models broadly agree for the sources with inclinations of 30°. Only with the high-inclination sources do we start seeing significant intra-waveform differences for extrinsic parameters. We see a few instances where two posteriors are nearly disjoint: for $q = 3$ and $q = 6$ at SNR 70, the `IMRXHM` posterior is in strong tension with `IMRp` and even more so with `IMRpT` (the tension with the EOB models is milder since those have longer tails, e.g., Fig. 4-24). The three NSBH-tuned models do not perform better than the other tidal models regarding the measurement of distance and inclination.

4.5 Conclusion

Observations of NSBHs can lead to significant insights into the nature of NSs, for example yielding a precise measurement of their mass and radius or providing information on their formation channels. However, GWs from NSBHs are very challenging to simulate with current NR tools. The presence of matter as well as a singularity at the same time, of HOMs enhanced by the high mass ratio, of potential BH spin precession, and the fact that the late inspiral and merger phases will be in a more

sensitive frequency band of the GW detectors than that for BNSs, make it imperative to verify the role of waveform systematics.

In this chapter, we have created NSBH hybrid waveforms with recent NSBH NR simulations at three mass ratios, $q = 2, 3, 6$. We projected the signal into a three-interferometer network and ran a full PE campaign, using most of the relevant waveform families available in the LIGO Algorithm Library [190], including three that were specially built for NSBH systems. For each mass ratio, we have considered four configurations, where the orbital orientation and the network SNR had all of the pairwise combinations of $\theta_{JN} = 30°, 70°$ and SNR $= 30, 70$. This gave a total of 88 PE runs, making this study one of the most extensive studies of the statistical and systematic uncertainties in analyzing NSBH systems to date.

We found that for signals with an SNR of 30, comparable to the loudest CBC signals detected to date, systematic uncertainties due to waveform modeling are smaller than statistical ones. Some differences are visible, for example, in the NS tidal deformability, $\Lambda_{\rm NS}$, where in some cases, the posterior distributions can cluster in two different groups even at SNR 30. This is more visible for $q = 3$, Fig. 4-9a, than $q = 2$, Fig. 4-7a.

Significant offsets are also found for the source-frame chirp mass, although they are not due to waveform modeling as much as to a failure to correctly measure the source luminosity distance, which is required to convert the detector-frame masses (which are the quantities actually measured from GW data) to the source-frame ones. This is particularly visible for highly inclined sources, Figs. 4-2a, 4-4a and 4-6a. The underlying reason, as discussed in Sec. 4.4, is that the likelihood penalty for measuring an orientation closer to face-on, and hence a larger distance, can be more than compensated for by the fact that the Bayesian prior increases with the distance, unless the true inclination angle is within $\sim 15°$ from 90° [119]. This effect will not be seen for a typical detection, as most sources are expected to be detected at small inclination angles (i.e., close to 0° or 180°) [265]. It is also worth stressing that this offset is smaller for the `IMRXHM` waveform at $q = 6$ since the detectable HOM contribution to the actual signal allows the `IMRXHM` model to break the distance-inclination degeneracy. For the

waveform models tuned against NSBH systems, `IMRNSBH`, `LEA+`, and `SEOBNSBH`, at SNR 30, we obtain 90% statistical CIs on the NS source-frame mass of $\sim 0.2-0.5\ M_{\odot}$. These uncertainties are comparable to those reported for the BNS GW170817 [5]. This comparison is not entirely fair, as both the dimensionality of the models and the priors used are different. The settings of our `IMRpT` analyses are more directly comparable to Ref. [5]: for the $q = 2$ analysis and SNR 30, we find a 90% CI for the NS mass of $0.5\ M_{\odot}$. While this is less constraining than the results from GW170817, it must be remembered that the mass posteriors for GW170817 have a hard prior bound (enforcing $m_1 \leq m_2$, Fig. 5 of Ref. [5]), which helps to explain why those posteriors appear narrower.

The situation is starkly different at SNR 70, with biases comparable to, or larger than, the statistical uncertainties. At $q = 2$, waveform models that do not account for tidal effects yield posterior measurements that do not include the true value in their 90% CIs for the mass ratio, the component masses, and the effective spin. The overall trend is the same with $q = 3$, but the biases are smaller due to the reduced impact of tides on the GW signal. In this case, whether the true value is excluded depends on the exact approximant used. The situation is somewhat reversed at $q = 6$, a configuration for which tidal effects, though formally included in the simulated source, do not play a significant role. Waveform approximants that do not include tides actually perform well, while waveforms with post-inspiral evolution tuned against nearly equal-mass BNS NR simulations, `SEOBT` and `IMRpT`, yield the most severe biases. For those, the recovered masses and spins are systematically offset from the true value and entirely different from those from all the other waveforms, with `IMRpT` yielding a larger bias than `SEOBT`.

We should stress that we are using these two waveform families in a region of mass ratios quite far from their calibrated regions; hence, these biases should not be surprising. However, we report them since they clearly show the importance of using well-calibrated and faithful waveform models for the systems of interest. While we have not done this test in our study, it would be interesting to show if the opposite is true: whether NSBH-tuned waveforms would suffer from similar biases if used to

characterize BNS sources.

Bayes factors between pairs of models can be used to reveal whether, and to what extent, some waveform models are inadequate at matching the data. We reported them for a subset of the approximants we used, Sec. 4.3.2, and show that the BNS-tuned models are clearly disfavored at $q = 6$ even when compared to models that do not include matter effects. These tests could be used to decide which waveform families should be used for specific analysis or to combine samples from different waveforms to marginalize inaccuracies and differences between waveforms [320].

The effective inspiral spin is usually measured accurately and precisely by NSBH-tuned approximants, when applicable, for all configurations. At SNR 70, systematic biases are visible for $q = 3$ from all non-tidal approximants but are more significant for $q = 2$, where they are larger than statistical uncertainties. It is worth stressing that we cannot constrain the NS spin to be smaller than ~ 0.4 (the true value is 0) with any of the approximants, for any of the simulated sources. This suggests that even with loud NSBHs, it might be challenging to set constraints on the NS spin to values comparable to those found in galactic pulsars. This conclusion might need to be checked against NSBH sources in which the BH has a large spin misaligned with the orbital angular momentum, though existing work suggests it might still hold.

Finally, we found biases in measuring the NS tidal deformability, $\Lambda_{\rm NS}$. For the $q = 2$ and $q = 3$ sources, the differences in the posteriors are visible even at SNR 30, though much smaller than the statistical uncertainty (which in itself is very large, more than 100% of the true value). Perhaps the most interesting of the SNR 30 comparisons is the one shown in Fig. 4-9a since it shows tension between two approximants tuned against NSBH NR simulations, `SEOBNSBH` and `IMRNSBH`. While the offsets are still much smaller than the statistical uncertainties at SNR 30, they are worth stressing as one would have expected `IMRNSBH` and `SEOBNSBH` to perform similarly. It is also worth stressing that `LEA+`, which belongs to the EOB-baseline family, agrees with `IMRNSBH`, suggesting the differences we see are not merely due to the underlying difference between EOB or IMRPhenom models but the specific technical details, such as the way each approximant implements tidal terms and the reference point-particle models.

This tension becomes much more visible at SNR 70, Figs. 4-7b, 4-8b, 4-9b and 4-10b, especially for $q = 3$. Again, `LEA+` and `IMRNSBH` roughly agree with each other (and are found to overestimate $\Lambda_{\rm NS}$), while `IMRpT`, `SEOBT`, and `SEOBNSBH` recover different and smaller values of $\Lambda_{\rm NS}$. Since measuring $\Lambda_{\rm NS}$ away from 0 is perhaps the best way of showing that the secondary object is not a BH when no EM counterpart is detected, these differences are particularly interesting. `IMRNSBH`, together with `LEA+` when it is valid, would exclude $\Lambda_{\rm NS} = 0$ for nearly all of the $q = 2$ and $q = 3$ simulations, whereas `SEOBNSBH`, `IMRpT`, and `SEOBT` would have stronger support for $\Lambda_{\rm NS} = 0$. This said, none of the models exclude the true value of $\Lambda_{\rm NS}$: for $q = 2$, we find a general tendency to underestimate the tidal deformability, while for $q = 3$, some approximants overestimate and others underestimate it, with the true value found roughly in the middle, e.g., Fig. 4-10b. The most stringent constraints are found for the $q = 2$ sources at SNR 70, with a 90% CI of $500 - 600$. For the SNR 30 sources, only an upper bound can be placed.

For $q = 6$, the simulated signals do not carry information about tides. We indeed find that nearly all families return a posterior on $\Lambda_{\rm NS}$ that is very similar to the prior at SNR 30 and only exclude extremely large values at SNR 70, Figs. 4-11b and 4-12b. `IMRpT` differs significantly from the other approximants and recovers a $\Lambda_{\rm NS}$ posterior that peaks at small values. As discussed above, the reason is that `IMRpT` is used far from its calibrated range since it is tuned for BNS systems.

The mass and $\Lambda_{\rm NS}$ posteriors can be converted, using phenomenological fits, to a measurement for the NS radius, $r_{\rm NS}$, with the approach described in Sec. C.2. We find that, at SNRs of 30, all approximants yield comparable constraints on the radius, with 90% CIs of 5 km or larger (which is larger than what was inferred for GW170817 [5]). Interestingly, even for sources where some discrepancy in $\Lambda_{\rm NS}$ is visible, the posteriors on the radius show a smaller spread. This shows that most of the information comes from the measurement of the NS mass, with $\Lambda_{\rm NS}$ contributing less to the inference of $r_{\rm NS}$.

Overall, we find that while the three waveform approximants that have been specifically tuned with NSBH NR simulations agree well with each other for most

parameters, they already show differences at an SNR of 30 when measuring the NS tidal parameters. These differences are usually smaller or at most comparable to the 1-σ statistical uncertainty even at an SNR of 70, and thus *might* not be problematic for most of the potential NSBH sources in the next few years. However, the residual differences between these approximants that are nominally on equal footing might cause issues for tests of GR using GWs from NSBHs. Moreover, when we reach the next-generation detector era [321] where typical SNRs will be ten times higher, these differences will pose more serious challenges. At such high SNRs, we will be able to distinguish NSBHs with mass ratios considered in this chapter from BBHs or BNSs at a waveform level (see Fig. 2 of Ref. [270]), making waveforms calibrated to NR simulations crucial for accurate characterization of the system's source properties.

To address these limitations, a more extensive set of NR simulations that covers a wider range of the parameter space is necessary. This will require further development of the NR simulation codes [322, 323] to balance the computational efficiency with the required resolution to incorporate all significant physical effects [321, 324, 325].

Furthermore, the simulated signals used in this study do not have spin, presenting a favorable but still possibly realistic scenario given that most of the BHs detected to date are consistent with not having spins. If the actual signal came from an NSBH with a large precessing BH spin, it is likely that even the two NSBH-tuned models in this study may produce biased PE results.

Chapter 5

Calibration Errors

The Hubble constant, H_0, is the current expansion rate of the Universe and serves an important role in our understanding of cosmic expansion history. However, there is currently a beyond 4-σ tension between the measurements of the early and the late Universe. Planck satellite's observations of the cosmic microwave background anisotropies, assuming the standard flat cosmological model, lead to an inferred late-Universe measurement of $H_0 = 67.36 \pm 0.54$ km s^{-1}Mpc^{-1} [326, 327]. Direct measurements in the local universe lead to a different result: the SH0ES team measured $H_0 = 73.30 \pm 1.04$ km s^{-1}Mpc^{-1} using the Cepheid-supernova distance ladder [328–330], which is consistent with the results from H0LiCOW using lensed quasars [331, 332], from the Carnegie-Chicago Hubble program using the Tip of the Red Giant Branch method to calibrate the distances [333–335], and from the Hubble Space Telescope photometry and Gaia parallaxes [336].

CBCs that emit both EM radiation and substantial GWs provide an independent method to measure H_0, and have the potential to resolve the above-mentioned tension [337–345]. Combining the luminosity distance D_L measurement from the GW observations and the Hubble flow velocity v_H from the EM observations leads to a direct estimation of H_0, a method often referred to as a standard siren or "bright siren" measurement. Since EM-bright GW sources detected by the second-generation GW detectors will be relatively local, we can use bright sirens to constrain only H_0. Other cosmological parameters can be measured with methods that rely on the NS

EoS [346–348], dark sirens [337, 344, 349–351], features in the mass distribution of BNSs and BBHs [352–355], or the spatial clustering scale of GW sources with known galaxies [356, 357].

The observations of GW170817 [358–360], the kilonova AT2017gfo and the gamma-ray burst GRB170817A served as the first demonstration of the bright siren approach, leading to a measurement of $H_0 = 70.0^{+12.0}_{-8.0}$ km s^{-1}Mpc^{-1} [361–365]. This method can be very powerful as we observe more such events. Ref. [341] presented a 5% precision in the H_0 measurement after 15 BNSs with EM counterparts and 1% with 30 such sources.

However, GW observations may suffer from underlying systematic biases in their estimate of D_L, and one needs to understand these biases before interpreting the resulting H_0 measurements. One such bias is the systematic error in the production and calibration of the detectors' primary data stream [366–368], referred to as calibration errors (CEs). Such errors are uncorrelated with the astrophysical event rate, evolve independently in each detector, and may be present in one or more detectors during several astrophysical events. CEs may bias the amplitude of the strain data in the same way over multiple observations, and lead to a biased inference of H_0.

Previous studies have estimated the impact of typical values of CEs on individual events observed during the first and second observing runs of LIGO-Virgo [369–371], or attempted to refine the estimates of CEs using detected [372] or expected astrophysical signals [373]. Our study instead uses large CEs experienced during atypical times in the LIGO-Virgo's O3 to probe their worst-case impact on astrophysical PE for both the single-event characterization and the joint inference of H_0.

More specifically, we simulate a collection of BNS detections and introduce into the GW data stream of each signal artificial CEs that follow the six cases of particularly large CEs from the Advanced LIGO detectors at Hanford (LHO) or Livingston (LLO) during O3 [367, 368]. We pick the instantiation that leads to the worst bias in the astrophysical measurements of D_L, apply it to varying fractions of one hundred simulated BNSs, and infer H_0 to explore the progressive impact of large CEs. In Sec. 5.2, we will discuss the method we use to produce the miscalibrated data stream

and to perform PE. In Sec. 5.3, we report how CEs impact the D_L results for individual events, as well as the H_0 results when we combine multiple sources.

5.1 Calibration

For each detector at any given time, the conversion from its voltage signal $\boldsymbol{e}_{\rm IFO}$ to its data stream $\boldsymbol{d}_{\rm IFO}$ is made by a complex-valued, frequency-dependent response function, $R(f;t)$,

$$\boldsymbol{d}_{\rm IFO} = R_{\rm IFO}(f;t)\ \boldsymbol{e}_{\rm IFO}{}^{1}, \tag{5.1}$$

where f is frequency and t is time. The model of the response function, $R_{\rm model,IFO}(f;t)$, is constructed from the expected behavior of the detectors, coupled with supporting measurements of the model parameters as described in Ref. [374, 375]. Imperfections in $R_{\rm model,IFO}(f;t)$, and thus in $\boldsymbol{d}_{\rm IFO}$, are referred to as calibration errors, or CEs [366–368]. The errors may be represented by the ratio of the actual, "true", response function, $R_{\rm true,IFO}(f;t)$, and the model, $R_{\rm model,IFO}(f;t)$, by [2]

$$\eta_{\rm IFO}(f;t) = R_{\rm true,IFO}(f;t)/R_{\rm model,IFO}(f;t). \tag{5.2}$$

In the ideal case, $R_{\rm model,IFO}(f;t)$ will be identical to $R_{\rm true,IFO}(f;t)$, and $\eta_{\rm IFO}(f;t)$ becomes a frequency-independent constant with unity magnitude and zero phases. In reality, $\eta_{\rm IFO}(f;t)$ is usually a function of frequency and time. Since $R_{\rm model,IFO}(f;t)$, $R_{\rm true,IFO}(f;t)$, and $\eta_{\rm IFO}(f;t)$ always depend on f and t in our case and evolve independently in every detector, we will drop the $(f;t)$ arguments and the IFO subscript henceforth unless we need to specify f, t, or IFO.

While $R_{\rm model}$ is known, $R_{\rm true}$ may only be inferred by direct measurements that are invasive for observations and would reduce the duty cycle of the detector. Instead, at any given reference time T_0, the parameters of $R_{\rm true}$ are numerically estimated to create 10^4 samples of the probability distribution of $\{\eta(T_0)\}$, with relatively large

[1] $\boldsymbol{d}_{\rm IFO}$ and $\boldsymbol{e}_{\rm IFO}$ are implicit functions of f and t.
[2] $\eta_{\rm IFO}(f;t)$ is referred to as $\eta_R(f;t)$ in Ref. [367, 368].

uncertainties. Later, additional measurements and models are crafted to better inform or correct the estimated $\{\eta(T_0)\}$ in retrospect.

5.2 Method

We summarize how we simulate the data stream in Sec. 5.2.1, how we define CEs and artificially add them to the data stream in Sec. 5.2.2, and how we perform PE and infer H_0 in Sec. 5.2.3.

5.2.1 Simulations

We simulate five thousand BNSs with uniform-in-cosine inclinations and uniformly distributed sky locations. Each event is assigned a D_L randomly drawn from a uniform-in-comoving-volume distribution, with the maximum D_L set at 600 Mpc, larger than the horizon[3] of the LIGO-Virgo network at the design sensitivity [358, 359]. We randomly draw one hundred events with optimal network SNRs above 12 to form our set of EM-bright GW events.

We simulate non-spinning BNSs with component masses $m_1 = 2M_\odot$ and $m_2 = 1.5M_\odot$, with the phenomenological waveform model `IMRPhenomPv2` [101, 111, 194, 195], which does not model NS matter effects. We use the same waveform model during PE to avoid any systematics caused by waveform mismatch[4]. We assume an EM counterpart yielded an exact redshift measurement for each event. Since the uncertainties on the sky localization from the EM measurements are much smaller than the typical uncertainties on the GW measurement, we assume the sky positions of the sources are exactly known from the EM observations prior to the GW analysis. We also disregard effects from the peculiar velocity of the sources, as most of the events considered here are close to the horizon of GW detections.

We produce Gaussian noise $\mathbf{n}$ colored by the LIGO-Virgo design sensitivities [359], then project the signal, which is the sum of the modeled waveforms and the noise, to

[3]For events with an optimal network SNR of 12.

[4]Previous papers have looked into waveform systematics for BNSs, for example, Ref. [324, 376, 377].

each detector in the network to obtain the data stream.

5.2.2 Systematic Calibration Errors

In O3, the probability distribution of η for each detector was estimated at discrete times $\{T\}$ with hourly cadence when the detector was stable in the observing mode. The estimated $\{\eta\}$ may vary slowly in time, either continuously with drifts in the detector's alignment or thermal state, or discretely with changes made in the detector's control system between different configuration periods. In most cases, the slow time-dependent variation is appropriately tracked and accounted for when producing $\boldsymbol{e}_{\mathrm{IFO}}$. The time variation of $\{\eta\}$ is thus negligible for the majority of the observing time as long as the detector's sensing and control configurations remain unchanged. Over each observing period with static configurations, we can choose an arbitrary time T_k, and uses $\{\eta(T_k)\}$ to represent the typical CE distribution of this period, referred to as $\{\eta^{\mathrm{typ}}(T_k)\}$.

However, the detectors' sensing and control configurations do not remain static for the entire observing run. There may be planned changes typically to improve the detector sensitivity, or unplanned changes due to issues with the hardware, electronics, or computers. Such changes get fixed in a temporary fashion such that the observation may resume with an acceptable error, but may not be fully investigated or resolved until later. The entire detector's response, R_{true}, is checked weekly and monitored continuously at a few select frequencies, to ensure coverage of any unexpected situations. When issues are found in the detector behavior, additional measurements may also be made to model and include the CE in $\{\eta\}$ retroactively. If at a time t_i, $\{\eta(t_i)\}$ is significantly different from the typical behavior of the time period $\{\eta^{\mathrm{typ}}(T_i)\}$, henceforth $\{\eta^{\mathrm{typ}}\}_i$, measured at a nearby time T_i, we refer to these outliers as $\{\eta^{\mathrm{out}}(t_i)\}$, henceforth $\{\eta^{\mathrm{out}}\}_i$. During O3, six such outliers have been identified in either LLO or LHO.

For example, in Fig. 5-1, we compare the median and 1-σ boundaries of the magnitude and phase of $\{\eta^{\mathrm{out}}\}_{6,\mathrm{LLO}}$ against its corresponding $\{\eta^{\mathrm{typ}}\}_{6,\mathrm{LLO}}$. We include plots for the distributions of $\{\eta^{\mathrm{out}}\}_i$ and $\{\eta^{\mathrm{typ}}\}_i$ for $i = 1...5$ in App. D.1. In reality, if there happens to be an astrophysical signal at a time similar to one of the t_i, the

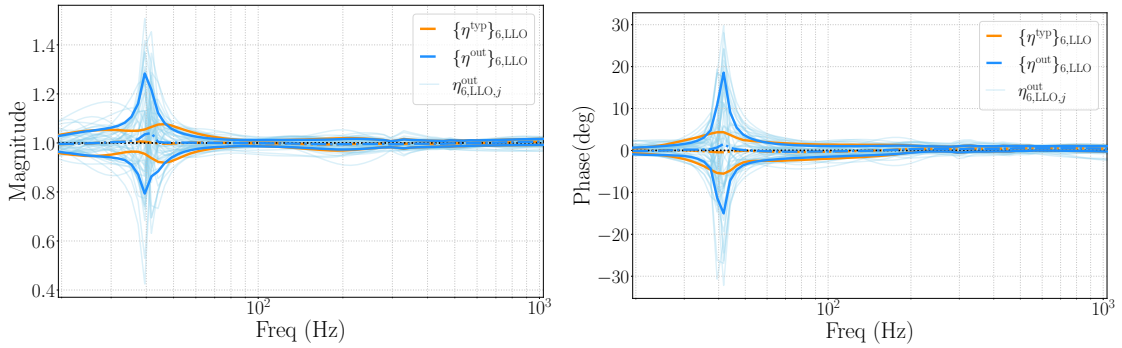

Figure 5-1: The median (dash-dotted) and the 1-σ bounds (solid, thick) of one example of a large CE, $\{\eta^{\rm out}\}_{6,\rm LLO}$ from O3, in magnitude (left) and phase (right) as a function of frequency. The thin light blue curves represent some of the individual realizations, $\eta^{\rm out}_{6,\rm LLO,j}$ during this time. The orange curves are the corresponding typical distribution $\{\eta^{\rm typ}\}_{6,\rm LLO}$.

$\{\eta^{\rm out}\}_i$ may not be readily available at the time of the PE analyses, so $\{\eta^{\rm typ}\}_i$ will be used instead. This is the scenario we investigate in this study: when the actual CEs are very different from the CEs known and used at the time of PE.

We introduce artificial CEs to the data streams $\boldsymbol{d}_{\rm LLO}$ and $\boldsymbol{d}_{\rm LHO}$. For all six cases, $\{\eta^{\rm out}\}_i$ is applied to only *one* of the Advanced LIGO detectors. We first select the worst realization from each $\{\eta^{\rm out}\}_i$, denoted by $\eta_i^{\rm mis}$, to maximize its impact on the amplitude of the data, and hence on the estimation of D_L. We define the impact, weighted by the detector sensitivity and integrated over the bandwidth:

$$\mathcal{D}_{i,j} \equiv \int_{f_{\rm low}}^{f_{\rm high}} \frac{|\eta_{i,j}| - \widetilde{|\eta_i^{\rm typ}|}}{\sqrt{S_n(f)}} {\rm d}f, \tag{5.3}$$

where j indexes the individual curves from each $\{\eta^{\rm out}\}_i$ distribution. At each frequency, we take the difference between the magnitude of the $j^{\rm th}$ sample, $|\eta_{i,j}|$, and $\widetilde{|\eta_i^{\rm typ}|}$, the median of the magnitudes of samples in $\{\eta^{\rm typ}\}_i$ (the dot-dashed orange curve in Fig. 5-1). $\sqrt{S_n(f)}$ is the detector's amplitude spectral density, for which we use the design sensitivity of the Advanced LIGO [358, 359]. The frequency limits of the integral, $f_{\rm low}$ and $f_{\rm high}$, have been chosen as 20 Hz and 1024 Hz, respectively, with a frequency resolution of 0.25 Hz. We select the curve that maximizes $\mathcal{D}_{i,j}$ in the

negative direction[5], denoted by $\eta_i^{\rm mis}$,

$$\eta_i^{\rm mis} \equiv \min_j \mathcal{D}_{i,j}. \tag{5.4}$$

Fig. 5-2 shows the amplitude and phase of the selected $\eta_{6,\rm LLO}^{\rm mis}$ compared with $\{\eta^{\rm typ}\}_{6,\rm LLO}$ from Fig. 5-1. We apply $\eta_{6,\rm LLO}^{\rm mis}$ to miscalibrate the LLO data, the sum of the noise and the modeled waveform, as,

$$\boldsymbol{d}_i^{\rm mis} = \eta_i^{\rm mis}\ \boldsymbol{d}. \tag{5.5}$$

The noise, as part of $\boldsymbol{d}$, will thus also be scaled by $\eta_i^{\rm mis}$. Each detector's resulting amplitude spectral density is $\eta_i^{\rm mis}\sqrt{S_n(f)}$.

For the other Advanced LIGO detector, in this case, LHO, we will select a curve $\eta_{6,\rm LHO}^{\rm mis}$ that lies within the 1-σ CI of $\{\eta^{\rm typ}\}_{6,\rm LHO}$ to miscalibrate the data, in the same way as Eq. (5.5). No CEs are added to the Advanced Virgo data since the full η distributions of Advanced Virgo are not available at the time of writing. In this case, $\{\eta_{6,\rm LLO}^{\rm mis}, \eta_{6,\rm LHO}^{\rm mis}, 1\}$ forms the sixth set of curves to miscalibrate the data, $\eta_6^{\rm mis}$.

We also prepare a separate set of *control runs* in which we do not add *any* CE in any of the detectors. When comparing the PE results of the miscalibrated and control runs, we can observe the biases caused exclusively by the large added CEs in the former.

Next, we select one CE realization that leads to the most significant bias in the D_L likelihood, and apply it to one hundred segments of data, each containing a different BNS event, as described in Sec. 5.2.1. To select the desired CE realization, we first consider a single BNS event with an optimal network SNR of 50, an inclination of 30°, and a sky location right above LLO. We add each of the six distinctive sets of CEs to a data chunk containing this BNS and compare the resulting D_L likelihoods. As we only consider single-event results in this part of the study, we need to eliminate the random effects of noise realizations. We work with the zero-noise realization [264]

[5]We also performed the full PE analysis with the curve that maximizes $\mathcal{D}_{i,j}$ in the positive direction, but observed smaller biases in the PE results.

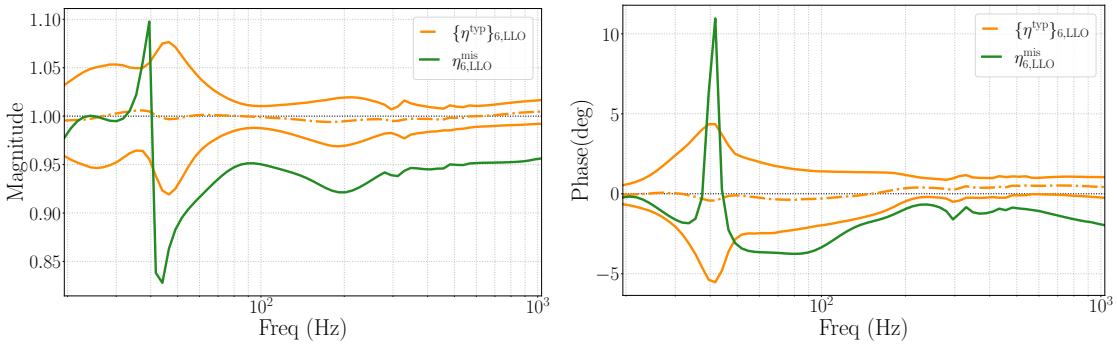

Figure 5-2: $\eta^{\rm mis}_{6,\rm LLO}$ (green) shown in magnitude and phase (deg) as a function of frequency (Hz). Also plotted are the 1-σ bounds and the median of typical CE distributions, $\{\eta^{\rm typ}\}_{6,\rm LLO}$ (orange).

where the noise $\mathbf{n}$ has a mean of $\mathbf{0}$ and standard deviation equal to the detector's power spectral density. Lastly, we infer H_0 from the one hundred events.

5.2.3 Parameter Estimation and Inference of H_0

We perform Bayesian inference [82, 378] to obtain the likelihood $\mathcal{L}(\boldsymbol{d}|\boldsymbol{\theta}, H_0, \mathcal{H})$, as described in Sec. 1.3. We write H_0 explicitly here because it is the hyper-parameter that we are interested in. We can obtain the likelihood $\mathcal{L}(\boldsymbol{d}|H_0, \mathcal{H})$ by integrating over all astrophysical parameters,

$$\mathcal{L}(\boldsymbol{d}|H_0, \mathcal{H}) = \int \mathrm{d}\boldsymbol{\theta} \mathcal{L}(\boldsymbol{d}|\boldsymbol{\theta}, H_0, \mathcal{H}) \pi(\boldsymbol{\theta}|H_0, \mathcal{H}), \tag{5.6}$$

where $\pi(\boldsymbol{\theta}|H_0, \mathcal{H})$ is the prior. Since not all events have equal chances of detection, we follow Ref. [342, 379] to account for the selection effect and refer to the function of detectable sources as $\beta(H_0)$. Since all sources in our simulations have the same source-frame masses, the selection function only needs to be calculated once.

We can obtain the posterior for H_0 by applying a uniform prior of $\pi(H_0|\mathcal{H}) = [20, 150]$ km s^{-1}Mpc^{-1},

$$p(H_0|\boldsymbol{d}, \mathcal{H}) = \frac{\pi(H_0|\mathcal{H}) \mathcal{L}(\boldsymbol{d}|H_0, \mathcal{H})}{\beta(H_0)}. \tag{5.7}$$

As all of the one hundred BNSs are independent, their joint likelihood can be calculated

by simply multiplying the likelihoods of each event [380],

$$\mathcal{L}(\boldsymbol{d}|H_0,\mathcal{H}) = \prod_{i=1}^{100}\mathcal{L}_i(\boldsymbol{d}|H_0,\mathcal{H}). \tag{5.8}$$

One caveat is that our PE analysis adopts a standard, uniform-in-individual-masses prior with additional bounds on the chirp mass $\mathcal{M}$, as defined in Eq. (1.2), and the mass ratio, while our simulated events all have the same masses and the function of event detectability in Eq. (5.7) is calculated assuming so. This may introduce a small bias, but it will be present for both the miscalibrated and control runs, thus not affecting their differential behaviors.

We can marginalize CEs during PE through two approaches: the Spline interpolation method [381] and the physiCal method [370, 371]. Both methods treat the CEs as independent in each detector. The Spline method models η by fitting a cubic spline polynomial at a small number of logarithmically-spaced frequencies $\{f_m\}$. At each frequency, the prior on the magnitude and phase is a Gaussian distribution with the same mean and standard deviation as those of $\{\eta^{\rm typ}(f_m)\}$. The recently developed physiCal method [370, 371] is more computationally efficient and physically motivated and estimates the physical parameters in the models for η along with $\boldsymbol{\theta}$ during PE. PhysiCal directly draws samples from $\{\eta^{\rm typ}\}$ to form the prior.

In all PE analyses to date, known CEs are marginalized. In this study, we are interested in the scenarios where large calibration errors $\eta_i^{\rm mis}$ are *not* fully captured and marginalized in PE. We assume we do not know the actual error distribution $\{\eta^{\rm out}\}_i$, but only have and use $\{\eta^{\rm typ}\}_i$ as the prior. Similarly, we utilize the medians and 1-σ bounds of $\{\eta^{\rm typ}\}_i$ as the prior for the Spline method. As mentioned in Sec. 5.2.2, since the full $\{\eta\}$ distributions of Advanced Virgo are unavailable at the time of writing, we only adopt the Spline method to marginalize CEs in Advanced Virgo.

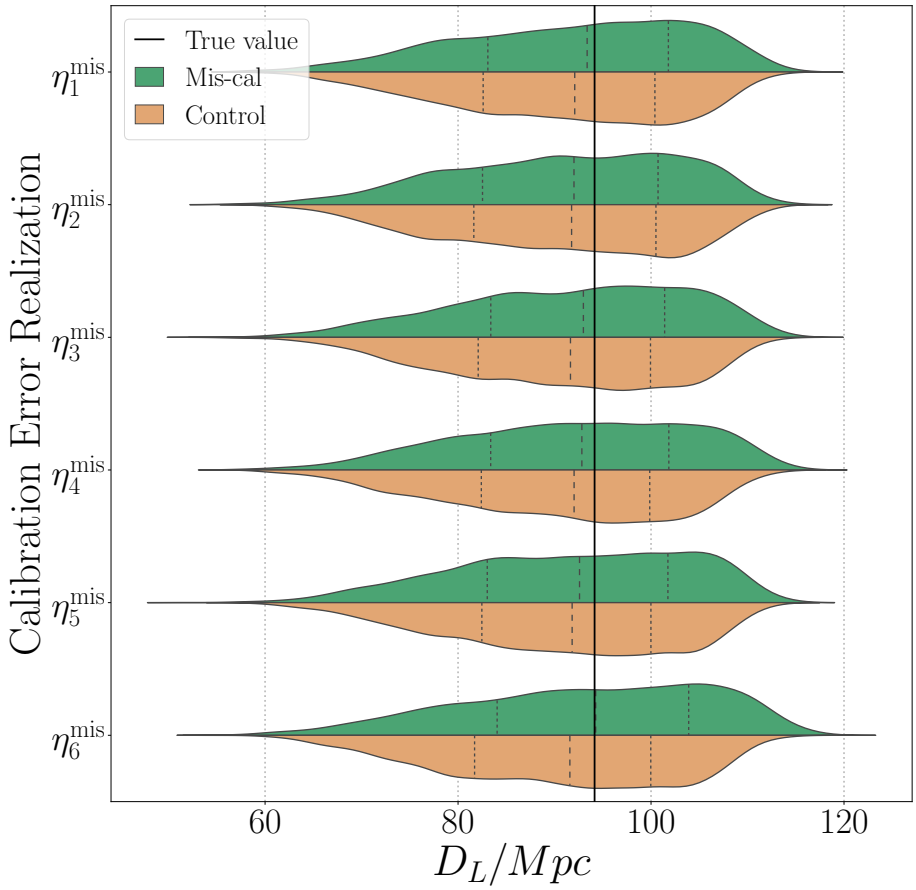

Figure 5-3: D_L likelihood for the six scenarios, miscalibrated (green) vs. control (orange) runs, the vertical dashed lines mark the 25%, 50%, and 75% percentiles.

5.3 Results

First, we present the D_L likelihoods when we apply the six sets of η^{mis} (selected using the method described in Sec. 5.2.2) to a single BNS event with an optimal network SNR of 50. The likelihoods for the miscalibrated runs are plotted as green kernel density plots in Fig. 5-3, and the results for the corresponding control run are plotted in orange. We report the normalized difference $\Delta D_L = (D_{L,\mathrm{med}} - D_{L,\mathrm{true}})/D_{L,\mathrm{true}}$, between the true value $D_{L,\mathrm{true}}$ and the median of the recovered likelihoods, $D_{L,\mathrm{med}}$, in Tab. 5.1.

The results from using the physiCal and Spline methods agree very well. Thus, we only show the results from the physiCal methods in Fig. 5-3 and Tab. 5.1, and the ones from the Spline method in App. D.2.

CE Realization	Mis-calibrated	Control
$\eta_1^{\rm mis}$	-1.0%	-2.5%
$\eta_2^{\rm mis}$	-2.3%	-2.3%
$\eta_3^{\rm mis}$	-1.2%	-2.1%
$\eta_4^{\rm mis}$	-0.9%	-2.3%
$\eta_5^{\rm mis}$	-1.5%	-2.5%
$\eta_6^{\rm mis}$	0.5%	-2.6%

Table 5.1: ΔD_L in the likelihoods for the physiCal runs with and without large CEs.

Compared with the control runs, where the offsets are between -2.1% to -2.6%, $\eta_6^{\rm mis}$ leads to the most significant differences in the D_L likelihoods. We note the control runs all show a negative ΔD_L due to the well-known correlation between D_L and inclination [119]. Since all sources in Fig. 5-3 have an inclination θ_{JN} of 30°, but the inclination prior follows $\sin\theta_{JN}$, we expect an offset towards larger inclination values, where the prior is larger, and thus smaller D_L.

Next, we apply $\eta_6^{\rm mis}$ to the data of one hundred BNSs. This offset will *no longer* be present in the analysis since the inclinations are drawn from a uniform-in-cosine distribution (effectively $\sin\theta_{JN}{\rm d}\theta_{JN}$), the same as the prior.

In Fig. 5-4, we vary the fraction of the miscalibrated BNSs and show the posterior distributions of the dimensionless h_0, defined as $H_0 = h_0 100$ km s^{-1}Mpc^{-1}. We apply $\eta_6^{\rm mis}$ to $x\%$ of the BNSs, while the other events do not suffer from any miscalibration. The joint h_0 posterior shifts towards smaller values as the miscalibrated fraction increases. The posterior excludes the true value of $h_0 = 0.679$ from the 90% CI when the data of more than 50% BNSs are miscalibrated.

Additionally, we vary the total number of detected events. We randomly draw n detections without repetition for $\lfloor 100/n \rfloor$ trials (i.e. rounding down $100/n$ to an integer), and randomly miscalibrate $x\%$ of the events in each trial. We calculate the median and the bounds of the 90% CI for each trial. In Fig. 5-5, for each pair of

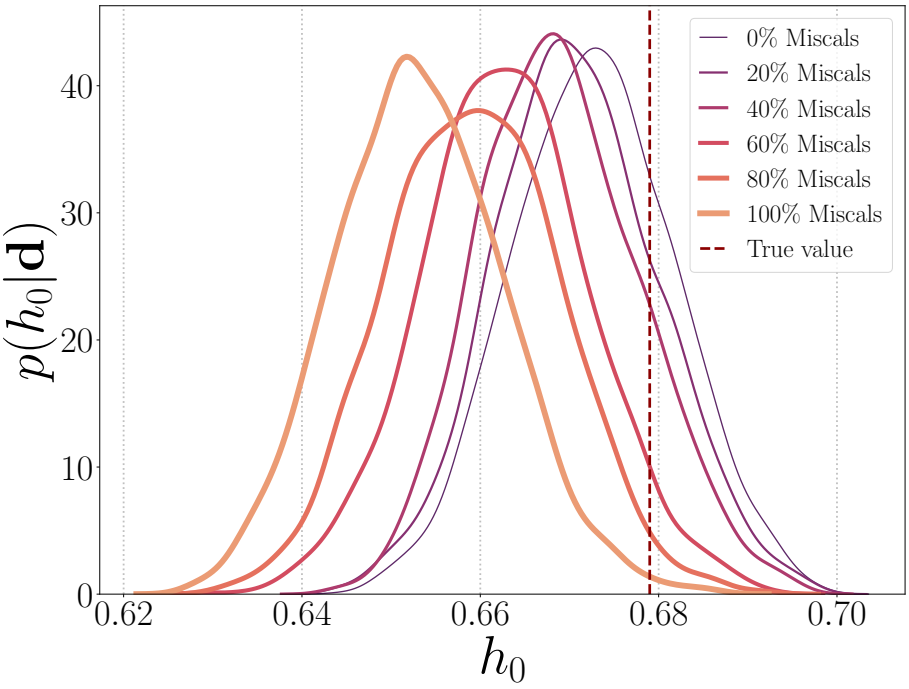

Figure 5-4: h_0 posteriors for different fractions of miscalibration. Thicker curves indicate results with more BNS events miscalibrated.

$\{n, x\}$, the green points are medians of the $\lfloor 100/n \rfloor$ medians from all the trials, and the error bars are the medians of the 90% CI bounds from all the trials. The orange points and error bars indicate the results of the control runs[6]. We overlay the latest results from SH0ES (2022) [330] in blue and from Planck (2018) [327] in purple, for their $1-\sigma$ (darker bar) and $2-\sigma$ ranges. Note that the "true" value of h_0 for the simulated events in this chapter is chosen to be 0.679, thus consistent with the Planck results. When 100% of the events are miscalibrated, our h_0 results are still consistent with the Hubble measurements from Planck.

With 100% of the detected events miscalibrated, the joint h_0 posterior excludes the true value from its 90% CI after 50 detections or more. With 50% or a smaller fraction of the events miscalibrated, the posterior includes the true h_0 even after one hundred detections. In Fig. 5-5, the rightmost set of points in each subplot represents

[6]The medians of the control runs for under 30 events jump above and below the true value. As we increase n, there are fewer trials, and our results show more dependence on specific noise realizations. In this case of noise realization, the median falls below the true value. If we apply different noise realizations, the results will jump around the true value like the trials with fewer events.

the same scenario as Fig. 5-4.

5.4 Conclusion

GW observations of EM-bright CBCs provide an independent way to measure the Hubble constant and potentially break the existing tension between the early and late universe H_0 measurements. As we observe more such events, the resulting H_0 posterior will be increasingly constraining, making it essential to thoroughly control and understand potential systematic biases.

In this study, we applied large CEs to the GW data stream and investigated their effects on the inference of H_0. Our analysis was constructed not to contain any systematic errors or statistical uncertainties from the EM observations like peculiar velocities [382, 383] or viewing angles [384], or from the waveform systematics.

We found that the H_0 posterior does not exclude the true value from its 90% CI, corresponding to a 2–3% systematic error, *unless* we are inferring H_0 with more than 50 BNS detections that all suffer from the same significant CEs. When 50% or a smaller fraction of the BNSs are miscalibrated, the true value is not excluded even after one hundred BNS detections. For comparison, systematic errors due to the EM observation side, for example, kilonova viewing angles, will be 2% after 50 BNS detections [384].

All of the outliers $\{\eta^{\rm out}\}_i$ that motivated our study are based on the estimated CE around times of real physical changes or malfunctions of the detectors during O3. These events are generally rare and relatively short-lived; typically $< 1\%$ of the time over any few-month observing period – the typical duration of stable detector configurations during an observing run [367, 368]. In our analysis, we assume we only know and use $\{\eta^{\rm typ}\}_i$ to marginalize CEs during PE, whereas $\{\eta^{\rm out}\}_i$ is assumed to be unknown and uncharacterized although coinciding with some fraction of the detected BNS events. Given the current estimate of astrophysical event rate, 320^{+490}_{-240} Gpc^{3}yr^{-1} [385], there is a very low probability that a large CE remains uncharacterized over a period of stable configurations during which dozens of BNSs may be detected.

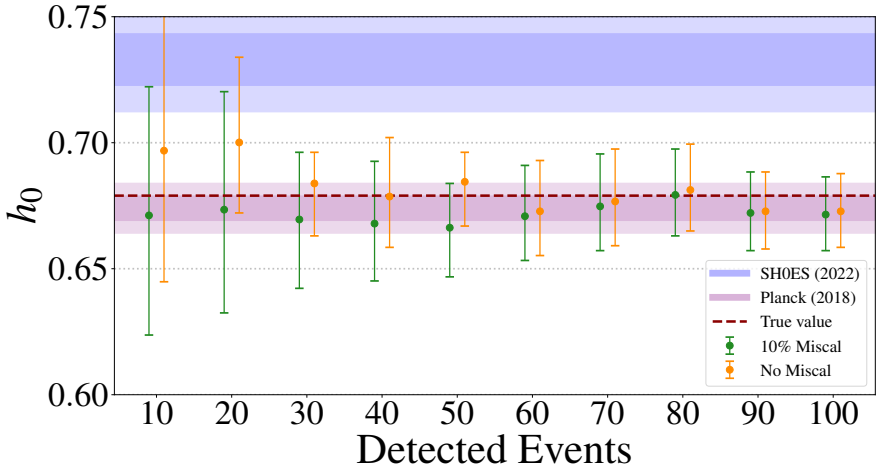

(a) 10% of the events miscalibrated.

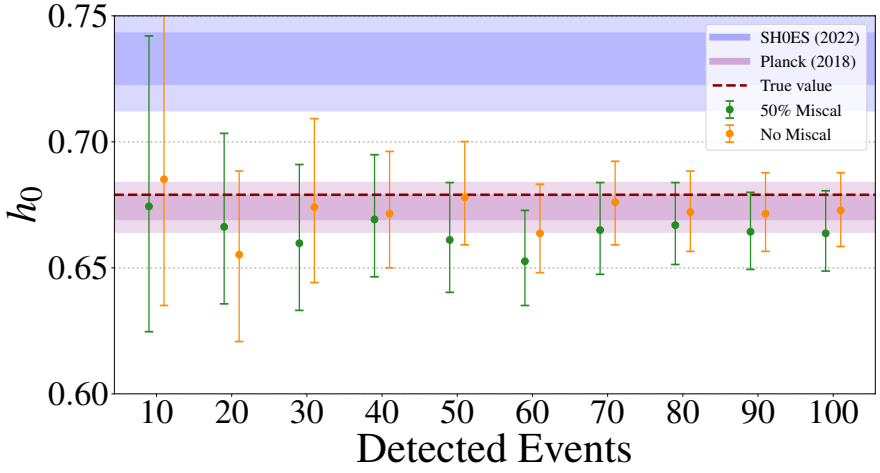

(b) 50% of the events miscalibrated.

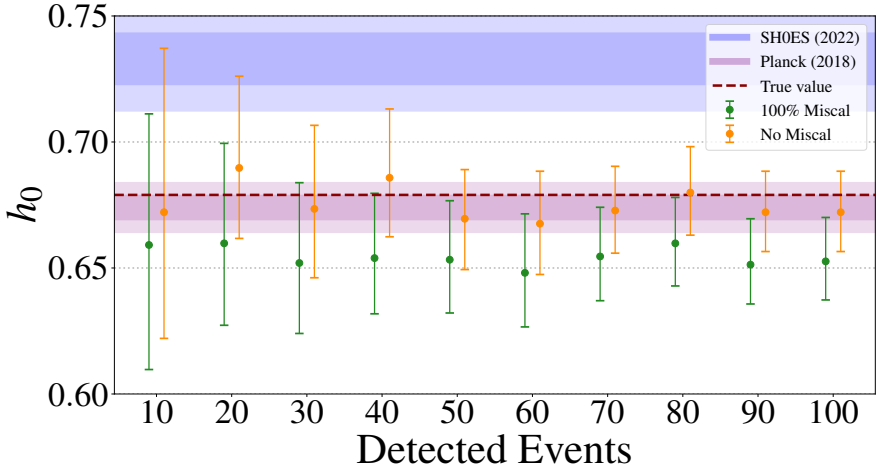

(c) 100% of the events miscalibrated.

Figure 5-5: h_0 posteriors when we have a certain number of detections, plotted when 10%, 50%, and 100% of the events are miscalibrated. We introduce an artificial offset on the x-axis for plotting purposes. We overlay the latest $1-\sigma$ (darker bar) and $2-\sigma$ results from SH0ES (2022) [330] in blue and from Planck (2018) [327] in purple.

Our results imply that CEs will not be a significant concern in measuring the Hubble constant with the bright-siren method for the next many years. In the most realistic yet unlikely case, where large instances of CEs like the ones described in this chapter affect a small fraction of the sources, CEs will not become the limiting factor until more than one hundred BNSs, each with an EM counterpart, have been found. Since the bright-siren method will likely have the smallest statistical uncertainties, other approaches to constrain H_0 using distance measurements from GW sources will be even less sensitive to CEs.

Chapter 6

Summary & Outlook

This thesis examines the key sources of systematic errors in GW data analysis and their effects on the PE results and subsequent astrophysical implications. As the next generation of GW detectors, such as the third-generation ground-based interferometers with longer detector arms, such as Cosmic Explorer and Einstein Telescope, and the proposed space-based probe LISA, come online, new opportunities and challenges arise. The increasing rate of GW detections necessitates prompt and reliable PE and a thorough understanding of when and how to include PE results for a population study of the sources. Moreover, GW signals with different characteristics will require improved waveform modeling and a deeper understanding of potential systematic sources.

This thesis first investigates the PE process in the context of marginal CBC signals by studying simulated events in Chap. 2 and re-analyzing real data containing astrophysical signals in Chap. 3. In particular, Chap. 3 examines the analysis of seven weak astrophysical BBH signals, among which one was claimed to have highly spinning BHs by a data analysis pipeline independent of LVK. For this specific BBH, the choices of priors on the BH spin significantly affect the spin posteriors. In general, when the signals are marginal, the assumption that the noise is Gaussian and stationary can break down, and the realizations of noise can mimic astrophysical signals, as demonstrated in Chap. 2. The choices made during PE, like the choices of priors, the waveform models, the characterization of background noise, and the sampler, can thus

significantly impact the results. The observations made in these two chapters will remain relevant for future GW detections, as more marginal sources will be detected with the improving detector sensitivity in the coming decades.

The second half of this thesis delves into the opposite limit, dealing with high-SNR signals that clearly have astrophysical origins. In this case, the signal is strong enough to shrink the statistical uncertainties of the PE results and the inaccuracy of the waveform models (discussed in Chap. 4), as well as the instrumental calibration errors (discussed in Chap. 5), become important factors to consider. The findings indicate that these two sources of systematic errors will not significantly impact the precision of PE until much higher detector sensitivities are achieved (for example, to detect multiple events with SNRs ten times as high as that of the currently loudest event). Nevertheless, ongoing efforts to minimize and account for these errors are essential.

This thesis makes a significant contribution to the field of GW astrophysics by thoroughly examining the systematic errors that can arise during data analysis by performing extensive PE runs not previously found in the literature. The findings and conclusions of this thesis have the potential to provide direction for the interpretation of PE results and offer practical guidance for future systematic error studies. Additionally, the insights gained from these studies can be applied to related fields that involve analyzing noisy and complex data, such as signal processing and machine learning.

Appendices

Appendix A

Analysis Details for Marginal Event Simulation

A.1 Sampling Convergence

As mentioned in Chap. 2, sampling algorithms are only guaranteed to return the correct posteriors in the limit where they run for an infinite amount of time. Especially at low SNRs, there is the risk that the sampler does not reach the right part of the parameter space, or gets stuck in a local and unrelated maximum. We use the maximum value of the recovered log likelihood as a probe of the convergence of the PE run, by comparing it with the log likelihood corresponding to the exact waveform parameters.

For a well-converged run, the difference:

$$\Delta \log L \equiv \log L_{\text{injected}} - \max\left(\log L_{\text{recovered}}\right) \tag{A.1}$$

should be slightly negative and not exactly zero since the component of the noise that happens to be correlated across the network can contribute to the maximum recovered log likelihood. Conversely, positive values would suggest that the code failed to collect all the available evidence, indicating a problem with convergence.

We show $\Delta \log L$ for all sources in Figure A-1. We find the expected behavior for

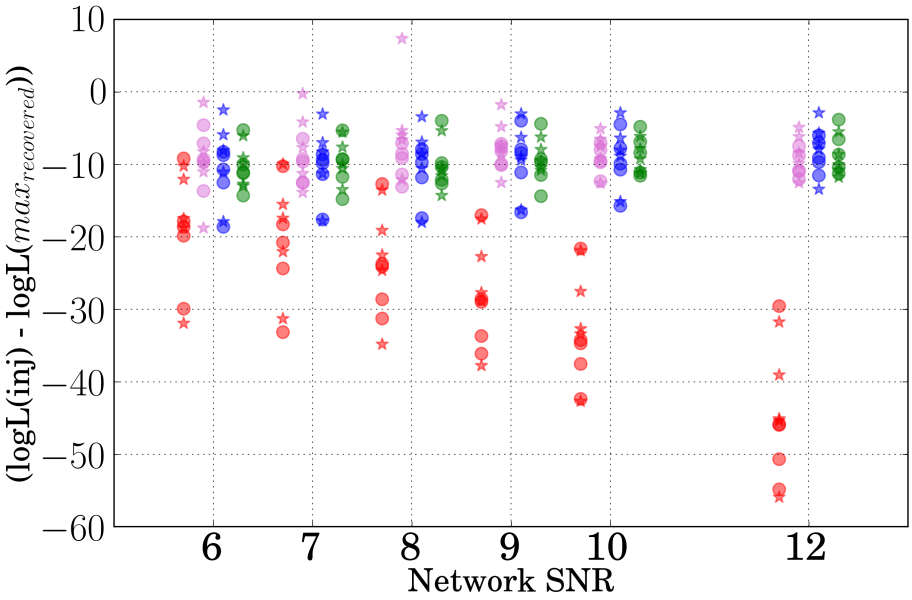

Figure A-1: Log likelihood for injection minus the maximum recovered log likelihood vs. network SNR.

all sources except for BNSs, for which a downward trend is visible. This difference is due to a known issue for long signals in the implementation of the ROQ likelihood in the *lscsoft* algorithm repository as of the time of writing [72]. Imperfections in the waveform reconstruction used in the ROQ basis can explain the different behavior of the BNS data.

To verify that the uncertainties we obtained for the BNS runs are meaningful, we have checked that the BNS runs do recover the correct SNRs. Furthermore, we have run PE on a small number of BNS sources (the ones used in Ref. [72]) both with and without the ROQ likelihood and found that the uncertainties are similar.

A.2 K-L Divergence

Here we report the median of K-L divergence (in nats) over five GPS times for luminosity distance d_L, right ascension α, declination δ, effective spin $\chi_{\rm eff}$, effective precessing spin $\chi_{\rm p}$, chirp mass $\mathcal{M}$, and mass ratio q, for the four morphologies and the two inclinations. Numbers close to zero imply the data is not informative about that parameter (at a given SNR). Conversely, large K-L divergence implies the prior

and posteriors are significantly different.

The effective precession spin, $\chi_{\rm p}$, is notoriously hard to measure, even for louder events [85, 112, 114–117, 386, 387]. The tables below show that for weak events we nearly always recover the prior, which is why we have not reported $\chi_{\rm p}$ uncertainties in Chap. 2.

Network SNR	6	7	8	9	10	12
d_L ($\theta_{JN} = 30°$)	0.01	0.01	1.85	5.00	5.62	6.51
d_L ($\theta_{JN} = 80°$)	0.01	0.00	3.39	5.10	5.68	6.67
α ($\theta_{JN} = 30°$)	0.00	0.00	0.32	0.77	0.80	0.89
α ($\theta_{JN} = 80°$)	0.00	0.01	0.82	0.90	0.92	1.22
δ ($\theta_{JN} = 30°$)	0.00	0.00	0.07	0.19	0.21	0.25
δ ($\theta_{JN} = 80°$)	0.00	0.00	0.24	0.25	0.29	0.51
$\chi_{\rm eff}$ ($\theta_{JN} = 30°$)	0.00	0.00	0.04	0.05	0.07	0.08
$\chi_{\rm eff}$ ($\theta_{JN} = 80°$)	0.00	0.00	0.07	0.08	0.09	0.13
$\chi_{\rm p}$ ($\theta_{JN} = 30°$)	0.00	0.00	0.04	0.06	0.04	0.05
$\chi_{\rm p}$ ($\theta_{JN} = 80°$)	0.00	0.00	0.07	0.06	0.05	0.06
$\mathcal{M}$ ($\theta_{JN} = 30°$)	0.04	0.12	4.69	9.67	10.31	10.36
$\mathcal{M}$ ($\theta_{JN} = 80°$)	0.08	0.24	5.83	10.76	11.01	11.01
q ($\theta_{JN} = 30°$)	0.00	0.03	1.13	1.74	1.76	1.88
q ($\theta_{JN} = 80°$)	0.01	0.06	1.79	1.93	1.99	2.06

Table A.1: Median of K-L divergence (in nats) over five GPS times for BNSs.

Network SNR	6	7	8	9	10	12
d_L ($\theta_{JN} = 30°$)	0.01	0.60	4.04	4.85	5.38	6.37
d_L ($\theta_{JN} = 80°$)	0.01	0.01	0.00	3.99	7.31	8.90
α ($\theta_{JN} = 30°$)	0.00	0.21	1.03	2.10	2.05	2.23
α ($\theta_{JN} = 80°$)	0.00	0.00	0.00	1.10	1.17	1.89
δ ($\theta_{JN} = 30°$)	0.00	0.22	0.64	1.56	1.62	1.86
δ ($\theta_{JN} = 80°$)	0.00	0.00	0.00	0.55	0.66	1.61
χ_{eff} ($\theta_{JN} = 30°$)	0.01	1.19	2.43	2.71	2.86	2.85
χ_{eff} ($\theta_{JN} = 80°$)	0.01	0.01	0.02	3.28	3.46	4.05
χ_{p} ($\theta_{JN} = 30°$)	0.00	0.06	0.16	0.19	0.09	0.31
χ_{p} ($\theta_{JN} = 80°$)	0.00	0.00	0.00	1.76	1.35	1.68
$\mathcal{M}$ ($\theta_{JN} = 30°$)	0.05	2.35	6.53	7.47	7.58	7.42
$\mathcal{M}$ ($\theta_{JN} = 80°$)	0.05	0.08	0.17	5.21	6.88	7.49
q ($\theta_{JN} = 30°$)	0.01	0.20	0.34	0.48	0.46	0.26
q ($\theta_{JN} = 80°$)	0.00	0.01	0.00	0.94	0.79	1.11

Table A.2: Median of K-L divergence (in nats) over five GPS times for NSBHs.

Network SNR	6	7	8	9	10	12
d_L ($\theta_{JN} = 30°$)	0.11	2.78	4.45	5.23	5.80	6.62
d_L ($\theta_{JN} = 80°$)	0.00	0.04	2.99	5.78	6.67	7.73
α ($\theta_{JN} = 30°$)	0.02	0.67	0.99	1.18	1.28	1.30
α ($\theta_{JN} = 80°$)	0.00	0.01	0.60	1.08	1.23	1.36
δ ($\theta_{JN} = 30°$)	0.01	0.21	0.34	0.41	0.52	0.64
δ ($\theta_{JN} = 80°$)	0.00	0.01	0.15	0.28	0.34	0.57
χ_{eff} ($\theta_{JN} = 30°$)	0.02	0.22	0.48	1.36	1.68	1.97
χ_{eff} ($\theta_{JN} = 80°$)	0.01	0.06	0.83	1.50	1.74	2.01
χ_{p} ($\theta_{JN} = 30°$)	0.02	0.10	0.02	0.08	0.09	0.09
χ_{p} ($\theta_{JN} = 80°$)	0.00	0.00	0.47	0.68	0.84	1.10
$\mathcal{M}$ ($\theta_{JN} = 30°$)	0.64	2.91	3.62	4.88	5.60	5.96
$\mathcal{M}$ ($\theta_{JN} = 80°$)	0.01	0.14	3.19	4.81	5.16	5.52
q ($\theta_{JN} = 30°$)	0.01	0.01	0.29	0.56	0.66	0.73
q ($\theta_{JN} = 80°$)	0.00	0.01	0.24	0.48	0.50	0.77

Table A.3: Median of K-L divergence (in nats) over five GPS times for BBHs.

Network SNR	6	7	8	9	10	12
d_L ($\theta_{JN} = 30°$)	2.53	3.96	5.09	5.73	6.42	7.28
d_L ($\theta_{JN} = 80°$)	1.99	4.05	5.10	5.68	6.39	7.38
α ($\theta_{JN} = 30°$)	0.45	0.77	0.90	1.14	1.41	2.12
α ($\theta_{JN} = 80°$)	0.39	0.68	0.93	0.97	1.32	1.56
δ ($\theta_{JN} = 30°$)	0.28	0.40	0.65	0.75	0.97	1.65
δ ($\theta_{JN} = 80°$)	0.20	0.52	0.67	0.52	0.89	1.20
χ_{eff} ($\theta_{JN} = 30°$)	0.67	1.40	1.31	1.31	1.38	1.58
χ_{eff} ($\theta_{JN} = 80°$)	0.52	0.59	0.74	0.84	1.01	1.57
χ_{p} ($\theta_{JN} = 30°$)	0.02	0.08	0.10	0.10	0.13	0.06
χ_{p} ($\theta_{JN} = 80°$)	0.02	0.01	0.08	0.05	0.04	0.05
$\mathcal{M}$ ($\theta_{JN} = 30°$)	1.24	1.54	1.87	2.28	2.56	3.05
$\mathcal{M}$ ($\theta_{JN} = 80°$)	1.25	1.81	2.22	2.50	2.78	3.20
q ($\theta_{JN} = 30°$)	0.02	0.05	0.05	0.04	0.04	0.05
q ($\theta_{JN} = 80°$)	0.10	0.06	0.14	0.29	0.38	0.33

Table A.4: Median of K-L divergence (in nats) over five GPS times for hBBHs.

Appendix B

Further Investigation on GW151216

Among the events discussed in Chap. 3, GW151216 shows the biggest differences in its inferred parameters between the three configurations. We summarized the differences in Sec. 3.2.1. In this appendix, we present the results of a deeper investigation into the possible causes. As we mentioned in Sec. 3.1, the configurations used in this study differ along five axes: (a) the segment of data used, (b) the algorithm used to estimate the PSD, and consequently, compute the likelihood $\mathcal{L}(d|\boldsymbol{\theta})$, (c) the sampler, (d) the waveform model, and finally (e) the prior on the spins of the BHs. It is not practical to explore every combination of factors; hence, we perform a few controlled experiments by varying the choices that we expect to be the most important. We have already checked that the different choices of the waveform model made no difference in this case, so we omit that factor from the rest of the discussion.

From the results in Ref. [73] as well as Sec. 3.2.1, we expect that the choice of prior can play a significant role. The configurations in Tab. 3.1 differ in both the prior and other analysis choices. Hence it is worthwhile to fix the prior and vary the other choices.

We first restrict to the flat-in-$\chi_{\rm eff}$ spin prior of Config. C. Fig. B-1 shows the effect of successively changing the sampler and the method of PSD estimation from those of Config. C to those of Configs. A and B. Firstly, Fig. B-1a shows the effect of varying the samplers, pyMultiNest and LALInference, while keeping the rest of the configuration identical to Config. C. Next, Fig. B-1b shows the impact of varying

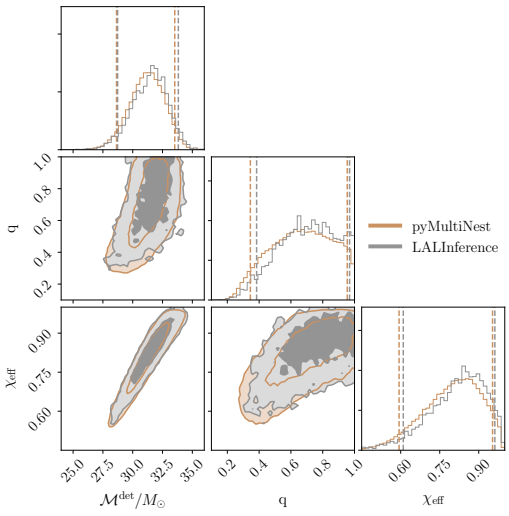

(a) Effects of different samplers.

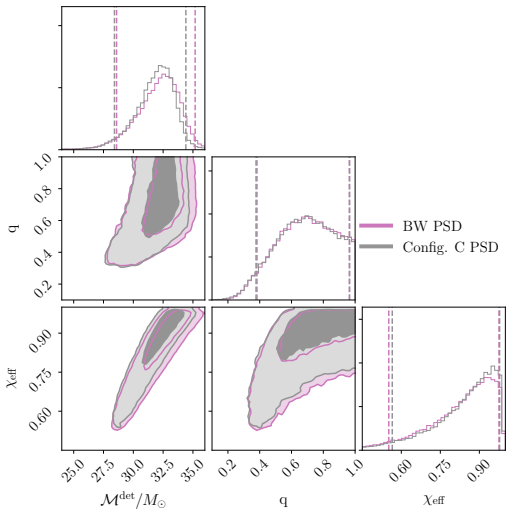

(b) Effects of different algorithms used to estimate the PSD.

Figure B-1: Corner plot for posterior distributions for GW151216, using a flat-in-$\chi_{\rm eff}$ spin prior, IMRPhenomD, and a 128-second-long data segment. The left and right panels, respectively, show the effects of successively changing the sampler and the method of PSD estimation from those of Config. C to those of Configs. A and B. The gray-filled contours show the posterior using the sampler in LALINFERENCE, and the PSD estimated using the Welch method (with a drift correction factor, used in Config. C). On the left panel, the brown contours mark the same analysis done with the PYMULTINEST. On the right, the purple contours show the effect of changing only the PSD to the one estimated using BAYESWAVE (also used in Configs. A and B). This figure shows that under the flat-in-$\chi_{\rm eff}$ prior, the inference is insensitive to other analysis choices.

the method used to estimate the PSD from the Welch method to BAYESWAVE. We see that the posteriors are identical to those of Config. C, which implies that under the flat-in-$\chi_{\rm eff}$ prior, the rest of the analysis choices do not significantly impact the PE results, and consequently, the only way to go to the results of Config. B (and A) is to choose a different spin prior.

The above tests were performed with the flat-in $\chi_{\rm eff}$ prior, and hence do not look for residual effects of the analysis methods under the alternative isotropic spin prior of Configs. A and B. To do this, we compare the results of Config. B to those of a run with a modified version of Config. C with the isotropic spin prior (henceforth Config. C1), Fig. B-2. Similar to the comparisons in Fig. B-1, these two runs have the same prior but differ in analysis methods (additionally, they use data segments of

different lengths). We observe that (a) the differences are less pronounced than those in Sec. 3.2.1, which is consistent with our understanding that the choice of spin priors is the most significant driver of the differences in Fig. 3-3, and (b) unlike in Fig. B-1, the data segments used and the analysis methods make some difference here. The two sets of results are formally consistent with each other, but the posteriors of Config. B are broader and encompass those of Config. C1. In particular, the posterior on the effective spin has a fatter tail towards $\chi_{\rm eff} = 0$ in Config. B.

The above differences should be caused by the three remaining points of departure, i.e., the method of PSD estimation, the length of the data used, and the sampler: the simplest one to vary in isolation is the sampler (analogous to Fig. B-1a). Toward this end, the pink contours in Fig. B-2a show the posteriors with the first two choices fixed to those of Config. B (i.e., using the `BayesWave` PSD and a four-second-long segment of data), and changing the sampler from LALInference to pyMultinest (henceforth, Config. B1). We see that contrary to the case of the "uniform-in-$\chi_{\rm eff}$" prior (as shown in Fig. B-1a), the choice of the sampler makes a small but noticeable difference here. The weight of the samples at $\chi_{\rm eff} \leq 0$ is reduced to between those of Configs. B and C1.

In Fig. B-3 we show the result of varying the segment length while keeping other choices identical to Config. B. Here, the effect is slightly more visible but still cannot account for the more prominent differences between the posteriors for chirp mass and effective spin seen in Fig. 3-3 when comparing Config. B with Config. C. A secondary mode in the spin posterior that supports zero $\chi_{\rm eff}$ is more visible for some segment lengths and is most prominent for 64 s and least evident for 128 s. We attribute these differences to the PSD estimation. Different segment lengths result in slightly different PSD estimates, which can have a visible impact on the PE results for low SNR events, as discussed in Chap. 2 (published as [87]). We further explore the assumptions used in estimating the PSDs below.

We next investigate the causes of the difference between the results from Configs. B1 and C1: these configurations differ in the method of PSD estimation and the length of the data segment analyzed. The Welch method with a drift factor, as used

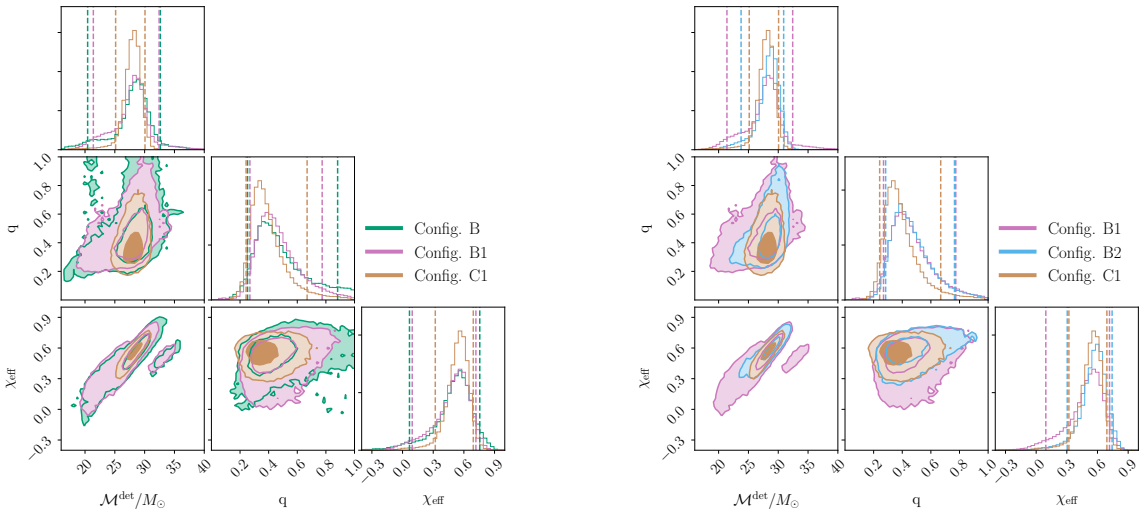

(a) Effects of different samplers.

(b) Effects of different PSDs.

Figure B-2: Corner plot for posterior distributions for GW151216 with the isotropic prior on spins. In the left panel, green, pink, and orange posteriors use Config. B, a version of Config. B with PYMULTINEST (B1) , and Config. C with the isotropic prior (C1), respectively. The blue contours in the right panel are for B2, a further modified version of B1 (data with loud lines notched out, and using the `BayesWave` continuum). Under this prior, there are residual effects of analysis choices (sampler between B and B1, treatment of lines in the data between B1 and B2, and PSD continuum between B2 and C1).

by Config. C, requires data segments much longer than four seconds, thus precluding a direct head-to-head comparison. A naive approach forward would be to reduce the frequency resolution of a PSD computed on longer segments (say, using the Welch method) onto a frequency grid conjugate to the four-second segment. Let us consider the validity of such an approach. The likelihood estimation in Eq. (1.7) works with the discrete Fourier transform (DFT) coefficients, $\tilde{d}(f_m)$, of the data d, where f_m is conjugate to the four-second segment. Given the PSD, $S_{n,\mathrm{w}}(f)$, computed using the Welch method on a very fine frequency grid (over a longer segment of data), the

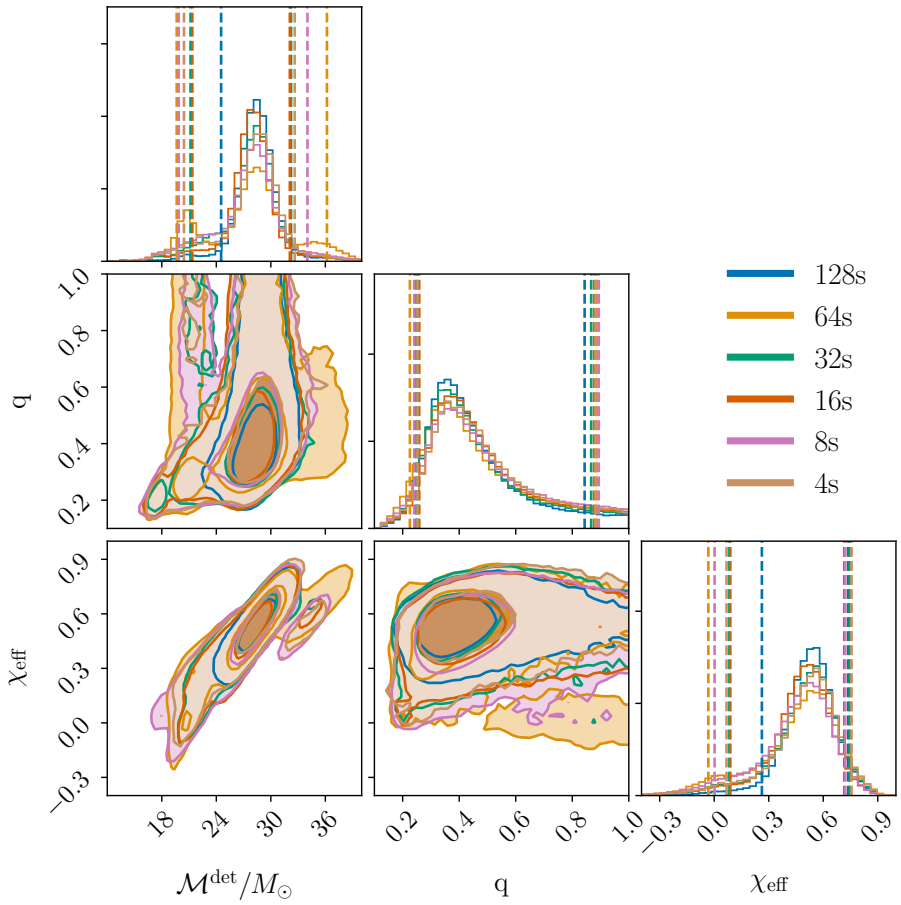

Figure B-3: Corner plot for posterior distributions for GW151216, with PSD estimation method, prior and waveform choices the same as those in Config. B. The only difference is the length of data segment used: 4 s (brown) vs. 8 s (purple) vs. 16 s (red) vs. 32 s (green) vs. 64 s (orange) vs. 128 s (blue), where all segments end two seconds after the merger time (defined as the peak of the absolute value of the strain amplitude at the geocenter).

covariance matrix of the DFT coefficients is

$$\begin{aligned}&\left\langle \tilde{d}\left(f_m\right)\left[\tilde{d}\left(f_{m'}\right)\right]^*\right\rangle \\ &= \frac{1}{4}\, e^{i\,\pi\,(f_{m'}-f_m)\,\Delta t}\times \\ &\int \mathrm{d}f\; S_{n,\mathrm{w}}(f)\,\widetilde{W}\left(f-f_m\right)\widetilde{W}\left(f-f_{m'}\right), \end{aligned} \tag{B.1}$$

where Δt is the sampling period, and $\tilde{W}$ is the Fourier transform of the window function applied to the data (typically a Tukey window). The noise PSD exhibits

spectral lines that are orders of magnitude louder than the continuum, so the window function W in Eq. (B.1) induces covariances between distinct frequencies in the vicinity of the lines (i.e., between $f_m \neq f_{m'}$). In such a case, the fundamental assumption in Eq. (1.7) that the frequencies can be separately analyzed when computing the likelihood breaks down.

We avoid dealing with these complications by using a further modified version of Config. B1, in which we (a) use Bessel filters to notch from the `BayesWave` PSD used by Config. B all loud spectral lines that we identified when analyzing 4096 s of data [1]; and (b) use only the continuum of the PSD to analyze this segment. This approach (henceforth Config. B2) is a heuristic way to mitigate the imperfect resolution of spectral lines arising from using a short segment. This is *not* an alternative approach to analyze GW151216, but instead a controlled experiment to investigate the extent to which the loud spectral lines in the PSD can impact the PE results. Fig. B-2b contrasts the posteriors under Config. B2 to the others: we see that the posteriors in $\chi_{\rm eff}$ are consistent with those of Config. C, but there are residual differences in the distributions of mass-ratio q (and a small bias by a fraction of a sigma in the other parameters as well).

Tab. B.1 reports the posterior weights in the region $\chi_{\rm eff} \leq 0$ and $\chi_{\rm eff} \geq 0.8$ for the various configurations considered in this section under the isotropic prior on spins, as well the values from Configs. B and C from Sec. 3.2.1 for comparison. The weight of the posteriors varies and is subject to significant measurement uncertainties. $\chi_{\rm eff} \leq 0$ contains only low-probability tails across all of the configurations considered here, while the support for high spin magnitude $\chi_{\rm eff} \geq 0.8$ is much more significant for Config. C than for the others.

[1]The sets of critical frequencies are as follows: (35.85, 35.95), (36.65, 36.74), (37.275, 37.325), (40.885, 41.05), (59.9, 60.05), (119.94, 120.03), (179.910, 180.05), (299.489, 299.594), (299.665, 299.745), (299.890, 300.02), (302.180, 302.260), (303.260, 303.345), (331.840, 331.955). In each tuple, the first and second numbers, respectively, are the lower and upper critical frequency for the notch filter, in Hz.

Configuration	Notes	$p(\chi_{\rm eff} \leq 0 \vert \mathbf{d})$	$p(\chi_{\rm eff} \geq 0.8 \vert \mathbf{d})$
B	See Tab. 3.1	3.4%	2.6%
B1	B + pyMultiNest	2.4%	0.7%
B2	B1 − lines	0.3%	1.1%
C	See Tab. 3.1	0.0%	52.5%
C1	C + Isotropic spin prior	0.5%	0.2%

Table B.1: The posterior weights in the region $\chi_{\rm eff} \leq 0$ for various configurations for GW151216.

Appendix C

Waveform Systematics

C.1 PE Tables

We report the PE results for an extended set of parameters relative to Sec. 4.3. The results are the median of the marginalized 1D posterior distributions for different parameters and the corresponding symmetric 90% CIs.

The $q = 2$ analyses are reported in Tab. C.1 for SNR 30 and Tab. C.2 for SNR 70. For $q = 3$, the SNR 30 results are shown in Tab. C.3 and the SNR 70 results in Tab. C.4. Finally, the $q = 6$ results are reported in Tab. C.5 for SNR 30 and Tab. C.6 for SNR 70.

C.2 NS Radii Calculation

The compactness of the NS is estimated using a fit from Ref. [388] (Eq. (78), in Sec. 4.4.1):

$$C_{\rm NS} = \sum_{k=0}^{2} a_k (\ln \Lambda_{\rm NS})^k, \tag{C.1}$$

with fitting parameters $a_0 = 0.371$, $a_1 = -0.0391$, and $a_2 = 0.001056$ from Ref. [389]. As reported in Ref. [388], this fit, when compared to a large set of NS EoS models, has the largest deviation of 6.5% that is significantly smaller than the statistical uncertainties reported in Sec. 4.3.2.

The NS radius $r_{\rm NS}$ is, in turn, related to the compactness through:

$$r_{\rm NS} = \frac{m_{\rm NS}}{C_{\rm NS}} \,, \tag{C.2}$$

with $m_{\rm NS}$ being the NS mass reported in the rest frame of the NSBH. Again, we use natural units, $G = c = 1$.

C.3 Prior

We use priors that are routinely used in LVK publications [4, 5, 83, 202–206], in Tab. C.7, C.8 and C.9, for $q = 2$, $q = 3$, and $q = 6$, respectively.

We use uniform priors for the *detector-frame* component masses. When using a ROQ, additional prior constraints are imposed on the detector-frame chirp mass and mass ratio, which limit their range. For one system, the mass prior bounds are the same for all the aligned-spin waveforms while slightly different from those for the precessing-spin waveforms due to the different choices by the ROQ basis. Note that the `LEA+` ROQ basis is constructed with prior constraints only on the component BH and NS masses.

The BH spin prior is uniform in the dimensionless spin magnitude in the range $[0, 0.99]$, and isotropic for the orientation for precessing-spin approximants. For non-precessing waveforms, the prior on the (aligned) spin magnitude is equal to the projection of an isotropic spin vector along the orbital angular momentum.

For waveform models that support tidal deformation of the NS, we use a prior uniform over $\Lambda_{\rm NS}$ within the range of validity.

We choose a prior for sky localization and the orientation of the orbital angular momentum with respect to the line of sight that is uniform over the sphere, a prior for the distance that is proportional to the luminosity distance squared, and a uniform prior over the arrival time and phase.

Approximant	$\mathcal{M}^{\rm source}/M_\odot$	q	$m_1^{\rm source}/M_\odot$	$m_2^{\rm source}/M_\odot$	$M_{\rm total}^{\rm source}/M_\odot$	$\chi_{\rm eff}$	$\lvert s_1\rvert$	$s_{1,z}$	$\lvert s_2\rvert$	$s_{2,z}$	Λ_2	$r_{\rm NS}$/km	D_L/Mpc	$\theta_{JN}/^\circ$
True value	1.65	2.0	2.72	1.36	4.08	0.00	0.0	0.0	0.0	0.0	791	14.4	136.5	30
SEOB	$1.66^{+0.02}_{-0.01}$	$2.3^{+0.9}_{-0.9}$	$2.9^{+0.6}_{-0.7}$	$1.3^{+0.4}_{-0.2}$	$4.2^{+0.4}_{-0.3}$	$0.03^{+0.09}_{-0.11}$	$0.07^{+0.17}_{-0.07}$	$0.0^{+0.2}_{-0.2}$	$0.13^{+0.41}_{-0.12}$	$0.0^{+0.5}_{-0.4}$	-	-	$131.4^{+25.9}_{-46.0}$	34^{+30}_{-25}
SEOBT	$1.66^{+0.02}_{-0.01}$	$2.0^{+0.8}_{-0.7}$	$2.7^{+0.5}_{-0.6}$	$1.4^{+0.3}_{-0.2}$	$4.1^{+0.3}_{-0.2}$	$0.00^{+0.09}_{-0.07}$	$0.07^{+0.19}_{-0.06}$	$0.0^{+0.2}_{-0.2}$	$0.12^{+0.41}_{-0.12}$	$0.0^{+0.4}_{-0.4}$	503^{+957}_{-426}	$12.5^{+3.0}_{-3.8}$	$131.8^{+25.1}_{-45.9}$	34^{+30}_{-24}
SEOBNSBH	$1.66^{+0.02}_{-0.01}$	$1.9^{+0.7}_{-0.8}$	$2.6^{+0.5}_{-0.6}$	$1.4^{+0.4}_{-0.2}$	$4.0^{+0.3}_{-0.2}$	$0.00^{+0.07}_{-0.07}$	$0.05^{+0.11}_{-0.05}$	$-0.0^{+0.1}_{-0.1}$	$0.00^{+0.00}_{-0.00}$	$0.0^{+0.0}_{-0.0}$	547^{+773}_{-415}	$12.9^{+3.2}_{-3.4}$	$131.9^{+22.8}_{-44.1}$	32^{+28}_{-23}
IMRNSBH	$1.65^{+0.02}_{-0.01}$	$1.9^{+0.6}_{-0.8}$	$2.7^{+0.5}_{-0.6}$	$1.4^{+0.4}_{-0.2}$	$4.1^{+0.3}_{-0.2}$	$0.00^{+0.07}_{-0.08}$	$0.04^{+0.11}_{-0.04}$	$0.0^{+0.1}_{-0.1}$	$0.00^{+0.00}_{-0.00}$	$0.0^{+0.0}_{-0.0}$	694^{+744}_{-492}	$13.2^{+2.9}_{-3.3}$	$133.4^{+23.5}_{-44.5}$	32^{+28}_{-23}
IMRp	$1.65^{+0.02}_{-0.01}$	$2.2^{+0.8}_{-0.8}$	$2.9^{+0.5}_{-0.6}$	$1.3^{+0.3}_{-0.2}$	$4.2^{+0.3}_{-0.3}$	$0.02^{+0.08}_{-0.09}$	$0.14^{+0.36}_{-0.13}$	$0.0^{+0.2}_{-0.2}$	$0.31^{+0.54}_{-0.28}$	$0.0^{+0.4}_{-0.3}$	-	-	$143.1^{+16.5}_{-47.3}$	24^{+34}_{-18}
IMRpT	$1.65^{+0.02}_{-0.01}$	$1.9^{+0.7}_{-0.7}$	$2.6^{+0.5}_{-0.6}$	$1.4^{+0.4}_{-0.2}$	$4.0^{+0.3}_{-0.2}$	$-0.01^{+0.08}_{-0.07}$	$0.13^{+0.40}_{-0.12}$	$0.0^{+0.1}_{-0.1}$	$0.25^{+0.53}_{-0.23}$	$-0.0^{+0.3}_{-0.2}$	569^{+782}_{-459}	$13.0^{+2.7}_{-3.5}$	$142.1^{+17.1}_{-46.9}$	25^{+33}_{-19}
XHM	$1.65^{+0.01}_{-0.01}$	$2.2^{+0.9}_{-0.9}$	$2.9^{+0.6}_{-0.7}$	$1.3^{+0.4}_{-0.2}$	$4.2^{+0.4}_{-0.3}$	$0.03^{+0.09}_{-0.10}$	$0.07^{+0.15}_{-0.06}$	$0.0^{+0.2}_{-0.2}$	$0.13^{+0.30}_{-0.12}$	$0.0^{+0.4}_{-0.3}$	-	-	$141.1^{+20.0}_{-41.6}$	27^{+28}_{-20}

(a) Inclination 30°.

Approximant	$\mathcal{M}^{\rm source}/M_\odot$	q	$m_1^{\rm source}/M_\odot$	$m_2^{\rm source}/M_\odot$	$M_{\rm total}^{\rm source}/M_\odot$	$\chi_{\rm eff}$	$\lvert s_1\rvert$	$s_{1,z}$	$\lvert s_2\rvert$	$s_{2,z}$	Λ_2	$r_{\rm NS}$/km	D_L/Mpc	$\theta_{JN}/^\circ$
True value	1.67	2.0	2.75	1.37	4.12	0.00	0.0	0.0	0.0	0.0	791	14.4	87.0	70
SEOB	$1.66^{+0.02}_{-0.01}$	$2.3^{+0.9}_{-0.9}$	$2.9^{+0.6}_{-0.7}$	$1.3^{+0.4}_{-0.2}$	$4.2^{+0.4}_{-0.3}$	$0.03^{+0.09}_{-0.11}$	$0.07^{+0.18}_{-0.07}$	$0.0^{+0.2}_{-0.2}$	$0.13^{+0.44}_{-0.13}$	$0.0^{+0.5}_{-0.4}$	-	-	$131.3^{+27.2}_{-50.2}$	35^{+37}_{-25}
SEOBT	$1.66^{+0.02}_{-0.01}$	$2.0^{+0.8}_{-0.8}$	$2.7^{+0.5}_{-0.6}$	$1.4^{+0.4}_{-0.2}$	$4.1^{+0.3}_{-0.2}$	$0.00^{+0.09}_{-0.07}$	$0.07^{+0.21}_{-0.06}$	$0.0^{+0.2}_{-0.2}$	$0.12^{+0.43}_{-0.11}$	$0.0^{+0.4}_{-0.4}$	502^{+953}_{-423}	$12.5^{+3.1}_{-3.8}$	$131.3^{+27.1}_{-49.1}$	35^{+36}_{-25}
SEOBNSBH	$1.66^{+0.02}_{-0.01}$	$1.9^{+0.7}_{-0.8}$	$2.6^{+0.5}_{-0.6}$	$1.4^{+0.4}_{-0.2}$	$4.0^{+0.3}_{-0.2}$	$-0.01^{+0.07}_{-0.07}$	$0.05^{+0.11}_{-0.05}$	$-0.0^{+0.1}_{-0.1}$	$0.00^{+0.00}_{-0.00}$	$0.0^{+0.0}_{-0.0}$	550^{+782}_{-406}	$13.0^{+3.2}_{-3.3}$	$131.0^{+25.2}_{-44.9}$	34^{+31}_{-24}
IMRNSBH	$1.65^{+0.02}_{-0.01}$	$2.0^{+0.6}_{-0.8}$	$2.7^{+0.4}_{-0.6}$	$1.4^{+0.4}_{-0.2}$	$4.1^{+0.3}_{-0.2}$	$0.00^{+0.06}_{-0.08}$	$0.04^{+0.11}_{-0.04}$	$0.0^{+0.1}_{-0.1}$	$0.00^{+0.00}_{-0.00}$	$0.0^{+0.0}_{-0.0}$	707^{+782}_{-486}	$13.3^{+2.9}_{-3.1}$	$133.8^{+24.9}_{-45.6}$	33^{+30}_{-23}
IMRp	$1.65^{+0.02}_{-0.01}$	$2.3^{+0.8}_{-0.8}$	$2.9^{+0.5}_{-0.6}$	$1.3^{+0.3}_{-0.2}$	$4.2^{+0.4}_{-0.3}$	$0.03^{+0.08}_{-0.10}$	$0.12^{+0.33}_{-0.11}$	$0.0^{+0.1}_{-0.1}$	$0.32^{+0.53}_{-0.28}$	$0.0^{+0.4}_{-0.3}$	-	-	$144.2^{+17.0}_{-54.0}$	24^{+41}_{-18}
IMRpT	$1.65^{+0.02}_{-0.01}$	$1.8^{+0.7}_{-0.7}$	$2.6^{+0.5}_{-0.6}$	$1.4^{+0.4}_{-0.2}$	$4.0^{+0.3}_{-0.2}$	$-0.02^{+0.08}_{-0.06}$	$0.14^{+0.43}_{-0.12}$	$0.0^{+0.1}_{-0.2}$	$0.24^{+0.49}_{-0.21}$	$-0.0^{+0.2}_{-0.2}$	538^{+732}_{-435}	$12.9^{+2.8}_{-3.6}$	$143.1^{+18.1}_{-53.4}$	25^{+40}_{-19}
XHM	$1.65^{+0.02}_{-0.01}$	$2.2^{+1.0}_{-0.7}$	$2.9^{+0.7}_{-0.5}$	$1.3^{+0.2}_{-0.2}$	$4.2^{+0.5}_{-0.3}$	$0.03^{+0.10}_{-0.08}$	$0.09^{+0.22}_{-0.09}$	$0.0^{+0.2}_{-0.3}$	$0.15^{+0.41}_{-0.14}$	$0.1^{+0.5}_{-0.3}$	-	-	$133.4^{+25.2}_{-43.3}$	34^{+30}_{-22}

(b) Inclination 70°.

Table C.1: Properties of the q=2, SNR 30 simulation, as recovered by the listed approximants. We report the 1D median and the symmetric 90% CI.

Approximant	$\mathcal{M}^{\rm source}/M_\odot$	q	$m_1^{\rm source}/M_\odot$	$m_2^{\rm source}/M_\odot$	$M_{\rm total}^{\rm source}/M_\odot$	$\chi_{\rm eff}$	$\lvert s_1\rvert$	$s_{1,z}$	$\lvert s_2\rvert$	$s_{2,z}$	Λ_2	$r_{\rm NS}$/km	D_L/Mpc	$\theta_{JN}/^\circ$
True value	1.68	2.0	2.76	1.38	4.15	0.00	0.0	0.0	0.0	0.0	791	14.4	58.6	30
SEOB	$1.68^{+0.01}_{-0.00}$	$2.5^{+0.4}_{-0.4}$	$3.1^{+0.3}_{-0.3}$	$1.2^{+0.1}_{-0.1}$	$4.4^{+0.2}_{-0.2}$	$0.06^{+0.04}_{-0.05}$	$0.07^{+0.15}_{-0.07}$	$0.1^{+0.2}_{-0.2}$	$0.14^{+0.40}_{-0.14}$	$0.1^{+0.4}_{-0.4}$	-	-	$57.8^{+8.5}_{-15.4}$	31^{+24}_{-22}
SEOBT	$1.68^{+0.01}_{-0.00}$	$2.0^{+0.5}_{-0.6}$	$2.8^{+0.4}_{-0.5}$	$1.4^{+0.3}_{-0.1}$	$4.1^{+0.2}_{-0.2}$	$0.00^{+0.06}_{-0.07}$	$0.06^{+0.19}_{-0.06}$	$0.0^{+0.2}_{-0.2}$	$0.11^{+0.41}_{-0.11}$	$-0.0^{+0.4}_{-0.4}$	415^{+264}_{-291}	$12.1^{+2.4}_{-2.9}$	$57.9^{+8.4}_{-16.0}$	31^{+24}_{-22}
SEOBNSBH	$1.68^{+0.01}_{-0.00}$	$1.9^{+0.4}_{-0.6}$	$2.7^{+0.3}_{-0.5}$	$1.4^{+0.3}_{-0.1}$	$4.1^{+0.2}_{-0.2}$	$0.00^{+0.04}_{-0.06}$	$0.03^{+0.09}_{-0.02}$	$0.0^{+0.1}_{-0.1}$	$0.00^{+0.00}_{-0.00}$	$0.0^{+0.0}_{-0.0}$	510^{+206}_{-205}	$12.7^{+2.1}_{-1.7}$	$58.1^{+7.4}_{-14.4}$	29^{+23}_{-20}
IMRNSBH	$1.68^{+0.01}_{-0.00}$	$2.0^{+0.4}_{-0.5}$	$2.7^{+0.3}_{-0.4}$	$1.4^{+0.2}_{-0.1}$	$4.1^{+0.2}_{-0.2}$	$0.00^{+0.04}_{-0.05}$	$0.02^{+0.08}_{-0.02}$	$0.0^{+0.1}_{-0.1}$	$0.00^{+0.00}_{-0.00}$	$0.0^{+0.0}_{-0.0}$	695^{+212}_{-225}	$13.2^{+1.6}_{-1.4}$	$59.2^{+7.2}_{-15.1}$	29^{+23}_{-20}
IMRp	$1.68^{+0.00}_{-0.00}$	$2.6^{+0.4}_{-0.4}$	$3.2^{+0.3}_{-0.3}$	$1.2^{+0.1}_{-0.1}$	$4.4^{+0.2}_{-0.2}$	$0.06^{+0.03}_{-0.04}$	$0.12^{+0.21}_{-0.11}$	$0.1^{+0.1}_{-0.1}$	$0.28^{+0.50}_{-0.24}$	$0.1^{+0.3}_{-0.3}$	-	-	$64.4^{+3.0}_{-12.6}$	15^{+26}_{-11}
IMRpT	$1.68^{+0.01}_{-0.00}$	$1.9^{+0.5}_{-0.7}$	$2.7^{+0.3}_{-0.6}$	$1.4^{+0.3}_{-0.1}$	$4.1^{+0.2}_{-0.2}$	$0.00^{+0.05}_{-0.06}$	$0.09^{+0.25}_{-0.08}$	$0.0^{+0.1}_{-0.1}$	$0.18^{+0.46}_{-0.16}$	$0.0^{+0.2}_{-0.2}$	502^{+284}_{-269}	$12.8^{+2.2}_{-2.3}$	$63.2^{+4.0}_{-15.2}$	19^{+27}_{-15}
XHM	$1.68^{+0.00}_{-0.00}$	$2.5^{+0.4}_{-0.3}$	$3.1^{+0.2}_{-0.2}$	$1.2^{+0.1}_{-0.1}$	$4.4^{+0.2}_{-0.1}$	$0.07^{+0.03}_{-0.04}$	$0.06^{+0.12}_{-0.05}$	$-0.0^{+0.1}_{-0.2}$	$0.28^{+0.43}_{-0.26}$	$0.3^{+0.4}_{-0.3}$	-	-	$62.8^{+4.2}_{-6.8}$	21^{+13}_{-12}

(a) Inclination 30°.

Approximant	$\mathcal{M}^{\rm source}/M_\odot$	q	$m_1^{\rm source}/M_\odot$	$m_2^{\rm source}/M_\odot$	$M_{\rm total}^{\rm source}/M_\odot$	$\chi_{\rm eff}$	$\lvert s_1\rvert$	$s_{1,z}$	$\lvert s_2\rvert$	$s_{2,z}$	Λ_2	$r_{\rm NS}$/km	D_L/Mpc	$\theta_{JN}/^\circ$
True value	1.69	2.0	2.78	1.39	4.17	0.00	0.0	0.0	0.0	0.0	791	14.4	37.3	70
SEOB	$1.68^{+0.01}_{-0.00}$	$2.5^{+0.4}_{-0.4}$	$3.1^{+0.3}_{-0.3}$	$1.2^{+0.1}_{-0.1}$	$4.4^{+0.2}_{-0.2}$	$0.06^{+0.04}_{-0.05}$	$0.07^{+0.14}_{-0.07}$	$0.1^{+0.1}_{-0.2}$	$0.14^{+0.40}_{-0.13}$	$0.0^{+0.4}_{-0.4}$	-	-	$53.3^{+13.1}_{-17.5}$	39^{+33}_{-29}
SEOBT	$1.68^{+0.01}_{-0.00}$	$2.0^{+0.5}_{-0.6}$	$2.7^{+0.4}_{-0.5}$	$1.4^{+0.3}_{-0.1}$	$4.1^{+0.2}_{-0.2}$	$0.00^{+0.06}_{-0.06}$	$0.06^{+0.20}_{-0.05}$	$0.0^{+0.2}_{-0.2}$	$0.11^{+0.41}_{-0.10}$	$0.0^{+0.4}_{-0.4}$	417^{+271}_{-296}	$12.2^{+2.3}_{-3.0}$	$53.4^{+13.1}_{-17.3}$	39^{+32}_{-29}
SEOBNSBH	$1.68^{+0.01}_{-0.00}$	$1.9^{+0.3}_{-0.5}$	$2.7^{+0.2}_{-0.4}$	$1.4^{+0.2}_{-0.1}$	$4.1^{+0.1}_{-0.2}$	$0.00^{+0.04}_{-0.05}$	$0.02^{+0.08}_{-0.02}$	$0.0^{+0.1}_{-0.1}$	$0.00^{+0.00}_{-0.00}$	$0.0^{+0.0}_{-0.0}$	507^{+203}_{-200}	$12.6^{+1.9}_{-1.6}$	$54.1^{+11.4}_{-17.7}$	37^{+33}_{-26}
IMRNSBH	$1.68^{+0.01}_{-0.00}$	$2.0^{+0.3}_{-0.5}$	$2.7^{+0.2}_{-0.4}$	$1.4^{+0.2}_{-0.1}$	$4.1^{+0.1}_{-0.2}$	$0.00^{+0.04}_{-0.05}$	$0.02^{+0.07}_{-0.02}$	$0.0^{+0.1}_{-0.1}$	$0.00^{+0.00}_{-0.00}$	$0.0^{+0.0}_{-0.0}$	693^{+215}_{-216}	$13.2^{+1.5}_{-1.4}$	$55.2^{+11.3}_{-18.2}$	36^{+33}_{-26}
IMRp	$1.68^{+0.01}_{-0.00}$	$2.5^{+0.4}_{-0.3}$	$3.1^{+0.2}_{-0.2}$	$1.2^{+0.1}_{-0.1}$	$4.4^{+0.2}_{-0.2}$	$0.06^{+0.03}_{-0.04}$	$0.12^{+0.15}_{-0.11}$	$0.0^{+0.1}_{-0.1}$	$0.30^{+0.44}_{-0.26}$	$0.1^{+0.3}_{-0.2}$	-	-	$64.1^{+3.8}_{-26.4}$	18^{+51}_{-14}
IMRpT	$1.68^{+0.01}_{-0.00}$	$1.9^{+0.4}_{-0.7}$	$2.7^{+0.3}_{-0.6}$	$1.4^{+0.3}_{-0.1}$	$4.1^{+0.2}_{-0.2}$	$0.00^{+0.05}_{-0.06}$	$0.09^{+0.24}_{-0.08}$	$0.0^{+0.1}_{-0.1}$	$0.16^{+0.52}_{-0.15}$	$0.0^{+0.2}_{-0.2}$	522^{+287}_{-264}	$12.9^{+2.1}_{-2.3}$	$62.5^{+5.2}_{-24.8}$	22^{+46}_{-18}
XHM	$1.68^{+0.00}_{-0.00}$	$2.6^{+0.4}_{-0.3}$	$3.2^{+0.3}_{-0.2}$	$1.2^{+0.1}_{-0.1}$	$4.4^{+0.2}_{-0.1}$	$0.07^{+0.03}_{-0.04}$	$0.06^{+0.11}_{-0.06}$	$0.1^{+0.1}_{-0.1}$	$0.12^{+0.31}_{-0.11}$	$0.1^{+0.3}_{-0.3}$	-	-	$54.8^{+8.2}_{-11.6}$	38^{+18}_{-15}

(b) Inclination 70°.

Table C.2: Properties of the q=2, SNR 70 simulation, as recovered by the listed approximants. We report the 1D median and the symmetric 90% CI.

Approximant	$\mathcal{M}^{\rm source}/M_\odot$	q	$m_1^{\rm source}/M_\odot$	$m_2^{\rm source}/M_\odot$	$M_{\rm total}^{\rm source}/M_\odot$	$\chi_{\rm eff}$	$\lvert s_1\rvert$	$s_{1,z}$	$\lvert s_2\rvert$	$s_{2,z}$	Λ_2	$r_{\rm NS}$/km	D_L/Mpc	$\theta_{JN}/^\circ$
True value	1.91	3.0	3.90	1.30	5.21	0.00	0.0	0.0	0.0	0.0	624	12.3	170.0	30
SEOB	$1.91^{+0.03}_{-0.01}$	$3.0^{+0.4}_{-0.6}$	$3.9^{+0.3}_{-0.5}$	$1.3^{+0.1}_{-0.1}$	$5.2^{+0.2}_{-0.3}$	$0.00^{+0.05}_{-0.08}$	$0.04^{+0.13}_{-0.04}$	$0.0^{+0.1}_{-0.2}$	$0.12^{+0.43}_{-0.12}$	$0.0^{+0.4}_{-0.4}$	-	-	$161.8^{+34.3}_{-61.9}$	36^{+41}_{-26}
SEOBT	$1.91^{+0.03}_{-0.01}$	$2.6^{+0.7}_{-1.1}$	$3.6^{+0.5}_{-0.9}$	$1.4^{+0.4}_{-0.1}$	$5.0^{+0.4}_{-0.5}$	$-0.05^{+0.08}_{-0.13}$	$0.07^{+0.24}_{-0.07}$	$-0.0^{+0.2}_{-0.3}$	$0.15^{+0.45}_{-0.15}$	$-0.0^{+0.4}_{-0.5}$	726^{+1131}_{-626}	$13.5^{+3.5}_{-4.2}$	$163.8^{+33.0}_{-64.0}$	35^{+42}_{-26}
SEOBNSBH	$1.91^{+0.02}_{-0.01}$	$2.7^{+0.5}_{-1.1}$	$3.7^{+0.4}_{-0.9}$	$1.4^{+0.4}_{-0.1}$	$5.1^{+0.3}_{-0.5}$	$-0.03^{+0.06}_{-0.13}$	$0.04^{+0.22}_{-0.04}$	$-0.0^{+0.1}_{-0.2}$	$0.00^{+0.00}_{-0.00}$	$0.0^{+0.0}_{-0.0}$	745^{+1086}_{-618}	$13.2^{+4.2}_{-3.7}$	$161.6^{+32.3}_{-59.0}$	35^{+35}_{-25}
LEA+	$1.91^{+0.02}_{-0.01}$	$3.0^{+0.5}_{-0.4}$	$3.9^{+0.4}_{-0.3}$	$1.3^{+0.1}_{-0.1}$	$5.2^{+0.3}_{-0.2}$	$0.00^{+0.05}_{-0.04}$	$0.02^{+0.05}_{-0.02}$	$0.0^{+0.1}_{-0.1}$	-	-	1105^{+1795}_{-949}	$13.2^{+2.9}_{-3.8}$	$162.7^{+33.6}_{-61.3}$	35^{+38}_{-26}
IMRNSBH	$1.91^{+0.02}_{-0.01}$	$2.9^{+0.5}_{-0.9}$	$3.8^{+0.3}_{-0.7}$	$1.3^{+0.3}_{-0.1}$	$5.1^{+0.3}_{-0.4}$	$-0.01^{+0.05}_{-0.11}$	$0.03^{+0.15}_{-0.03}$	$-0.0^{+0.1}_{-0.2}$	$0.00^{+0.00}_{-0.00}$	$0.0^{+0.0}_{-0.0}$	1005^{+1181}_{-778}	$13.5^{+3.3}_{-3.4}$	$164.3^{+31.5}_{-60.7}$	34^{+37}_{-24}
IMRp	$1.90^{+0.03}_{-0.01}$	$3.2^{+0.7}_{-0.7}$	$4.1^{+0.5}_{-0.5}$	$1.3^{+0.1}_{-0.1}$	$5.3^{+0.4}_{-0.4}$	$0.02^{+0.07}_{-0.07}$	$0.11^{+0.26}_{-0.10}$	$0.0^{+0.1}_{-0.1}$	$0.36^{+0.50}_{-0.33}$	$0.0^{+0.4}_{-0.4}$	-	-	$180.1^{+19.7}_{-71.2}$	23^{+59}_{-18}
IMRpT	$1.90^{+0.03}_{-0.01}$	$2.7^{+0.7}_{-1.4}$	$3.7^{+0.5}_{-1.2}$	$1.4^{+0.5}_{-0.1}$	$5.0^{+0.4}_{-0.6}$	$-0.04^{+0.09}_{-0.14}$	$0.11^{+0.33}_{-0.10}$	$-0.0^{+0.1}_{-0.2}$	$0.30^{+0.53}_{-0.27}$	$-0.0^{+0.3}_{-0.4}$	739^{+1289}_{-627}	$13.6^{+3.5}_{-4.3}$	$178.7^{+20.9}_{-67.9}$	25^{+59}_{-19}
XHM	$1.90^{+0.02}_{-0.01}$	$3.1^{+0.8}_{-0.7}$	$4.0^{+0.5}_{-0.5}$	$1.3^{+0.2}_{-0.1}$	$5.3^{+0.4}_{-0.4}$	$0.01^{+0.08}_{-0.09}$	$0.05^{+0.12}_{-0.05}$	$0.0^{+0.1}_{-0.1}$	$0.11^{+0.35}_{-0.10}$	$0.0^{+0.4}_{-0.3}$	-	-	$174.8^{+25.0}_{-48.1}$	30^{+119}_{-21}

(a) Inclination 30°.

Approximant	$\mathcal{M}^{\rm source}/M_\odot$	q	$m_1^{\rm source}/M_\odot$	$m_2^{\rm source}/M_\odot$	$M_{\rm total}^{\rm source}/M_\odot$	$\chi_{\rm eff}$	$\lvert s_1\rvert$	$s_{1,z}$	$\lvert s_2\rvert$	$s_{2,z}$	Λ_2	$r_{\rm NS}$/km	D_L/Mpc	$\theta_{JN}/^\circ$
True value	1.94	3.0	3.97	1.32	5.30	0.00	0.0	0.0	0.0	0.0	624	12.3	85.5	70
SEOB	$1.91^{+0.03}_{-0.01}$	$3.0^{+0.4}_{-0.6}$	$4.0^{+0.3}_{-0.5}$	$1.3^{+0.1}_{-0.1}$	$5.2^{+0.2}_{-0.3}$	$0.00^{+0.05}_{-0.08}$	$0.04^{+0.13}_{-0.04}$	$0.0^{+0.1}_{-0.2}$	$0.13^{+0.43}_{-0.12}$	$0.0^{+0.5}_{-0.4}$	-	-	$159.2^{+34.0}_{-63.1}$	36^{+40}_{-26}
SEOBT	$1.91^{+0.03}_{-0.01}$	$2.6^{+0.7}_{-1.0}$	$3.6^{+0.5}_{-0.8}$	$1.4^{+0.3}_{-0.1}$	$5.0^{+0.4}_{-0.5}$	$-0.05^{+0.08}_{-0.13}$	$0.07^{+0.21}_{-0.06}$	$-0.0^{+0.1}_{-0.2}$	$0.15^{+0.44}_{-0.15}$	$-0.0^{+0.4}_{-0.5}$	712^{+1173}_{-618}	$13.4^{+3.7}_{-4.3}$	$159.7^{+33.7}_{-63.3}$	36^{+41}_{-26}
SEOBNSBH	$1.91^{+0.02}_{-0.01}$	$2.7^{+0.6}_{-1.1}$	$3.7^{+0.4}_{-0.9}$	$1.4^{+0.4}_{-0.1}$	$5.1^{+0.3}_{-0.5}$	$-0.03^{+0.06}_{-0.13}$	$0.05^{+0.21}_{-0.04}$	$-0.0^{+0.1}_{-0.2}$	$0.00^{+0.00}_{-0.00}$	$0.0^{+0.0}_{-0.0}$	718^{+1117}_{-597}	$13.1^{+4.3}_{-3.7}$	$158.8^{+31.5}_{-59.6}$	35^{+35}_{-24}
LEA+	$1.91^{+0.03}_{-0.01}$	$3.0^{+0.5}_{-0.4}$	$3.9^{+0.4}_{-0.3}$	$1.3^{+0.1}_{-0.1}$	$5.2^{+0.3}_{-0.2}$	$0.00^{+0.06}_{-0.04}$	$0.02^{+0.05}_{-0.02}$	$0.0^{+0.1}_{-0.1}$	-	-	1113^{+1747}_{-949}	$13.3^{+2.8}_{-3.8}$	$159.9^{+33.7}_{-64.3}$	35^{+40}_{-26}
IMRNSBH	$1.91^{+0.02}_{-0.01}$	$2.9^{+0.5}_{-0.9}$	$3.8^{+0.3}_{-0.7}$	$1.3^{+0.2}_{-0.1}$	$5.2^{+0.2}_{-0.4}$	$-0.01^{+0.05}_{-0.10}$	$0.03^{+0.14}_{-0.03}$	$-0.0^{+0.1}_{-0.2}$	$0.00^{+0.00}_{-0.00}$	$0.0^{+0.0}_{-0.0}$	985^{+1123}_{-753}	$13.4^{+3.2}_{-3.3}$	$161.5^{+31.6}_{-61.5}$	35^{+37}_{-24}
IMRp	$1.90^{+0.03}_{-0.01}$	$3.2^{+0.6}_{-0.5}$	$4.1^{+0.4}_{-0.4}$	$1.3^{+0.1}_{-0.1}$	$5.3^{+0.3}_{-0.3}$	$0.03^{+0.06}_{-0.07}$	$0.08^{+0.21}_{-0.07}$	$0.0^{+0.1}_{-0.1}$	$0.33^{+0.48}_{-0.30}$	$0.0^{+0.4}_{-0.2}$	-	-	$176.2^{+20.3}_{-64.5}$	25^{+44}_{-19}
IMRpT	$1.90^{+0.03}_{-0.01}$	$2.7^{+0.7}_{-1.1}$	$3.7^{+0.5}_{-0.9}$	$1.4^{+0.4}_{-0.1}$	$5.0^{+0.4}_{-0.5}$	$-0.04^{+0.08}_{-0.12}$	$0.11^{+0.29}_{-0.10}$	$-0.0^{+0.1}_{-0.2}$	$0.30^{+0.51}_{-0.28}$	$-0.0^{+0.3}_{-0.4}$	817^{+1228}_{-693}	$13.6^{+3.2}_{-4.3}$	$176.7^{+20.3}_{-64.4}$	25^{+48}_{-19}
XHM	$1.92^{+0.02}_{-0.02}$	$3.2^{+0.7}_{-0.6}$	$4.0^{+0.5}_{-0.5}$	$1.3^{+0.1}_{-0.1}$	$5.3^{+0.4}_{-0.3}$	$0.02^{+0.07}_{-0.08}$	$0.05^{+0.12}_{-0.05}$	$0.0^{+0.1}_{-0.2}$	$0.15^{+0.41}_{-0.15}$	$0.0^{+0.5}_{-0.4}$	-	-	$131.9^{+45.6}_{-44.8}$	53^{+76}_{-27}

(b) Inclination 70°.

Table C.3: Properties of the q=3, SNR 30 simulation, as recovered by the listed approximants. We report the 1D median and the symmetric 90% CI.

Approximant	$\mathcal{M}^{\rm source}/M_\odot$	q	$m_1^{\rm source}/M_\odot$	$m_2^{\rm source}/M_\odot$	$M_{\rm total}^{\rm source}/M_\odot$	$\chi_{\rm eff}$	$\lvert s_1\rvert$	$s_{1,z}$	$\lvert s_2\rvert$	$s_{2,z}$	Λ_2	$r_{\rm NS}$/km	D_L/Mpc	$\theta_{JN}/^\circ$
True value	1.95	3.0	3.99	1.33	5.31	0.00	0.0	0.0	0.0	0.0	624	12.3	73.0	30
SEOB	$1.95^{+0.01}_{-0.01}$	$3.1^{+0.3}_{-0.3}$	$4.1^{+0.2}_{-0.2}$	$1.3^{+0.1}_{-0.1}$	$5.4^{+0.2}_{-0.1}$	$0.02^{+0.03}_{-0.03}$	$0.04^{+0.12}_{-0.03}$	$0.0^{+0.1}_{-0.1}$	$0.11^{+0.40}_{-0.10}$	$0.0^{+0.4}_{-0.4}$	-	-	$71.1^{+11.8}_{-21.9}$	33^{+26}_{-24}
SEOBT	$1.95^{+0.01}_{-0.00}$	$2.8^{+0.4}_{-0.6}$	$3.8^{+0.3}_{-0.4}$	$1.4^{+0.1}_{-0.1}$	$5.2^{+0.2}_{-0.3}$	$-0.02^{+0.04}_{-0.07}$	$0.05^{+0.15}_{-0.04}$	$-0.0^{+0.1}_{-0.2}$	$0.11^{+0.41}_{-0.11}$	$0.0^{+0.4}_{-0.4}$	380^{+606}_{-342}	$11.7^{+3.1}_{-3.5}$	$71.7^{+11.3}_{-21.6}$	32^{+27}_{-23}
SEOBNSBH	$1.95^{+0.01}_{-0.00}$	$2.8^{+0.3}_{-0.5}$	$3.9^{+0.2}_{-0.4}$	$1.4^{+0.1}_{-0.1}$	$5.2^{+0.2}_{-0.2}$	$-0.02^{+0.04}_{-0.05}$	$0.03^{+0.08}_{-0.02}$	$-0.0^{+0.0}_{-0.1}$	$0.00^{+0.00}_{-0.00}$	$0.0^{+0.0}_{-0.0}$	481^{+358}_{-359}	$12.0^{+2.0}_{-2.6}$	$71.7^{+10.7}_{-21.2}$	31^{+26}_{-22}
LEA+	$1.95^{+0.01}_{-0.00}$	$3.0^{+0.3}_{-0.3}$	$4.0^{+0.2}_{-0.3}$	$1.3^{+0.1}_{-0.1}$	$5.3^{+0.2}_{-0.2}$	$0.00^{+0.04}_{-0.04}$	$0.02^{+0.04}_{-0.02}$	$0.0^{+0.0}_{-0.1}$	-	-	888^{+512}_{-556}	$13.1^{+1.6}_{-2.4}$	$71.5^{+11.5}_{-22.7}$	32^{+28}_{-23}
IMRNSBH	$1.95^{+0.01}_{-0.00}$	$2.9^{+0.3}_{-0.5}$	$3.9^{+0.2}_{-0.4}$	$1.3^{+0.1}_{-0.1}$	$5.3^{+0.2}_{-0.3}$	$0.00^{+0.03}_{-0.05}$	$0.02^{+0.07}_{-0.02}$	$-0.0^{+0.0}_{-0.1}$	$0.00^{+0.00}_{-0.00}$	$0.0^{+0.0}_{-0.0}$	831^{+377}_{-419}	$13.0^{+1.7}_{-1.9}$	$72.5^{+10.6}_{-21.3}$	31^{+26}_{-22}
IMRp	$1.94^{+0.01}_{-0.00}$	$3.3^{+0.3}_{-0.2}$	$4.2^{+0.2}_{-0.2}$	$1.3^{+0.0}_{-0.1}$	$5.5^{+0.2}_{-0.1}$	$0.04^{+0.03}_{-0.03}$	$0.07^{+0.14}_{-0.06}$	$0.0^{+0.1}_{-0.1}$	$0.28^{+0.43}_{-0.22}$	$0.1^{+0.2}_{-0.2}$	-	-	$79.9^{+4.2}_{-18.8}$	17^{+28}_{-13}
IMRpT	$1.94^{+0.01}_{-0.00}$	$2.5^{+0.7}_{-1.3}$	$3.6^{+0.5}_{-1.1}$	$1.4^{+0.6}_{-0.1}$	$5.1^{+0.4}_{-0.6}$	$-0.04^{+0.07}_{-0.11}$	$0.17^{+0.34}_{-0.15}$	$-0.1^{+0.1}_{-0.3}$	$0.34^{+0.52}_{-0.31}$	$0.0^{+0.3}_{-0.4}$	371^{+685}_{-319}	$12.8^{+3.2}_{-3.9}$	$81.2^{+3.4}_{-16.8}$	14^{+28}_{-11}
XHM	$1.95^{+0.00}_{-0.00}$	$3.3^{+0.3}_{-0.3}$	$4.2^{+0.2}_{-0.2}$	$1.3^{+0.1}_{-0.1}$	$5.5^{+0.2}_{-0.2}$	$0.04^{+0.03}_{-0.03}$	$0.04^{+0.10}_{-0.04}$	$0.0^{+0.1}_{-0.1}$	$0.13^{+0.39}_{-0.13}$	$0.1^{+0.4}_{-0.3}$	-	-	$75.3^{+6.0}_{-8.3}$	27^{+12}_{-10}

(a) Inclination 30°.

Approximant	$\mathcal{M}^{\rm source}/M_\odot$	q	$m_1^{\rm source}/M_\odot$	$m_2^{\rm source}/M_\odot$	$M_{\rm total}^{\rm source}/M_\odot$	$\chi_{\rm eff}$	$\lvert s_1\rvert$	$s_{1,z}$	$\lvert s_2\rvert$	$s_{2,z}$	Λ_2	$r_{\rm NS}$/km	D_L/Mpc	$\theta_{JN}/^\circ$
True value	1.96	3.0	4.02	1.34	5.36	0.00	0.0	0.0	0.0	0.0	624	12.3	36.6	70
SEOB	$1.95^{+0.01}_{-0.01}$	$3.1^{+0.3}_{-0.3}$	$4.1^{+0.2}_{-0.2}$	$1.3^{+0.1}_{-0.1}$	$5.4^{+0.2}_{-0.1}$	$0.02^{+0.03}_{-0.03}$	$0.04^{+0.11}_{-0.03}$	$0.0^{+0.1}_{-0.1}$	$0.10^{+0.39}_{-0.10}$	$0.0^{+0.4}_{-0.4}$	-	-	$65.5^{+15.8}_{-27.1}$	39^{+32}_{-28}
SEOBT	$1.95^{+0.01}_{-0.01}$	$2.8^{+0.4}_{-0.6}$	$3.8^{+0.3}_{-0.5}$	$1.4^{+0.2}_{-0.1}$	$5.2^{+0.2}_{-0.3}$	$-0.02^{+0.04}_{-0.07}$	$0.05^{+0.18}_{-0.05}$	$-0.0^{+0.1}_{-0.2}$	$0.13^{+0.45}_{-0.12}$	$0.0^{+0.5}_{-0.4}$	357^{+577}_{-318}	$11.6^{+3.2}_{-3.4}$	$65.8^{+15.6}_{-27.8}$	39^{+33}_{-28}
SEOBNSBH	$1.95^{+0.01}_{-0.01}$	$2.9^{+0.3}_{-0.5}$	$3.9^{+0.2}_{-0.4}$	$1.4^{+0.1}_{-0.1}$	$5.3^{+0.2}_{-0.2}$	$-0.01^{+0.03}_{-0.05}$	$0.02^{+0.07}_{-0.02}$	$-0.0^{+0.0}_{-0.1}$	$0.00^{+0.00}_{-0.00}$	$0.0^{+0.0}_{-0.0}$	474^{+362}_{-350}	$12.0^{+2.0}_{-2.5}$	$66.7^{+14.0}_{-27.5}$	37^{+33}_{-26}
LEA+	$1.95^{+0.01}_{-0.01}$	$3.0^{+0.4}_{-0.3}$	$4.0^{+0.3}_{-0.2}$	$1.3^{+0.1}_{-0.1}$	$5.3^{+0.2}_{-0.2}$	$0.00^{+0.04}_{-0.04}$	$0.02^{+0.04}_{-0.02}$	$0.0^{+0.0}_{-0.1}$	-	-	891^{+510}_{-570}	$13.1^{+1.6}_{-2.4}$	$64.7^{+16.6}_{-26.9}$	40^{+32}_{-29}
IMRNSBH	$1.95^{+0.01}_{-0.01}$	$2.9^{+0.3}_{-0.5}$	$3.9^{+0.2}_{-0.4}$	$1.3^{+0.1}_{-0.1}$	$5.3^{+0.2}_{-0.3}$	$0.00^{+0.03}_{-0.05}$	$0.02^{+0.06}_{-0.02}$	$0.0^{+0.0}_{-0.1}$	$0.00^{+0.00}_{-0.00}$	$0.0^{+0.0}_{-0.0}$	852^{+357}_{-407}	$13.1^{+1.7}_{-1.8}$	$67.7^{+13.7}_{-28.3}$	36^{+33}_{-26}
IMRp	$1.94^{+0.01}_{-0.00}$	$3.4^{+0.3}_{-0.2}$	$4.3^{+0.2}_{-0.2}$	$1.3^{+0.0}_{-0.0}$	$5.5^{+0.1}_{-0.1}$	$0.04^{+0.02}_{-0.03}$	$0.08^{+0.16}_{-0.06}$	$0.0^{+0.1}_{-0.1}$	$0.27^{+0.51}_{-0.24}$	$0.1^{+0.3}_{-0.3}$	-	-	$78.7^{+4.1}_{-21.5}$	17^{+32}_{-13}
IMRpT	$1.94^{+0.01}_{-0.00}$	$2.8^{+0.4}_{-1.4}$	$3.8^{+0.3}_{-1.2}$	$1.4^{+0.5}_{-0.1}$	$5.2^{+0.2}_{-0.7}$	$-0.02^{+0.05}_{-0.13}$	$0.07^{+0.30}_{-0.07}$	$-0.0^{+0.1}_{-0.3}$	$0.23^{+0.55}_{-0.21}$	$-0.0^{+0.3}_{-0.4}$	530^{+639}_{-422}	$12.9^{+3.0}_{-3.4}$	$78.7^{+4.5}_{-33.3}$	18^{+47}_{-14}
XHM	$1.96^{+0.00}_{-0.01}$	$3.3^{+0.3}_{-0.3}$	$4.3^{+0.2}_{-0.2}$	$1.3^{+0.1}_{-0.0}$	$5.5^{+0.2}_{-0.2}$	$0.04^{+0.03}_{-0.03}$	$0.04^{+0.09}_{-0.04}$	$0.0^{+0.1}_{-0.1}$	$0.15^{+0.38}_{-0.14}$	$0.1^{+0.4}_{-0.3}$	-	-	$47.8^{+12.3}_{-10.8}$	61^{+13}_{-15}

(b) Inclination 70°.

Table C.4: Properties of the q=3, SNR 70 simulation, as recovered by the listed approximants. We report the 1D median and the symmetric 90% CI.

Approximant	$\mathcal{M}^{\rm source}/M_\odot$	q	$m_1^{\rm source}/M_\odot$	$m_2^{\rm source}/M_\odot$	$M_{\rm total}^{\rm source}/M_\odot$	$\chi_{\rm eff}$	$\lvert s_1\rvert$	$s_{1,z}$	$\lvert s_2\rvert$	$s_{2,z}$	Λ_2	$r_{\rm NS}$/km	D_L/Mpc	$\theta_{JN}/^\circ$
True value	2.65	6.0	8.00	1.33	9.33	0.00	0.0	0.0	0.0	0.0	526	13.3	229.5	30
SEOB	$2.652^{+0.043}_{-0.023}$	$6.1^{+0.9}_{-0.8}$	$8.1^{+0.7}_{-0.6}$	$1.3^{+0.1}_{-0.1}$	$9.4^{+0.6}_{-0.5}$	$0.01^{+0.06}_{-0.07}$	$0.03^{+0.08}_{-0.03}$	$0.0^{+0.1}_{-0.1}$	$0.15^{+0.45}_{-0.14}$	$0.0^{+0.5}_{-0.5}$	-	-	$221.4^{+44.0}_{-77.4}$	34^{+30}_{-25}
SEOBT	$2.650^{+0.043}_{-0.024}$	$5.4^{+1.1}_{-1.4}$	$7.5^{+0.8}_{-1.2}$	$1.4^{+0.2}_{-0.1}$	$8.9^{+0.7}_{-1.0}$	$-0.05^{+0.09}_{-0.14}$	$0.06^{+0.20}_{-0.06}$	$-0.1^{+0.1}_{-0.2}$	$0.18^{+0.49}_{-0.17}$	$0.0^{+0.5}_{-0.6}$	1990^{+1788}_{-1790}	$15.7^{+4.0}_{-5.2}$	$221.5^{+44.5}_{-78.6}$	34^{+31}_{-25}
SEOBNSBH	$2.651^{+0.041}_{-0.022}$	$5.8^{+0.7}_{-1.2}$	$7.9^{+0.6}_{-0.9}$	$1.4^{+0.1}_{-0.1}$	$9.2^{+0.5}_{-0.8}$	$-0.01^{+0.05}_{-0.10}$	$0.03^{+0.11}_{-0.03}$	$-0.0^{+0.1}_{-0.1}$	$0.00^{+0.00}_{-0.00}$	$0.0^{+0.0}_{-0.0}$	1938^{+2524}_{-1691}	$15.3^{+3.8}_{-4.8}$	$221.9^{+40.9}_{-75.4}$	33^{+29}_{-23}
IMRNSBH	$2.648^{+0.042}_{-0.022}$	$6.0^{+0.7}_{-1.0}$	$8.0^{+0.5}_{-0.8}$	$1.3^{+0.1}_{-0.1}$	$9.3^{+0.5}_{-0.7}$	$0.00^{+0.05}_{-0.08}$	$0.02^{+0.08}_{-0.02}$	$0.0^{+0.1}_{-0.1}$	$0.00^{+0.00}_{-0.00}$	$0.0^{+0.0}_{-0.0}$	2591^{+2120}_{-2212}	$15.9^{+3.0}_{-4.8}$	$227.3^{+40.8}_{-76.9}$	33^{+29}_{-23}
IMRp	$2.640^{+0.040}_{-0.014}$	$6.2^{+0.6}_{-0.5}$	$8.1^{+0.5}_{-0.4}$	$1.3^{+0.0}_{-0.1}$	$9.5^{+0.4}_{-0.3}$	$0.01^{+0.05}_{-0.04}$	$0.05^{+0.12}_{-0.04}$	$0.0^{+0.1}_{-0.0}$	$0.32^{+0.54}_{-0.28}$	$0.0^{+0.4}_{-0.3}$	-	-	$243.9^{+25.8}_{-75.2}$	22^{+33}_{-17}
IMRpT	$2.636^{+0.040}_{-0.014}$	$5.6^{+0.8}_{-3.2}$	$7.6^{+0.6}_{-2.9}$	$1.4^{+0.6}_{-0.1}$	$9.0^{+0.6}_{-2.3}$	$-0.04^{+0.07}_{-0.26}$	$0.09^{+0.43}_{-0.08}$	$-0.0^{+0.1}_{-0.4}$	$0.37^{+0.53}_{-0.33}$	$0.0^{+0.5}_{-0.6}$	1710^{+1986}_{-1527}	$15.7^{+5.3}_{-5.3}$	$248.3^{+23.9}_{-73.6}$	20^{+33}_{-15}
XHM	$2.644^{+0.020}_{-0.014}$	$6.3^{+0.8}_{-0.7}$	$8.2^{+0.6}_{-0.5}$	$1.3^{+0.1}_{-0.1}$	$9.5^{+0.5}_{-0.5}$	$0.02^{+0.05}_{-0.05}$	$0.03^{+0.07}_{-0.03}$	$0.0^{+0.1}_{-0.1}$	$0.13^{+0.34}_{-0.13}$	$0.0^{+0.4}_{-0.4}$	-	-	$237.1^{+27.3}_{-37.0}$	28^{+14}_{-13}

(a) Inclination 30°.

Approximant	$\mathcal{M}^{\rm source}/M_\odot$	q	$m_1^{\rm source}/M_\odot$	$m_2^{\rm source}/M_\odot$	$M_{\rm total}^{\rm source}/M_\odot$	$\chi_{\rm eff}$	$\lvert s_1\rvert$	$s_{1,z}$	$\lvert s_2\rvert$	$s_{2,z}$	Λ_2	$r_{\rm NS}$/km	D_L/Mpc	$\theta_{JN}/^\circ$
True value	2.72	6.0	8.23	1.37	9.60	0.00	0.0	0.0	0.0	0.0	526	13.3	95.4	70
SEOB	$2.651^{+0.045}_{-0.023}$	$6.1^{+0.9}_{-0.8}$	$8.1^{+0.7}_{-0.6}$	$1.3^{+0.1}_{-0.1}$	$9.4^{+0.6}_{-0.5}$	$0.01^{+0.06}_{-0.07}$	$0.03^{+0.08}_{-0.03}$	$0.0^{+0.1}_{-0.1}$	$0.15^{+0.47}_{-0.15}$	$0.0^{+0.5}_{-0.5}$	-	-	$222.5^{+44.3}_{-80.5}$	34^{+29}_{-25}
SEOBT	$2.648^{+0.043}_{-0.023}$	$5.4^{+1.0}_{-1.4}$	$7.6^{+0.8}_{-1.2}$	$1.4^{+0.2}_{-0.1}$	$9.0^{+0.7}_{-1.0}$	$-0.05^{+0.09}_{-0.14}$	$0.06^{+0.19}_{-0.05}$	$-0.0^{+0.1}_{-0.2}$	$0.16^{+0.48}_{-0.16}$	$0.0^{+0.5}_{-0.5}$	1936^{+1857}_{-1738}	$15.6^{+3.9}_{-5.2}$	$224.3^{+43.3}_{-79.0}$	34^{+29}_{-24}
SEOBNSBH	$2.650^{+0.040}_{-0.021}$	$5.8^{+0.7}_{-1.1}$	$7.9^{+0.6}_{-0.9}$	$1.4^{+0.1}_{-0.1}$	$9.2^{+0.5}_{-0.8}$	$-0.01^{+0.05}_{-0.10}$	$0.03^{+0.11}_{-0.03}$	$-0.0^{+0.1}_{-0.1}$	$0.00^{+0.00}_{-0.00}$	$0.0^{+0.0}_{-0.0}$	1864^{+2526}_{-1619}	$15.1^{+3.8}_{-4.6}$	$223.0^{+40.8}_{-73.8}$	33^{+27}_{-23}
IMRNSBH	$2.647^{+0.042}_{-0.021}$	$6.0^{+0.7}_{-0.9}$	$8.0^{+0.5}_{-0.7}$	$1.3^{+0.1}_{-0.1}$	$9.3^{+0.5}_{-0.6}$	$0.00^{+0.05}_{-0.08}$	$0.02^{+0.07}_{-0.02}$	$0.0^{+0.1}_{-0.1}$	$0.00^{+0.00}_{-0.00}$	$0.0^{+0.0}_{-0.0}$	2449^{+2227}_{-2108}	$15.7^{+3.1}_{-4.8}$	$229.5^{+40.2}_{-77.5}$	32^{+28}_{-23}
IMRp	$2.639^{+0.039}_{-0.014}$	$6.2^{+0.7}_{-0.5}$	$8.2^{+0.5}_{-0.4}$	$1.3^{+0.0}_{-0.1}$	$9.5^{+0.5}_{-0.3}$	$0.01^{+0.05}_{-0.04}$	$0.05^{+0.12}_{-0.04}$	$0.0^{+0.1}_{-0.0}$	$0.30^{+0.56}_{-0.28}$	$0.0^{+0.4}_{-0.3}$	-	-	$245.0^{+25.9}_{-72.9}$	23^{+31}_{-17}
IMRpT	$2.634^{+0.037}_{-0.013}$	$5.4^{+1.0}_{-3.1}$	$7.5^{+0.8}_{-2.9}$	$1.4^{+0.6}_{-0.1}$	$8.9^{+0.7}_{-2.2}$	$-0.05^{+0.09}_{-0.28}$	$0.11^{+0.45}_{-0.10}$	$-0.0^{+0.1}_{-0.4}$	$0.41^{+0.50}_{-0.36}$	$0.0^{+0.5}_{-0.5}$	1549^{+2108}_{-1389}	$15.8^{+5.9}_{-5.3}$	$250.8^{+22.8}_{-67.5}$	19^{+31}_{-14}
XHM	$2.685^{+0.031}_{-0.027}$	$6.4^{+0.8}_{-0.6}$	$8.4^{+0.6}_{-0.5}$	$1.3^{+0.1}_{-0.1}$	$9.8^{+0.5}_{-0.4}$	$0.03^{+0.05}_{-0.05}$	$0.04^{+0.08}_{-0.04}$	$0.0^{+0.1}_{-0.1}$	$0.14^{+0.37}_{-0.13}$	$0.0^{+0.4}_{-0.4}$	-	-	$162.3^{+48.7}_{-54.6}$	54^{+14}_{-15}

(b) Inclination 70°.

Table C.5: Properties of the q=6, SNR 30 simulation, as recovered by the listed approximants. We report the 1D median and the symmetric 90% CI.

Approximant	$\mathcal{M}^{\rm source}/M_\odot$	q	$m_1^{\rm source}/M_\odot$	$m_2^{\rm source}/M_\odot$	$M_{\rm total}^{\rm source}/M_\odot$	$\chi_{\rm eff}$	$\lvert s_1\rvert$	$s_{1,z}$	$\lvert s_2\rvert$	$s_{2,z}$	Λ_2	$r_{\rm NS}$/km	D_L/Mpc	$\theta_{JN}/^\circ$
True value	2.72	6.0	8.22	1.37	9.59	0.00	0.0	0.0	0.0	0.0	526	13.3	98.4	30
SEOB	$2.721^{+0.016}_{-0.009}$	$6.1^{+0.4}_{-0.4}$	$8.3^{+0.3}_{-0.3}$	$1.4^{+0.0}_{-0.0}$	$9.7^{+0.3}_{-0.3}$	$0.01^{+0.03}_{-0.03}$	$0.02^{+0.06}_{-0.02}$	$0.0^{+0.1}_{-0.1}$	$0.13^{+0.42}_{-0.13}$	$0.0^{+0.5}_{-0.4}$	-	-	$97.2^{+14.9}_{-26.5}$	31^{+24}_{-23}
SEOBT	$2.719^{+0.016}_{-0.009}$	$5.4^{+0.6}_{-0.6}$	$7.7^{+0.5}_{-0.5}$	$1.4^{+0.1}_{-0.1}$	$9.1^{+0.4}_{-0.4}$	$-0.04^{+0.05}_{-0.05}$	$0.08^{+0.13}_{-0.07}$	$-0.1^{+0.1}_{-0.1}$	$0.21^{+0.55}_{-0.20}$	$0.1^{+0.6}_{-0.4}$	921^{+2273}_{-852}	$14.1^{+4.2}_{-4.6}$	$97.8^{+14.6}_{-26.6}$	31^{+24}_{-22}
SEOBNSBH	$2.720^{+0.015}_{-0.008}$	$6.0^{+0.4}_{-0.4}$	$8.2^{+0.3}_{-0.4}$	$1.4^{+0.0}_{-0.0}$	$9.6^{+0.3}_{-0.3}$	$0.00^{+0.03}_{-0.04}$	$0.01^{+0.03}_{-0.01}$	$0.0^{+0.0}_{-0.0}$	$0.00^{+0.00}_{-0.00}$	$0.0^{+0.0}_{-0.0}$	979^{+1225}_{-831}	$13.6^{+2.6}_{-3.6}$	$99.0^{+13.6}_{-25.7}$	30^{+24}_{-21}
IMRNSBH	$2.720^{+0.015}_{-0.008}$	$6.1^{+0.4}_{-0.5}$	$8.3^{+0.3}_{-0.4}$	$1.4^{+0.0}_{-0.0}$	$9.7^{+0.3}_{-0.3}$	$0.00^{+0.03}_{-0.03}$	$0.02^{+0.03}_{-0.01}$	$0.0^{+0.0}_{-0.0}$	$0.00^{+0.00}_{-0.00}$	$0.0^{+0.0}_{-0.0}$	1562^{+2058}_{-1281}	$14.6^{+3.1}_{-3.9}$	$99.5^{+13.9}_{-25.8}$	30^{+23}_{-21}
IMRp	$2.715^{+0.013}_{-0.003}$	$6.3^{+0.4}_{-0.2}$	$8.4^{+0.3}_{-0.2}$	$1.3^{+0.0}_{-0.0}$	$9.8^{+0.3}_{-0.2}$	$0.02^{+0.03}_{-0.02}$	$0.04^{+0.09}_{-0.03}$	$0.0^{+0.1}_{-0.0}$	$0.24^{+0.51}_{-0.21}$	$0.1^{+0.4}_{-0.3}$	-	-	$108.1^{+5.6}_{-23.2}$	17^{+27}_{-13}
IMRpT	$2.708^{+0.004}_{-0.003}$	$2.9^{+0.9}_{-0.8}$	$5.5^{+0.9}_{-0.9}$	$1.9^{+0.3}_{-0.2}$	$7.3^{+0.7}_{-0.6}$	$-0.18^{+0.09}_{-0.11}$	$0.42^{+0.16}_{-0.14}$	$-0.4^{+0.1}_{-0.1}$	$0.66^{+0.29}_{-0.50}$	$0.4^{+0.3}_{-0.3}$	262^{+801}_{-247}	$14.9^{+3.9}_{-4.5}$	$112.8^{+3.5}_{-7.2}$	8^{+16}_{-6}
XHM	$2.720^{+0.005}_{-0.004}$	$6.4^{+0.5}_{-0.4}$	$8.5^{+0.4}_{-0.3}$	$1.3^{+0.0}_{-0.0}$	$9.9^{+0.3}_{-0.3}$	$0.03^{+0.03}_{-0.03}$	$0.03^{+0.06}_{-0.03}$	$0.0^{+0.1}_{-0.1}$	$0.14^{+0.41}_{-0.14}$	$0.1^{+0.5}_{-0.4}$	-	-	$100.5^{+6.4}_{-8.0}$	29^{+7}_{-7}

(a) Inclination 30°.

Approximant	$\mathcal{M}^{\rm source}/M_\odot$	q	$m_1^{\rm source}/M_\odot$	$m_2^{\rm source}/M_\odot$	$M_{\rm total}^{\rm source}/M_\odot$	$\chi_{\rm eff}$	$\lvert s_1\rvert$	$s_{1,z}$	$\lvert s_2\rvert$	$s_{2,z}$	Λ_2	$r_{\rm NS}$/km	D_L/Mpc	$\theta_{JN}/^\circ$
True value	2.75	6.0	8.32	1.39	9.71	0.00	0.0	0.0	0.0	0.0	526	13.3	40.9	70
SEOB	$2.727^{+0.025}_{-0.014}$	$6.2^{+0.4}_{-0.4}$	$8.4^{+0.3}_{-0.3}$	$1.4^{+0.0}_{-0.0}$	$9.7^{+0.3}_{-0.3}$	$0.01^{+0.03}_{-0.03}$	$0.02^{+0.07}_{-0.02}$	$0.0^{+0.1}_{-0.1}$	$0.14^{+0.43}_{-0.13}$	$0.0^{+0.5}_{-0.4}$	-	-	$87.1^{+24.6}_{-42.1}$	41^{+27}_{-30}
SEOBT	$2.725^{+0.025}_{-0.014}$	$5.3^{+0.7}_{-0.6}$	$7.7^{+0.6}_{-0.5}$	$1.4^{+0.1}_{-0.1}$	$9.2^{+0.5}_{-0.5}$	$-0.04^{+0.05}_{-0.05}$	$0.08^{+0.14}_{-0.08}$	$-0.1^{+0.1}_{-0.1}$	$0.24^{+0.56}_{-0.23}$	$0.2^{+0.6}_{-0.5}$	973^{+2407}_{-911}	$14.2^{+4.3}_{-4.8}$	$87.6^{+24.5}_{-42.0}$	41^{+27}_{-30}
SEOBNSBH	$2.725^{+0.026}_{-0.013}$	$6.0^{+0.3}_{-0.4}$	$8.2^{+0.3}_{-0.3}$	$1.4^{+0.0}_{-0.0}$	$9.6^{+0.2}_{-0.3}$	$0.00^{+0.03}_{-0.03}$	$0.01^{+0.03}_{-0.01}$	$0.0^{+0.0}_{-0.0}$	$0.00^{+0.00}_{-0.00}$	$0.0^{+0.0}_{-0.0}$	986^{+807}_{-829}	$13.7^{+1.9}_{-3.5}$	$89.5^{+22.5}_{-43.0}$	39^{+28}_{-28}
IMRNSBH	$2.726^{+0.026}_{-0.014}$	$6.2^{+0.4}_{-0.4}$	$8.4^{+0.3}_{-0.3}$	$1.4^{+0.0}_{-0.0}$	$9.7^{+0.3}_{-0.3}$	$0.01^{+0.03}_{-0.03}$	$0.02^{+0.03}_{-0.02}$	$0.0^{+0.0}_{-0.0}$	$0.00^{+0.00}_{-0.00}$	$0.0^{+0.0}_{-0.0}$	1350^{+1672}_{-1106}	$14.2^{+2.8}_{-3.6}$	$89.7^{+23.5}_{-43.2}$	40^{+28}_{-29}
IMRp	$2.715^{+0.018}_{-0.003}$	$6.4^{+0.4}_{-0.3}$	$8.5^{+0.3}_{-0.2}$	$1.3^{+0.0}_{-0.0}$	$9.8^{+0.2}_{-0.2}$	$0.03^{+0.03}_{-0.02}$	$0.04^{+0.08}_{-0.04}$	$0.0^{+0.1}_{-0.0}$	$0.29^{+0.47}_{-0.26}$	$0.1^{+0.3}_{-0.3}$	-	-	$108.9^{+5.2}_{-32.0}$	16^{+34}_{-12}
IMRpT	$2.708^{+0.005}_{-0.003}$	$2.6^{+1.0}_{-0.8}$	$5.1^{+1.0}_{-0.9}$	$2.0^{+0.4}_{-0.3}$	$7.1^{+0.8}_{-0.6}$	$-0.22^{+0.12}_{-0.11}$	$0.47^{+0.24}_{-0.16}$	$-0.4^{+0.1}_{-0.2}$	$0.48^{+0.41}_{-0.36}$	$0.3^{+0.3}_{-0.2}$	186^{+713}_{-178}	$14.9^{+4.2}_{-4.4}$	$113.2^{+3.6}_{-7.5}$	8^{+17}_{-6}
XHM	$2.748^{+0.008}_{-0.009}$	$6.4^{+0.5}_{-0.4}$	$8.6^{+0.4}_{-0.3}$	$1.3^{+0.0}_{-0.0}$	$10.0^{+0.3}_{-0.3}$	$0.03^{+0.02}_{-0.03}$	$0.03^{+0.07}_{-0.03}$	$0.0^{+0.1}_{-0.1}$	$0.16^{+0.41}_{-0.15}$	$0.1^{+0.5}_{-0.4}$	-	-	$52.5^{+15.4}_{-13.8}$	64^{+8}_{-9}

(b) Inclination 70°.

Table C.6: Properties of the q=6, SNR 70 simulation, as recovered by the listed approximants. We report the 1D median and the symmetric 90% CI.

Approximant	$\mathcal{M}^{\rm det}/M_\odot$	q	$m_1^{\rm det}/M_\odot$	$m_2^{\rm det}/M_\odot$	s_1	s_2	Λ_2	D_L/Mpc
SEOB	[1.480,2.711]	[1.0,8.0]	[1.043, 9.664]	[1.043, 9.664]	[-0.99,0.99]	[-0.99,0.99]	-	[0,500]
SEOBT	[1.480,2.711]	[1.0,8.0]	[1.043, 9.664]	[1.043, 9.664]	[-0.99,0.99]	[-0.99,0.99]	[0,4000]	[0,500]
SEOBNSBH	[1.480,2.711]	[1.0,8.0]	[1.043, 9.664]	[1.043, 3.000]	[-0.5,0.8]	-	[0,5000]	[0,500]
IMRNSBH	[1.480,2.711]	[1.0,8.0]	[1.043, 9.664]	[1.043, 3.000]	[-0.5,0.5]	-	[0,5000]	[0,500]
IMRp	[1.421,2.602]	[1.0,8.0]	[1.001, 9.277]	[1.001, 9.277]	[-0.99,0.99]	[-0.99,0.99]	-	[0,500]
IMRpT	[1.421,2.602]	[1.0,8.0]	[1.001, 9.277]	[1.001, 9.277]	[-0.99,0.99]	[-0.99,0.99]	[0,4000]	[0,500]
XHM	[1.480,2.711]	[1.0,8.0]	[1.043, 9.664]	[1.043, 9.664]	[-0.99,0.99]	[-0.99,0.99]	-	[0,500]

Table C.7: Prior bounds for the q=2 simulation.

Approximant	$\mathcal{M}^{\rm det}/M_\odot$	q	$m_1^{\rm det}/M_\odot$	$m_2^{\rm det}/M_\odot$	s_1	s_2	Λ_2	D_L/Mpc
SEOB	[1.776,3.253]	[1.0,8.0]	[1.252,11.597]	[1.252,11.597]	[-0.99,0.99]	[-0.99,0.99]	-	[0,500]
SEOBT	[1.776,3.253]	[1.0,8.0]	[1.252,11.597]	[1.252,11.597]	[-0.99,0.99]	[-0.99,0.99]	[0,4000]	[0,500]
SEOBNSBH	[1.776,3.253]	[1.0,8.0]	[1.252,11.597]	[1.252, 3.000]	[-0.5,0.8]	-	[0,5000]	[0,500]
LEA+	-	[2.0,5.0]	[3.0,7.2]	[1.2,1.45]	[-0.5,0.5]	-	[0,4000]	[0,500]
IMRNSBH	[1.776,3.253]	[1.0,8.0]	[1.252,11.597]	[1.252, 3.000]	[-0.5,0.5]	-	[0,5000]	[0,500]
IMRp	[1.421,2.602]	[1.0,8.0]	[1.001, 9.277]	[1.001, 9.277]	[-0.99,0.99]	[-0.99,0.99]	-	[0,500]
IMRpT	[1.421,2.602]	[1.0,8.0]	[1.001, 9.277]	[1.001, 9.277]	[-0.99,0.99]	[-0.99,0.99]	[0,4000]	[0,500]
XHM	[1.776,3.253]	[1.0,8.0]	[1.252,11.597]	[1.252,11.597]	[-0.99,0.99]	[-0.99,0.99]	-	[0,500]

Table C.8: Prior bounds for the q=3 simulation.

Approximant	$\mathcal{M}^{\rm det}/M_\odot$	q	$m_1^{\rm det}/M_\odot$	$m_2^{\rm det}/M_\odot$	s_1	s_2	Λ_2	D_L/Mpc
SEOB	[2.184,4.016]	[1.000,17.944]	[1.000,22.953]	[1.000,22.953]	[-0.99,0.99]	[-0.99,0.99]	-	[0,500]
SEOBT	[2.184,4.016]	[1.000,17.944]	[1.000,22.953]	[1.000,22.953]	[-0.99,0.99]	[-0.99,0.99]	[0,4000]	[0,500]
SEOBNSBH	[2.184,4.016]	[1.000,17.944]	[1.000,22.953]	[1.000,3.000]	[-0.5,0.8]	-	[0,5000]	[0,500]
IMRNSBH	[2.184,4.016]	[1.000,17.944]	[1.000,22.953]	[1.000,3.000]	[-0.5,0.5]	-	[0,5000]	[0,500]
IMRp	[2.184,4.016]	[1.000,8.000]	[1.001,14.317]	[1.001,14.317]	[-0.99,0.99]	[-0.99,0.99]	-	[0,500]
IMRpT	[2.184,4.016]	[1.000,8.000]	[1.001,14.317]	[1.001,14.317]	[-0.99,0.99]	[-0.99,0.99]	[0,4000]	[0,500]
XHM	[2.184,4.016]	[1.000,17.944]	[1.000,22.953]	[1.000,22.953]	[-0.99,0.99]	[-0.99,0.99]	-	[0,500]

Table C.9: Prior bounds for the q=6 simulation.

Appendix D

Analysis Details for Calibration Error Study

D.1 η^{mis}, $\{\eta^{\mathrm{out}}\}$ and $\{\eta^{\mathrm{typ}}\}$ for the Other Five Realizations

Here, in Figs. D-1 to D-5, we show the η^{mis}, $\{\eta^{\mathrm{out}}\}$, and $\{\eta^{\mathrm{typ}}\}$ for the other five outlier cases identified for CEs during O3.

D.2 Spline Results

In Fig. D-6, we show the distance likelihoods for BNSs at an SNR of 50, where the green and purple shaded distributions are obtained from the runs with the physiCal and Spline methods, respectively, both miscalibrated by the same η^{mis}. We report ΔD_L in Tab. D.1. The differences between the results are quite small compared to those between the physiCal runs with and without CEs.

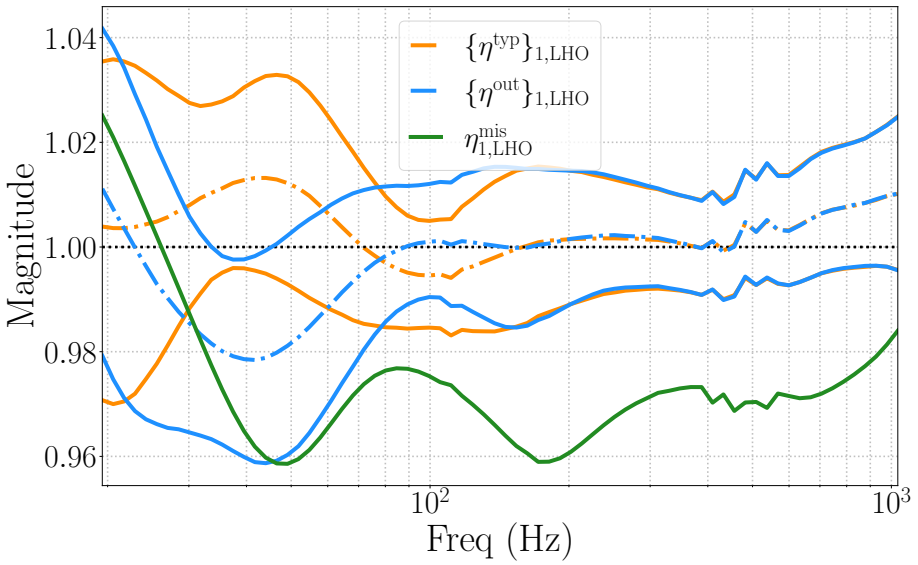

(a) Amplitude.

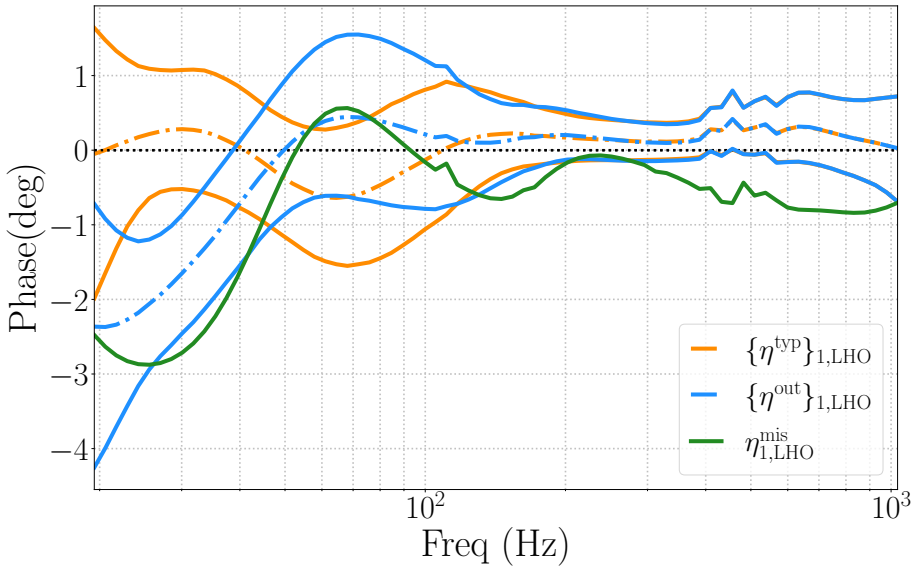

(b) Phase.

Figure D-1: Large CEs, $\{\eta^{\mathrm{out}}\}_{1,\mathrm{LHO}}$(blue), compared to the corresponding typical distribution, $\{\eta^{\mathrm{typ}}\}_{1,\mathrm{LHO}}$ (orange), both showing the edges of the 1-σ CIs in each frequency bin. $\eta^{\mathrm{mis}}_{1,\mathrm{LHO}}$ is plotted in green.

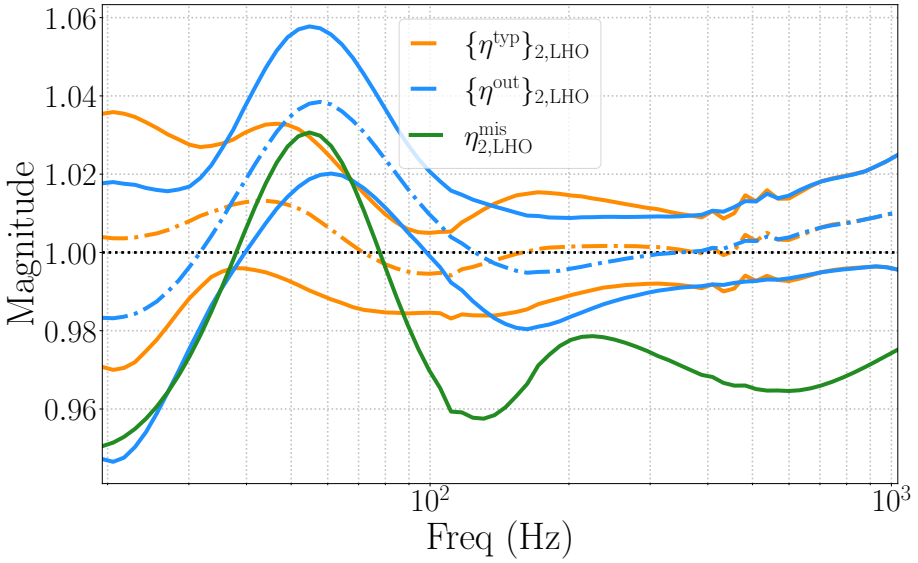

(a) Amplitude.

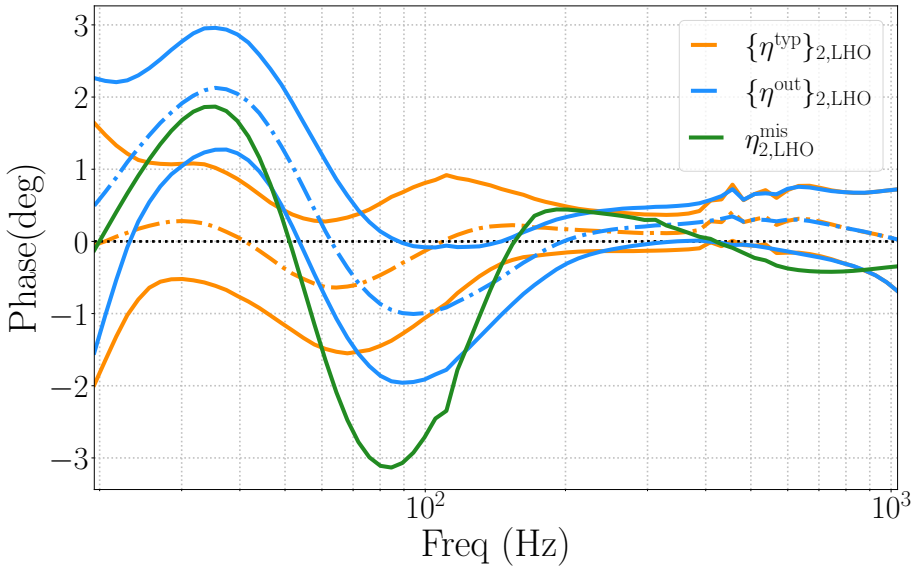

(b) Phase.

Figure D-2: Large CEs, $\{\eta^{\mathrm{out}}\}_{2,\mathrm{LHO}}$(blue), compared to the corresponding typical distribution, $\{\eta^{\mathrm{typ}}\}_{2,\mathrm{LHO}}$ (orange), both showing the edges of the 1-σ CIs in each frequency bin. $\eta^{\mathrm{mis}}_{2,\mathrm{LHO}}$ is plotted in green.

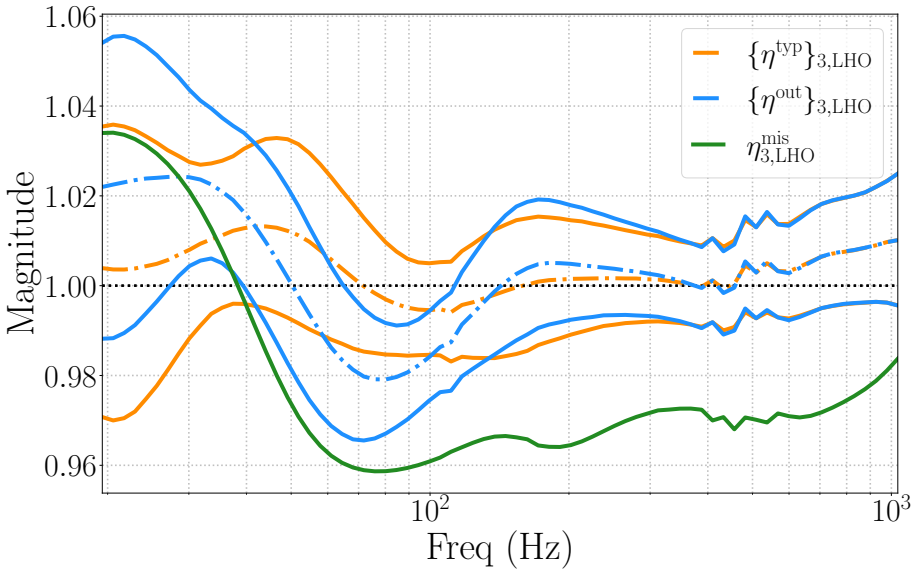

(a) Amplitude.

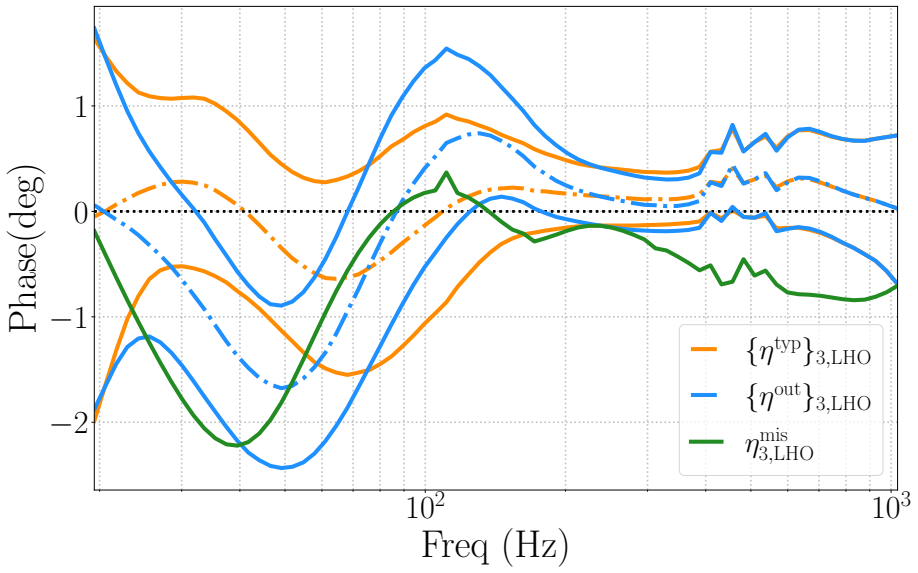

(b) Phase.

Figure D-3: Large CEs, $\{\eta^{\text{out}}\}_{3,\text{LHO}}$(blue), compared to the corresponding typical distribution, $\{\eta^{\text{typ}}\}_{3,\text{LHO}}$ (orange), both showing the edges of the 1-σ CIs in each frequency bin. $\eta^{\text{mis}}_{3,\text{LHO}}$ is plotted in green.

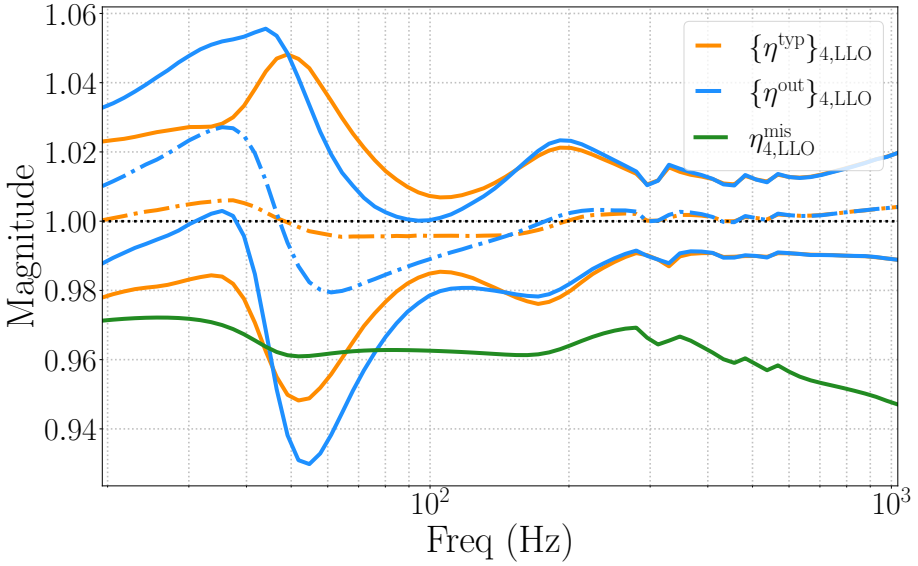

(a) Amplitude.

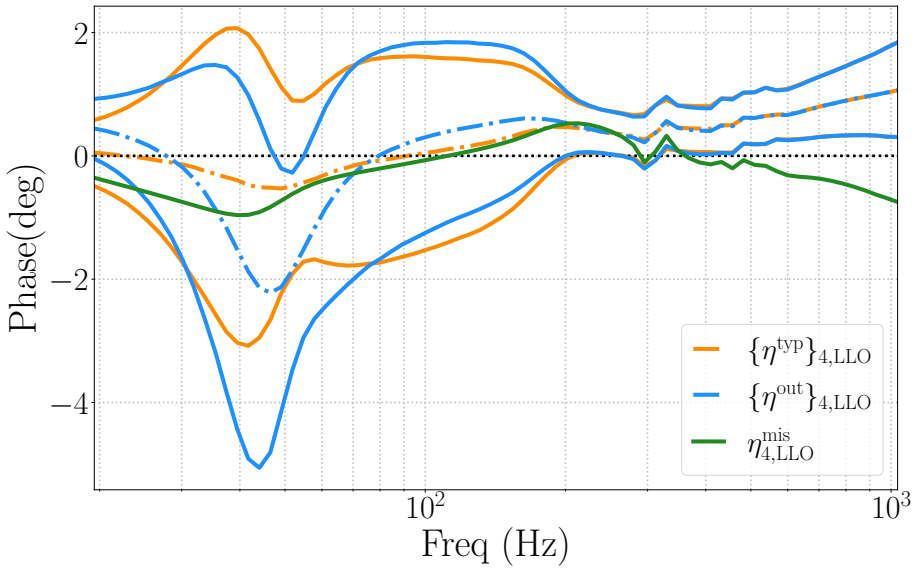

(b) Phase.

Figure D-4: Large CEs, $\{\eta^{\mathrm{out}}\}_{4,\mathrm{LLO}}$(blue), compared to the corresponding typical distribution, $\{\eta^{\mathrm{typ}}\}_{4,\mathrm{LLO}}$ (orange), both showing the edges of the 1-σ CIs in each frequency bin. $\eta^{\mathrm{mis}}_{4,\mathrm{LLO}}$ is plotted in green.

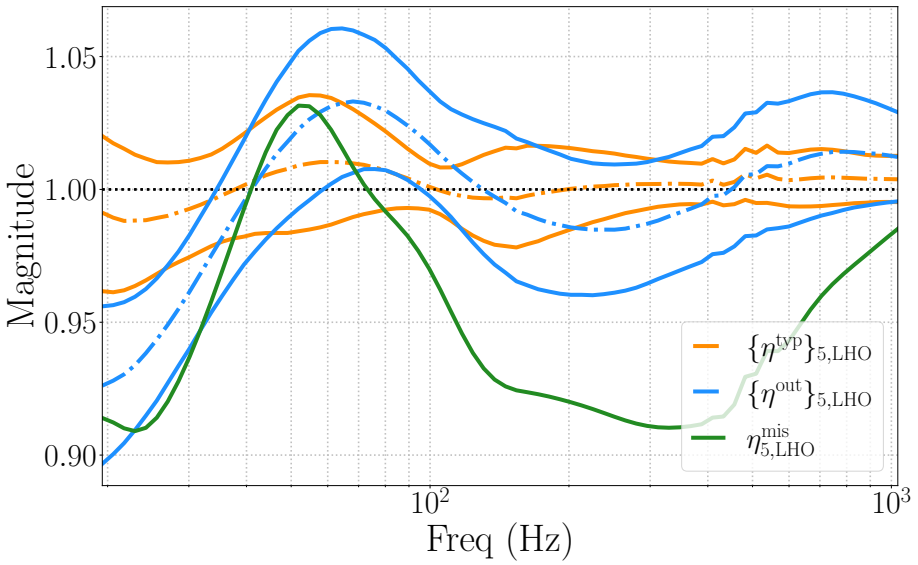

(a) Amplitude.

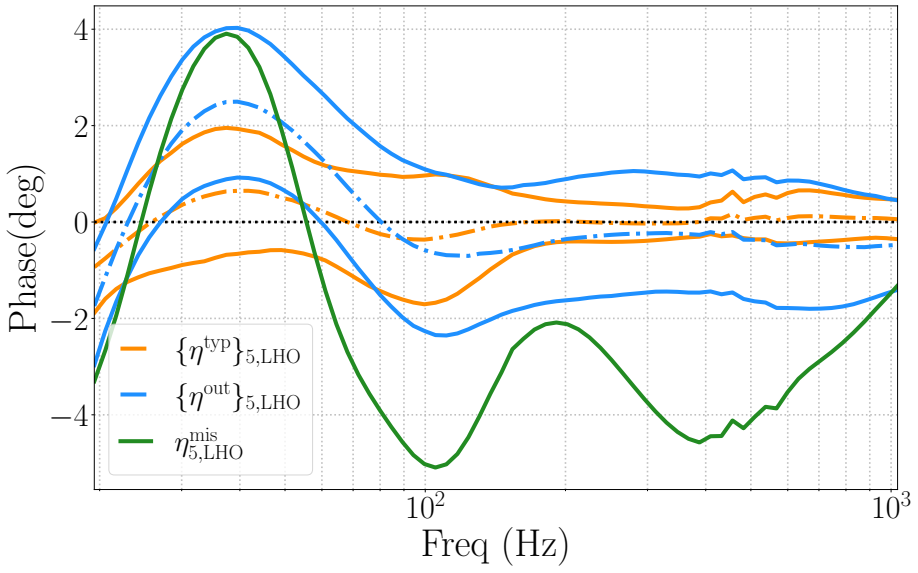

(b) Phase.

Figure D-5: Large CEs, $\{\eta^{\mathrm{out}}\}_{5,\mathrm{LHO}}$(blue), compared to the corresponding typical distribution, $\{\eta^{\mathrm{typ}}\}_{5,\mathrm{LHO}}$ (orange), both showing the edges of the 1-σ CIs in each frequency bin. $\eta^{\mathrm{mis}}_{5,\mathrm{LHO}}$ is plotted in green.

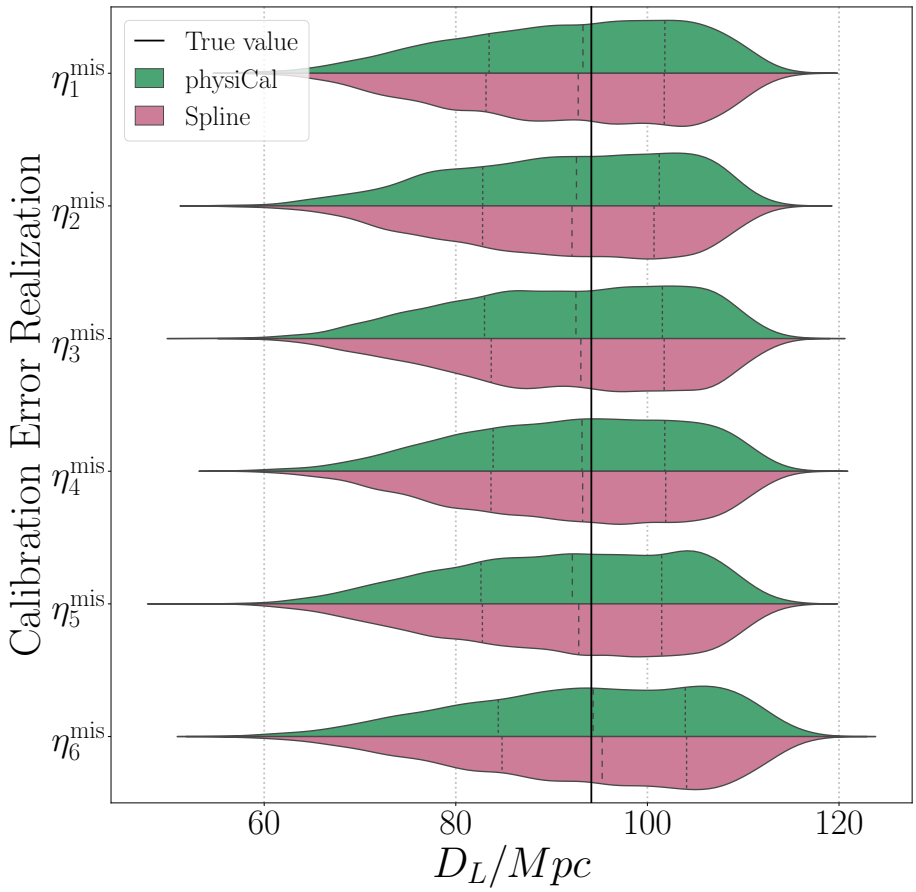

Figure D-6: D_L likelihoods for the six scenarios, miscalibrated, physiCal (green) vs. Spline (purple) runs, the vertical dashed lines mark the 25%, 50%, and 75% percentiles.

CE Realization	physiCal	Spline
$\eta_1^{\rm mis}$	-0.8%	-1.5%
$\eta_2^{\rm mis}$	-2.0%	-2.6%
$\eta_3^{\rm mis}$	-1.6%	-1.4%
$\eta_4^{\rm mis}$	-0.8%	-0.6%
$\eta_5^{\rm mis}$	-1.7%	-1.2%
$\eta_6^{\rm mis}$	0.2%	1.0%

Table D.1: ΔD_L in the likelihoods for physiCal vs. Spline results.

Bibliography

[1] Maggiore, M. Gravitational Waves, Volume 1: Theory and Experiments. Oxford University Press, 2007.

[2] J. Aasi et al. "Advanced LIGO". In: Class.Quant.Grav. 32 (2015), p. 074001. DOI: 10.1088/0264-9381/32/7/074001. arXiv: 1411.4547 [gr-qc].

[3] R. A. Hulse and J. H. Taylor. "Discovery of a pulsar in a binary system". In: Astrophys. J. Lett. 195 (1975), pp. L51–L53. DOI: 10.1086/181708.

[4] B. P. Abbott et al. "GW170817: Observation of Gravitational Waves from a Binary Neutron Star Inspiral". In: Phys. Rev. Lett. 119.16 (2017), p. 161101. DOI: 10.1103/PhysRevLett.119.161101. arXiv: 1710.05832 [gr-qc].

[5] B. P. Abbott et al. "Properties of the binary neutron star merger GW170817". In: Phys. Rev. X9.1 (2019), p. 011001. DOI: 10.1103/PhysRevX.9.011001. arXiv: 1805.11579 [gr-qc].

[6] D.A. Coulter et al. "Swope Supernova Survey 2017a (SSS17a), the Optical Counterpart to a Gravitational Wave Source". In: Science 358 (2017), p. 1556. DOI: 10.1126/science.aap9811. arXiv: 1710.05452 [astro-ph.HE].

[7] B.P. Abbott et al. "Multi-messenger Observations of a Binary Neutron Star Merger". In: Astrophys. J. Lett. 848.2 (2017), p. L12. DOI: 10.3847/2041-8213/aa91c9. arXiv: 1710.05833 [astro-ph.HE].

[8] M. Soares-Santos et al. "The Electromagnetic Counterpart of the Binary Neutron Star Merger LIGO/Virgo GW170817. I. Discovery of the Optical Coun-

terpart Using the Dark Energy Camera". In: Astrophys. J. Lett. 848.2 (2017), p. L16. DOI: 10.3847/2041-8213/aa9059. arXiv: 1710.05459 [astro-ph.HE].

[9] G. Hallinan et al. "A Radio Counterpart to a Neutron Star Merger". In: Science 358 (2017), p. 1579. DOI: 10.1126/science.aap9855. arXiv: 1710.05435 [astro-ph.HE].

[10] B.P. Abbott et al. "Gravitational Waves and Gamma-rays from a Binary Neutron Star Merger: GW170817 and GRB 170817A". In: Astrophys. J. Lett. 848.2 (2017), p. L13. DOI: 10.3847/2041-8213/aa920c. arXiv: 1710.05834 [astro-ph.HE].

[11] D. A. Coulter et al. "Swope Supernova Survey 2017a (SSS17a), the optical counterpart to a gravitational wave source". In: Science 358 (Dec. 2017), pp. 1556–1558. DOI: 10.1126/science.aap9811. arXiv: 1710.05452 [astro-ph.HE].

[12] B. P. Abbott et al. "Multi-messenger Observations of a Binary Neutron Star Merger". In: ApJ 848, L12 (Oct. 2017), p. L12. DOI: 10.3847/2041-8213/aa91c9. arXiv: 1710.05833 [astro-ph.HE].

[13] LIGO Scientific Collaboration, Fermi Gamma-ray Burst Monitor Virgo Collaboration, and INTEGRAL. "Gravitational Waves and Gamma-Rays from a Binary Neutron Star Merger: GW170817 and GRB 170817A". In: The Astrophysical Journal Letters 848.2 (2017), p. L13. URL: http://stacks.iop.org/2041-8205/848/i=2/a=L13.

[14] M. Soares-Santos et al. "The Electromagnetic Counterpart of the Binary Neutron Star Merger LIGO/Virgo GW170817. I. Discovery of the Optical Counterpart Using the Dark Energy Camera". In: ApJ 848, L16 (Oct. 2017), p. L16. DOI: 10.3847/2041-8213/aa9059. arXiv: 1710.05459 [astro-ph.HE].

[15] G. Hallinan et al. "A radio counterpart to a neutron star merger". In: Science 358 (Dec. 2017), pp. 1579–1583. DOI: 10.1126/science.aap9855. arXiv: 1710.05435 [astro-ph.HE].

[16] B.P. Abbott et al. "GW170817: Measurements of neutron star radii and equation of state". In: Phys. Rev. Lett. 121.16 (2018), p. 161101. DOI: 10.1103/PhysRevLett.121.161101. arXiv: 1805.11581 [gr-qc].

[17] Brian D. Metzger. "Kilonovae". In: Living Rev. Rel. 20.1 (2017), p. 3. DOI: 10.1007/s41114-017-0006-z. arXiv: 1610.09381 [astro-ph.HE].

[18] Rodrigo Fernández and Brian D. Metzger. "Electromagnetic Signatures of Neutron Star Mergers in the Advanced LIGO Era". In: Ann. Rev. Nucl. Part. Sci. 66 (2016), pp. 23–45. DOI: 10.1146/annurev-nucl-102115-044819. arXiv: 1512.05435 [astro-ph.HE].

[19] B.D. Metzger and E. Berger. "What is the Most Promising Electromagnetic Counterpart of a Neutron Star Binary Merger?" In: Astrophys. J. 746 (2012), p. 48. DOI: 10.1088/0004-637X/746/1/48. arXiv: 1108.6056 [astro-ph.HE].

[20] B.D. Metzger et al. "Electromagnetic Counterparts of Compact Object Mergers Powered by the Radioactive Decay of R-process Nuclei". In: Mon. Not. Roy. Astron. Soc. 406 (2010), p. 2650. DOI: 10.1111/j.1365-2966.2010.16864.x. arXiv: 1001.5029 [astro-ph.HE].

[21] Nevin N. Weinberg. "Constraining the p-mode–g-mode tidal instability with GW170817". In: (2018). arXiv: 1808.08676 [astro-ph.HE].

[22] M. R. Drout et al. "Light curves of the neutron star merger GW170817/SSS17a: Implications for r-process nucleosynthesis". In: Science 358 (Dec. 2017), pp. 1570–1574. DOI: 10.1126/science.aaq0049. arXiv: 1710.05443 [astro-ph.HE].

[23] B. D. Metzger, T. A. Thompson, and E. Quataert. "A Magnetar Origin for the Kilonova Ejecta in GW170817". In: ApJ 856, 101 (Apr. 2018), p. 101. DOI: 10.3847/1538-4357/aab095. arXiv: 1801.04286 [astro-ph.HE].

[24] V. A. Villar et al. "The Combined Ultraviolet, Optical, and Near-infrared Light Curves of the Kilonova Associated with the Binary Neutron Star Merger GW170817: Unified Data Set, Analytic Models, and Physical Implications". In:

ApJ 851, L21 (Dec. 2017), p. L21. DOI: 10.3847/2041-8213/aa9c84. arXiv: 1710.11576 [astro-ph.HE].

[25] P. A. Evans et al. "Swift and NuSTAR observations of GW170817: Detection of a blue kilonova". In: Science 358 (Dec. 2017), pp. 1565–1570. DOI: 10.1126/science.aap9580. arXiv: 1710.05437 [astro-ph.HE].

[26] The LIGO Scientific Collaboration et al. "A gravitational-wave standard siren measurement of the Hubble constant". In: Nature 551.7678 (Nov. 2017), pp. 85–88. URL: http://dx.doi.org/10.1038/nature24471.

[27] R. Abbott et al. "GWTC-3: Compact Binary Coalescences Observed by LIGO and Virgo During the Second Part of the Third Observing Run". In: (Nov. 2021). arXiv: 2111.03606 [gr-qc].

[28] R. Abbott et al. "GWTC-2.1: Deep Extended Catalog of Compact Binary Coalescences Observed by LIGO and Virgo During the First Half of the Third Observing Run". In: (Aug. 2021). arXiv: 2108.01045 [gr-qc].

[29] R. Abbott et al. "GWTC-2: Compact Binary Coalescences Observed by LIGO and Virgo During the First Half of the Third Observing Run". In: Phys. Rev. X 11 (2021), p. 021053. DOI: 10.1103/PhysRevX.11.021053. arXiv: 2010.14527 [gr-qc].

[30] B. P. Abbott et al. "GWTC-1: A Gravitational-Wave Transient Catalog of Compact Binary Mergers Observed by LIGO and Virgo during the First and Second Observing Runs". In: Phys. Rev. X9.3 (2019), p. 031040. DOI: 10.1103/PhysRevX.9.031040. arXiv: 1811.12907 [astro-ph.HE].

[31] B. P. Abbott, R. Abbott, T. D. Abbott, et al. "Astrophysical Implications of the Binary Black-Hole Merger GW150914". In: 818.2 (2016), p. L22. DOI: 10.3847/2041-8205/818/2/L22. arXiv: 1602.03846 [astro-ph.HE].

[32] LIGO Scientific Collaboration and Virgo Collaboration. "The Rate of Binary Black Hole Mergers Inferred from Advanced LIGO Observations Surrounding

GW150914". In: The Astrophysical Journal Letters 833.1 (2016), p. L1. URL: http://stacks.iop.org/2041-8205/833/i=1/a=L1.

[33] Salvatore Vitale et al. "Use of gravitational waves to probe the formation channels of compact binaries". In: Class. Quant. Grav. 34.3 (2017), 03LT01. DOI: 10.1088/1361-6382/aa552e. arXiv: 1503.04307 [gr-qc].

[34] B. Farr, D. E. Holz, and W. M. Farr. "Using spin to understand the formation of LIGO's black holes". In: ArXiv e-prints (Sept. 2017). arXiv: 1709.07896 [astro-ph.HE].

[35] W. M. Farr et al. "Distinguishing spin-aligned and isotropic black hole populations with gravitational waves". In: Nature 548 (Aug. 2017), pp. 426–429. DOI: 10.1038/nature23453. arXiv: 1706.01385 [astro-ph.HE].

[36] S. Stevenson, C. P. L. Berry, and I. Mandel. "Hierarchical analysis of gravitational-wave measurements of binary black hole spin-orbit misalignments". In: MNRAS 471 (Nov. 2017), pp. 2801–2811. DOI: 10.1093/mnras/stx1764. arXiv: 1703.06873 [astro-ph.HE].

[37] I. Mandel et al. "Model-independent inference on compact-binary observations". In: ArXiv e-prints (Aug. 2016). arXiv: 1608.08223 [astro-ph.HE].

[38] Salvatore Vitale et al. "Measuring the Spin of Black Holes in Binary Systems Using Gravitational Waves". In: Phys. Rev. Lett. 112 (25 2014), p. 251101. DOI: 10.1103/PhysRevLett.112.251101. URL: http://link.aps.org/doi/10.1103/PhysRevLett.112.251101.

[39] Salvatore Vitale et al. "Parameter estimation for heavy binary-black holes with networks of second-generation gravitational-wave detectors". In: Phys. Rev. D 95.6 (2017), p. 064053. DOI: 10.1103/PhysRevD.95.064053. arXiv: 1611.01122 [gr-qc].

[40] M. van der Sluys et al. "Parameter estimation for signals from compact binary inspirals injected into LIGO data". In: Classical and Quantum Gravity 26.20,

204010 (Oct. 2009), p. 204010. DOI: 10.1088/0264-9381/26/20/204010. arXiv: 0905.1323 [gr-qc].

[41] B. P. Abbott et al. "Tests of General Relativity with GW150914". In: Physical Review Letters 116.22, 221101 (June 2016), p. 221101. DOI: 10.1103/PhysRevLett.116.221101. arXiv: 1602.03841 [gr-qc].

[42] P. D. Lasky et al. "Detecting Gravitational-Wave Memory with LIGO: Implications of GW150914". In: Physical Review Letters 117.6, 061102 (Aug. 2016), p. 061102. DOI: 10.1103/PhysRevLett.117.061102. arXiv: 1605.01415 [astro-ph.HE].

[43] A. Ghosh et al. "Testing general relativity using golden black-hole binaries". In: Phys. Rev. D 94.2, 021101 (July 2016), p. 021101. DOI: 10.1103/PhysRevD.94.021101. arXiv: 1602.02453 [gr-qc].

[44] N. Yunes, K. Yagi, and F. Pretorius. "Theoretical Physics Implications of the Binary Black-Hole Mergers GW150914 and GW151226". In: ArXiv e-prints (Mar. 2016). arXiv: 1603.08955 [gr-qc].

[45] M. Agathos et al. "TIGER: A data analysis pipeline for testing the strong-field dynamics of general relativity with gravitational wave signals from coalescing compact binaries". In: Phys. Rev. D 89.8, 082001 (Apr. 2014), p. 082001. DOI: 10.1103/PhysRevD.89.082001. arXiv: 1311.0420 [gr-qc].

[46] T. G. F. Li et al. "Towards a generic test of the strong field dynamics of general relativity using compact binary coalescence". In: Phys. Rev. D 85.8, 082003 (Apr. 2012), p. 082003. DOI: 10.1103/PhysRevD.85.082003. arXiv: 1110.0530 [gr-qc].

[47] B.P. Abbott et al. "GW190425: Observation of a Compact Binary Coalescence with Total Mass $\sim 3.4 M_{\odot}$". In: Astrophys. J. Lett. 892 (2020), p. L3. DOI: 10.3847/2041-8213/ab75f5. arXiv: 2001.01761 [astro-ph.HE].

[48] R. Abbott et al. "GW190521: A Binary Black Hole Merger with a Total Mass of $150M_{\odot}$". In: Phys. Rev. Lett. 125.10 (2020), p. 101102. DOI: 10.1103/PhysRevLett.125.101102. arXiv: 2009.01075 [gr-qc].

[49] R. Abbott et al. "GW190412: Observation of a Binary-Black-Hole Coalescence with Asymmetric Masses". In: Phys. Rev. D 102.4 (2020), p. 043015. DOI: 10.1103/PhysRevD.102.043015. arXiv: 2004.08342 [astro-ph.HE].

[50] R. Abbott et al. "GW190814: Gravitational Waves from the Coalescence of a 23 Solar Mass Black Hole with a 2.6 Solar Mass Compact Object". In: Astrophys. J. 896.2 (2020), p. L44. DOI: 10.3847/2041-8213/ab960f. arXiv: 2006.12611 [astro-ph.HE].

[51] H. T. Cromartie et al. "Relativistic Shapiro delay measurements of an extremely massive millisecond pulsar". In: Nature Astron. 4.1 (2019), pp. 72–76. DOI: 10.1038/s41550-019-0880-2. arXiv: 1904.06759 [astro-ph.HE].

[52] Charles D. Bailyn et al. "The Mass Distribution of Stellar Black Holes". In: The Astrophysical Journal 499.1 (1998), p. 367. DOI: 10.1086/305614. URL: https://dx.doi.org/10.1086/305614.

[53] F. Özel et al. "The Black Hole Mass Distribution in the Galaxy". In: ApJ 725 (Dec. 2010), pp. 1918–1927. DOI: 10.1088/0004-637X/725/2/1918. arXiv: 1006.2834.

[54] Will M. Farr et al. "The Mass Distribution of Stellar-Mass Black Holes". In: Astrophys. J. 741 (2011), p. 103. DOI: 10.1088/0004-637X/741/2/103. arXiv: 1011.1459 [astro-ph.GA].

[55] Feryal Özel et al. "ON THE MASS DISTRIBUTION AND BIRTH MASSES OF NEUTRON STARS". In: The Astrophysical Journal 757.1 (2012), p. 55. DOI: 10.1088/0004-637X/757/1/55. URL: https://dx.doi.org/10.1088/0004-637X/757/1/55.

[56] R. Abbott et al. "Observation of Gravitational Waves from Two Neutron Star–Black Hole Coalescences". In: Astrophys. J. Lett. 915.1 (2021), p. L5. DOI: 10.3847/2041-8213/ac082e. arXiv: 2106.15163 [astro-ph.HE].

[57] Halim Ashkar et al. "The H.E.S.S. gravitational wave rapid follow-up program". In: Journal of Cosmology and Astroparticle Physics 2021.03 (2021), p. 045. DOI: 10.1088/1475-7516/2021/03/045. URL: https://dx.doi.org/10.1088/1475-7516/2021/03/045.

[58] Danielle Frostig et al. "An Infrared Search for Kilonovae with the WINTER Telescope. I. Binary Neutron Star Mergers". In: Astrophys. J. 926.2 (2022), p. 152. DOI: 10.3847/1538-4357/ac4508. arXiv: 2110.01622 [astro-ph.HE].

[59] Matthew J. Graham et al. "The Zwicky Transient Facility: Science Objectives". In: Publ. Astron. Soc. Pac. 131.1001 (2019), p. 078001. DOI: 10.1088/1538-3873/ab006c. arXiv: 1902.01945 [astro-ph.IM].

[60] David Reitze et al. "Cosmic Explorer: The U.S. Contribution to Gravitational-Wave Astronomy beyond LIGO". In: Bull. Am. Astron. Soc. 51.7 (2019), p. 035. arXiv: 1907.04833 [astro-ph.IM].

[61] M. Punturo et al. "The Einstein Telescope: A third-generation gravitational wave observatory". In: Class. Quant. Grav. 27 (2010). Ed. by Fulvio Ricci, p. 194002. DOI: 10.1088/0264-9381/27/19/194002.

[62] Pau Amaro-Seoane et al. "Laser Interferometer Space Antenna". In: (Feb. 2017). arXiv: 1702.00786 [astro-ph.IM].

[63] Caltech/MIT/LIGOLab. Basic Michelson with Fabry Perot cavities and Power Recycling mirror Dec. 2022. URL: https://www.ligo.caltech.edu/page/ligos-ifo.

[64] Aaron Buikema et al. "Sensitivity and performance of the Advanced LIGO detectors in the third observing run". In: Physical Review D 102.6 (2020), p. 062003.

[65] Fet al Acernese et al. “Advanced Virgo: a second-generation interferometric gravitational wave detector”. In: Classical and Quantum Gravity 32.2 (2014), p. 024001.

[66] Aaron Viets et al. “Reconstructing the calibrated strain signal in the Advanced LIGO detectors”. In: Class. Quant. Grav. 35.9 (2018), p. 095015. DOI: 10.1088/1361-6382/aab658. arXiv: 1710.09973 [astro-ph.IM].

[67] Thibault Damour. “Coalescence of two spinning black holes: an effective one-body approach”. In: Phys. Rev. D64 (2001), p. 124013. DOI: 10.1103/PhysRevD.64.124013. arXiv: gr-qc/0103018 [gr-qc].

[68] Etienne Racine. “Analysis of spin precession in binary black hole systems including quadrupole-monopole interaction”. In: Phys. Rev. D78 (2008), p. 044021. DOI: 10.1103/PhysRevD.78.044021. arXiv: 0803.1820 [gr-qc].

[69] L. Santamaria et al. “Matching post-Newtonian and numerical relativity waveforms: systematic errors and a new phenomenological model for non-precessing black hole binaries”. In: Phys. Rev. D82 (2010), p. 064016. DOI: 10.1103/PhysRevD.82.064016. arXiv: 1005.3306 [gr-qc].

[70] P. Ajith et al. “Inspiral-merger-ringdown waveforms for black-hole binaries with non-precessing spins”. In: Phys. Rev. Lett. 106 (2011), p. 241101. DOI: 10.1103/PhysRevLett.106.241101. arXiv: 0909.2867 [gr-qc].

[71] B. P. Abbott et al. “Binary Black Hole Population Properties Inferred from the First and Second Observing Runs of Advanced LIGO and Advanced Virgo”. In: Astrophys. J. 882.2 (2019), p. L24. DOI: 10.3847/2041-8213/ab3800. arXiv: 1811.12940 [astro-ph.HE].

[72] Ken K. Y. Ng et al. “Gravitational-wave astrophysics with effective-spin measurements: asymmetries and selection biases”. In: Phys. Rev. D98.8 (2018), p. 083007. DOI: 10.1103/PhysRevD.98.083007. arXiv: 1805.03046 [gr-qc].

[73] Barak Zackay et al. “Highly spinning and aligned binary black hole merger in the Advanced LIGO first observing run”. In: Phys. Rev. D100.2 (2019), p. 023007. DOI: 10.1103/PhysRevD.100.023007. arXiv: 1902.10331 [astro-ph.HE].

[74] Tejaswi Venumadhav et al. “New Binary Black Hole Mergers in the Second Observing Run of Advanced LIGO and Advanced Virgo”. In: ArXiv e-prints (2019). arXiv: 1904.07214 [astro-ph.HE].

[75] É. É. Flanagan and T. Hinderer. “Constraining neutron-star tidal Love numbers with gravitational-wave detectors”. In: Phys. Rev. D 77.2, 021502 (Jan. 2008), p. 021502. DOI: 10.1103/PhysRevD.77.021502. arXiv: 0709.1915.

[76] L. Wade et al. “Systematic and statistical errors in a Bayesian approach to the estimation of the neutron-star equation of state using advanced gravitational wave detectors”. In: Phys. Rev. D 89.10, 103012 (May 2014), p. 103012. DOI: 10.1103/PhysRevD.89.103012. arXiv: 1402.5156 [gr-qc].

[77] B. P. Abbott et al. “GW170817: Observation of Gravitational Waves from a Binary Neutron Star Inspiral”. In: Physical Review Letters 119.16, 161101 (Oct. 2017), p. 161101. DOI: 10.1103/PhysRevLett.119.161101. arXiv: 1710.05832 [gr-qc].

[78] J. M. Lattimer. “The Nuclear Equation of State and Neutron Star Masses”. In: Annual Review of Nuclear and Particle Science 62 (Nov. 2012), pp. 485–515. DOI: 10.1146/annurev-nucl-102711-095018. arXiv: 1305.3510 [nucl-th].

[79] K. Yagi and N. Yunes. “Love number can be hard to measure”. In: Phys. Rev. D 89.2, 021303 (Jan. 2014), p. 021303. DOI: 10.1103/PhysRevD.89.021303. arXiv: 1310.8358 [gr-qc].

[80] C. Cutler and É. E. Flanagan. “Gravitational waves from merging compact binaries: How accurately can one extract the binary’s parameters from the inspiral waveform?” In: Phys. Rev. D 49 (Mar. 1994), pp. 2658–2697. DOI: 10.1103/PhysRevD.49.2658. eprint: gr-qc/9402014.

[81] B. S. Sathyaprakash and B. F. Schutz. "Physics, Astrophysics and Cosmology with Gravitational Waves". In: Living Reviews in Relativity 12 (Mar. 2009), p. 2. arXiv: 0903.0338 [gr-qc].

[82] J. Veitch et al. "Parameter estimation for compact binaries with ground-based gravitational-wave observations using the LALInference software library". In: Phys. Rev. D 91.4 (2015), p. 042003. DOI: 10.1103/PhysRevD.91.042003. arXiv: 1409.7215 [gr-qc].

[83] B. P. Abbott et al. "Properties of the Binary Black Hole Merger GW150914". In: Phys. Rev. Lett. 116.24 (2016), p. 241102. DOI: 10.1103/PhysRevLett.116.241102. arXiv: 1602.03840 [gr-qc].

[84] J. Veitch et al. "Parameter estimation for compact binaries with ground-based gravitational-wave observations using the LALInference software library". In: Phys. Rev. D 91.4, 042003 (Feb. 2015), p. 042003. DOI: 10.1103/PhysRevD.91.042003. arXiv: 1409.7215 [gr-qc].

[85] B. P. Abbott et al. "Properties of the Binary Black Hole Merger GW150914". In: Physical Review Letters 116.24, 241102 (June 2016), p. 241102. DOI: 10.1103/PhysRevLett.116.241102. arXiv: 1602.03840 [gr-qc].

[86] J. Veitch and A. Vecchio. "Bayesian coherent analysis of in-spiral gravitational wave signals with a detector network". In: Phys. Rev. D 81 (6 2010), p. 062003. DOI: 10.1103/PhysRevD.81.062003. URL: https://link.aps.org/doi/10.1103/PhysRevD.81.062003.

[87] Yiwen Huang et al. "Characterization of low-significance gravitational-wave compact binary sources". In: Phys. Rev. D98.12 (2018), p. 123021. DOI: 10.1103/PhysRevD.98.123021. arXiv: 1810.10035 [gr-qc].

[88] Yiwen Huang et al. "Source properties of the lowest signal-to-noise-ratio binary black hole detections". In: Phys. Rev. D 102.10 (2020), p. 103024. DOI: 10.1103/PhysRevD.102.103024. arXiv: 2003.04513 [gr-qc].

[89] Yiwen Huang et al. "Statistical and systematic uncertainties in extracting the source properties of neutron star - black hole binaries with gravitational waves". In: Phys. Rev. D 103.8 (2021), p. 083001. DOI: 10.1103/PhysRevD.103.083001. arXiv: 2005.11850 [gr-qc].

[90] Yiwen Huang et al. "Impact of calibration uncertainties on Hubble constant measurements from gravitational-wave sources". In: (Apr. 2022). arXiv: 2204.03614 [gr-qc].

[91] B. P. Abbott, R. Abbott, T. D. Abbott, et al. "Characterization of transient noise in Advanced LIGO relevant to gravitational wave signal GW150914". In: (2016). https://dcc.ligo.org/LIGO-P1500238/public/main. arXiv: 1602.03844 [gr-qc].

[92] S. A. Usman et al. "The PyCBC search for gravitational waves from compact binary coalescence". In: Classical and Quantum Gravity 33.21, 215004 (Nov. 2016), p. 215004. DOI: 10.1088/0264-9381/33/21/215004. arXiv: 1508.02357 [gr-qc].

[93] K. Cannon, C. Hanna, and D. Keppel. "Method to estimate the significance of coincident gravitational-wave observations from compact binary coalescence". In: Phys. Rev. D 88.2, 024025 (July 2013), p. 024025. DOI: 10.1103/PhysRevD.88.024025. arXiv: 1209.0718 [gr-qc].

[94] J. Abadie et al. "Search for gravitational waves from low mass compact binary coalescence in LIGO's sixth science run and Virgo's science runs 2 and 3". In: Phys. Rev. D 85 (8 2012), p. 082002. DOI: 10.1103/PhysRevD.85.082002. URL: https://link.aps.org/doi/10.1103/PhysRevD.85.082002.

[95] A. H. Nitz et al. "Detecting Binary Compact-object Mergers with Gravitational Waves: Understanding and Improving the Sensitivity of the PyCBC Search". In: ApJ 849, 118 (Nov. 2017), p. 118. DOI: 10.3847/1538-4357/aa8f50. arXiv: 1705.01513 [gr-qc].

[96] Ryan Lynch et al. "Observational implications of lowering the LIGO-Virgo alert threshold". In: Astrophys. J. 861.2 (2018), p. L24. DOI: 10.3847/2041-8213/aacf9f. arXiv: 1803.02880 [astro-ph.HE].

[97] Thibault Damour. "Coalescence of two spinning black holes: An effective one-body approach". In: Phys. Rev. D 64 (12 2001), p. 124013. DOI: 10.1103/PhysRevD.64.124013. URL: http://link.aps.org/doi/10.1103/PhysRevD.64.124013.

[98] Étienne Racine. "Analysis of spin precession in binary black hole systems including quadrupole-monopole interaction". In: Phys. Rev. D 78 (4 2008), p. 044021. DOI: 10.1103/PhysRevD.78.044021. URL: http://link.aps.org/doi/10.1103/PhysRevD.78.044021.

[99] L. Santamaría et al. "Matching post-Newtonian and numerical relativity waveforms: Systematic errors and a new phenomenological model for nonprecessing black hole binaries". In: Phys. Rev. D 82 (6 2010), p. 064016. DOI: 10.1103/PhysRevD.82.064016. URL: http://link.aps.org/doi/10.1103/PhysRevD.82.064016.

[100] P. Ajith et al. "Inspiral-Merger-Ringdown Waveforms for Black-Hole Binaries with Nonprecessing Spins". In: Physical Review Letters 106.24, 241101 (June 2011), p. 241101. DOI: 10.1103/PhysRevLett.106.241101. arXiv: 0909.2867 [gr-qc].

[101] Rory Smith et al. "Fast and accurate inference on gravitational waves from precessing compact binaries". In: Phys. Rev. D 94.4 (2016), p. 044031. DOI: 10.1103/PhysRevD.94.044031. arXiv: 1604.08253 [gr-qc].

[102] LIGO Collaboration and Virgo Collaboration. https://www.gw-openscience.org/events/. 2016.

[103] Kipp Cannon et al. "Singular value decomposition applied to compact binary coalescence gravitational-wave signals". In: Phys. Rev. D 82.4 (2010), p. 044025. DOI: 10.1103/PhysRevD.82.044025. URL: http://arxiv.org/abs/1005.0012.

[104] K. Cannon, C. Hanna, and D. Keppel. "Efficiently enclosing the compact binary parameter space by singular-value decomposition". In: Phys. Rev. D 84.8, 084003 (Oct. 2011), p. 084003. DOI: 10.1103/PhysRevD.84.084003. arXiv: 1101.4939 [gr-qc].

[105] K. Cannon, C. Hanna, and J. Peoples. "Likelihood-Ratio Ranking Statistic for Compact Binary Coalescence Candidates with Rate Estimation". In: ArXiv e-prints (Apr. 2015). arXiv: 1504.04632 [astro-ph.IM].

[106] C. Messick et al. "Analysis framework for the prompt discovery of compact binary mergers in gravitational-wave data". In: Phys. Rev. D 95.4, 042001 (Feb. 2017), p. 042001. DOI: 10.1103/PhysRevD.95.042001. arXiv: 1604.04324 [astro-ph.IM].

[107] B. P. Abbott et al. "Prospects for observing and localizing gravitational-wave transients with Advanced LIGO, Advanced Virgo and KAGRA". In: Living Rev. Rel. 21.1 (2018), p. 3. DOI: 10.1007/s41114-020-00026-9. arXiv: 1304.0670 [gr-qc].

[108] N. J. Cornish and T. B. Littenberg. "Bayeswave: Bayesian inference for gravitational wave bursts and instrument glitches". In: Classical and Quantum Gravity 32.13, 135012 (July 2015), p. 135012. DOI: 10.1088/0264-9381/32/13/135012. arXiv: 1410.3835 [gr-qc].

[109] P. Ajith et al. "Inspiral-Merger-Ringdown Waveforms for Black-Hole Binaries with Nonprecessing Spins". In: Phys. Rev. Lett. 106 (24 2011), p. 241101. DOI: 10.1103/PhysRevLett.106.241101. URL: http://link.aps.org/doi/10.1103/PhysRevLett.106.241101.

[110] J. Aasi et al. "Parameter estimation for compact binary coalescence signals with the first generation gravitational-wave detector network". In: Phys. Rev. D 88.6, 062001 (Sept. 2013), p. 062001. DOI: 10.1103/PhysRevD.88.062001. arXiv: 1304.1775 [gr-qc].

[111] Mark Hannam et al. “Simple Model of Complete Precessing Black-Hole-Binary Gravitational Waveforms”. In: Phys. Rev. Lett. 113.15 (2014), p. 151101. DOI: 10.1103/PhysRevLett.113.151101. arXiv: 1308.3271 [gr-qc].

[112] B. P. Abbott et al. In: Phys. Rev. X 6 (4 2016), p. 041015. DOI: 10.1103/PhysRevX.6.041015. arXiv: 1606.04856 [gr-qc]. URL: http://link.aps.org/doi/10.1103/PhysRevX.6.041015.

[113] B. P. Abbott, R. Abbott, T. D. Abbott, et al. “Observation of Gravitational Waves from a Binary Black Hole Merger”. In: 116 (2016), p. 061102. arXiv: 1602.03837 [gr-qc].

[114] B. P. Abbott et al. “GW151226: Observation of Gravitational Waves from a 22-Solar-Mass Binary Black Hole Coalescence”. In: Physical Review Letters 116.24, 241103 (June 2016), p. 241103. DOI: 10.1103/PhysRevLett.116.241103.

[115] B. P. Abbott et al. “GW170104: Observation of a 50-Solar-Mass Binary Black Hole Coalescence at Redshift 0.2”. In: Physical Review Letters 118.22, 221101 (June 2017), p. 221101. DOI: 10.1103/PhysRevLett.118.221101. arXiv: 1706.01812 [gr-qc].

[116] B. P. Abbott et al. “GW170608: Observation of a 19 Solar-mass Binary Black Hole Coalescence”. In: ApJ 851, L35 (Dec. 2017), p. L35. DOI: 10.3847/2041-8213/aa9f0c. arXiv: 1711.05578 [astro-ph.HE].

[117] B. P. Abbott et al. “GW170814: A Three-Detector Observation of Gravitational Waves from a Binary Black Hole Coalescence”. In: Physical Review Letters 119.14, 141101 (Oct. 2017), p. 141101. DOI: 10.1103/PhysRevLett.119.141101. arXiv: 1709.09660 [gr-qc].

[118] Alexander H. Nitz et al. “Detecting Binary Compact-object Mergers with Gravitational Waves: Understanding and Improving the Sensitivity of the PyCBC Search”. In: The Astrophysical Journal 849.2 (2017), p. 118. URL: http://stacks.iop.org/0004-637X/849/i=2/a=118.

[119] Hsin-Yu Chen, Salvatore Vitale, and Ramesh Narayan. "Viewing angle of binary neutron star mergers". In: Phys. Rev. X 9.3 (2019), p. 031028. DOI: 10.1103/PhysRevX.9.031028. arXiv: 1807.05226 [astro-ph.HE].

[120] Salvatore Vitale and Hsin-Yu Chen. "Measuring the Hubble constant with neutron star black hole mergers". In: Phys. Rev. Lett. 121.2 (2018), p. 021303. DOI: 10.1103/PhysRevLett.121.021303. arXiv: 1804.07337 [astro-ph.CO].

[121] Samantha A. Usman, Joseph C. Mills, and Stephen Fairhurst. "Constraining the Inclination of Binary Mergers from Gravitational-wave Observations". In: (2018). arXiv: 1809.10727 [gr-qc].

[122] J. Skilling. "Nested Sampling". In: American Institute of Physics Conference Series. Ed. by R. Fischer, R. Preuss, and U. V. Toussaint. Vol. 735. American Institute of Physics Conference Series. Nov. 2004, pp. 395–405. DOI: 10.1063/1.1835238.

[123] K. Hotokezaka et al. "Radio Counterparts of Compact Binary Mergers Detectable in Gravitational Waves: A Simulation for an Optimized Survey". In: ApJ 831, 190 (Nov. 2016), p. 190. DOI: 10.3847/0004-637X/831/2/190. arXiv: 1605.09395 [astro-ph.HE].

[124] Ehud Nakar and Tsvi Piran. "Detectable radio flares following gravitational waves from mergers of binary neutron stars". In: Nature 478 (Sept. 2011), 82 EP –. URL: http://dx.doi.org/10.1038/nature10365.

[125] N. T. Palliyaguru et al. "Radio Follow-up of Gravitational-wave Triggers during Advanced LIGO O1". In: ApJ 829, L28 (Oct. 2016), p. L28. DOI: 10.3847/2041-8205/829/2/L28. arXiv: 1608.06518 [astro-ph.HE].

[126] L. P. Singer et al. "The First Two Years of Electromagnetic Follow-Up with Advanced LIGO and Virgo". In: ArXiv e-prints (Apr. 2014). arXiv: 1404.5623 [astro-ph.HE].

[127] Theocharis A. Apostolatos et al. "Spin-induced orbital precession and its modulation of the gravitational waveforms from merging binaries". In: Phys. Rev. D

49 (12 1994), pp. 6274–6297. DOI: 10.1103/PhysRevD.49.6274. URL: https://link.aps.org/doi/10.1103/PhysRevD.49.6274.

[128] B. Farr et al. "Parameter Estimation on Gravitational Waves from Neutron-star Binaries with Spinning Components". In: ApJ 825, 116 (July 2016), p. 116. DOI: 10.3847/0004-637X/825/2/116. arXiv: 1508.05336 [astro-ph.HE].

[129] J. Veitch et al. "Estimating parameters of coalescing compact binaries with proposed advanced detector networks". In: Phys. Rev. D 85.10, 104045 (May 2012), p. 104045. DOI: 10.1103/PhysRevD.85.104045. arXiv: 1201.1195 [astro-ph.HE].

[130] L. Blanchet. "Gravitational Radiation from Post-Newtonian Sources and Inspiralling Compact Binaries". In: Living Reviews in Relativity 9 (June 2006), p. 4. DOI: 10.12942/lrr-2006-4.

[131] S. Vitale and M. Zanolin. "Parameter estimation from gravitational waves generated by nonspinning binary black holes with laser interferometers: Beyond the Fisher information". In: Phys. Rev. D 82.12, 124065 (Dec. 2010), p. 124065. DOI: 10.1103/PhysRevD.82.124065. arXiv: 1004.4537 [gr-qc].

[132] M. Zanolin, S. Vitale, and N. Makris. "Application of asymptotic expansions for maximum likelihood estimators errors to gravitational waves from binary mergers: The single interferometer case". In: Phys. Rev. D 81.12, 124048 (June 2010), p. 124048. DOI: 10.1103/PhysRevD.81.124048. arXiv: 0912.0065 [gr-qc].

[133] K. G. Arun et al. "Parameter estimation of inspiralling compact binaries using 3.5 post-Newtonian gravitational wave phasing: The nonspinning case". In: Phys. Rev. D 71.8, 084008 (Apr. 2005), p. 084008. DOI: 10.1103/PhysRevD.71.084008. eprint: gr-qc/0411146.

[134] SciPy.org. https://docs.scipy.org/doc/scipy/reference/generated/scipy.signal.find_peaks.html. 2018.

[135] Michael Pürrer, Mark Hannam, and Frank Ohme. "Can we measure individual black-hole spins from gravitational-wave observations?" In: Phys. Rev. D 93 (8 2016), p. 084042. DOI: 10.1103/PhysRevD.93.084042. URL: http://link.aps.org/doi/10.1103/PhysRevD.93.084042.

[136] C. Talbot and E. Thrane. "Determining the population properties of spinning black holes". In: Phys. Rev. D 96.2, 023012 (July 2017), p. 023012. DOI: 10.1103/PhysRevD.96.023012. arXiv: 1704.08370 [astro-ph.HE].

[137] Davide Gerosa et al. "Resonant-plane locking and spin alignment in stellar-mass black-hole binaries: A diagnostic of compact-binary formation". In: Phys. Rev. D 87 (10 2013), p. 104028. DOI: 10.1103/PhysRevD.87.104028. URL: http://link.aps.org/doi/10.1103/PhysRevD.87.104028.

[138] David J.C. MacKay. "Information Theory, Inference, and Learning Algorithms". In: first. The address: Cambridge University Press, 2003, p. 34. ISBN: 0521642981.

[139] B P Abbott et al. "Effects of data quality vetoes on a search for compact binary coalescences in Advanced LIGO's first observing run". In: Class. Quant. Grav. 35.6 (2018), p. 065010. DOI: 10.1088/1361-6382/aaaafa. arXiv: 1710.02185 [gr-qc].

[140] Sebastian M. Gaebel et al. "Digging the population of compact binary mergers out of the noise". In: Mon. Not. Roy. Astron. Soc. 484.3 (2019), pp. 4008–4023. DOI: 10.1093/mnras/stz225. arXiv: 1809.03815 [astro-ph.IM].

[141] Stephen Fairhurst. "Triangulation of gravitational wave sources with a network of detectors". In: New J.Phys. 11 (2009), p. 123006. DOI: 10.1088/1367-2630/11/12/123006,10.1088/1367-2630/13/6/069602. arXiv: 0908.2356 [gr-qc].

[142] L. P. Singer et al. "The First Two Years of Electromagnetic Follow-up with Advanced LIGO and Virgo". In: ApJ 795, 105 (Nov. 2014), p. 105. DOI: 10.1088/0004-637X/795/2/105. arXiv: 1404.5623 [astro-ph.HE].

[143] T. Sidery et al. “Reconstructing the sky location of gravitational-wave detected compact binary systems: Methodology for testing and comparison”. In: Phys. Rev. D 89.8, 084060 (Apr. 2014), p. 084060. DOI: 10.1103/PhysRevD.89.084060. arXiv: 1312.6013 [astro-ph.IM].

[144] D. E. Holz and S. A. Hughes. “Using Gravitational-Wave Standard Sirens”. In: ApJ 629 (Aug. 2005), pp. 15–22. DOI: 10.1086/431341. eprint: astro-ph/0504616.

[145] S. Nissanke et al. “Determining the Hubble constant from gravitational wave observations of merging compact binaries”. In: ArXiv e-prints (July 2013). arXiv: 1307.2638 [astro-ph.CO].

[146] H.-Y. Chen, M. Fishbach, and D. E. Holz. “A 2 per cent Hubble constant measurement from standard sirens within 5 years”. In: ArXiv e-prints (Dec. 2017). arXiv: 1712.06531.

[147] Bernard F. Schutz. “Determining the Hubble constant from gravitational wave observations”. In: Nature 323 (Sept. 1986), 310 EP –. URL: http://dx.doi.org/10.1038/323310a0.

[148] W. Del Pozzo. “Inference of cosmological parameters from gravitational waves: Applications to second generation interferometers”. In: Phys. Rev. D 86.4, 043011 (Aug. 2012), p. 043011. DOI: 10.1103/PhysRevD.86.043011. arXiv: 1108.1317 [astro-ph.CO].

[149] G. Nelemans, L. R. Yungelson, and Simon F. Portegies Zwart. “The gravitational wave signal from the galactic disk population of binaries containing two compact objects”. In: Astron. Astrophys. 375 (2001), pp. 890–898. DOI: 10.1051/0004-6361:20010683. arXiv: astro-ph/0105221 [astro-ph].

[150] Krzysztof Belczynski, Vassiliki Kalogera, and Tomasz Bulik. “A Comprehensive study of binary compact objects as gravitational wave sources: Evolutionary channels, rates, and physical properties”. In: Astrophys. J. 572 (2001), pp. 407–431. DOI: 10.1086/340304. arXiv: astro-ph/0111452 [astro-ph].

[151] Rasmus Voss and Thomas M. Tauris. "Galactic distribution of merging neutron stars and black holes - Prospects for short gamma-ray burst progenitors and LIGO/VIRGO". In: Mon. Not. Roy. Astron. Soc. 342 (2003), p. 1169. DOI: 10.1046/j.1365-8711.2003.06616.x. arXiv: astro-ph/0303227 [astro-ph].

[152] Krzysztof Belczynski et al. "On the rarity of double black hole binaries: Consequences for gravitational-wave detection". In: Astrophys. J. 662 (2007), pp. 504–512. DOI: 10.1086/513562. arXiv: astro-ph/0612032 [astro-ph].

[153] Krzystof Belczynski et al. "Compact object modeling with the startrack population synthesis code". In: Astrophys. J. Suppl. 174 (2008), p. 223. DOI: 10.1086/521026. arXiv: astro-ph/0511811 [astro-ph].

[154] Michal Dominik et al. "Double Compact Objects II: Cosmological Merger Rates". In: Astrophys. J. 779 (2013), p. 72. DOI: 10.1088/0004-637X/779/1/72. arXiv: 1308.1546 [astro-ph.HE].

[155] Krzysztof Belczynski et al. "The Formation and Gravitational-Wave Detection of Massive Stellar Black-Hole Binaries". In: Astrophys. J. 789.2 (2014), p. 120. DOI: 10.1088/0004-637X/789/2/120. arXiv: 1403.0677 [astro-ph.HE].

[156] N. Mennekens and D. Vanbeveren. "Massive double compact object mergers: gravitational wave sources and r-process-element production sites". In: Astron. Astrophys. 564 (2014), A134. DOI: 10.1051/0004-6361/201322198. arXiv: 1307.0959 [astro-ph.SR].

[157] Mario Spera, Michela Mapelli, and Alessandro Bressan. "The mass spectrum of compact remnants from the PARSEC stellar evolution tracks". In: Mon. Not. Roy. Astron. Soc. 451.4 (2015), pp. 4086–4103. DOI: 10.1093/mnras/stv1161. arXiv: 1505.05201 [astro-ph.SR].

[158] J. J. Eldridge and E. R. Stanway. "BPASS predictions for Binary Black-Hole Mergers". In: Mon. Not. Roy. Astron. Soc. 462.3 (2016), pp. 3302–3313. DOI: 10.1093/mnras/stw1772. arXiv: 1602.03790 [astro-ph.HE].

[159] Simon Stevenson et al. “Formation of the first three gravitational-wave observations through isolated binary evolution”. In: Nature Communications 8, 14906 (2017), p. 14906. DOI: 10.1038/ncomms14906. arXiv: 1704.01352 [astro-ph.HE].

[160] Michela Mapelli et al. “The cosmic merger rate of stellar black hole binaries from the Illustris simulation”. In: Mon. Not. Roy. Astron. Soc. 472.2 (2017), pp. 2422–2435. DOI: 10.1093/mnras/stx2123. arXiv: 1708.05722 [astro-ph.GA].

[161] Nicola Giacobbo, Michela Mapelli, and Mario Spera. “Merging black hole binaries: the effects of progenitor’s metallicity, mass-loss rate and Eddington factor”. In: Mon. Not. Roy. Astron. Soc. 474.3 (2018), pp. 2959–2974. DOI: 10.1093/mnras/stx2933. arXiv: 1711.03556 [astro-ph.SR].

[162] Nicola Giacobbo and Michela Mapelli. “The progenitors of compact-object binaries: impact of metallicity, common envelope and natal kicks”. In: Mon. Not. Roy. Astron. Soc. 480.2 (2018), pp. 2011–2030. DOI: 10.1093/mnras/sty1999. arXiv: 1806.00001 [astro-ph.HE].

[163] Matthias U. Kruckow et al. “Progenitors of gravitational wave mergers: Binary evolution with the stellar grid-based code ComBinE”. In: Mon. Not. Roy. Astron. Soc. 481.2 (2018), pp. 1908–1949. DOI: 10.1093/mnras/sty2190. arXiv: 1801.05433 [astro-ph.SR].

[164] Kedron Silsbee and Scott Tremaine. “Lidov-Kozai Cycles with Gravitational Radiation: Merging Black Holes in Isolated Triple Systems”. In: Astrophys. J. 836.1 (2017), p. 39. DOI: 10.3847/1538-4357/aa5729. arXiv: 1608.07642 [astro-ph.HE].

[165] Leor Barack et al. “Black holes, gravitational waves and fundamental physics: a roadmap”. In: Class. Quant. Grav. 36.14 (2019), p. 143001. DOI: 10.1088/1361-6382/ab0587. arXiv: 1806.05195 [gr-qc].

[166] Anna Lisa Varri et al. “A MODEST review”. In: Computational Astrophysics and Cosmology 5.1 (2018), p. 2. DOI: 10.1186/s40668-018-0024-6. URL: https://doi.org/10.1186/s40668-018-0024-6.

[167] Fabio Antonini and Hagai B. Perets. "Secular evolution of compact binaries near massive black holes: Gravitational wave sources and other exotica". In: Astrophys. J. 757 (2012), p. 27. DOI: 10.1088/0004-637X/757/1/27. arXiv: 1203.2938 [astro-ph.GA].

[168] B. McKernan et al. "Intermediate mass black holes in AGN disks: I. Production & Growth". In: Mon. Not. Roy. Astron. Soc. 425 (2012), p. 460. DOI: 10.1111/j.1365-2966.2012.21486.x. arXiv: 1206.2309 [astro-ph.GA].

[169] Nicholas C. Stone, Brian D. Metzger, and Zoltán Haiman. "Assisted inspirals of stellar mass black holes embedded in AGN discs: solving the 'final au problem'". In: Mon. Not. Roy. Astron. Soc. 464.1 (2017), pp. 946–954. DOI: 10.1093/mnras/stw2260. arXiv: 1602.04226 [astro-ph.GA].

[170] Imre Bartos et al. "Rapid and Bright Stellar-mass Binary Black Hole Mergers in Active Galactic Nuclei". In: Astrophys. J. 835.2 (2017), p. 165. DOI: 10.3847/1538-4357/835/2/165. arXiv: 1602.03831 [astro-ph.HE].

[171] Katerina Chatziioannou et al. "On the properties of the massive binary black hole merger GW170729". In: Phys. Rev. D100.10 (2019), p. 104015. DOI: 10.1103/PhysRevD.100.104015. arXiv: 1903.06742 [gr-qc].

[172] Chase Kimball, Christopher P. L. Berry, and Vicky Kalogera. "What GW170729's exceptional mass and spin tells us about its family tree". In: Research Notes of the American Astro 4.1, 2 (2020), p. 2. DOI: 10.3847/2515-5172/ab66be. arXiv: 1903.07813 [astro-ph.HE].

[173] Carl L. Rodriguez et al. "Black holes: The next generation—repeated mergers in dense star clusters and their gravitational-wave properties". In: Phys. Rev. D100.4 (2019), p. 043027. DOI: 10.1103/PhysRevD.100.043027. arXiv: 1906.10260 [astro-ph.HE].

[174] Carl L. Rodriguez et al. "Illuminating Black Hole Binary Formation Channels with Spins in Advanced LIGO". In: Astrophys. J. 832.1 (2016), p. L2. DOI: 10.3847/2041-8205/832/1/L2. arXiv: 1609.05916 [astro-ph.HE].

[175] Salvatore Vitale et al. "Measuring the spin of black holes in binary systems using gravitational waves". In: Phys. Rev. Lett. 112.25 (2014), p. 251101. DOI: 10.1103/PhysRevLett.112.251101. arXiv: 1403.0129 [gr-qc].

[176] Michael Pürrer, Mark Hannam, and Frank Ohme. "Can we measure individual black-hole spins from gravitational-wave observations?" In: Phys. Rev. D93.8 (2016), p. 084042. DOI: 10.1103/PhysRevD.93.084042. arXiv: 1512.04955 [gr-qc].

[177] Colm Talbot and Eric Thrane. "Determining the population properties of spinning black holes". In: Phys. Rev. D96.2 (2017), p. 023012. DOI: 10.1103/PhysRevD.96.023012. arXiv: 1704.08370 [astro-ph.HE].

[178] Simon Stevenson, Christopher P.L. Berry, and Ilya Mandel. "Hierarchical analysis of gravitational-wave measurements of binary black hole spin–orbit misalignments". In: Mon. Not. Roy. Astron. Soc. 471.3 (2017), pp. 2801–2811. DOI: 10.1093/mnras/stx1764. arXiv: 1703.06873 [astro-ph.HE].

[179] Ben Farr, Daniel E. Holz, and Will M. Farr. "Using Spin to Understand the Formation of LIGO and Virgo's Black Holes". In: Astrophys. J. Lett. 854.1 (2018), p. L9. DOI: 10.3847/2041-8213/aaaa64. arXiv: 1709.07896 [astro-ph.HE].

[180] Will M. Farr et al. "Distinguishing Spin-Aligned and Isotropic Black Hole Populations With Gravitational Waves". In: Nature 548 (2017), p. 426. DOI: 10.1038/nature23453. arXiv: 1706.01385 [astro-ph.HE].

[181] Michele Vallisneri et al. "The LIGO Open Science Center". In: J. Phys. Conf. Ser. 610.1 (2015), p. 012021. DOI: 10.1088/1742-6596/610/1/012021. arXiv: 1410.4839 [gr-qc].

[182] LIGO Scientific Collaboration, Virgo Collaboration. Gravitational Wave Open Science Center – T 2018. DOI: 10.7935/K57P8W9D.

[183] LIGO Scientific Collaboration, Virgo Collaboration. Gravitational Wave Open Science Center – T 2019. DOI: 10.7935/CA75-FM95.

[184] Rich Abbott et al. “Open data from the first and second observing runs of Advanced LIGO and Advanced Virgo”. In: ArXiv e-prints (2019). arXiv: 1912.11716 [gr-qc].

[185] Tejaswi Venumadhav et al. “New search pipeline for compact binary mergers: Results for binary black holes in the first observing run of Advanced LIGO”. In: Phys. Rev. D100.2 (2019), p. 023011. DOI: 10.1103/PhysRevD.100.023011. arXiv: 1902.10341 [astro-ph.IM].

[186] B. S. Sathyaprakash and B. F. Schutz. “Physics, Astrophysics and Cosmology with Gravitational Waves”. In: Living Rev. Rel. 12 (2009), p. 2. DOI: 10.12942/lrr-2009-2. arXiv: 0903.0338 [gr-qc].

[187] Salvatore Vitale et al. “Impact of Bayesian Priors on the Characterization of Binary Black Hole Coalescences”. In: Phys. Rev. Lett. 119.25 (2017), p. 251103. DOI: 10.1103/PhysRevLett.119.251103. arXiv: 1707.04637 [gr-qc].

[188] Katerina Chatziioannou et al. “Noise spectral estimation methods and their impact on gravitational wave measurement of compact binary mergers”. In: Phys. Rev. D100.10 (2019), p. 104004. DOI: 10.1103/PhysRevD.100.104004. arXiv: 1907.06540 [gr-qc].

[189] Barak Zackay, Liang Dai, and Tejaswi Venumadhav. “Relative Binning and Fast Likelihood Evaluation for Gravitational Wave Parameter Estimation”. In: arXiv e-prints, arXiv:1806.08792 (June 2018), arXiv:1806.08792. arXiv: 1806.08792 [astro-ph.IM].

[190] LIGO Scientific Collaboration. LIGO Algorithm Library - LALSuite. free software (GPL). 2018. DOI: 10.7935/GT1W-FZ16.

[191] J. Veitch and A. Vecchio. “Bayesian coherent analysis of in-spiral gravitational wave signals with a detector network”. In: Phys. Rev. D81 (2010), p. 062003. DOI: 10.1103/PhysRevD.81.062003. arXiv: 0911.3820 [astro-ph.CO].

[192] Tyson B. Littenberg and Neil J. Cornish. "Bayesian inference for spectral estimation of gravitational wave detector noise". In: Phys. Rev. D91.8 (2015), p. 084034. DOI: 10.1103/PhysRevD.91.084034. arXiv: 1410.3852 [gr-qc].

[193] Neil J. Cornish and Tyson B. Littenberg. "BayesWave: Bayesian Inference for Gravitational Wave Bursts and Instrument Glitches". In: Class. Quant. Grav. 32.13 (2015), p. 135012. DOI: 10.1088/0264-9381/32/13/135012. arXiv: 1410.3835 [gr-qc].

[194] Sascha Husa et al. "Frequency-domain gravitational waves from nonprecessing black-hole binaries. I. New numerical waveforms and anatomy of the signal". In: Phys. Rev. D 93.4 (2016), p. 044006. DOI: 10.1103/PhysRevD.93.044006. arXiv: 1508.07250 [gr-qc].

[195] Sebastian Khan et al. "Frequency-domain gravitational waves from nonprecessing black-hole binaries. II. A phenomenological model for the advanced detector era". In: Phys. Rev. D 93.4 (2016), p. 044007. DOI: 10.1103/PhysRevD.93.044007. arXiv: 1508.07253 [gr-qc].

[196] Alejandro Bohé et al. "Improved effective-one-body model of spinning, nonprecessing binary black holes for the era of gravitational-wave astrophysics with advanced detectors". In: Phys. Rev. D95.4 (2017), p. 044028. DOI: 10.1103/PhysRevD.95.044028. arXiv: 1611.03703 [gr-qc].

[197] Farhan Feroz and M. P. Hobson. "Multimodal nested sampling: an efficient and robust alternative to MCMC methods for astronomical data analysis". In: Mon. Not. Roy. Astron. Soc. 384 (2008), p. 449. DOI: 10.1111/j.1365-2966.2007.12353.x. arXiv: 0704.3704 [astro-ph].

[198] F. Feroz, M. P. Hobson, and M. Bridges. "MultiNest: an efficient and robust Bayesian inference tool for cosmology and particle physics". In: Mon. Not. Roy. Astron. Soc. 398 (2009), pp. 1601–1614. DOI: 10.1111/j.1365-2966.2009.14548.x. arXiv: 0809.3437 [astro-ph].

[199] Farhan Feroz et al. "Importance Nested Sampling and the MultiNest Algorithm". In: The Open Journal of Astrophysics 2.1, 10 (2019), p. 10. DOI: 10.21105/astro.1306.2144. arXiv: 1306.2144 [astro-ph.IM].

[200] J. Buchner et al. "X-ray spectral modelling of the AGN obscuring region in the CDFS: Bayesian model selection and catalogue". In: Astron. Astrophys. 564 (2014), A125. DOI: 10.1051/0004-6361/201322971. arXiv: 1402.0004 [astro-ph.HE].

[201] Barak Zackay et al. "Detecting Gravitational Waves in Data with Non-Gaussian Noise". In: arXiv e-prints, arXiv:1908.05644 (Aug. 2019), arXiv:1908.05644. arXiv: 1908.05644 [astro-ph.IM].

[202] B. P. Abbott et al. "Observation of Gravitational Waves from a Binary Black Hole Merger". In: Phys. Rev. Lett. 116.6 (2016), p. 061102. DOI: 10.1103/PhysRevLett.116.061102. arXiv: 1602.03837 [gr-qc].

[203] B. P. Abbott et al. "GW151226: Observation of Gravitational Waves from a 22-Solar-Mass Binary Black Hole Coalescence". In: Phys. Rev. Lett. 116.24 (2016), p. 241103. DOI: 10.1103/PhysRevLett.116.241103. arXiv: 1606.04855 [gr-qc].

[204] Benjamin P. Abbott et al. "GW170104: Observation of a 50-Solar-Mass Binary Black Hole Coalescence at Redshift 0.2". In: Phys. Rev. Lett. 118.22 (2017). [Erratum: Phys. Rev. Lett.121,no.12,129901(2018)], p. 221101. DOI: 10.1103/PhysRevLett.118.221101,10.1103/PhysRevLett.121.129901. arXiv: 1706.01812 [gr-qc].

[205] B.. P.. Abbott et al. "GW170608: Observation of a 19-solar-mass Binary Black Hole Coalescence". In: Astrophys. J. 851.2 (2017), p. L35. DOI: 10.3847/2041-8213/aa9f0c. arXiv: 1711.05578 [astro-ph.HE].

[206] B. P. Abbott et al. "GW170814: A Three-Detector Observation of Gravitational Waves from a Binary Black Hole Coalescence". In: Phys. Rev. Lett. 119.14 (2017), p. 141101. DOI: 10.1103/PhysRevLett.119.141101. arXiv: 1709.09660 [gr-qc].

[207] Walter Del Pozzo et al. "Testing general relativity with compact coalescing binaries: comparing exact and predictive methods to compute the Bayes factor". In: Class. Quant. Grav. 31.20 (2014), p. 205006. DOI: 10.1088/0264-9381/31/20/205006. arXiv: 1408.2356 [gr-qc].

[208] Emily Baird et al. "Degeneracy between mass and spin in black-hole-binary waveforms". In: Phys. Rev. D87.2 (2013), p. 024035. DOI: 10.1103/PhysRevD.87.024035. arXiv: 1211.0546 [gr-qc].

[209] Javier Roulet and Matias Zaldarriaga. "Constraints on binary black hole populations from LIGO–Virgo detections". In: Mon. Not. Roy. Astron. Soc. 484.3 (2019), pp. 4216–4229. DOI: 10.1093/mnras/stz226. arXiv: 1806.10610 [astro-ph.HE].

[210] Alexander H. Nitz et al. "2-OGC: Open Gravitational-wave Catalog of binary mergers from analysis of public Advanced LIGO and Virgo data". In: ArXiv e-prints (2019). arXiv: 1910.05331 [astro-ph.HE].

[211] B. P. Abbott et al. "Binary Black Hole Mergers in the first Advanced LIGO Observing Run". In: Phys. Rev. X6.4 (2016). [erratum: Phys. Rev.X8,no.3,039903(2018)], p. 041015. DOI: 10.1103/PhysRevX.6.041015,10.1103/PhysRevX.8.039903. arXiv: 1606.04856 [gr-qc].

[212] Shanika Galaudage, Colm Talbot, and Eric Thrane. "Gravitational-wave inference in the catalog era: evolving priors and marginal events". In: ArXiv e-prints (2019). arXiv: 1912.09708 [astro-ph.HE].

[213] Frans Pretorius. "Evolution of binary black hole spacetimes". In: Phys. Rev. Lett. 95 (2005), p. 121101. DOI: 10.1103/PhysRevLett.95.121101. arXiv: gr-qc/0507014.

[214] Manuela Campanelli et al. "Accurate evolutions of orbiting black-hole binaries without excision". In: Phys. Rev. Lett. 96 (2006), p. 111101. DOI: 10.1103/PhysRevLett.96.111101. arXiv: gr-qc/0511048.

[215] John G. Baker et al. "Gravitational wave extraction from an inspiraling configuration of merging black holes". In: Phys. Rev. Lett. 96 (2006), p. 111102. DOI: 10.1103/PhysRevLett.96.111102. arXiv: gr-qc/0511103.

[216] Michael Boyle et al. "The SXS Collaboration catalog of binary black hole simulations". In: Class. Quant. Grav. 36.19 (2019), p. 195006. DOI: 10.1088/1361-6382/ab34e2. arXiv: 1904.04831 [gr-qc].

[217] Francois Foucart et al. "First direct comparison of nondisrupting neutron star-black hole and binary black hole merger simulations". In: Phys. Rev. D88.6 (2013), p. 064017. DOI: 10.1103/PhysRevD.88.064017. arXiv: 1307.7685 [gr-qc].

[218] Francois Foucart et al. "Neutron star-black hole mergers with a nuclear equation of state and neutrino cooling: Dependence in the binary parameters". In: Phys. Rev. D 90 (2014), p. 024026. DOI: 10.1103/PhysRevD.90.024026. arXiv: 1405.1121 [astro-ph.HE].

[219] Tanja Hinderer et al. "Effects of neutron-star dynamic tides on gravitational waveforms within the effective-one-body approach". In: Phys. Rev. Lett. 116.18 (2016), p. 181101. DOI: 10.1103/PhysRevLett.116.181101. arXiv: 1602.00599 [gr-qc].

[220] Kabir Chakravarti et al. "Systematic effects from black hole-neutron star waveform model uncertainties on the neutron star equation of state". In: Phys. Rev. D 99.2 (2019), p. 024049. DOI: 10.1103/PhysRevD.99.024049. arXiv: 1809.04349 [gr-qc].

[221] Francois Foucart et al. "Gravitational waveforms from spectral Einstein code simulations: Neutron star-neutron star and low-mass black hole-neutron star binaries". In: Phys. Rev. D99.4 (2019), p. 044008. DOI: 10.1103/PhysRevD.99.044008. arXiv: 1812.06988 [gr-qc].

[222] Benjamin D. Lackey et al. "Extracting equation of state parameters from black hole-neutron star mergers: aligned-spin black holes and a preliminary waveform

model". In: Phys. Rev. D89.4 (2014), p. 043009. DOI: 10.1103/PhysRevD.89.043009. arXiv: 1303.6298 [gr-qc].

[223] Tetsuro Yamamoto, Masaru Shibata, and Keisuke Taniguchi. "Simulating coalescing compact binaries by a new code SACRA". In: Phys. Rev. D 78 (2008), p. 064054. DOI: 10.1103/PhysRevD.78.064054. arXiv: 0806.4007 [gr-qc].

[224] C. Pankow et al. "Novel scheme for rapid parallel parameter estimation of gravitational waves from compact binary coalescences". In: Phys. Rev. D 92.2 (2015), p. 023002. DOI: 10.1103/PhysRevD.92.023002. arXiv: 1502.04370 [gr-qc].

[225] Jacob Lange, Richard O'Shaughnessy, and Monica Rizzo. "Rapid and accurate parameter inference for coalescing, precessing compact binaries". In: ArXiv e-prints (May 2018). arXiv: 1805.10457 [gr-qc].

[226] Gregory M. Harry. "Advanced LIGO: The next generation of gravitational wave detectors". In: Class. Quant. Grav. 27 (2010), p. 084006. DOI: 10.1088/0264-9381/27/8/084006.

[227] F. Acernese et al. "Advanced Virgo: a second-generation interferometric gravitational wave detector". In: Class. Quant. Grav. 32.2 (2015), p. 024001. DOI: 10.1088/0264-9381/32/2/024001. arXiv: 1408.3978 [gr-qc].

[228] Prayush Kumar, Michael Pürrer, and Harald P. Pfeiffer. "Measuring neutron star tidal deformability with Advanced LIGO: a Bayesian analysis of neutron star - black hole binary observations". In: Phys. Rev. D 95.4 (2017), p. 044039. DOI: 10.1103/PhysRevD.95.044039. arXiv: 1610.06155 [gr-qc].

[229] Benjamin D. Lackey et al. "Extracting equation of state parameters from black hole-neutron star mergers. I. Nonspinning black holes". In: Phys. Rev. D 85 (2012), p. 044061. DOI: 10.1103/PhysRevD.85.044061. arXiv: 1109.3402 [astro-ph.HE].

[230] Andrea Taracchini et al. "Effective-one-body model for black-hole binaries with generic mass ratios and spins". In: Phys. Rev. D 89.6 (2014), p. 061502. DOI: 10.1103/PhysRevD.89.061502. arXiv: 1311.2544 [gr-qc].

[231] Mark Hannam et al. "When can gravitational-wave observations distinguish between black holes and neutron stars?" In: Astrophys. J. Lett. 766 (2013), p. L14. DOI: 10.1088/2041-8205/766/1/L14. arXiv: 1301.5616 [gr-qc].

[232] Theocharis A. Apostolatos et al. "Spin induced orbital precession and its modulation of the gravitational wave forms from merging binaries". In: Phys. Rev. D 49 (1994), pp. 6274–6297. DOI: 10.1103/PhysRevD.49.6274.

[233] Stephen Fairhurst et al. "When will we observe binary black holes precessing?" In: Phys. Rev. D 102.4 (2020), p. 041302. DOI: 10.1103/PhysRevD.102.041302. arXiv: 1908.00555 [gr-qc].

[234] Stephen Fairhurst et al. "Two-harmonic approximation for gravitational waveforms from precessing binaries". In: Phys. Rev. D 102.2 (2020), p. 024055. DOI: 10.1103/PhysRevD.102.024055. arXiv: 1908.05707 [gr-qc].

[235] K.S. Thorne. "Multipole Expansions of Gravitational Radiation". In: Rev. Mod. Phys. 52 (1980), pp. 299–339. DOI: 10.1103/RevModPhys.52.299.

[236] Francois Foucart et al. "Black hole-neutron star mergers: effects of the orientation of the black hole spin". In: Phys. Rev. D 83 (2011), p. 024005. DOI: 10.1103/PhysRevD.83.024005. arXiv: 1007.4203 [astro-ph.HE].

[237] Francesco Pannarale et al. "Will black hole-neutron star binary inspirals tell us about the neutron star equation of state?" In: Phys. Rev. D 84 (2011), p. 104017. DOI: 10.1103/PhysRevD.84.104017. arXiv: 1103.3526 [astro-ph.HE].

[238] Koutarou Kyutoku et al. "Gravitational waves from spinning black hole-neutron star binaries: dependence on black hole spins and on neutron star equations of state". In: Phys. Rev. D 84 (2011), p. 064018. DOI: 10.1103/PhysRevD.84.064018. arXiv: 1108.1189 [astro-ph.HE].

[239] Francois Foucart. "Black Hole-Neutron Star Mergers: Disk Mass Predictions". In: Phys. Rev. D 86 (2012), p. 124007. DOI: 10.1103/PhysRevD.86.124007. arXiv: 1207.6304 [astro-ph.HE].

[240] Francois Foucart et al. "Black hole-neutron star mergers at realistic mass ratios: Equation of state and spin orientation effects". In: Phys. Rev. D 87 (2013), p. 084006. DOI: 10.1103/PhysRevD.87.084006. arXiv: 1212.4810 [gr-qc].

[241] Kyohei Kawaguchi et al. "Black hole-neutron star binary merger: Dependence on black hole spin orientation and equation of state". In: Phys. Rev. D 92.2 (2015), p. 024014. DOI: 10.1103/PhysRevD.92.024014. arXiv: 1506.05473 [astro-ph.HE].

[242] Francois Foucart et al. "Dynamical ejecta from precessing neutron star-black hole mergers with a hot, nuclear-theory based equation of state". In: Class. Quant. Grav. 34.4 (2017), p. 044002. DOI: 10.1088/1361-6382/aa573b. arXiv: 1611.01159 [astro-ph.HE].

[243] Francois Foucart, Tanja Hinderer, and Samaya Nissanke. "Remnant baryon mass in neutron star-black hole mergers: Predictions for binary neutron star mimickers and rapidly spinning black holes". In: Phys. Rev. D 98.8 (2018), p. 081501. DOI: 10.1103/PhysRevD.98.081501. arXiv: 1807.00011 [astro-ph.HE].

[244] Francesco Pannarale et al. "Aligned spin neutron star-black hole mergers: a gravitational waveform amplitude model". In: Phys. Rev. D 92.8 (2015), p. 084050. DOI: 10.1103/PhysRevD.92.084050. arXiv: 1509.00512 [gr-qc].

[245] Stefano Ascenzi et al. "Constraining the Neutron Star Radius with Joint Gravitational-wave and Short Gamma-Ray Burst Observations of Neutron Star–Black Hole Coalescing Binaries". In: Astrophys. J. 877.2 (2019), p. 94. DOI: 10.3847/1538-4357/ab1b15. arXiv: 1808.06848 [astro-ph.HE].

[246] Luc Blanchet. "Gravitational Radiation from Post-Newtonian Sources and Inspiralling Compact Binaries". In: Living Rev. Rel. 17 (2014), p. 2. DOI: 10.12942/lrr-2014-2. arXiv: 1310.1528 [gr-qc].

[247] Milton Ruiz et al. "Multipole expansions for energy and momenta carried by gravitational waves". In: Gen. Rel. Grav. 40 (2008), p. 2467. DOI: 10.1007/s10714-007-0570-8. arXiv: 0707.4654 [gr-qc].

[248] Luc Blanchet et al. "The Third post-Newtonian gravitational wave polarisations and associated spherical harmonic modes for inspiralling compact binaries in quasi-circular orbits". In: Class. Quant. Grav. 25 (2008). [Erratum: Class.Quant.Grav. 29, 239501 (2012)], p. 165003. DOI: 10.1088/0264-9381/25/16/165003. arXiv: 0802.1249 [gr-qc].

[249] Lawrence E. Kidder. "Using full information when computing modes of post-Newtonian waveforms from inspiralling compact binaries in circular orbit". In: Phys. Rev. D 77 (2008), p. 044016. DOI: 10.1103/PhysRevD.77.044016. arXiv: 0710.0614 [gr-qc].

[250] James Healy et al. "Template Mode Hierarchies for Binary Black Hole Mergers". In: Phys. Rev. D 88.2 (2013), p. 024034. DOI: 10.1103/PhysRevD.88.024034. arXiv: 1302.6953 [gr-qc].

[251] Yi Pan et al. "Inspiral-merger-ringdown multipolar waveforms of nonspinning black-hole binaries using the effective-one-body formalism". In: Phys. Rev. D 84 (2011), p. 124052. DOI: 10.1103/PhysRevD.84.124052. arXiv: 1106.1021 [gr-qc].

[252] Vijay Varma and Parameswaran Ajith. "Effects of nonquadrupole modes in the detection and parameter estimation of black hole binaries with nonprecessing spins". In: Phys. Rev. D 96.12 (2017), p. 124024. DOI: 10.1103/PhysRevD.96.124024. arXiv: 1612.05608 [gr-qc].

[253] Collin Capano, Yi Pan, and Alessandra Buonanno. "Impact of higher harmonics in searching for gravitational waves from nonspinning binary black holes". In: Phys. Rev. D 89.10 (2014), p. 102003. DOI: 10.1103/PhysRevD.89.102003. arXiv: 1311.1286 [gr-qc].

[254] Vijay Varma et al. "Gravitational-wave observations of binary black holes: Effect of nonquadrupole modes". In: Phys. Rev. D 90.12 (2014), p. 124004. DOI: 10.1103/PhysRevD.90.124004. arXiv: 1409.2349 [gr-qc].

[255] Juan Calderón Bustillo et al. "Impact of gravitational radiation higher order modes on single aligned-spin gravitational wave searches for binary black holes". In: Phys. Rev. D 93.8 (2016), p. 084019. DOI: 10.1103/PhysRevD.93.084019. arXiv: 1511.02060 [gr-qc].

[256] Philip B. Graff, Alessandra Buonanno, and B. S. Sathyaprakash. "Missing Link: Bayesian detection and measurement of intermediate-mass black-hole binaries". In: Phys. Rev. D 92.2 (2015), p. 022002. DOI: 10.1103/PhysRevD.92.022002. arXiv: 1504.04766 [gr-qc].

[257] Feroz H. Shaik et al. "Impact of subdominant modes on the interpretation of gravitational-wave signals from heavy binary black hole systems". In: Phys. Rev. D 101.12 (2020), p. 124054. DOI: 10.1103/PhysRevD.101.124054. arXiv: 1911.02693 [gr-qc].

[258] Jocelyn S. Read et al. "Constraints on a phenomenologically parameterized neutron-star equation of state". In: Phys. Rev. D79 (2009), p. 124032. DOI: 10.1103/PhysRevD.79.124032. arXiv: 0812.2163 [astro-ph].

[259] Matthew D. Duez et al. "Evolving black hole-neutron star binaries in general relativity using pseudospectral and finite difference methods". In: Phys. Rev. D 78 (2008), p. 104015. DOI: 10.1103/PhysRevD.78.104015. arXiv: 0809.0002 [gr-qc].

[260] Thierry Mora and Clifford M. Will. "A PostNewtonian diagnostic of quasiequilibrium binary configurations of compact objects". In: Phys. Rev. D 69 (2004). [Erratum: Phys.Rev.D 71, 129901 (2005)], p. 104021. DOI: 10.1103/PhysRevD.71.129901. arXiv: gr-qc/0312082.

[261] Vijay Varma et al. "Surrogate model of hybridized numerical relativity binary black hole waveforms". In: Phys. Rev. D 99.6 (2019), p. 064045. DOI: 10.1103/PhysRevD.99.064045. arXiv: 1812.07865 [gr-qc].

[262] Kevin Barkett et al. "Gravitational waveforms of binary neutron star inspirals using post-Newtonian tidal splicing". In: Phys. Rev. D 102.2 (2020), p. 024031. DOI: 10.1103/PhysRevD.102.024031. arXiv: 1911.10440 [gr-qc].

[263] Patricia Schmidt, Ian W. Harry, and Harald P. Pfeiffer. "Numerical Relativity Injection Infrastructure". In: ArXiv e-prints (Mar. 2017). arXiv: 1703.01076 [gr-qc].

[264] Michele Vallisneri. "Use and abuse of the Fisher information matrix in the assessment of gravitational-wave parameter-estimation prospects". In: Phys. Rev. D 77 (2008), p. 042001. DOI: 10.1103/PhysRevD.77.042001. arXiv: gr-qc/0703086.

[265] Bernard F. Schutz. "Networks of gravitational wave detectors and three figures of merit". In: Class. Quant. Grav. 28 (2011), p. 125023. DOI: 10.1088/0264-9381/28/12/125023. arXiv: 1102.5421 [astro-ph.IM].

[266] Michael Pürrer. "Frequency domain reduced order models for gravitational waves from aligned-spin compact binaries". In: Class. Quant. Grav. 31.19 (2014), p. 195010. DOI: 10.1088/0264-9381/31/19/195010. arXiv: 1402.4146 [gr-qc].

[267] Tim Dietrich, Sebastiano Bernuzzi, and Wolfgang Tichy. "Closed-form tidal approximants for binary neutron star gravitational waveforms constructed from high-resolution numerical relativity simulations". In: Phys. Rev. D 96.12 (2017), p. 121501. DOI: 10.1103/PhysRevD.96.121501. arXiv: 1706.02969 [gr-qc].

[268] Tim Dietrich et al. "Matter imprints in waveform models for neutron star binaries: Tidal and self-spin effects". In: Phys. Rev. D 99.2 (2019), p. 024029. DOI: 10.1103/PhysRevD.99.024029. arXiv: 1804.02235 [gr-qc].

[269] Andrew Matas et al. "Aligned-spin neutron-star–black-hole waveform model based on the effective-one-body approach and numerical-relativity simulations". In: Phys. Rev. D 102.4 (2020), p. 043023. DOI: 10.1103/PhysRevD.102.043023. arXiv: 2004.10001 [gr-qc].

[270] Jonathan E. Thompson et al. "Modeling the gravitational wave signature of neutron star black hole coalescences". In: Phys. Rev. D 101.12 (2020), p. 124059. DOI: 10.1103/PhysRevD.101.124059. arXiv: 2002.08383 [gr-qc].

[271] Cecilio García-Quirós et al. "Accelerating the evaluation of inspiral-merger-ringdown waveforms with adapted grids". In: ArXiv e-prints (2020). arXiv: 2001.10897 [gr-qc].

[272] Cecilio García-Quirós et al. "Multimode frequency-domain model for the gravitational wave signal from nonprecessing black-hole binaries". In: Phys. Rev. D 102.6 (2020), p. 064002. DOI: 10.1103/PhysRevD.102.064002. arXiv: 2001.10914 [gr-qc].

[273] A. Buonanno and T. Damour. "Effective one-body approach to general relativistic two-body dynamics". In: Phys. Rev. D 59 (1999), p. 084006. DOI: 10.1103/PhysRevD.59.084006. arXiv: gr-qc/9811091.

[274] Enrico Barausse and Alessandra Buonanno. "Extending the effective-one-body Hamiltonian of black-hole binaries to include next-to-next-to-leading spin-orbit couplings". In: Phys. Rev. D 84 (2011), p. 104027. DOI: 10.1103/PhysRevD.84.104027. arXiv: 1107.2904 [gr-qc].

[275] Ian Hinder et al. "Error-analysis and comparison to analytical models of numerical waveforms produced by the NRAR Collaboration". In: Class. Quant. Grav. 31 (2014), p. 025012. DOI: 10.1088/0264-9381/31/2/025012. arXiv: 1307.5307 [gr-qc].

[276] Tanja Hinderer et al. "Periastron advance in spinning black hole binaries: comparing effective-one-body and Numerical Relativity". In: Phys. Rev. D 88.8 (2013), p. 084005. DOI: 10.1103/PhysRevD.88.084005. arXiv: 1309.0544 [gr-qc].

[277] Geraint Pratten et al. "Setting the cornerstone for a family of models for gravitational waves from compact binaries: The dominant harmonic for nonprecessing quasicircular black holes". In: Phys. Rev. D 102.6 (2020), p. 064001. DOI: 10.1103/PhysRevD.102.064001. arXiv: 2001.11412 [gr-qc].

[278] Tim Dietrich et al. "Improving the NRTidal model for binary neutron star systems". In: Phys. Rev. D 100.4 (2019), p. 044003. DOI: 10.1103/PhysRevD.100.044003. arXiv: 1905.06011 [gr-qc].

[279] Roberto Cotesta et al. "Enriching the Symphony of Gravitational Waves from Binary Black Holes by Tuning Higher Harmonics". In: Phys. Rev. D 98.8 (2018), p. 084028. DOI: 10.1103/PhysRevD.98.084028. arXiv: 1803.10701 [gr-qc].

[280] Serguei Ossokine et al. "Multipolar Effective-One-Body Waveforms for Precessing Binary Black Holes: Construction and Validation". In: Phys. Rev. D 102.4 (2020), p. 044055. DOI: 10.1103/PhysRevD.102.044055. arXiv: 2004.09442 [gr-qc].

[281] Roberto Cotesta, Sylvain Marsat, and Michael Pürrer. "Frequency domain reduced order model of aligned-spin effective-one-body waveforms with higher-order modes". In: Phys. Rev. D 101.12 (2020), p. 124040. DOI: 10.1103/PhysRevD.101.124040. arXiv: 2003.12079 [gr-qc].

[282] P.A.R. Ade et al. "Planck 2015 results. XIII. Cosmological parameters". In: Astron. Astrophys. 594 (2016), A13. DOI: 10.1051/0004-6361/201525830. arXiv: 1502.01589 [astro-ph.CO].

[283] Scott Lawrence et al. "An Upper Bound on Neutron Star Masses from Models of Short Gamma-ray Bursts". In: Astrophys. J. 808 (2015), p. 186. DOI: 10.1088/0004-637X/808/2/186. arXiv: 1505.00231 [astro-ph.HE].

[284] Justin Alsing, Hector O. Silva, and Emanuele Berti. "Evidence for a maximum mass cut-off in the neutron star mass distribution and constraints on the equation of state". In: Mon. Not. Roy. Astron. Soc. 478.1 (2018), pp. 1377–1391. DOI: 10.1093/mnras/sty1065. arXiv: 1709.07889 [astro-ph.HE].

[285] H. Thankful Cromartie et al. "Relativistic Shapiro delay measurements of an extremely massive millisecond pulsar". In: Nat. Astron. 4.1 (2019), pp. 72–76. DOI: 10.1038/s41550-019-0880-2. arXiv: 1904.06759 [astro-ph.HE].

[286] Andreas Bauswein et al. "Equation of state constraints from the threshold binary mass for prompt collapse of neutron star mergers". In: Phys. Rev. Lett. 125.14 (2020), p. 141103. DOI: 10.1103/PhysRevLett.125.141103. arXiv: 2004.00846 [astro-ph.HE].

[287] Katerina Chatziioannou and Will M. Farr. "Inferring the maximum and minimum mass of merging neutron stars with gravitational waves". In: Phys. Rev. D 102.6 (2020), p. 064063. DOI: 10.1103/PhysRevD.102.064063. arXiv: 2005.00482 [astro-ph.HE].

[288] Ben Farr et al. "Parameter estimation on gravitational waves from neutron-star binaries with spinning components". In: Astrophys. J. 825.2 (2016), p. 116. DOI: 10.3847/0004-637X/825/2/116. arXiv: 1508.05336 [astro-ph.HE].

[289] Jason W.T. Hessels et al. "A radio pulsar spinning at 716-hz". In: Science 311 (2006), pp. 1901–1904. DOI: 10.1126/science.1123430. arXiv: astro-ph/0601337.

[290] T.M. Tauris et al. "Formation of Double Neutron Star Systems". In: Astrophys. J. 846.2 (2017), p. 170. DOI: 10.3847/1538-4357/aa7e89. arXiv: 1706.09438 [astro-ph.HE].

[291] Walter Del Pozzo et al. "Demonstrating the feasibility of probing the neutron star equation of state with second-generation gravitational wave detectors". In: Phys. Rev. Lett. 111.7 (2013), p. 071101. DOI: 10.1103/PhysRevLett.111.071101. arXiv: 1307.8338 [gr-qc].

[292] M. Coleman Miller, Cecilia Chirenti, and Frederick K. Lamb. "Constraining the equation of state of high-density cold matter using nuclear and astronomical measurements". In: ArXiv e-prints (Apr. 2019). DOI: 10.3847/1538-4357/ab4ef9. arXiv: 1904.08907 [astro-ph.HE].

[293] Tanja Hinderer. "Tidal Love numbers of neutron stars". In: Astrophys. J. 677 (2008), pp. 1216–1220. DOI: 10.1086/533487. arXiv: 0711.2420 [astro-ph].

[294] Thibault Damour and Alessandro Nagar. "Relativistic tidal properties of neutron stars". In: Phys. Rev. D 80 (2009), p. 084035. DOI: 10.1103/PhysRevD.80.084035. arXiv: 0906.0096 [gr-qc].

[295] Taylor Binnington and Eric Poisson. "Relativistic theory of tidal Love numbers". In: Phys. Rev. D 80 (2009), p. 084018. DOI: 10.1103/PhysRevD.80.084018. arXiv: 0906.1366 [gr-qc].

[296] Justin Vines, Eanna E. Flanagan, and Tanja Hinderer. "Post-1-Newtonian tidal effects in the gravitational waveform from binary inspirals". In: Phys. Rev. D 83 (2011), p. 084051. DOI: 10.1103/PhysRevD.83.084051. arXiv: 1101.1673 [gr-qc].

[297] Laura Kreidberg et al. "Mass Measurements of Black Holes in X-Ray Transients: Is There a Mass Gap?" In: Astrophys. J. 757 (2012), p. 36. DOI: 10.1088/0004-637X/757/1/36. arXiv: 1205.1805 [astro-ph.HE].

[298] Anuradha Gupta et al. "Black holes in the low mass gap: Implications for gravitational wave observations". In: Phys. Rev. D 101.10 (2020), p. 103036. DOI: 10.1103/PhysRevD.101.103036. arXiv: 1909.05804 [gr-qc].

[299] Koutarou Kyutoku et al. "On the Possibility of GW190425 Being a Black Hole–Neutron Star Binary Merger". In: Astrophys. J. Lett. 890.1 (2020), p. L4. DOI: 10.3847/2041-8213/ab6e70. arXiv: 2001.04474 [astro-ph.HE].

[300] Ryan J. Foley et al. "Updated Parameter Estimates for GW190425 Using Astrophysical Arguments and Implications for the Electromagnetic Counterpart". In: Mon. Not. Roy. Astron. Soc. 494.1 (2020), pp. 190–198. DOI: 10.1093/mnras/staa725. arXiv: 2002.00956 [astro-ph.HE].

[301] F. Özel. "Soft equations of state for neutron-star matter ruled out by EXO 0748-676". In: Nature 441 (2006), pp. 1115–1117. DOI: 10.1038/nature04858. arXiv: astro-ph/0605106.

[302] Andrew W. Steiner, James M. Lattimer, and Edward F. Brown. "The Equation of State from Observed Masses and Radii of Neutron Stars". In: Astrophys. J. 722 (2010), pp. 33–54. DOI: 10.1088/0004-637X/722/1/33. arXiv: 1005.0811 [astro-ph.HE].

[303] M.C. Miller et al. "PSR J0030+0451 Mass and Radius from $NICER$ Data and Implications for the Properties of Neutron Star Matter". In: Astrophys. J. Lett. 887.1 (2019), p. L24. DOI: 10.3847/2041-8213/ab50c5. arXiv: 1912.05705 [astro-ph.HE].

[304] Slavko Bogdanov et al. "Constraining the Neutron Star Mass–Radius Relation and Dense Matter Equation of State with $NICER$. I. The Millisecond Pulsar X-Ray Data Set". In: Astrophys. J. Lett. 887.1 (2019), p. L25. DOI: 10.3847/2041-8213/ab53eb. arXiv: 1912.05706 [astro-ph.HE].

[305] Slavko Bogdanov et al. "Constraining the Neutron Star Mass–Radius Relation and Dense Matter Equation of State with $NICER$. II. Emission from Hot Spots on a Rapidly Rotating Neutron Star". In: Astrophys. J. Lett. 887.1 (2019), p. L26. DOI: 10.3847/2041-8213/ab5968. arXiv: 1912.05707 [astro-ph.HE].

[306] David MacKay. Information theory, inference, and learning algorithms. Cambridge, UK: Cambridge University Press, 2003. ISBN: 978-0521642989.

[307] Xingjiang Zhu et al. "Inferring the population properties of binary neutron stars with gravitational-wave measurements of spin". In: Phys. Rev. D 98 (2018), p. 043002. DOI: 10.1103/PhysRevD.98.043002. arXiv: 1711.09226 [astro-ph.HE].

[308] Simona Miller, Thomas A. Callister, and Will Farr. "The Low Effective Spin of Binary Black Holes and Implications for Individual Gravitational-Wave Events". In: Astrophys. J. 895.2 (2020), p. 128. DOI: 10.3847/1538-4357/ab80c0. arXiv: 2001.06051 [astro-ph.HE].

[309] Carl-Johan Haster et al. "Inference on gravitational waves from coalescences of stellar-mass compact objects and intermediate-mass black holes". In: Mon. Not. Roy. Astron. Soc.

457.4 (2016), pp. 4499–4506. DOI: 10.1093/mnras/stw233. arXiv: 1511.01431 [astro-ph.HE].

[310] Ilya Mandel et al. "Distinguishing types of compact-object binaries using the gravitational-wave signatures of their mergers". In: Mon. Not. Roy. Astron. Soc. 450.1 (2015), pp. L85–L89. DOI: 10.1093/mnrasl/slv054. arXiv: 1503.03172 [astro-ph.HE].

[311] M. Zanolin, S. Vitale, and N. Makris. "Application of asymptotic expansions of maximum likelihood estimators errors to gravitational waves from binary mergers: the single interferometer case". In: Phys. Rev. D 81 (2010), p. 124048. DOI: 10.1103/PhysRevD.81.124048. arXiv: 0912.0065 [gr-qc].

[312] S. Vitale and M. Zanolin. "Parameter estimation from Gravitational waves generated by non-spinning binary black holes with laser interferometers: beyond the Fisher information". In: Phys. Rev. D 82 (2010), p. 124065. DOI: 10.1103/PhysRevD.82.124065. arXiv: 1004.4537 [gr-qc].

[313] Salvatore Vitale and Michele Zanolin. "Application of asymptotic expansions for maximum likelihood estimators' errors to gravitational waves from binary mergers: the network case". In: Phys. Rev. D 84 (2011), p. 104020. DOI: 10.1103/PhysRevD.84.104020. arXiv: 1108.2410 [gr-qc].

[314] William H. Lee and Enrico Ramirez-Ruiz. "The Progenitors of Short Gamma-Ray Bursts". In: New J. Phys. 9 (2007), p. 17. DOI: 10.1088/1367-2630/9/1/017. arXiv: astro-ph/0701874.

[315] Ehud Nakar. "Short-Hard Gamma-Ray Bursts". In: Phys. Rept. 442 (2007), pp. 166–236. DOI: 10.1016/j.physrep.2007.02.005. arXiv: astro-ph/0701748.

[316] J. Clark et al. "Prospects for joint gravitational wave and short gamma-ray burst observations". In: Astrophys. J. 809.1 (2015), p. 53. DOI: 10.1088/0004-637X/809/1/53. arXiv: 1409.8149 [astro-ph.HE].

[317] Francesco Pannarale and Frank Ohme. "Prospects for joint gravitational-wave and electromagnetic observations of neutron-star–black-hole coalescing binaries". In: Astrophys. J. Lett. 791 (2014), p. L7. DOI: 10.1088/2041-8205/791/1/L7. arXiv: 1406.6057 [gr-qc].

[318] Brian D. Metzger. "Kilonovae". In: Living Rev. Rel. 23.1 (2020), p. 1. DOI: 10.1007/s41114-019-0024-0. arXiv: 1910.01617 [astro-ph.HE].

[319] Juan Calderón Bustillo, Pablo Laguna, and Deirdre Shoemaker. "Detectability of gravitational waves from binary black holes: Impact of precession and higher modes". In: Phys. Rev. D 95.10 (2017), p. 104038. DOI: 10.1103/PhysRevD.95.104038. arXiv: 1612.02340 [gr-qc].

[320] Gregory Ashton and Sebastian Khan. "Multiwaveform inference of gravitational waves". In: Phys. Rev. D 101.6 (2020), p. 064037. DOI: 10.1103/PhysRevD.101.064037. arXiv: 1910.09138 [gr-qc].

[321] Michael Pürrer and Carl-Johan Haster. "Ready for what lies ahead? – Gravitational waveform accuracy requirements for future ground based detectors". In: Phys. Rev. Res. 2.2 (2020), p. 023151. DOI: 10.1103/PhysRevResearch.2.023151. arXiv: 1912.10055 [gr-qc].

[322] The SXS Collaboration. SpECTRE. https://spectre-code.org. 2020.

[323] Lawrence E. Kidder et al. "SpECTRE: A Task-based Discontinuous Galerkin Code for Relativistic Astrophysics". In: J. Comput. Phys. 335 (2017), pp. 84–114. DOI: 10.1016/j.jcp.2016.12.059. arXiv: 1609.00098 [astro-ph.HE].

[324] Anuradha Samajdar and Tim Dietrich. "Waveform systematics for binary neutron star gravitational wave signals: effects of the point-particle baseline and tidal descriptions". In: Phys. Rev. D 98.12 (2018), p. 124030. DOI: 10.1103/PhysRevD.98.124030. arXiv: 1810.03936 [gr-qc].

[325] Reetika Dudi et al. "Relevance of tidal effects and post-merger dynamics for binary neutron star parameter estimation". In: Phys. Rev. D 98.8 (2018), p. 084061. DOI: 10.1103/PhysRevD.98.084061. arXiv: 1808.09749 [gr-qc].

[326] T. M. C. Abbott et al. "Dark Energy Survey Year 1 Results: A Precise H0 Estimate from DES Y1, BAO, and D/H Data". In: Mon. Not. Roy. Astron. Soc. 480.3 (2018), pp. 3879–3888. DOI: 10.1093/mnras/sty1939. arXiv: 1711.00403 [astro-ph.CO].

[327] N. Aghanim et al. "Planck 2018 results. VI. Cosmological parameters". In: Astron. Astrophys. 641 (2020), A6. DOI: 10.1051/0004-6361/201833910. arXiv: 1807.06209 [astro-ph.CO].

[328] Adam G. Riess et al. "A 2.4% Determination of the Local Value of the Hubble Constant". In: Astrophys. J. 826.1 (2016), p. 56. DOI: 10.3847/0004-637X/826/1/56. arXiv: 1604.01424 [astro-ph.CO].

[329] Adam G. Riess et al. "Milky Way Cepheid Standards for Measuring Cosmic Distances and Application to Gaia DR2: Implications for the Hubble Constant". In: Astrophys. J. 861.2 (2018), p. 126. DOI: 10.3847/1538-4357/aac82e. arXiv: 1804.10655 [astro-ph.CO].

[330] Adam G. Riess et al. "A Comprehensive Measurement of the Local Value of the Hubble Constant with 1 km s-1 Mpc-1 Uncertainty from the Hubble Space Telescope and the SH0ES Team". In: The Astrophysical Journal Letters 934.1 (2022), p. L7. DOI: 10.3847/2041-8213/ac5c5b. URL: https://dx.doi.org/10.3847/2041-8213/ac5c5b.

[331] S. Birrer et al. "H0LiCOW - IX. Cosmographic analysis of the doubly imaged quasar SDSS 1206+4332 and a new measurement of the Hubble constant". In: Mon. Not. Roy. Astron. Soc. 484 (2019), p. 4726. DOI: 10.1093/mnras/stz200. arXiv: 1809.01274 [astro-ph.CO].

[332] Kenneth C. Wong et al. "H0LiCOW – XIII. A 2.4 per cent measurement of H0 from lensed quasars: 5.3σ tension between early- and late-Universe probes". In: Mon. Not. Roy. Astron. Soc. 498.1 (2020), pp. 1420–1439. DOI: 10.1093/mnras/stz3094. arXiv: 1907.04869 [astro-ph.CO].

[333] In Sung Jang and Myung Gyoon Lee. "The Tip of the Red Giant Branch Distances to Typa Ia Supernova Host Galaxies. V. NGC 3021, NGC 3370, and NGC 1309 and the Value of the Hubble Constant". In: Astrophys. J. 836.1 (2017), p. 74. DOI: 10.3847/1538-4357/836/1/74. arXiv: 1702.01118 [astro-ph.CO].

[334] Wendy L. Freedman et al. "The Carnegie-Chicago Hubble Program. VIII. An Independent Determination of the Hubble Constant Based on the Tip of the Red Giant Branch". In: (July 2019). DOI: 10.3847/1538-4357/ab2f73. arXiv: 1907.05922 [astro-ph.CO].

[335] Yoo Jung Kim et al. "Determination of the Local Hubble Constant from Virgo Infall Using TRGB Distances". In: Astrophys. J. 905.2 (2020), p. 104. DOI: 10.3847/1538-4357/abbd97. arXiv: 2010.01364 [astro-ph.CO].

[336] Adam G. Riess et al. "Cosmic Distances Calibrated to 1% Precision with Gaia EDR3 Parallaxes and Hubble Space Telescope Photometry of 75 Milky Way Cepheids Confirm Tension with ΛCDM". In: Astrophys. J. Lett. 908.1 (2021), p. L6. DOI: 10.3847/2041-8213/abdbaf. arXiv: 2012.08534 [astro-ph.CO].

[337] Bernard F. Schutz. "Determining the Hubble Constant from Gravitational Wave Observations". In: Nature 323 (1986), pp. 310–311. DOI: 10.1038/323310a0.

[338] Daniel E. Holz and Scott A. Hughes. "Using gravitational-wave standard sirens". In: Astrophys. J. 629 (2005), pp. 15–22. DOI: 10.1086/431341. arXiv: astro-ph/0504616.

[339] Neal Dalal et al. "Short grb and binary black hole standard sirens as a probe of dark energy". In: Phys. Rev. D 74 (2006), p. 063006. DOI: 10.1103/PhysRevD.74.063006. arXiv: astro-ph/0601275.

[340] Samaya Nissanke et al. "Exploring short gamma-ray bursts as gravitational-wave standard sirens". In: Astrophys. J. 725 (2010), pp. 496–514. DOI: 10.1088/0004-637X/725/1/496. arXiv: 0904.1017 [astro-ph.CO].

[341] Samaya Nissanke et al. "Determining the Hubble constant from gravitational wave observations of merging compact binaries". In: (July 2013). arXiv: 1307.2638 [astro-ph.CO].

[342] Hsin-Yu Chen, Maya Fishbach, and Daniel E. Holz. "A two per cent Hubble constant measurement from standard sirens within five years". In: Nature 562.7728 (2018), pp. 545–547. DOI: 10.1038/s41586-018-0606-0. arXiv: 1712.06531 [astro-ph.CO].

[343] Kenta Hotokezaka et al. "A Hubble constant measurement from superluminal motion of the jet in GW170817". In: Nature Astron. 3.10 (2019), pp. 940–944. DOI: 10.1038/s41550-019-0820-1. arXiv: 1806.10596 [astro-ph.CO].

[344] M. Soares-Santos et al. "First Measurement of the Hubble Constant from a Dark Standard Siren using the Dark Energy Survey Galaxies and the LIGO/Virgo Binary–Black-hole Merger GW170814". In: Astrophys. J. Lett. 876.1 (2019), p. L7. DOI: 10.3847/2041-8213/ab14f1. arXiv: 1901.01540 [astro-ph.CO].

[345] Stephen M. Feeney et al. "Prospects for Measuring the Hubble Constant with Neutron-Star–Black-Hole Mergers". In: Phys. Rev. Lett. 126.17 (2021), p. 171102. DOI: 10.1103/PhysRevLett.126.171102. arXiv: 2012.06593 [astro-ph.CO].

[346] C. Messenger and J. Read. "Measuring a cosmological distance-redshift relationship using only gravitational wave observations of binary neutron star coalescences". In: Phys. Rev. Lett. 108 (2012), p. 091101. DOI: 10.1103/PhysRevLett.108.091101. arXiv: 1107.5725 [gr-qc].

[347] Walter Del Pozzo, Tjonnie G. F. Li, and Chris Messenger. "Cosmological inference using only gravitational wave observations of binary neutron stars". In: Phys. Rev. D 95.4 (2017), p. 043502. DOI: 10.1103/PhysRevD.95.043502. arXiv: 1506.06590 [gr-qc].

[348] Tim Dietrich et al. "Multimessenger constraints on the neutron-star equation of state and the Hubble constant". In: Science 370.6523 (2020), pp. 1450–1453. DOI: 10.1126/science.abb4317. arXiv: 2002.11355 [astro-ph.HE].

[349] Walter Del Pozzo. "Inference of the cosmological parameters from gravitational waves: application to second generation interferometers". In: Phys. Rev. D 86 (2012), p. 043011. DOI: 10.1103/PhysRevD.86.043011. arXiv: 1108.1317 [astro-ph.CO].

[350] B. P. Abbott et al. "A Gravitational-wave Measurement of the Hubble Constant Following the Second Observing Run of Advanced LIGO and Virgo". In: Astrophys. J. 909.2 (2021), p. 218. DOI: 10.3847/1538-4357/abdcb7. arXiv: 1908.06060 [astro-ph.CO].

[351] Rachel Gray et al. "Cosmological inference using gravitational wave standard sirens: A mock data analysis". In: Phys. Rev. D 101.12 (2020), p. 122001. DOI: 10.1103/PhysRevD.101.122001. arXiv: 1908.06050 [gr-qc].

[352] Stephen R. Taylor, Jonathan R. Gair, and Ilya Mandel. "Hubble without the Hubble: Cosmology using advanced gravitational-wave detectors alone". In: Phys. Rev. D 85 (2012), p. 023535. DOI: 10.1103/PhysRevD.85.023535. arXiv: 1108.5161 [gr-qc].

[353] Will M. Farr et al. "A Future Percent-Level Measurement of the Hubble Expansion at Redshift 0.8 With Advanced LIGO". In: Astrophys. J. Lett. 883.2 (2019), p. L42. DOI: 10.3847/2041-8213/ab4284. arXiv: 1908.09084 [astro-ph.CO].

[354] S. Mastrogiovanni et al. "On the importance of source population models for gravitational-wave cosmology". In: Phys. Rev. D 104.6 (2021), p. 062009. DOI: 10.1103/PhysRevD.104.062009. arXiv: 2103.14663 [gr-qc].

[355] Andreas Finke et al. "Cosmology with LIGO/Virgo dark sirens: Hubble parameter and modified gravitational wave propagation". In: JCAP 08 (2021), p. 026. DOI: 10.1088/1475-7516/2021/08/026. arXiv: 2101.12660 [astro-ph.CO].

[356] Suvodip Mukherjee et al. "Accurate precision Cosmology with redshift unknown gravitational wave sources". In: Phys. Rev. D 103.4 (2021), p. 043520. DOI: 10.1103/PhysRevD.103.043520. arXiv: 2007.02943 [astro-ph.CO].

[357] Cristina Cigarran Diaz and Suvodip Mukherjee. "Mapping the cosmic expansion history from LIGO-Virgo-KAGRA in synergy with DESI and SPHEREx". In: (July 2021). arXiv: 2107.12787 [astro-ph.CO].

[358] B. P. Abbott et al. "Prospects for Observing and Localizing Gravitational-Wave Transients with Advanced LIGO, Advanced Virgo and KAGRA". In: Living Rev. Rel. 21.1 (2018), p. 3. DOI: 10.1007/s41114-018-0012-9. arXiv: 1304.0670 [gr-qc].

[359] Lisa Barsotti et al. Updated Advanced LIGO sensitivity design curve. Tech. rep. LIGO-T1800044. LIGO Laboratory, 2018. URL: https://dcc.ligo.org/LIGO-T1800044/public.

[360] M. Tse et al. "Quantum-Enhanced Advanced LIGO Detectors in the Era of Gravitational-Wave Astronomy". In: Phys. Rev. Lett. 123 (23 2019), p. 231107. DOI: 10.1103/PhysRevLett.123.231107. URL: https://link.aps.org/doi/10.1103/PhysRevLett.123.231107.

[361] B. P. Abbott et al. "A gravitational-wave standard siren measurement of the Hubble constant". In: Nature 551.7678 (2017), pp. 85–88. DOI: 10.1038/nature24471. arXiv: 1710.05835 [astro-ph.CO].

[362] B. P. Abbott et al. "Gravitational Waves and Gamma-rays from a Binary Neutron Star Merger: GW170817 and GRB 170817A". In: Astrophys. J. Lett. 848.2 (2017), p. L13. DOI: 10.3847/2041-8213/aa920c. arXiv: 1710.05834 [astro-ph.HE].

[363] B. P. Abbott et al. "GW170817: Observation of Gravitational Waves from a Binary Neutron Star Inspiral". In: Phys. Rev. Lett. 119.16 (2017), p. 161101. DOI: 10.1103/PhysRevLett.119.161101. arXiv: 1710.05832 [gr-qc].

[364] B. P. Abbott et al. "Multi-messenger Observations of a Binary Neutron Star Merger". In: Astrophys. J. Lett. 848.2 (2017), p. L12. DOI: 10.3847/2041-8213/aa91c9. arXiv: 1710.05833 [astro-ph.HE].

[365] B. P. Abbott et al. “Properties of the binary neutron star merger GW170817”. In: Phys. Rev. X 9.1 (2019), p. 011001. DOI: 10.1103/PhysRevX.9.011001. arXiv: 1805.11579 [gr-qc].

[366] Evan D. Hall et al. “Systematic calibration error requirements for gravitational-wave detectors via the Cramér–Rao bound”. In: Class. Quant. Grav. 36.20 (2019), p. 205006. DOI: 10.1088/1361-6382/ab368c. arXiv: 1712.09719 [astro-ph.IM].

[367] Ling Sun et al. “Characterization of systematic error in Advanced LIGO calibration”. In: Class. Quant. Grav. 37.22 (2020), p. 225008. DOI: 10.1088/1361-6382/abb14e. arXiv: 2005.02531 [astro-ph.IM].

[368] Ling Sun et al. “Characterization of systematic error in Advanced LIGO calibration in the second half of O3”. In: ArXiv e-prints (June 2021). arXiv: 2107.00129 [astro-ph.IM].

[369] Salvatore Vitale et al. “Effect of calibration errors on Bayesian parameter estimation for gravitational wave signals from inspiral binary systems in the Advanced Detectors era”. In: Phys. Rev. D 85 (2012), p. 064034. DOI: 10.1103/PhysRevD.85.064034. arXiv: 1111.3044 [gr-qc].

[370] Ethan Payne et al. “Gravitational-wave astronomy with a physical calibration model”. In: Phys. Rev. D 102 (2020), p. 122004. DOI: 10.1103/PhysRevD.102.122004. arXiv: 2009.10193 [astro-ph.IM].

[371] Salvatore Vitale et al. “Physical approach to the marginalization of LIGO calibration uncertainties”. In: Phys. Rev. D 103.6 (2021), p. 063016. DOI: 10.1103/PhysRevD.103.063016. arXiv: 2009.10192 [gr-qc].

[372] Reed Essick and Daniel E. Holz. “Calibrating gravitational-wave detectors with GW170817”. In: Class. Quant. Grav. 36.12 (2019), p. 125002. DOI: 10.1088/1361-6382/ab2142. arXiv: 1902.08076 [astro-ph.IM].

[373] B. F. Schutz and B. S. Sathyaprakash. "Self-calibration of Networks of Gravitational Wave Detectors". In: ArXiv e-prints (Sept. 2020). arXiv: 2009.10212 [gr-qc].

[374] B. P. Abbott et al. "Calibration of the Advanced LIGO detectors for the discovery of the binary black-hole merger GW150914". In: Phys. Rev. D 95.6 (2017), p. 062003. DOI: 10.1103/PhysRevD.95.062003. arXiv: 1602.03845 [gr-qc].

[375] D. Tuyenbayev et al. "Improving LIGO calibration accuracy by tracking and compensating for slow temporal variations". In: Class. Quant. Grav. 34.1 (2017), p. 015002. DOI: 10.1088/0264-9381/34/1/015002. arXiv: 1608.05134 [astro-ph.IM].

[376] Frank Ohme et al. "Statistical and systematic errors for gravitational-wave inspiral signals: A principal component analysis". In: Phys. Rev. D 88.4 (2013), p. 042002. DOI: 10.1103/PhysRevD.88.042002. arXiv: 1304.7017 [gr-qc].

[377] Christopher P. L. Berry et al. "Parameter estimation for binary neutron-star coalescences with realistic noise during the Advanced LIGO era". In: Astrophys. J. 804.2 (2015), p. 114. DOI: 10.1088/0004-637X/804/2/114. arXiv: 1411.6934 [astro-ph.HE].

[378] B. P. Abbott et al. "Properties of the Binary Black Hole Merger GW150914". In: Phys. Rev. Lett. 116.24 (2016), p. 241102. DOI: 10.1103/PhysRevLett.116.241102. arXiv: 1602.03840 [gr-qc].

[379] Salvatore Vitale et al. "Inferring the properties of a population of compact binaries in presence of selection effects". In: ArXiv e-prints (July 2020). arXiv: 2007.05579 [astro-ph.IM].

[380] Aaron Zimmerman, Carl-Johan Haster, and Katerina Chatziioannou. "On combining information from multiple gravitational wave sources". In: Phys. Rev. D 99.12 (2019), p. 124044. DOI: 10.1103/PhysRevD.99.124044. arXiv: 1903.11008 [astro-ph.IM].

[381] W. Farr, B. Farr, and T. Littenberg. Updated Advanced LIGO sensitivity design curve. Tech. rep. LIGO-T1400682. LIGO Laboratory, 2014. URL: https://dcc.ligo.org/LIGO-T1400682/public.

[382] Cullan Howlett and Tamara M. Davis. "Standard siren speeds: improving velocities in gravitational-wave measurements of H_0". In: Mon. Not. Roy. Astron. Soc. 492.3 (2020), pp. 3803–3815. DOI: 10.1093/mnras/staa049. arXiv: 1909.00587 [astro-ph.CO].

[383] Suvodip Mukherjee et al. "Velocity correction for Hubble constant measurements from standard sirens". In: Astron. Astrophys. 646 (2021), A65. DOI: 10.1051/0004-6361/201936724. arXiv: 1909.08627 [astro-ph.CO].

[384] Hsin-Yu Chen. "Systematic Uncertainty of Standard Sirens from the Viewing Angle of Binary Neutron Star Inspirals". In: Phys. Rev. Lett. 125.20 (2020), p. 201301. DOI: 10.1103/PhysRevLett.125.201301. arXiv: 2006.02779 [astro-ph.HE].

[385] LIGO Scientific Collaboration and Virgo Collaboration. "GWTC-2: Compact Binary Coalescences Observed by LIGO and Virgo during the First Half of the Third Observing Run". In: Phys. Rev. X 11 (2 2021), p. 021053. DOI: 10.1103/PhysRevX.11.021053. URL: https://link.aps.org/doi/10.1103/PhysRevX.11.021053.

[386] The LIGO Scientific Collaboration et al. "An improved analysis of GW150914 using a fully spin-precessing waveform model". In: ArXiv e-prints (June 2016). arXiv: 1606.01210 [gr-qc].

[387] S. Vitale et al. "Impact of Bayesian Priors on the Characterization of Binary Black Hole Coalescences". In: Physical Review Letters 119.25, 251103 (Dec. 2017), p. 251103. DOI: 10.1103/PhysRevLett.119.251103. arXiv: 1707.04637 [gr-qc].

[388] Kent Yagi and Nicolás Yunes. "Approximate Universal Relations for Neutron Stars and Quark Stars". In: Phys. Rept. 681 (2017), pp. 1–72. DOI: 10.1016/j.physrep.2017.03.002. arXiv: 1608.02582 [gr-qc].

[389] Andrea Maselli et al. “Equation-of-state-independent relations in neutron stars”. In: Phys. Rev. D 88.2 (2013), p. 023007. DOI: 10.1103/PhysRevD.88.023007. arXiv: 1304.2052 [gr-qc].